Changes in Metabolism during Zebrafish Development, Wound Healing and Regeneration

A thesis submitted to The University of Manchester for the degree of Doctor of Philosophy in the Faculty of Biology, Medicine and Health

2021

Claire A. Scott

School of Biological Sciences
Division of Cell Matrix Biology & Regenerative Medicine

List of Contents

Word count: 46,661

List of Figures & Tables

List of Abbreviations

2-APB	2-aminoethoxydiphenyl borate
2DG	2-deoxy-D-glucose
AA	antimycin A
acetyl Co-A	acetyl coenzyme A
ADP	adenosine diphosphate
Akt	protein kinase B
ATP	adenosine triphosphate
BMP	bone morphogenic protein
Cdk1	cyclin-dependent kinase 1
CFP	cyan fluorescent protein
cpFP	cyclically permuted fluorescent protein
cpYFP	cyclically permuted yellow fluorescent protein
DAG	diacylglycerol
DMSO	dimethyl sulfoxide
DPI	diphenyleneiodonium
DUOX	dual oxidase
EGFR	epidermal growth factor receptor
EMT	epithelial to mesenchymal transition
EpiSC	post-implantation epiblast stem cells
ERK	extracellular signal-regulated kinase
ESC	embryonic stem cell
ETC	electron transport chain
FGF	fibroblast growth factor
FRET	förster resonance energy transfer
FX11	7-benzyl-2,3-dihydroxy-6-methyl-4-propyl-1-naphthoic acid
GAPDH	glyceraldehyde-3-phosphate dehydrogenase
GECIs	genetically encoded calcium indicators
GFP	green fluorescent protein
GSSG/GSH	oxidised/reduced glutathione
H_2O_2	hydrogen peroxide
HIF1α	hypoxia-inducible factor-1-alpha
hpa	hours post amputation

hpf	hours post fertilisation
ICM	inner cell mass
IP_3	inositol trisphosphate
iPSCs	induced pluripotent stem cells
LDH	lactate dehydrogenase
MAPK	mitogen-activated protein kinase
MAS	malate-aspartate shuttle
MBT	midblastula transition
MEK	mitogen-activated protein kinase
minspa	minutes post amputation
MS	mass spectrometry
NAD/H	nicotinamide adenine dinucleotide
NADP/H	nicotinamide adenine dinucleotide phosphate
NaN_3	sodium azide
NF-κB	nuclear factor kappa B
NMR	nuclear magnetic resonance
OXPHOS	oxidative phosphorylation
PFBSF	pentafluorobenzenesulfonyl fluorescein
PI3K	phosphatidylinositol 3-kinase
PIP_2	phosphatidylinositol 4,5-bisphosphate
PKC	protein kinase C
PKM2/M2	pyruvate kinase isozyme M1/M2
PLC	phospholipase C
PMA	phorbol-12-myristate-13-acetate
PPP	pentose phosphate pathway
ROS	reactive oxygen species
TGF-β	transforming growth factor beta
YFP	yellow fluorescent protein

Abstract

An interest in metabolism dates back centuries, with Charles Manning Child being the first to propose a role for metabolism in specifying developing structures during embryogenesis in the 1900s. Modern tools and techniques are now available to allow the detailed analysis of patterns and changes in metabolites, such as with genetically encoded biosensors, which permit the study of metabolism with spatial and temporal resolution *in vivo*. In this thesis, I ask the central question: Can genetically encoded biosensors be used in zebrafish to observe changes in metabolism during development or regeneration and wound healing? If changes occur, is this metabolic reprogramming important and consequential for these systems? Evidence of metabolites such as hydrogen peroxide (H_2O_2) and lactate acting as second messengers or influencing signalling pathways are becoming increasingly apparent. An initial burst and subsequent oscillations of mitochondrial H_2O_2 have been shown to be important for the cleavage stage *Xenopus* embryo, while H_2O_2 and a switch to glycolytic metabolism are essential for successful regeneration, with blastemal cells displaying up-regulated expression of glycolytic genes. Inhibition of either H_2O_2 production or glycolysis reduces the number of proliferating cells in the regenerating zebrafish fin and heart, and this link leads us to postulate that the Warburg effect—associated with providing molecules for the generation of biomass in highly proliferative systems—may be activated in regeneration. Development involves significant growth, and is therefore also a promising candidate for metabolic reprogramming and the Warburg effect. This project aims to determine whether a more diverse role for metabolic alteration in development and wound healing can be distinguished using genetically encoded biosensors in the zebrafish model. The sensors were sub-cloned into constructs for testing *in vivo* via mRNA injections, followed by the generation of transgenic lines to yield brightly expressing embryos at both early developmental stages and two days post fertilisation for larval fin amputations. I establish that the sensors Laconic, for lactate detection, and SoNar, for monitoring NADH/NAD+ ratio, are viable in zebrafish embryos; using transgenic lines of these two sensors and HyPer, for H_2O_2, combined with pharmacological treatment, I demonstrate that lactate increases following the midblastula transition, suggesting possible employment of Warburg metabolism upon increased growth of the embryo, while an increase in lactate occurs immediately following amputation, putatively to generate rapid ATP for the contraction of the actomyosin cable responsible for wound closure. Inhibition of glycolysis over the entire period of regeneration results in attenuated regeneration, concurring with existing literature citing the importance of glycolysis in zebrafish regeneration. I also investigate H_2O_2, calcium, lactate, and NADH/NAD+ ratio in a zebrafish mutant for *hai1a* and show the phenotype shares similarities with a constitutively healing wound, including high H_2O_2 levels, sterile inflammation, and elevated lactate levels in abnormally proliferative keratinocyte aggregates. The work in this thesis contributes further evidence of the importance of glycolytic metabolism in a systems biology context with a function besides ATP generation, forming a foundation for future work, potentially presenting a target for regenerative therapies.

Declaration

No portion of the work referred to in the thesis has been submitted in support of an application for another degree or qualification of this or any other university or other institute of learning

Copyright Statement

Acknowledgements

I would like to take the opportunity to thank everyone who has assisted in the extended journey of my PhD, both in Manchester and in Singapore, be it in person or over the internet, your support has been immeasurably valuable.

Firstly, I would like to thank my supervisors Enrique Amaya and Tom Carney for their guidance, patience and support throughout, and particularly for their understanding during the periods I faced personal additional challenges. I would also like to thank the members of both labs, for all your advice and help, and for welcoming me and making me laugh each day. You all helped me improve as a team member and a human being, and it was a pleasure to come to work every day and all do science together. In particular thank you to Kat Marsay, for adopting me into her life when I was new in the country, and Kunal Chopra, for his infectiously ridiculous demeanour and cheering me up on numerous occasions.

Thank you to my friends and family, especially Matt Bradley (for being a reliable source of bird related internet content and helping me drink all the gin so I didn't suffer from lonely alcohol poisoning), Cam Ross (for making an effort during the lockdown(s) of 2020+ to just be my friend), Fritha Turner (for reminding me I'm not the only crazy person and nurturing my few remaining serotonin molecules with empathy), and Steph Scott (for not disowning me). To the many others I haven't mentioned by name, I still value your friendship and presence in my life, but my fingers are too tired to type out an extensive list of names after writing the roughly 50,000 words that comprise this detailed record of four years worth of modest distress. Sorry.

Thanks also goes to Peter March for his help and patience with my slightly panicked and more than slightly frustrated cries for microscope help. Similarly, thanks to Balakrishnan Kannan of the Lee Kong Chian School of Medicine at the Nanyang Technological University, Singapore, for being so accommodating and assisting with microscopy.

Thank you to the University of Manchester and the A*STAR institute for providing funding for my PhD; needless to say, I couldn't have done it without you.

And finally, thank you to all the pigeons of the world for always being there when I needed some time out of real life, never judging me, and accepting me as one of your own.

1: General Introduction

1.1 The Warburg Effect and Glycolysis

Originally described in cancer cells by Otto Warburg (Warburg, 1925), the Warburg effect is also known as aerobic glycolysis, characterised by the increased use of the glycolytic pathway in preference to oxidative phosphorylation (OXPHOS) and the mitochondria (FIG 1.1). Initially, it was proposed that cancer cells possessed defective mitochondria, though this was found not to be the case (Fantin et al., 2006), and furthermore it was calculated that availability of adenosine triphosphate (ATP) is not a limiting factor in tumours or biosynthesis (Kilburn et al., 1969; reviewed in Vander Heiden et al., 2009). Instead, the most commonly taken view now presents the Warburg effect as a way of accommodating the requirements of the cellular growth and anabolism involved in rapid proliferation (reviewed in Lunt & Vander Heiden, 2011).

Under normal circumstances, the cell will metabolise glucose into pyruvate to produce ATP for energy via the efficient Krebs cycle and mitochondrial OXPHOS. Glycolytic metabolism of glucose is far less efficient, producing only two molecules of ATP per molecule of glucose as opposed to the generally accepted ~36 made by the mitochondria, and usually only active in anaerobic conditions when there is insufficient oxygen to support OXPHOS (Alberts et al., 2002). However, cell proliferation requires not only energy from ATP – for example, carbon for the generation of macromolecules, and nicotinamide adenine dinucleotide phosphate (NADPH) as a reducing agent. OXPHOS, though incredibly efficient in terms of ATP production, generates carbon dioxide and thus expends many carbon molecules that could otherwise be incorporated into nucleotides, amino acids, and lipids, for constructing cellular components. The complete metabolism of glucose via OXPHOS thus creates an imbalance of necessary ingredients, with too much ATP and too few available carbons (reviewed in: Vander Heiden et al., 2009; Lunt & Vander Heiden, 2011; X. Chen et al., 2015; Liberti & Locasale, 2016). ATP production is not a priority; by contrast, the intermediates from glycolysis and the pentose phosphate pathway (PPP), which branches from and feeds back into glycolysis, can be used as substrates for biosynthesis (FIG 1.2), making a reduction in mitochondrial activity and an increase in glycolysis favourable for proliferative systems.

Indeed, in addition to its initial discovery in cancer cells, the Warburg effect or application of aerobic glycolysis has been documented in other highly proliferative systems or those that involve significant cellular growth. The Warburg effect has been demonstrated in development of *Xenopus* retina (Fiske & Vander Heiden, 2012) and early mouse embryos (Houghton et al., 1996) (glucose metabolism in development is discussed in more detail in 3: Metabolism in Early Zebrafish Development), and a glycolytic switch is required for proliferation in zebrafish heart and larval tail regeneration (Honkoop et al., 2019; Sinclair et al., 2020) (glucose metabolism in regeneration is discussed in more detail in 4: Metabolism in the Zebrafish Fin Amputation Model of Wound Healing and Regeneration).

The immune response is also a known system that employs a switch to glycolytic metabolism (reviewed in E. L. Pearce & Pearce, 2013 and Palsson-McDermott et al., 2015). First seen in lymphocytes as early as the 1970s (Roos & Loos, 1970; Tingchung Wang et al., 1976), the same metabolic shift was then identified in macrophages (Newsholme et al., 1986), dendritic cells (Kelly & O'Neill, 2015), and neutrophils (Borregaard & Herlin, 1982). The latter possesses few mitochondria which do not seem to contribute to energy production, and rather have a role in apoptosis (Maianski et al., 2004) and regulation of glycolysis (van Raam et al., 2008). Inhibition of glycolysis in macrophages also decreases the immune response, while mitochondrial inhibitors produce no such effects (Kelly & O'Neill, 2015).

The inflammatory immune response is well-linked to wound healing, as one of the early responses to injury (reviewed in Eming et al., 2007). Not only does regeneration involve an immune response, but also requires a high degree of proliferation to replace lost biomass. As such, regeneration is a likely candidate for the Warburg effect, and there is in fact evidence showing up-regulation of glycolysis genes in *Xenopus* tadpole tail (Love et al., 2014), zebrafish heart (Honkoop et al., 2019) and zebrafish larval tail (Sinclair et al., 2020) regeneration.

Precisely how this metabolic switch is regulated is largely unknown, however several signalling pathways and molecules have been implicated. Pyruvate kinase (PK) is the enzyme responsible for mediating the flow of glucose into the citric acid cycle in the mitochondria, and can be one of two isoforms created from the same alternatively spliced RNA transcript. The adult form, PKM1, is expressed in terminally differentiated cells that require high amounts of ATP, while PKM2 is preferentially expressed in cancer (reviewed in Prakasam et al., 2018), embryonic (Noguchi et al., 1986), and regenerating tissues (Garnett et al., 1974). PKM2 is thus linked to proliferation, for instance in murine heart regeneration as a regulator of the cell cycle (Magadum et al., 2020), and has a known positive influence on glycolytic activity: replacing PKM2 with the M1 isoform abolishes the Warburg effect in cancer cells, suggesting the M2 form is necessary for aerobic glycolysis in these cells (Christofk et al., 2008). PKM1 is constitutively active, whereas PKM2 is subject to regulation. Reactive oxygen species (ROS) are one of the ways PKM2 activity can be altered, acting as an inhibitor (Anastasiou et al., 2011) (ie. preventing the entry of pyruvate into the citric acid cycle) and thus driving metabolism towards glycolysis rather than OXPHOS. Besides this, epidermal growth factor receptor (EGFR) activation promotes translocation of PKM2 into the nucleus where it interacts with β-catenin to induce expression of cell cycle protein, cyclin D1 (Yang et al., 2011), demonstrating a non-metabolic role of PKM2 in stimulating proliferation. Another glycolytic enzyme, 6-phosphofructo-2-kinase/ fructose-2,6-biphosphatase 4 (PFKFB4), can also directly interact with cell cycle regulators to promote proliferation in a likewise non-metabolic approach (Dasgupta et al., 2018).

PKM2 is also able to interact with hypoxia-inducible factor-1-alpha (HIF1α) in the nucleus to stimulate the expression of glycolytic genes in cancer cells (Luo et al., 2011), and is both up-regulated in preference to its M1 counterpart by HIF1α (Prigione et al., 2014; Williams et al., 2018) and capable of causing an increase in HIF1α signalling to critically regulate the Warburg effect in macrophages (Palsson-McDermott et al., 2015). Together with PKM2, HIF1α is important for the glycolytic switch required for the dedifferentiation of induced pluripotent stem

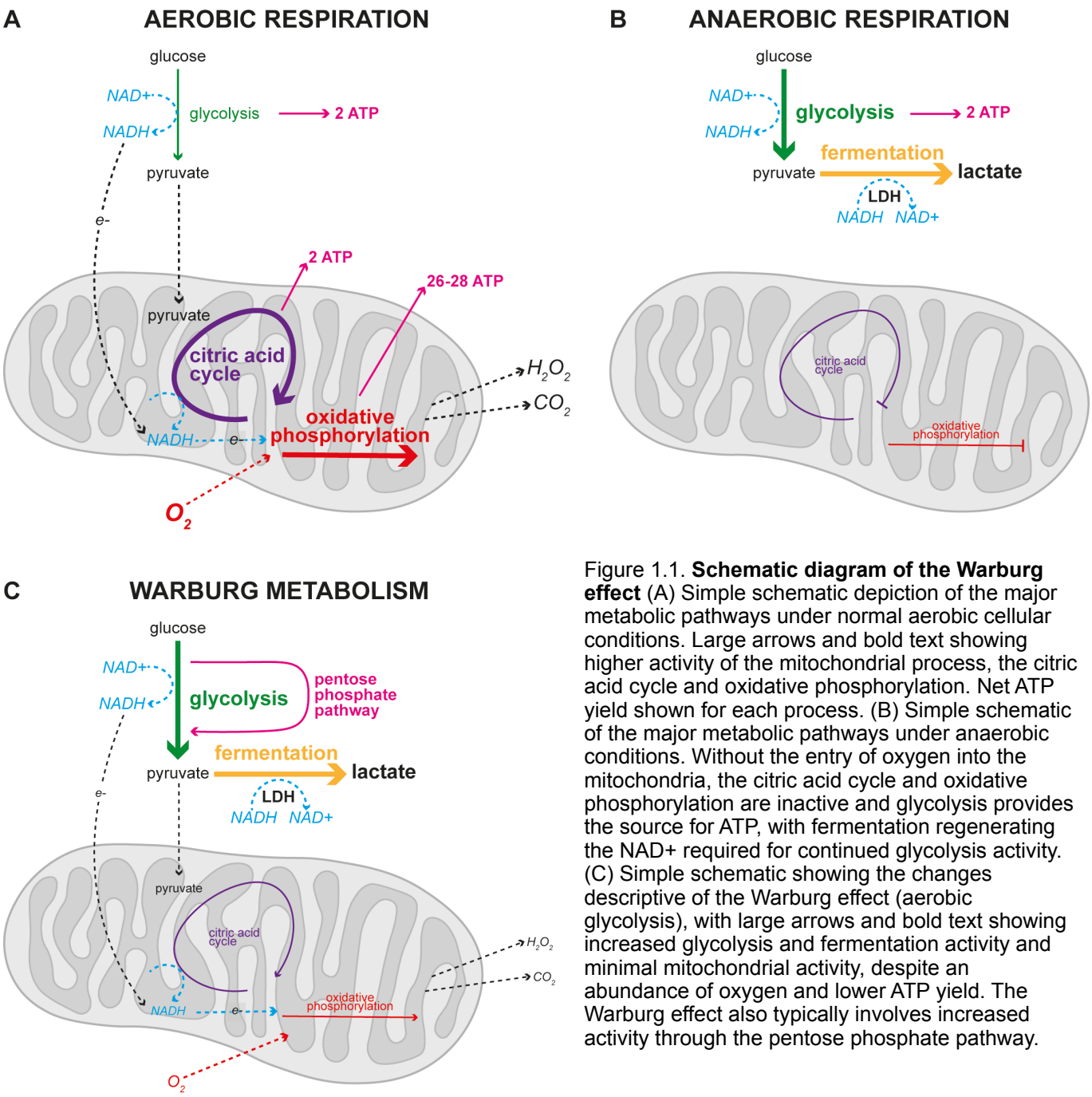

Figure 1.1. **Schematic diagram of the Warburg effect** (A) Simple schematic depiction of the major metabolic pathways under normal aerobic cellular conditions. Large arrows and bold text showing higher activity of the mitochondrial process, the citric acid cycle and oxidative phosphorylation. Net ATP yield shown for each process. (B) Simple schematic of the major metabolic pathways under anaerobic conditions. Without the entry of oxygen into the mitochondria, the citric acid cycle and oxidative phosphorylation are inactive and glycolysis provides the source for ATP, with fermentation regenerating the NAD+ required for continued glycolysis activity. (C) Simple schematic showing the changes descriptive of the Warburg effect (aerobic glycolysis), with large arrows and bold text showing increased glycolysis and fermentation activity and minimal mitochondrial activity, despite an abundance of oxygen and lower ATP yield. The Warburg effect also typically involves increased activity through the pentose phosphate pathway.

cells (Prigione et al., 2014), as a knockdown of HIF signalling prevents human fibroblast cells from returning to pluripotency (Mathieu et al., 2014). HIF1α signalling is also sufficient for inducing the switch to glycolytic metabolism in mouse embryonic stem cells (Zhou et al., 2012), and known to have a positive effect on glycolysis, such as in cancer (reviewed in Nagao et al., 2019) and macrophages (Ting Wang et al., 2017). Its over-expression in many types of cancer correlates with increased cell proliferation, in line with the hallmarks of the Warburg effect, and advocates growth and metastasis (Zhong et al., 1999).

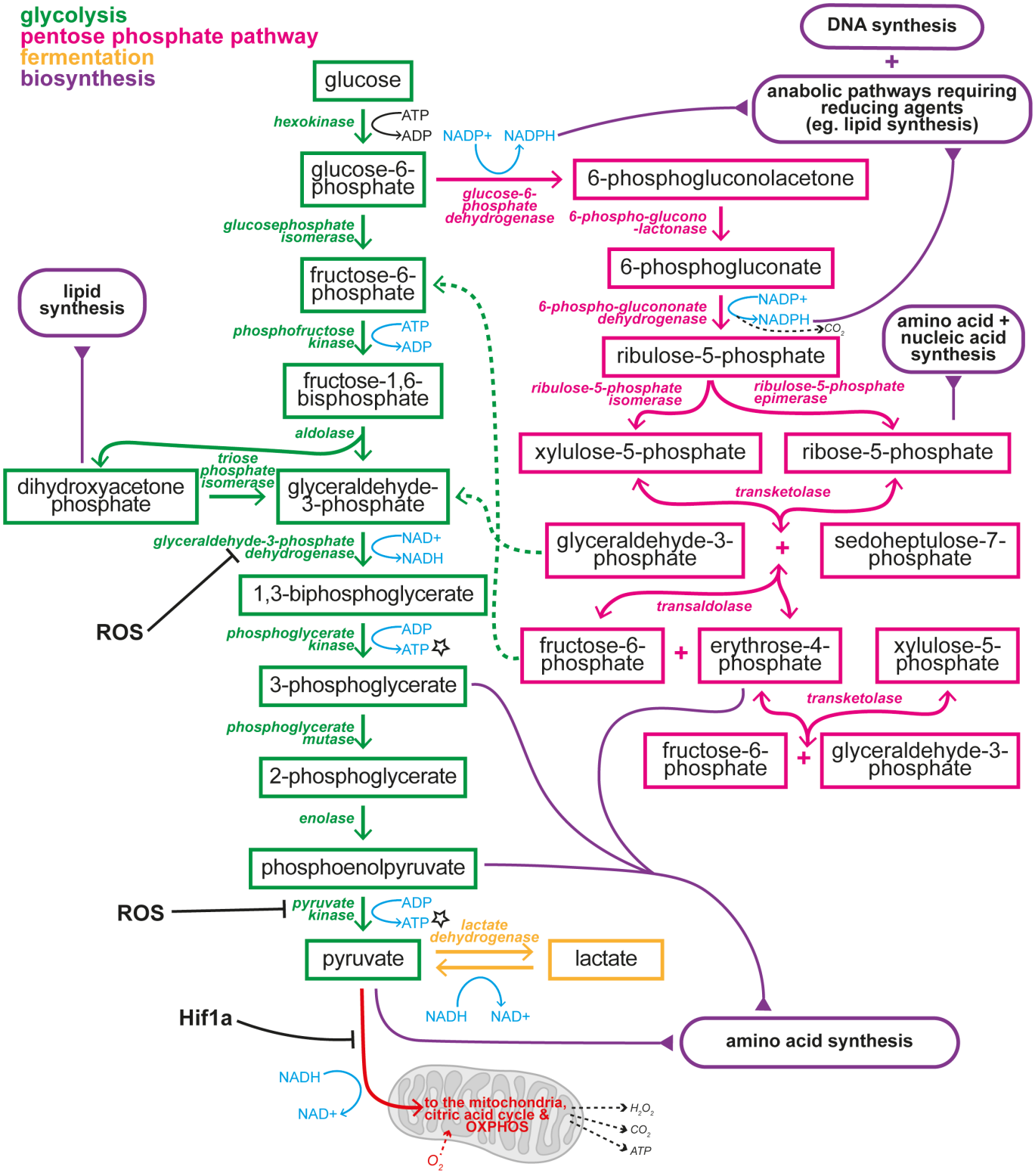

Figure 1.2. **Simplified schematic of the glycolysis and pentose phosphate pathway (PPP) intermediates.** Pathways of glycolysis (green) and the PPP (pink), with enzymes in italicised text and contributions of intermediates to anabolism (purple). Green dashed arrow show re-entry of PPP molecules into glycolysis. Co-factor reactions shown in blue, fermentation for anaerobic glycolysis or the Warburg effect shown in yellow, potential inhibitory interactions of reactive oxygen species (ROS) and HIF1α shown in black. Starred icon indicates production of ATP. Adapted from Love et al., 2014. Figure 2.

1.2 Reactive Oxygen Species

Reactive oxygen species (ROS) is a term that includes multiple compounds generated by oxygen metabolism, such as superoxides, hydroxyl radicals, and peroxides, most notably hydrogen peroxide (H_2O_2). Traditionally, ROS are considered damaging, with cells experiencing "oxidative stress" as a by-product of oxidative phosphorylation (OXPHOS) and mitochondrial metabolism. However, studies are increasingly revealing an importance of H_2O_2 and ROS in physiological processes and multiple consequential signalling cascades (reviewed in Q. Zhang et al., 2016). To date, ROS have been implicated in differentiation, apoptosis, ageing, migration, and proliferation (Finkel & Holbrook, 2000; Sauer et al., 2001; Lambeth, 2004; reviewed in Schieber & Chandel, 2014; Pak et al., 2020). See FIG 1.3A for a simplified summary of some of the relevant pathways and processes which which ROS interact discussed throughout this chapter.

1.2.1 Sources of reactive oxygen species

There are two well-recognised primary sources of ROS: the more overt being its generation during aerobic metabolism in the mitochondria (reviewed in Murphy, 2009), and also by NADP oxidases (NOXes) (reviewed in Bedard & Krause, 2007) (FIG 1.3B). There are multiple sites within the mitochondria at which superoxides, which are then processed into H_2O_2, are formed, the principal positions being at complexes I and III, though ROS are also generated by other metabolic enzymes such as pyruvate dehydrogenase (reviewed in Holmström & Finkel, 2014) (FIG 1.3C). Mitochondrial ROS are important for example in early *Xenopus* embryos (Y. Han et al., 2018; see 3: Metabolism in Early Zebrafish Development, section 3.1.2) and H_2O_2 from the calcium-sensitive NOX variant, dual oxidase (DUOX), which is able to respond to ROS as well as generate it, is important for instance in regeneration of *Xenopus* (Love et al., 2013) and zebrafish (Niethammer et al., 2009; see 4: Metabolism in the Zebrafish Fin Amputation Model of Wound Healing and Regeneration, section 4.1.2). It has additionally been shown that NOX generated H_2O_2 is able to regulate mitochondrial production of superoxide (Ahmed et al., 2012) and vice versa (Dikalova et al., 2010), indicating a potential importance of cross-regulation between ROS. ROS are also produced by other, less studied sources, arising for instance as an enzymatic byproduct of nitric oxide and xanthine oxidase (reviewed in Holmström & Finkel, 2014).

1.2.2 Target effects of reactive oxygen species

Redox signalling refers to the interaction between two molecules exchanging electrons, typically a sensor signalling protein and a second messenger. In reductive reactions, the second messenger acts as a reductant to donate electrons to the target protein, while in oxidative reactions the inverse occurs and the second messenger accepts electrons (reviewed in Forman et al., 2014). One of the key groups of molecules involved are reactive oxygen species (ROS), with superoxides and hydrogen peroxide (H_2O_2) accepting electrons for many oxidation-reduction reactions involved in cell growth, differentiation, and death. As such, metabolites like H_2O_2 can act as

second messengers. For instance, ROS interact with the nuclear factor kappa B (NFκB) signalling pathways, thus influencing the various processes associated with these pathways, including proliferation, differentiation, the cell cycle, apoptosis, and the immune response (reviewed in J. Zhang et al., 2016) (FIG 1.3A). Mitochondrial NFκB has in fact been shown to negatively regulate expression of electron transport chain genes in the mitochondria (Cogswell et al., 2003), thus ROS may feed back and further influence metabolism and mitochondrial respiration.

The amino acid cysteine is redox sensitive and proteins containing a cysteine residue can donate electrons to ROS (Rhee et al., 2000), resulting in alteration of their function (FIG 1.3D), and demonstrates another method in which ROS is able to influence signalling pathways and protein activity. In this way, H_2O_2 contributes to regulation of tyrosine kinases and transcription factors (reviewed in Covarrubias et al., 2008); particularly, this includes involvement in activation of mitogen-activated protein kinase (MAPK) pathways, which are important in cell proliferation (reviewed in W. Zhang & Liu, 2002). T-cell proliferation following activation by antigens is a ROS dependent mechanism, and mice lacking the ability to form mitochondrial ROS are unable to undergo specific activation and proliferation, due to absent gene activation by ROS signalling (Sena et al., 2013). ROS are thus implicated in many fundamental cellular processes, and by extension any phenomena that involve these processes, including regeneration and cancer. The intrinsic importance of these reactions means their regulation is tightly monitored, such that oxidant molecules are often found in conjunction with antioxidants or reductants, for example H_2O_2 with glutathione (reviewed in Schieber & Chandel, 2014).

Aside from redox biology, ROS have also been associated with regulation of glycolysis, linking ROS with both proliferation and the Warburg effect. HIF1α is largely associated with hypoxic conditions and has been shown to be directly regulated by ROS (Movafagh et al., 2015). In times of oxidative stress, glucose uptake is increased via HIF1α stabilisation to drive up-regulation and activity of glucose transporters (reviewed in Liemburg-Apers et al., 2015). Glucose enters the PPP to produce reduced glutathione which is used to detoxify H_2O_2, suggesting elevated import of glucose for the management of excess levels of ROS. In these situations, where concentration of H_2O_2 approaches the threshold after which apoptosis is triggered, it becomes energetically favourable to switch to a purely glycolytic metabolism. Mitochondrial activity results in more ROS being produced, and the energy generated by the electron transport chain would be consumed by the PPP to eliminate H_2O_2, therefore making oxidative metabolism inefficient due to the high energy demand for detoxification. H_2O_2 thereby drives glucose uptake and shunting of glucose into the PPP (Molavian et al., 2016). H_2O_2 is known to inhibit PKM2 (discussed in section 1.1), and in this instance could potentially be how it drives the metabolic shift to glycolysis. This provides evidence of ROS and glucose metabolism regulating one another, in that ROS can regulate glucose uptake, while glucose entering the PPP aids ROS scavenging, and conversely its entry into the mitochondria after conversion to pyruvate in glycolysis can increase ROS production.

Increasing H_2O_2 levels in tumour cells correspondingly increases glycolysis activity, and similarly decreasing H_2O_2 results in an attenuation of glycolysis activity (Shi et al., 2009). Contrastingly, H_2O_2 is also known to inhibit several enzymes involved in glycolysis, such as glyceraldehyde 3-phosphate dehydrogenase (GAPDH) (Colussi et

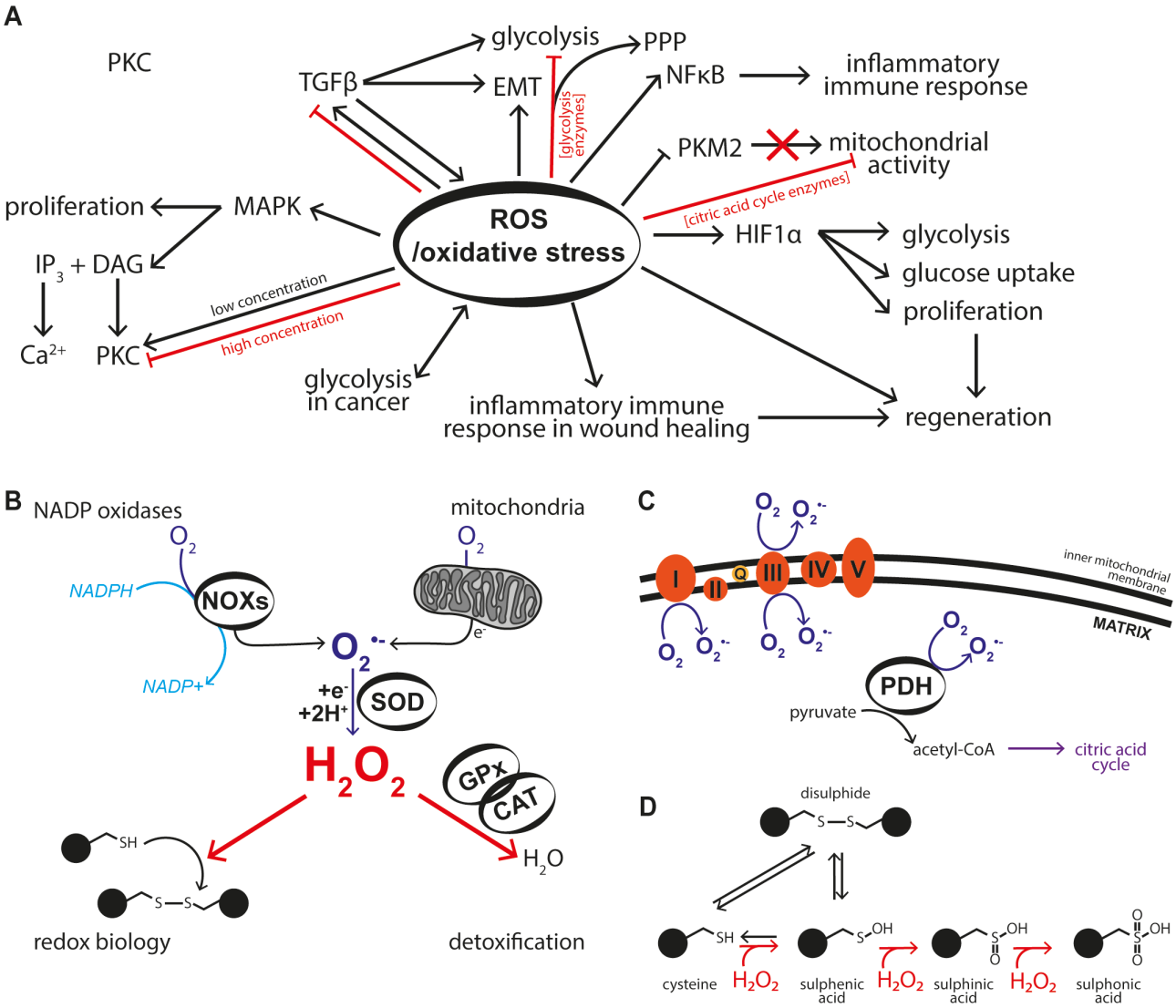

Figure 1.3 **Simplified schematic of select target effects and sources of reactive oxygen species.** (A) General summary of some of the relevant pathways and processes with which reactive oxygen species (ROS) interact. (B) Simplified depiction of the two main sources of ROS. Superoxide ($O^{\bullet-}$) is primarily made from NADPH oxidase enzymes (NOX) or the mitochondrial electron transport chain, primarily complexes I and III (C). Superoxide is converted to H_2O_2 by superoxide dismutases (SODs). H_2O_2 can go on to participate in redox signalling, for instance by oxidising cysteine residues on various proteins, or can be detoxified to water by antioxidants such as glutathione peroxidase (GPx) and catalase (CAT). Adapted from Schieber & Chandel, 2014, Figure 1. (C) Sources of superoxide from mitochondrial respiration, including the electron transport chain and the pyruvate dehydrogenase complex (PDH) responsible for converting pyruvate from glycolysis into acetyl-Co-A for entry into the citric acid cycle. (D) Oxidation of cysteine residues on proteins by ROS, altering their structure and function.

al., 2000; Mullarky & Cantley, 2015). This potentially serves as a strategy to direct intermediates into the PPP (Kuehne et al., 2015); however this inactivation of GAPDH by steady levels of elevated H_2O_2 is in actual fact also able to enhance activity of glycolysis and the PPP: the elevated levels of fructose 1,6-biphosphate (FBP) and 2-keto-3-deoxy-6-phosphogluconate (KDPG) (see FIG 1.2 for pathway) lead to dissociation of their corresponding glycolytic repressors (GapR and HexR, respectively) and results in de-repression of the glycolytic genes to overcome the originally H_2O_2-stalled glycolysis (Deng et al., 2014). Furthermore, H_2O_2 is capable of inactivating two enzymes involved in the citric acid cycle of the mitochondria (which feeds into the electron transport chain

and OXPHOS)—α-ketoglutarate dehydrogenase and succinate dehydrogenase—thereby decreasing mitochondrial activity, promoting a glycolytic switch and the Warburg effect (Nulton-Persson & Szweda, 2001).

1.3 Calcium

Calcium has a broad range of impacts on multiple aspects of biology, contributing to the physiology and biochemistry of cells, playing important roles in signalling transduction pathways, enzyme function, and membrane potential (reviewed in Clapham, 2007).

For instance, one of the common calcium signalling pathways is via release from the endoplasmic reticulum mediated by inositol trisphosphate (IP_3). G protein-coupled receptors cause the activation of phospholipase C (PLC), which in turn cleave the membrane protein phosphatidylinositol 4,5-bisphosphate (PIP_2) into IP_3 and diacylglycerol (DAG). The binding of IP_3 to its receptor (IP_3R) on the endoplasmic reticulum stimulates calcium release, which can go on to perform various roles within the cell cytoplasm (FIG 1.4A). This pathway is dominant in receptor biology and typically associated with the phrase "calcium signalling".

The following sections will focus only on calcium in development and regeneration, as these aspects are most relevant to this project, though the roles of calcium within biological systems extend beyond simply these two examples.

1.3.1 Calcium in development

A wave of calcium is seen following fertilisation of most, if not all, animals, including teleost fish, sea urchin, *Xenopus*, Drosophila, and mouse, causing resumption of the cell cycle, and this has been known for some time (Ridgway et al., 1977; Steinhardt et al., 1977; Cuthbertson et al., 1981; Busa & Nuccitelli, 1985; Z. Xu et al., 1994; Lee et al., 1999; Kaneuchi et al., 2015). A rise in H_2O_2 following *Xenopus* and sea urchin fertilisation is dependent on this calcium wave, and is required for correct development (Han et al., 2018; Heinecke & Shapiro, 1989).

Calcium oscillations are present during the cleavage divisions of both zebrafish (Chang & Meng, 1995; J. Chen et al., 2017) and *Xenopus* embryos (Muto et al., 1996). There is some discrepancy, however, between these two species regarding the role of calcium – in zebrafish, abundant evidence suggests the requirement of calcium for cytokinesis (Chan et al., 2015; reviewed in Webb et al., 2008), whereas suppression of calcium signalling in *Xenopus* did not affect cleavage (Noguchi & Mabuchi, 2002). Calcium gradients have also been suggested to play a role in axis specification, with the ventral side of early zebrafish embryos possessing higher levels of calcium at the shield stage, and the dorsal side showing relatively higher levels at slightly later stages (Gilland et al., 1999). Increasingly, cell migration during zebrafish epiboly has been shown to rely on calcium signalling. The leading migrating edge of the blastoderm is higher in calcium levels (Créton et al., 1998), and calcium waves propagate

along the blastoderm margin during the end of gastrulation and blastopore closure (Gilland et al., 1999; Webb & Miller, 2003a).

Thus, aside from its role to reactivate the cell cycle upon fertilisation, calcium has many roles as a second messenger throughout development and consequently affects a multitude of processes (reviewed in Webb & Miller, 2003b), and the underlying cause of many pathologies can be traced back to impaired calcium signalling or homeostasis (reviewed in Paudel et al., 2018). FIG 1.4B shows simplified schematic depictions of various calcium signalling during early zebrafish development.

1.3.2 Calcium in regeneration and wound healing

Calcium has been shown to be required for successful regeneration in various organisms. In all studies, calcium signalling appears to be from internal sources (Ghosh-Roy et al., 2010; S. Xu & Chisholm, 2011; Yoo et al., 2012; Tu & Borodinsky, 2014).

In *C. elegans*, rapid calcium waves induce signalling that mediates actin-dependent wound closure in the epidermis (S. Xu & Chisholm, 2011), while laser amputation of axons trigger similar calcium signals. Inhibition of this calcium signalling with a chelator reduces axon regrowth, while elevated calcium signalling increases regeneration (Ghosh-Roy et al., 2010).

Very rapid and very transient calcium waves propagate within three to five minutes post amputation in zebrafish larvae fin fold amputations, and short term inhibition with the inhibitor thapsigargin at the time of injury impairs later regeneration. Thus, early calcium signalling is required for successful overall regeneration, as are ROS (Niethammer et al., 2009; Yoo et al., 2012; Romero et al., 2018). However, inhibition of ROS production by NADPH oxidases by diphenyleneiodonium (DPI) does not affect calcium, and thapsigargin has no effect on the H_2O_2 gradient that is generated by amputation, indicating calcium and ROS in this instance are independent from one another (Yoo et al., 2012).

Calcium transients also occur in *Xenopus* tadpole tail amputations; these appear from two hours post amputation and are lost after 24 hours. They are not coincident with the early ROS production and are unlikely to have a role in stimulating DUOX activity, supporting the data in zebrafish suggesting that though presence of both early in the process is crucial, calcium and H_2O_2 act independently in the wound response. When treating with the calcium channel inhibitor ryanodine, the number of proliferating cells in the regenerating tail, in particular the muscle precursors, are reduced, demonstrating these calcium transients are important in the early regenerative stages for activation and proliferation, at least of muscle satellite cells (Tu & Borodinsky, 2014).

1.4 NADH/NAD+

Nicotinamide adenine dinucleotide (NAD) is a coenzyme and facilitates numerous biological reactions, in particular associated with metabolism. It exists in two forms: oxidised and reduced. The oxidised form (NAD+)

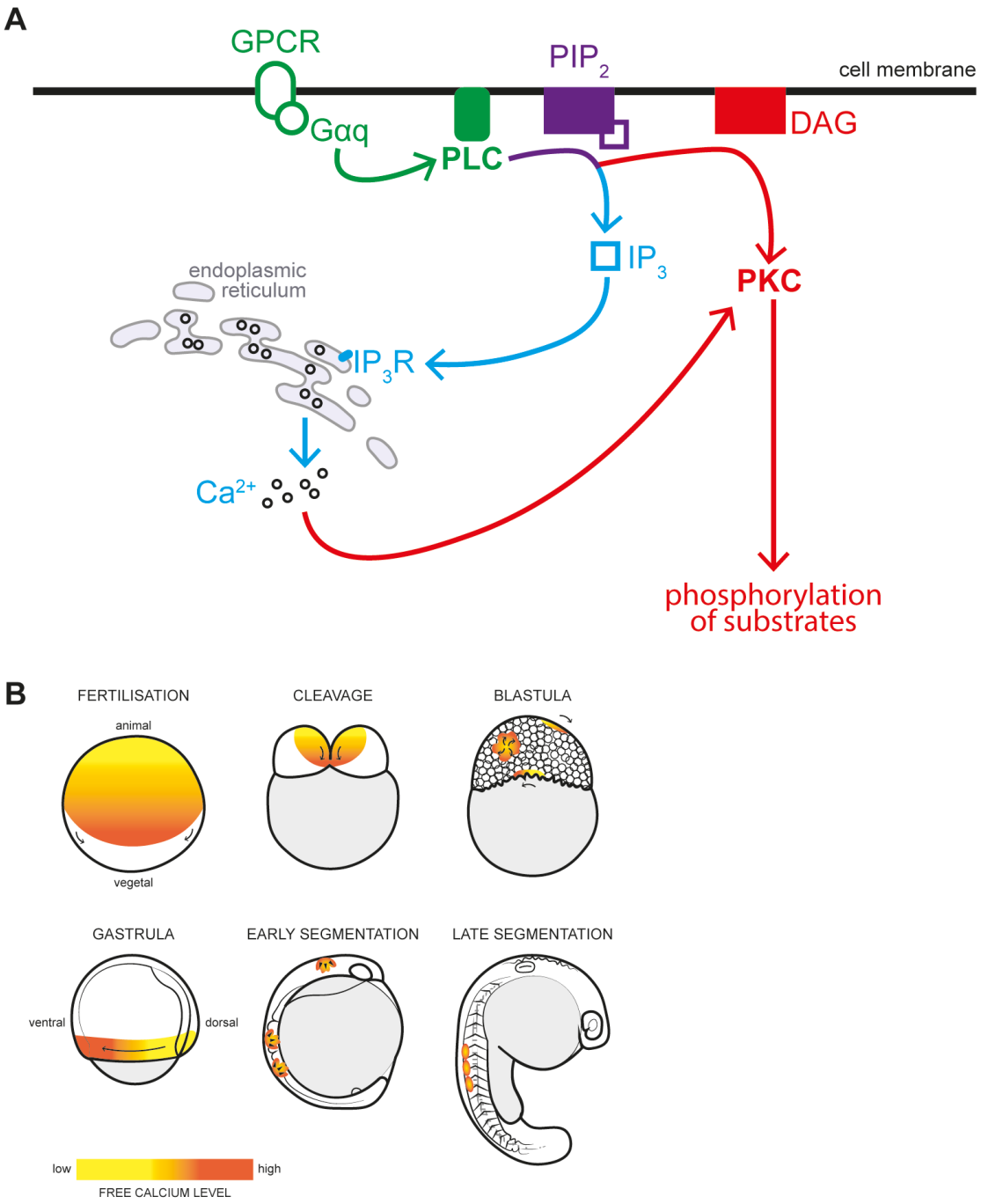

Figure 1.4. **Simplified calcium schematic.** (A) Schematic depiction of the inositol trisphosphate (IP_3) pathway for calcium release. Activation of a G protein-coupled receptor (GPCR) activates phospholipase C (PLC), which cleaves phosphatidylinositol 4,5-bisphosphate (PIP_2) into IP_3 and diacylglycerol (DAG). IP_3 binds to its receptor (IP_3R) on the endoplasmic reticulum to release calcium into the cytosol, which can go on to have a variety of effects, including activation of protein kinase C (PKC), which is additionally activated by DAG. (B) Examples of calcium signalling throughout early zebrafish development. Fertilisation triggers a global intracellular calcium wave. In subsequent cleavage, calcium signals are localised and transient, corresponding with cell divisions. Blastula stage embryos also demonstrate localised waves of intracellular calcium, while gastrula stage embryos have calcium gradients in addition to propagating waves at the leading edge of epiboly. During the segmentation stages, calcium signalling is apparent as localised, irregular pulses. Adapted from Webb & Miller, 2003. Figure 1.

consists of two nucleotides, an adenine and a positively charged nicotinamide, joined through their phosphate groups, while the reduced form (NADH) additionally possess a hydrogen on its nicotinamide (FIG 1.5A). NAD(H) is essential for cellular energy production and cell and DNA repair, as well as having antioxidant properties due to the reduced form's ability to donate electrons and thus prevent oxidation of other cellular molecules (Pollak et al., 2007). NAD+ and NADH are distinct from nicotinamide adenine dinucleotide phosphate (NADP+/H), the difference in their shapes allowing enzymes to distinguish between the two and each have distinct roles within the cell (Alberts et al., 2002).

In metabolism, NAD(H) is involved in redox reactions: NAD+ is an oxidising agent, able to accept electrons to become its reduced form, NADH. In turn, NADH is a reducing agent, donating electrons to become NAD+, the oxidised form. In the cytoplasm, NAD+ is required by the glycolysis enzyme glyceraldehyde-3-phosphate dehydrogenase (GAPDH) (FIG 1.5B), and regenerated by the transference of electrons into the mitochondria by the malate-aspartate shuttle (MAS) or by lactate dehydrogenase (LDH) in the fermentation reaction, converting pyruvate into lactate (FIG 1.5C) (reviewed in Akram, 2013 and Xiao et al., 2018). Furthermore, NAD(H) plays a consequential role in the mitochondrial citric acid cycle and electron transport chain as cofactors for several rate-limiting enzymes. Oxidative stress originates from an imbalance of ROS and antioxidants within the cell. Given the reducing properties of NADH and the ability of ROS to inhibit GAPDH, there are possible implications of oxidative stress on NAD(H) and the cellular redox environment (reviewed in Massudi et al., 2012). NAD redox is also involved in cell signalling, gene expression, and is linked with various metabolic disorders such as diabetes (Okabe et al., 2019). For instance, studies suggest that NAD+ is able to modulate ion channels, including for calcium (reviewed in Yu et al., 2020).

Thus, the NADH/NAD+ redox couple is known as a regulator of cellular energy metabolism (reviewed in Cantó et al., 2015), and its ratio within the cell is constantly in flux, with changes likely to be transient and potentially rapidly regulated or nullified by other reactions.

1.5 Chemical Interference of Metabolism

The two main metabolic pathways of interest in this study are oxidative phosphorylation (OXPHOS) and glycolysis. Both contribute to ATP production, with oxidative mitochondrial metabolism generally dominating under normal physiological conditions, and anaerobic glycolysis utilised under hypoxic or anoxic circumstances (FIG 1.1). In this study, I have selected a number of compounds to manipulate metabolism for my investigations, which will inhibit the electron transport chain or glycolytic enzymes (Table 1.1).

Antimycin A (AA) and sodium azide (NaN_3) both inhibit elements of the electron transport chain, complex III and IV, respectively, and thus mitochondrial metabolism (FIG 1.6A). One would expect that treatment with these drugs would cause an increase in glycolysis and fermentation to compensate for the loss of mitochondrial activity, thus resulting in elevation of lactate levels, and possibly NADH/NAD+ ratio if glycolysis proceeds at a faster rate than

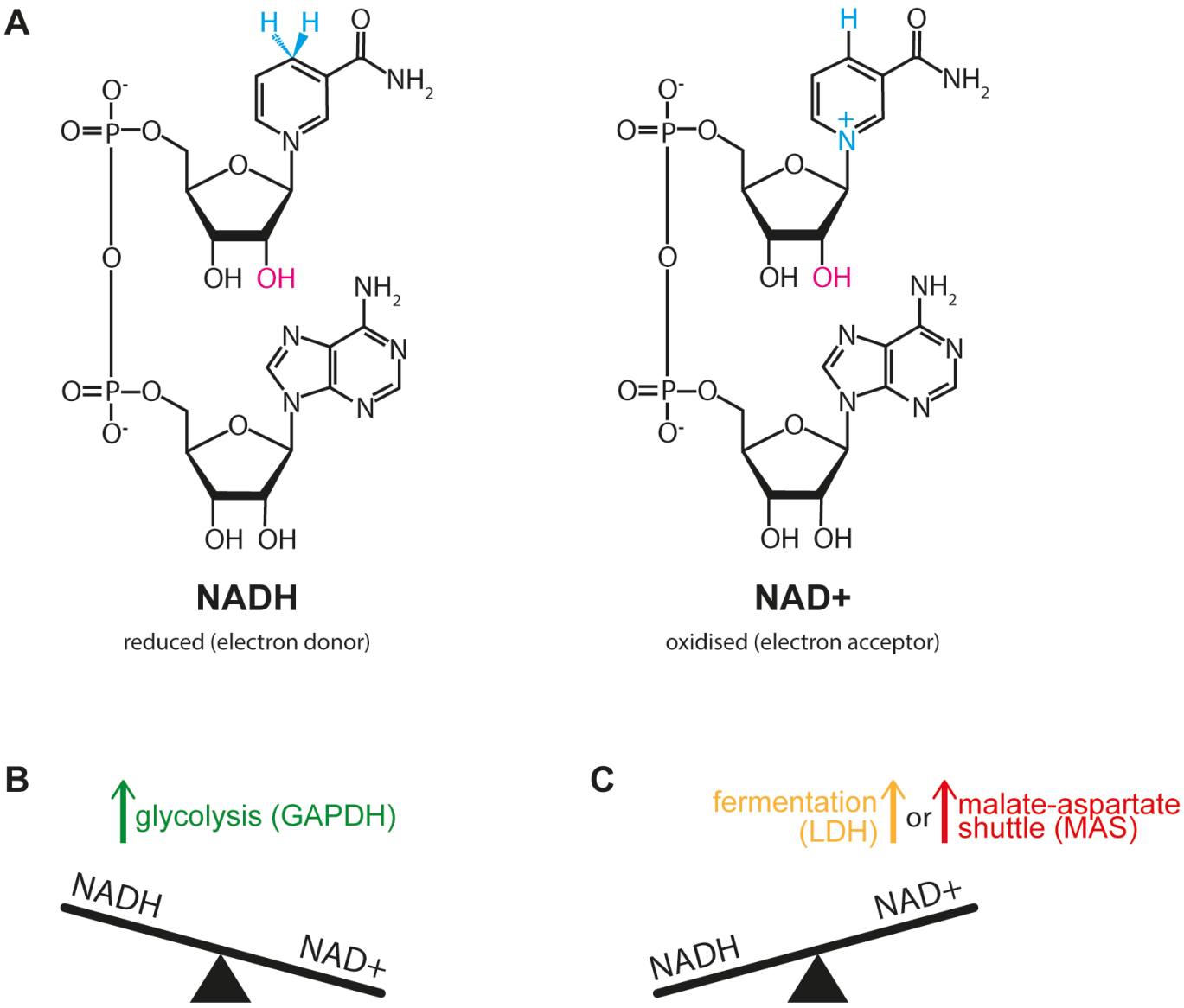

Figure 1.5. **Simplified schematic of NADH/NAD+ and its changes in the cytoplasm** (A) Skeletal structures of NADH and NAD+. Elements in blue highlight the differences between the reduced and oxidiseds forms. Hydroxyl group (OH) in pink is replaced with a phosphate group in NADP(H). (B) Glycolysis activity produces NADH via the enzyme glyceraldehyde-3-phosphate dehydrogenase (GAPDH). (C) NAD+ is regenerated by the activity of lactate dehydrogenase (LDH) in fermentation or the malate-aspartate shuttle (MAS) in translocating electrons into the mitochondria. With either aerobic or anaerobic respiration it would appear neither a net gain or loss of NADH or NAD+ occurs, and thus change in NADH/NAD+ ratio would depend on the speed of each reaction/pathway. Under normal conditions, NAD+ is the dominant form and NAD+ levels are kept higher than those of NADH.

fermentation. AA is soluble in DMSO and possesses both carbon rings and hydroxyl groups (FIG 1.6B), increasing the lipophilicity of the molecule and improving the likelihood of passing through the cell membrane. NaN_3 similarly is likely to pass into the cell, despite being charged and water soluble, due to the small size of the molecule (FIG 1.6C).

Sodium oxamate and 7-benzyl-2,3-dihydroxy-6-methyl-4-propyl-1-naphthoic acid (FX11) are competitive inhibitors of lactate dehydrogenase (LDH). Oxamate is a pyruvate analogue, while FX11 competes with NADH in order to reversibly inhibit the conversion of pyruvate to lactate in the fermentation reaction. One would expect

Compound	Molecular formula	Inhibition	Solvent	Expected result
Antimycin A (AA)	$C_{28}H_{40}N_2O_9$	Electron transport chain complex III	DMSO	Increased glycolysis activity & lactate production Decreased ROS production
Sodium azide	NaN_3	Electron transport chain complex IV	PBS	Increased glycolysis activity & lactate production Decreased ROS production
Sodium oxamate	$C_2H_2NNaO_3$	Lactate dehydrogenase	Water	Decreased lactate production
2-Deoxy-D-glucose (2DG)	$C_6H_{12}O_5$	Hexokinase	Water	Decreased glycolysis activity & lactate production
7-Benzyl-2,3-dihydroxy-6-methyl-4-propyl-1-naphthoic acid (FX11)	$C_{22}H_{22}O_4$	Lactate dehydrogenase	DMSO	Decreased lactate production

Table 1.1 **List of metabolic inhibitors.** Selected compounds with their molecular formula, action of inhibition, solvent (indicating the lipophilicity of the drug and thus likelihood of passing through the cell membrane), and expected outcome from treatment. Figure 1.6 demonstrates schematically the action and structures.

treatment with either of these compounds to reduce lactate levels and potentially increase NADH/NAD+ ratio (FIG 1.6D). Oxamate is water soluble and possesses poor lipophilicity due to it being a salt and polar in nature (FIG 1.6E), and therefore may not be proficient at passing through the membrane, potentially requiring assistance to enter cells. FX11, however, consists of multiple carbon rings and hydroxyl groups and is not soluble in water, thus suggesting it will be able to enter cells via submersion treatment (FIG 1.6F).

2-Deoxy-D-glucose (2DG) is a glycolysis inhibitor, specifically targeting hexokinase, which catalyses the first step in glycolysis (FIG 1.2). This would be anticipated to have a severe action on the cell, given it would be unable to carry out any downstream pathways, including glycolysis, the pentose phosphate pathway, and those occurring in the mitochondria. For instance, levels of lactate or NADH/NAD+ ratio may be expected to decrease (FIG 1.6G). As 2DG is water soluble and an analogue of glucose (FIG 1.6H), which is a large molecule unable to pass through the cell membrane through diffusion, thus it is unlikely that the drug will enter the cell unassisted, and require injection or entry via an open wound in order to achieve the desired effects of the compound.

Use of these inhibitory compounds will provide insight into the relationships between metabolites, metabolism, and various biological processes in an *in vivo* context.

1.6 Zebrafish as a Model Organism

Zebrafish were first utilised as a scientific model organism in the 1970s for their simplicity compared to the mouse, and amenability to genetic manipulation. There are many general advantages to the zebrafish (reviewed in Rahman Khan & Sulaiman Alhewairini, 2019): first and foremost is the relative ease of maintenance in the laboratory, with relatively low upkeep and cost. Secondly, many offspring are generated with each pairing, allowing for high sample numbers – one pair of zebrafish can produce a clutch of up to 200 eggs, and mating

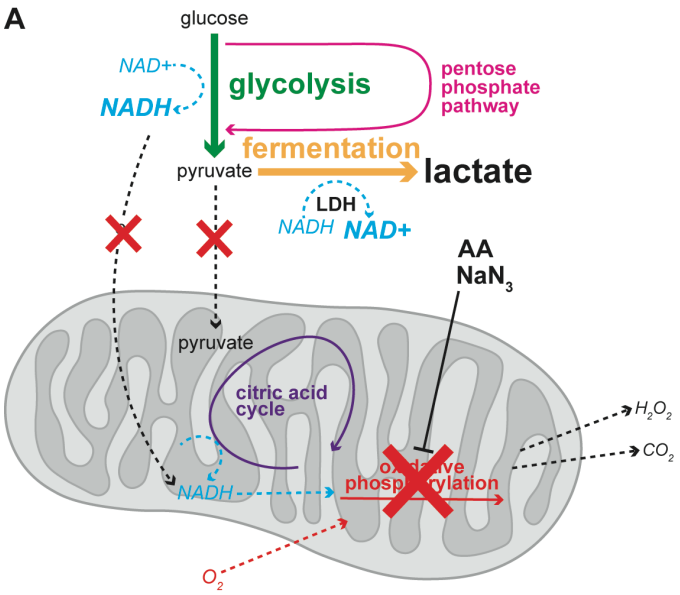

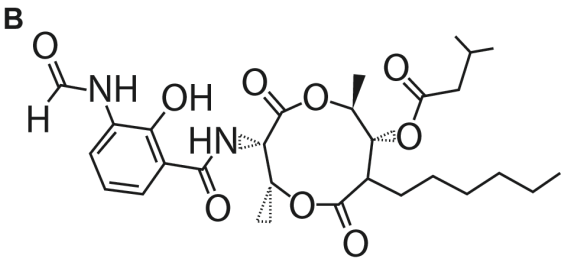

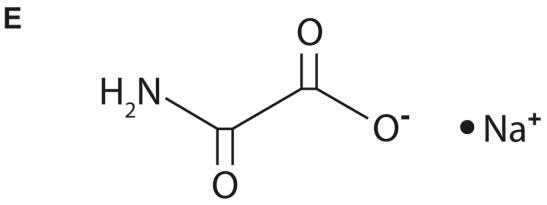

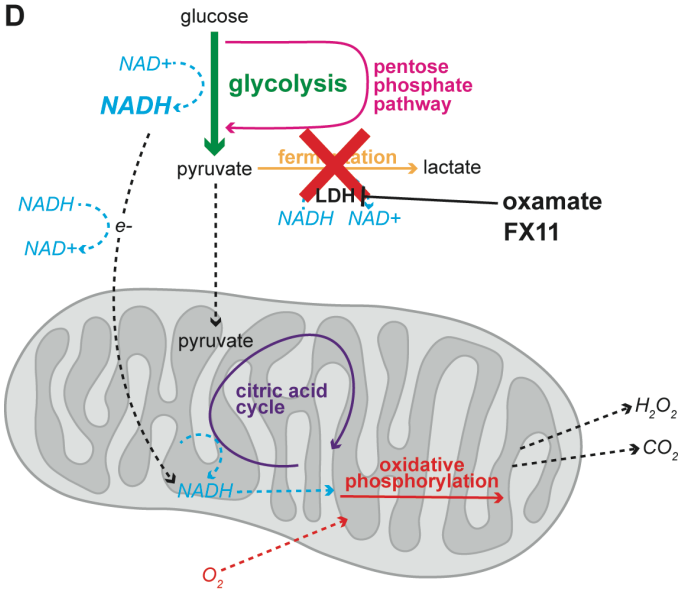

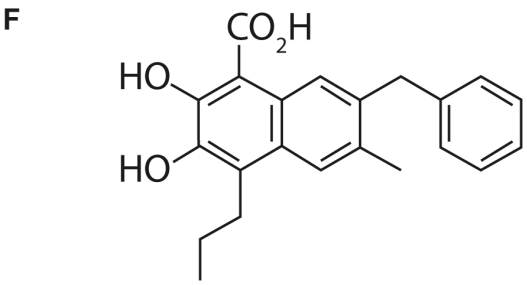

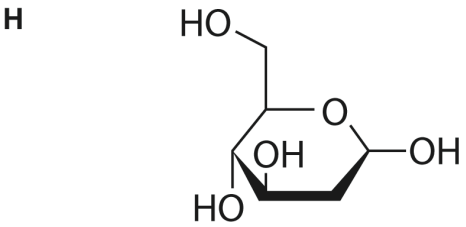

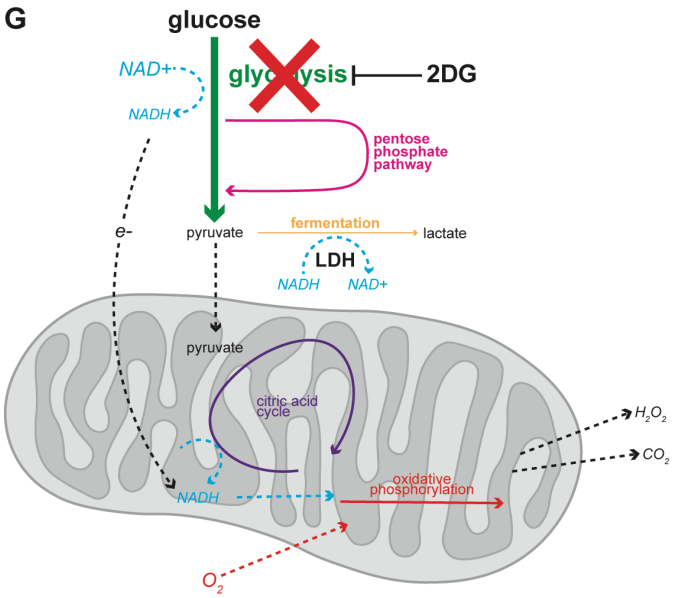

Figure 1.6. **Simplified schematics of chemical inhibitors of metabolism** (A) Simple schematic depiction of the major metabolic pathways under the action of antimycin A (AA) or sodium azide (NaN_3): inhibition of the electron transport chain and oxidative phosphorylation in the mitochondria, leading to up-regulation of glycolysis activity and increased fermentation, as shown by larger, bold typeface. (B) Skeletal structure of AA. (C) Skeletal structure of NaN_3. (D) Schematic showing the action of oxamate or FX11: inhibition of lactate dehydrogenase (LDH), preventing the reversible conversion of pyruvate, the end product of glycolysis, to lactate in the fermentation reaction to regenerate NAD+ from NADH for continued use in glycolysis. (E) Skeletal strucure of sodium oxamate. (F) Skeletal structure of FX11. (G) Schematic showing the action of 2-deoxy-D-glucose (2DG): inhibition of hexokinase, the first enzyme in the glycolysis pathway, and therefore inhibiting glycolysis and resulting in a cessation of pyruvate production and all downstream pathways. (H) Skeletal structure of 2DG.

occurs all year round under laboratory conditions. Furthermore, the appearance of light is a mating trigger for zebrafish, giving researchers increased control over the timing of embryo production, a potentially useful tool in circadian rhythm studies or obtaining specific developmental stages. Genetic manipulation is relatively simple, due to the ease of microinjection and diploid nature requiring only two copies of each gene to be targeted, compared to *Xenopus* laevis' four. Zebrafish have a fully sequenced genome which shares 70% similarity and homologues with the human genome (Howe et al., 2013), and as a vertebrate, the zebrafish has the same major organs and tissues with the same features as human systems. Therefore, findings made in the zebrafish are highly transferrable to application in humans.

Many of the advantages of zebrafish lend themselves well to study of development (reviewed in Link & Megason, 2008). The external nature of development of the zebrafish's comparatively large eggs are of particular benefit. Manipulation and observation of the embryos are therefore easy, allowing researchers to introduce RNA, oligonucleotides, drugs, or enzymes and monitor their effects. Transparency, naturally during the early stages and maintained during the larval stages with the use of inhibitors to prevent the production of melanin, is ideal for imaging, for instance with genetically encoded biosensors for various metabolites (see section 1.7), and embryos have a high survival rate under a microscope, permitting live imaging from even the one cell stage. With their rapid development and maturation time, results can be obtained faster, and generation of mutant or transgenic lines can be achieved without waiting for very long periods. Together with the large clutches and rapid ontogeny of conserved, but relatively simple, vertebrate organs and systems, these traits render the zebrafish an exemplary developmental model.

Zebrafish development has been well characterised (Kimmel et al., 1995), beginning with fertilisation. Meeting of the sperm and egg occurs externally, in the water, and is followed by cleavage, gastrulation, and neurulation (FIG 1.7). Subsequently, periods of segmentation, formation of the phylotypic body plan, and hatching occur. Kimmel et al. (1995) devised a system with a series of stages encompassing the aforementioned events and other morphogeneses, patterning, cell division, and growth. Many elements of these processes are largely conserved with other species, additionally allowing an evolutionary developmental biology approach to be considered.

1.7 Genetically Encoded Indicators of Metabolism

In the days of pioneering metabolic research, technology was limited. Experiments chiefly involved indirect chemical assays (Krebs & Johnson, 1937), but scientific techniques have come a long way since the early 20th century. For instance, the area of metabolomics, encompassing the biochemical study of metabolites, involves the use of much more sensitive analytical technologies to identify the metabolic state in a comprehensive and global manner of a biological system.

Metabolites refers to a diverse group of molecules involved in cellular metabolism, including organic acids, amino acids, and sugars, among others. Due to the vast variety present within a system's metabolic profile,

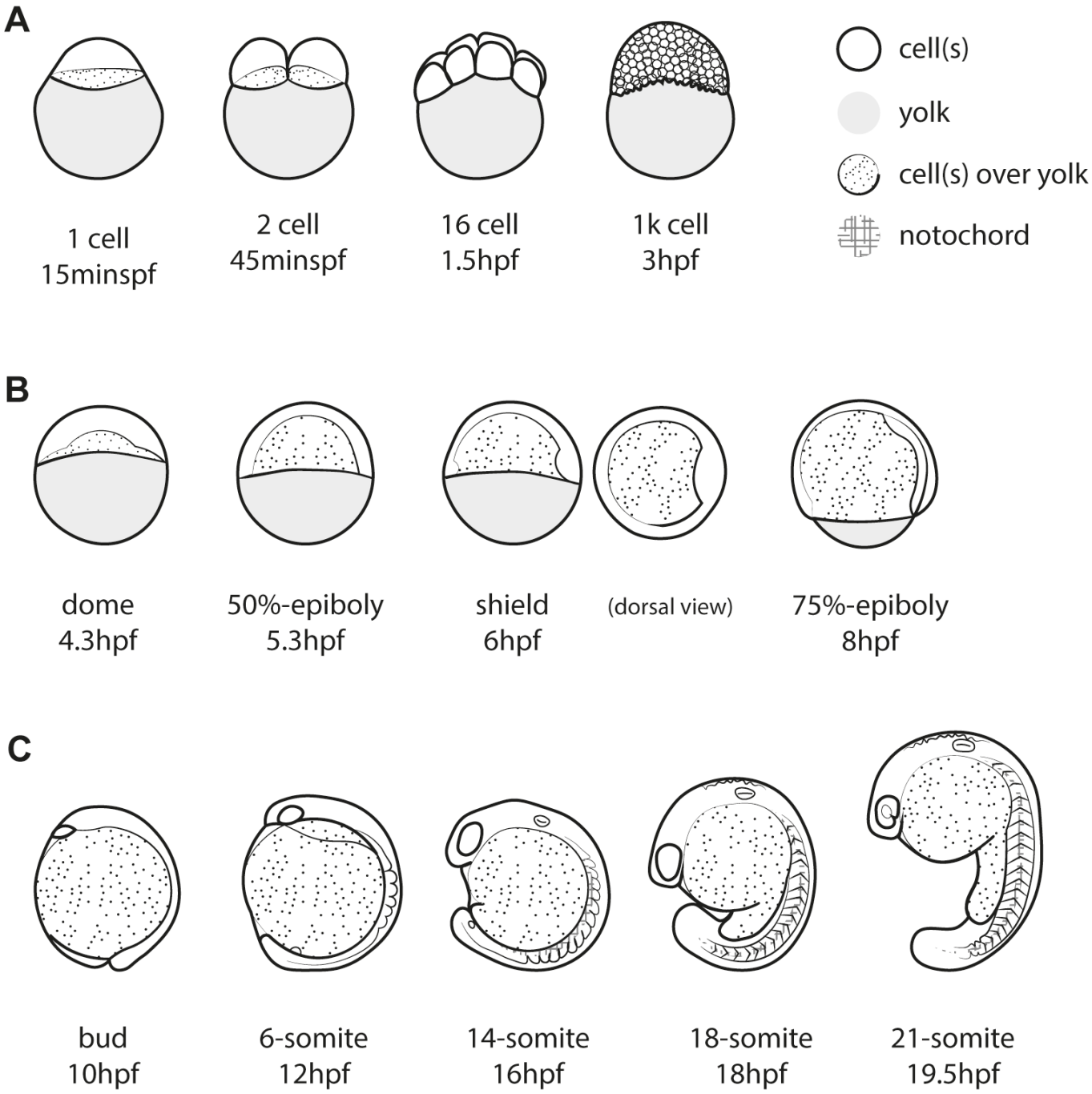

Figure 1.7. **Schematic diagram of zebrafish development.** In all stages shown embryos are still within their chorions. (A) Cleavage stages. (B) Epiboly and gastrulation. (C) Neurulation and segmentation. Adapted from Kimmel et al.,1995. Figure 1.

devising methods to evaluate them all is challenging (Burgess et al., 2014). The most commonly used metabolomics methods are based on spectroscopy, primarily assorted mass spectrometries (MS) and nuclear magnetic resonance (NMR), allowing the detection and measurement of large numbers of metabolites. MS is the more sensitive technique of the two, and produces an impressive amount of data per experiment, detailing the patterns of change in metabolites in a sample. Though less sensitive, NMR is noteworthy for its quantitative nature, and provision of information regarding molecular structure (Burgess et al., 2014). Analysis of the data attained from these techniques can be complicated, and extensive sample preparation is required, studying only a

singular point in time. As such, while highly sensitive and applicable to a wide range of metabolites, metabolomics is limited in terms of its inability to evaluate systems dynamically in real-time, and loss of spatial resolution.

Biological stains and, in particular, biosensors (reviewed in Pendin et al., 2017), however, permit the use of live samples. The latter, and in some instances the former (Kaur et al., 2016), allow for dynamic imaging and provide temporal and spatial resolution, compared to the static nature of metabolomics and most dyes (such as pentafluorobenzenesulphonyl-fluorescein (PFBSF) versus HyPer-YFP to detect H_2O_2). The toolbox of genetically encoded biosensors is still undergoing promising growth and is ever improving (see Table 1.2 for a brief list of examples).

Many genetically encoded indicators of metabolism are based either on Förster resonance energy transfer (FRET) or cyclically permuted fluorescent proteins (cpFPs). FRET is a mechanism describing the transference of energy between two chromophores, with the donor transfering energy to an acceptor when excited. The efficiency of this transfer is dependent on the distance between the chromophores. FRET-based biosensors contain a pair of fluorescent proteins fused with a metabolite binding protein, and when the metabolite of interest binds, a conformational change alters the distance between the donor and acceptor chromophores and thus changes the FRET efficiency (FIG 1.8A) (reviewed in Zadran et al., 2012). By calculating the ratio between the fluorescence intensity of the donor and acceptor, an indication of the changes in levels of the metabolite of interest can be attained. Examples of FRET-based sensors include Laconic for lactate levels (San Martín et al., 2013), Pyronic for detecting pyruvate (San Martín et al., 2014), and the FLIPglu-600μ sensors for monitoring glucose dynamics (Fehr et al., 2003).

cpFPs-based sensors are formed of fluorescent proteins that have their original termini fused, and new termini created near a sensory domain (reviewed in Kostyu et al., 2019). Similar to FRET-based biosensors, binding of the substrate at the sensory domain causes conformational changes and alters the chromophore environment, and thus also impacts the fluorescence intensity (FIG 1.8B). For example, the first cpFP-based sensor was GCaMP, for calcium, which consists of a cpGFP with the centre of the protein fused to calmodulin, a calcium binding domain, and the M13 domain of a myosin light chain kinase (FIG 1.8C). In the absence of calcium, the chromophore of cpGFP is protonated and fluoresces weakly. Conformational change upon calcium binding to the calmodulin element results in de-protonation of the chromophore and bright fluorescence (Qi Wang et al., 2008). As such, fluorescence intensity is a readout of calcium activity where the GCaMP protein is expressed. Other cpFP-based sensors include HyPer to detect H_2O_2 (Belousov et al., 2006), SoNar for NADH/NAD+ ratio (Zhao et al., 2015), and PercevalHR for ATP:ADP ratio (Tantama et al., 2013).

Both of these types of sensor are often ratiometric, possessing dual excitation or emission spectra, and thus are particularly beneficial as they are subject to limited artefacts, for example from amount of sensor protein present and excitation laser strength. However, they are instead restricted in the colours in which they are available and in using two wavelengths tend to take up the majority of the spectrum, making imaging multiple targets more difficult.

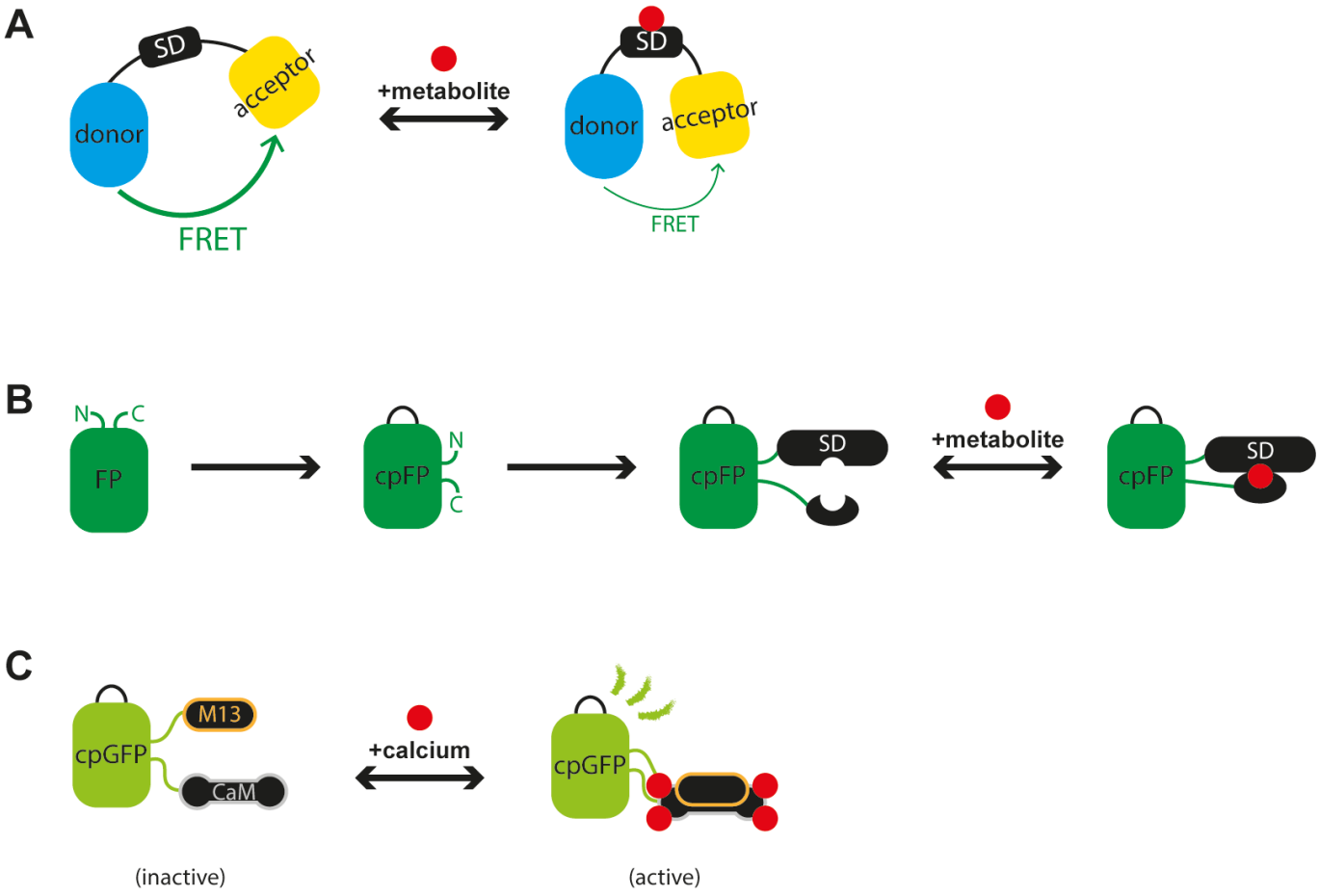

Figure 1.8. **FRET and cpFP mechanisms of genetically encoded biosensors** (A) Schematic example of Förster resonance energy transfer (FRET)-based indicator of metabolism. The FRET efficiency is altered by binding of the metabolite substrate at the sensory domain (SD) between two chromophores, causing a conformational change. (B) Schematic example of a cyclically permuted fluorescent protein (cpFP)-based indicator of metabolism. Initially, the original termini of the fluorescent protein are joined with a linker and new termini made. The new termini are then fused to a sensory domain (SD) which interacts with the metabolite substrate. (C) Schematic diagram of GCaMP, a cpFP-based indicator for calcium. Upon binding calcium, the sensory domain (M13 and CaM) interacts to activate fluorescence. M13, calmodulin-binding domain of skeletal muscle myosin light chain kinase; CaM, calmodulin.

Some of these genetically encoded indicators of metabolism have been utilised *in vivo*, such as HyPer in zebrafish (Niethammer et al., 2009; Yoo et al., 2012), *C. elegans* (Back et al., 2012), and *Xenopus* (Love et al., 2013), and GECIs (genetically encoded calcium indicators), which are commonly used in both cell culture and model organism systems, including zebrafish (reviewed in Podor et al., 2015). For example, to demonstrate the fluctuating calcium signalling along the cleavage furrow of early zebrafish embryos (J. Chen et al., 2017), and the requirement of calcium for complete zebrafish larval fin regeneration (Yoo et al., 2012). Others have not yet been optimised *in vivo*, or have been used in only invertebrate models. For instance Grx-roGFP2, a redox sensitive green fluorescent protein (roGFP)-based sensor for changes in oxidised glutathione (GSSG), has been used in cell culture (Gutscher et al., 2008), macrophages (Bhaskar et al., 2015) and *C. elegans* (Back et al., 2012), but has not yet been demonstrated in vertebrate models such as zebrafish, *Xenopus*, or mouse.

sensor	detects	emission (nm)	excitation (nm)	fluorescent protein(s)	↑ratio or intensity	citation
GEM-GECO	calcium	460/510	395	GFP/CFP	↑*calcium*	Yongxin Zhao et al., 2011
R-GECO	calcium	584	562	cpRFP	↑*calcium*	Yongxin Zhao et al., 2011
G-GECO	calcium	512	488	cpGFP	↑*calcium*	Yongxin Zhao et al., 2011
GCaMP	calcium	509	489	GFP	↑*calcium*	Nakai et al., 2001
HyPer2	H_2O_2	530	420/490	cpYFP	↑H_2O_2	Markvicheva et al., 2011
HyPerRed	H_2O_2	645	560	cpRed (from R-GECO1)	↑H_2O_2	Ermakova et al., 2014
pHRed (+mito)	pH	610	440/585	mKeima	↑*acidity*	Tantama et al., 2011
SypHer3 (+mito)	pH	530	420/490	cpYFP	↑*pH*	Ermakova et al., 2018
PercevalHR	ATP:ADP	530	490/405	cpYFP	↑*ATP:ADP*	Tantama et al., 2013
SoNar	NAD+/ NADH	530	420/485	cpYFP	↑*NADH:NAD+*	Yuzheng Zhao et al., 2015
Apollo-NADP+ (eg. Venus tagged)	NADP+	525	950	homoFRET Venus	↓*NADP+: NADPH*	Cameron et al., 2016
FLIPglu-600μΔ13	glucose	470/535	430	eCFP/Venus	↓*glucose*	Fehr et al., 2003
Laconic	lactate	528/485	430	Venus/mTFP	↑*lactate*	San Martín et al., 2013
Pyronic	pyruvate	528/485	430	Venus/mTFP	↑*pyruvate*	San Martín et al., 2014
Grx1-roGFP2 (+mito)	glutathione redox	510	488/405	roGFP	↑*oxidative stress (GSSG)*	Gutscher et al., 2008

Table 1.2 **Brief list of some of the available genetically encoded biosensors for metabolites.**

In this project, I endeavoured to take two sensors, for lactate (Laconic) and for NADH/NAD+ (SoNar), and optimise them *in vivo*, in the zebrafish, the results of which are discussed in detail in 2: Generating Tools for Imaging Metabolism in Zebrafish. I chose these two sensors specifically due to the potential for lactate to act as a readout of the Warburg effect (discussed in 1.1), and the importance of NADH and NAD+ in many metabolic pathways, including glycolysis, and its implication in metabolic diseases (discussed in 1.4).

1.8 Aims & Objectives

The title of this thesis alludes to the overarching question it aims to address: can we use genetically encoded biosensors to detect changes in metabolism during zebrafish development and regeneration?

The literature examined in this introduction prepares for the main themes of the project, specifically the roles of glucose metabolism and H_2O_2 in development and regeneration. Given the criteria for the Warburg effect and the suitability of development and regeneration as proliferative systems, is there evidence of changes in metabolism during development or regenerative and would healing systems? Following on from this, further and more specific

questions can be attended to – if metabolism is indeed altered, does manipulation of these metabolic pathways impact these processes?

Chapter 2:

- Can the genetically encoded biosensors Laconic (lactate) and SoNar (NADH/NAD+ ratio) be used in zebrafish?

Chapter 3:

- Do lactate or H_2O_2 levels change during the first 24 hours of zebrafish embryogenesis?

Chapter 4:

- Do lactate levels or NADH/NAD+ ratio change during fin fold and tail regeneration of larval zebrafish?
- Does inhibition of lactate production impact regeneration?
- Does H_2O_2 affect production of lactate in amputation?

Chapter 5:

- Are there similarities between the *hai1a* zebrafish mutant and regeneration, specifically regarding H_2O_2, calcium, and lactate?
- Does altering the level of H_2O_2 or calcium impact the mutant phenotype?

References

Akram, M. (2013). Mini-review on glycolysis and cancer. Journal of Cancer Education: the Official Journal of the American Association for Cancer Education, 28(3), 454–457. https://doi.org/10.1007/s13187-013-0486-9

Alberts, B., Johnson, A., Lewis, J., Raff, M., Roberts, K., & Walter, P. (2002). Chapter 2: Cell Chemistry and Biosynthesis. In *Molecular Biology of the Cell. 4th Edition* (4 ed., Number 2). https://doi.org/https://www.ncbi.nlm.nih.gov/books/NBK26838/

Anastasiou, D., Poulogiannis, G., Asara, J. M., Boxer, M. B., Jiang, J.-K., Shen, M., Bellinger, G., Sasaki, A. T., Locasale, J. W., Auld, D. S., Thomas, C. J., Vander Heiden, M. G., & Cantley, L. C. (2011). Inhibition of pyruvate kinase M2 by reactive oxygen species contributes to cellular antioxidant responses. *Science*, *334*(6060), 1278–1283. https://doi.org/10.1126/science.1211485

Back, P., De Vos, W. H., Depuydt, G. G., Matthijssens, F., Vanfleteren, J. R., & Braeckman, B. P. (2012). Exploring real-time in vivo redox biology of developing and aging Caenorhabditis elegans. *Free Radical Biology and Medicine*, *52*(5), 850–859. https://doi.org/https://doi.org/10.1016/j.freeradbiomed.2011.11.037

Bedard, K., & Krause, K.-H. (2007). The NOX Family of ROS-Generating NADPH Oxidases: Physiology and Pathophysiology. *Physiological Reviews*, *87*(1), 245–313. https://doi.org/10.1152/physrev.00044.2005

Belousov, V. V., Fradkov, A. F., Lukyanov, K. A., Staroverov, D. B., Shakhbazov, K. S., Terskikh, A. V., & Lukyanov, S. (2006). Genetically encoded fluorescent indicator for intracellular hydrogen peroxide. *Nature Methods*, *3*(4), 281–286. https://doi.org/10.1038/nmeth866

Bhaskar, A., Munshi, M., Khan, S. Z., Fatima, S., Arya, R., Jameel, S., & Singh, A. (2015). Measuring glutathione redox potential of HIV-1-infected macrophages. *The Journal of Biological Chemistry*, *290*(2), 1020–1038. https://doi.org/10.1074/jbc.M114.588913

Borregaard, N., & Herlin, T. (1982). Energy metabolism of human neutrophils during phagocytosis. *Journal of Clinical Investigation*, *70*(3), 550–557. https://doi.org/10.1172/jci110647

Burgess, K., Rankin, N., & Weidt, S. (2014). Chapter 10 - Metabolomics. In S. Padmanabhan (Ed.), *Handbook of Pharmacogenomics and Stratified Medicine* (pp. 181–205). Academic Press.

Busa, W. B., & Nuccitelli, R. (1985). An elevated free cytosolic Ca2+ wave follows fertilization in eggs of the frog, Xenopus laevis. *The Journal of Cell Biology*, *100*(4), 1325–1329.

Cantó, C., Menzies, K. J., & Auwerx, J. (2015). NAD(+) Metabolism and the Control of Energy Homeostasis: A Balancing Act between Mitochondria and the Nucleus. *Cell Metabolism*, *22*(1), 31–53. https://doi.org/10.1016/j.cmet.2015.05.023

Chan, C. M., Chen, Y., Hung, T. S., Miller, A. L., Shipley, A. M., & Webb, S. E. (2015). Inhibition of SOCE disrupts cytokinesis in zebrafish embryos via inhibition of cleavage furrow deepening. *The International Journal of Developmental Biology*, *59*(7-9), 289–301. https://doi.org/10.1387/ijdb.150209sw

Chang, D. C., & Meng, C. (1995). A localized elevation of cytosolic free calcium is associated with cytokinesis in the zebrafish embryo. *The Journal of Cell Biology*, *131*(6 Pt 1), 1539–1545. https://doi.org/10.1083/jcb.131.6.1539

Chen, J., Xia, L., Bruchas, M. R., & Solnica-Krezel, L. (2017). Imaging early embryonic calcium activity with GCaMP6s transgenic zebrafish. *Developmental Biology*. https://doi.org/10.1016/j.ydbio.2017.03.010

Chen, X., Qian, Y., & Wu, S. (2015). The Warburg effect: Evolving interpretations of an established concept. *Free Radical Biology and Medicine*, *79*, 253–263. https://doi.org/10.1016/j.freeradbiomed.2014.08.027

Christofk, H. R., Vander Heiden, M. G., Harris, M. H., Ramanathan, A., Gerszten, R. E., Wei, R., Fleming, M. D., Schreiber, S. L., & Cantley, L. C. (2008). The M2 splice isoform of pyruvate kinase is important for cancer metabolism and tumour growth. *Nature*, *452*(7184), 230–233. https://doi.org/10.1038/nature06734

Clapham, D. E. (2007). Calcium signaling. *Cell*, *131*(6), 1047–1058. https://doi.org/10.1016/j.cell.2007.11.028

Cogswell, P. C., Kashatus, D. F., Keifer, J. A., Guttridge, D. C., Reuther, J. Y., Bristow, C., Roy, S., Nicholson, D. W., & Baldwin, A. S. (2003). NF-kappa B and I kappa B alpha are found in the mitochondria. Evidence for regulation of mitochondrial gene expression by NF-kappa B. *The Journal of Biological Chemistry*, *278*(5), 2963–2968. https://doi.org/10.1074/jbc.M209995200

Colussi, C., Albertini, M. C., Coppola, S., Rovidati, S., Galli, F., & Ghibelli, L. (2000). H2O2-induced block of glycolysis as an active ADP-ribosylation reaction protecting cells from apoptosis. *FASEB Journal : Official Publication of the Federation of American Societies for Experimental Biology*, *14*(14), 2266–2276. https://doi.org/10.1096/fj.00-0074com

Covarrubias, L., Hernández-García, D., Schnabel, D., Salas-Vidal, E., & Castro-Obregón, S. (2008). Function of reactive oxygen species during animal development: passive or active? *Developmental Biology*, *320*(1), 1–11. https://doi.org/10.1016/j.ydbio.2008.04.041

Créton, R., Speksnijder, J. E., & Jaffe, L. F. (1998). Patterns of free calcium in zebrafish embryos. *Journal of Cell Science*, *111 (Pt 12)*, 1613–1622.

Cuthbertson, K. S., Whittingham, D. G., & Cobbold, P. H. (1981). Free Ca2+ increases in exponential phases during mouse oocyte activation. *Nature*, *294*(5843), 754–757. https://doi.org/10.1038/294754a0

Dasgupta, S., Rajapakshe, K., Zhu, B., Nikolai, B. C., Yi, P., Putluri, N., Choi, J. M., Jung, S. Y., Coarfa, C., Westbrook, T. F., Zhang, X. H.-F., Foulds, C. E., Tsai, S. Y., Tsai, M.-J., & O'Malley, B. W. (2018). Metabolic enzyme PFKFB4 activates transcriptional coactivator SRC-3 to drive breast cancer. *Nature*, *556*(7700), 249–254. https://doi.org/10.1038/s41586-018-0018-1

Deng, X., Liang, H., Ulanovskaya, O. A., Ji, Q., Zhou, T., Sun, F., Lu, Z., Hutchison, A. L., Lan, L., Wu, M., Cravatt, B. F., & He, C. (2014). Steady-state hydrogen peroxide induces glycolysis in Staphylococcus aureus and Pseudomonas aeruginosa. *Journal of Bacteriology*, *196*(14), 2499–2513. https://doi.org/10.1128/JB.01538-14

Dikalova, A. E., Bikineyeva, A. T., Budzyn, K., Nazarewicz, R. R., McCann, L., Lewis, W., Harrison, D. G., & Dikalov, S. I. (2010). Therapeutic targeting of mitochondrial superoxide in hypertension. *Circulation Research*, *107*(1), 106–116. https://doi.org/10.1161/CIRCRESAHA.109.214601

Eming, S. A., Krieg, T., & Davidson, J. M. (2007). Inflammation in wound repair: molecular and cellular mechanisms. *The Journal of Investigative Dermatology*, *127*(3), 514–525. https://doi.org/10.1038/sj.jid.5700701

Fantin, V. R., St-Pierre, J., & Leder, P. (2006). Attenuation of LDH-A expression uncovers a link between glycolysis, mitochondrial physiology, and tumor maintenance. *Cancer Cell*, *9*(6), 425–434. https://doi.org/10.1016/j.ccr.2006.04.023

Fehr, M., Lalonde, S., Lager, I., Wolff, M. W., & Frommer, W. B. (2003). In vivo imaging of the dynamics of glucose uptake in the cytosol of COS-7 cells by fluorescent nanosensors. *The Journal of Biological Chemistry*, *278*(21), 19127–19133. https://doi.org/10.1074/jbc.M301333200

Finkel, T., & Holbrook, N. J. (2000). Oxidants, oxidative stress and the biology of ageing. *Nature*, *408*(6809), 239–247. https://doi.org/10.1038/35041687

Fiske, B. P., & Vander Heiden, M. G. (2012, August). Seeing the Warburg effect in the developing retina. *Nature Cell Biology*, *14*(8), 790–791. https://doi.org/10.1038/ncb2554

Forman, H. J., Ursini, F., & Maiorino, M. (2014). An overview of mechanisms of redox signaling. *Journal of Molecular and Cellular Cardiology*, *73*, 2–9. https://doi.org/10.1016/j.yjmcc.2014.01.018

Garnett, M. E., Dyson, R. D., & Dost, F. N. (1974). Pyruvate kinase isozyme changes in parenchymal cells of regenerating rat liver. *The Journal of Biological Chemistry*, *249*(16), 5222–5226.

Ghosh-Roy, A., Wu, Z., Goncharov, A., Jin, Y., & Chisholm, A. D. (2010). Calcium and cyclic AMP promote axonal regeneration in Caenorhabditis elegans and require DLK-1 kinase. *The Journal of Neuroscience : the Official Journal of the Society for Neuroscience*, *30*(9), 3175–3183. https://doi.org/10.1523/JNEUROSCI.5464-09.2010

Gilland, E., Miller, A. L., Karplus, E., Baker, R., & Webb, S. E. (1999). Imaging of multicellular large-scale rhythmic calcium waves during zebrafish gastrulation. *Proceedings of the National Academy of Sciences of the United States of America*, *96*(1), 157–161. https://doi.org/10.1073/pnas.96.1.157

Gutscher, M., Pauleau, A.-L., Marty, L., Brach, T., Wabnitz, G. H., Samstag, Y., Meyer, A. J., & Dick, T. P. (2008). Real-time imaging of the intracellular glutathione redox potential. *Nature Methods*, *5*(6), 553–559. https://doi.org/https://doi.org/10.1038/nmeth.1212

Han, Y., Ishibashi, S., Iglesias-Gonzalez, J., Chen, Y., Love, N. R., & Amaya, E. (2018). Ca2+-Induced Mitochondrial ROS Regulate the Early Embryonic Cell Cycle. *Cell Reports*, *22*(1), 218–231. https://doi.org/10.1016/j.celrep.2017.12.042

Heinecke, J. W., & Shapiro, B. M. (1989). Respiratory burst oxidase of fertilization. *Proceedings of the National Academy of Sciences of the United States of America*, *86*(4), 1259–1263. https://doi.org/10.1073/pnas.86.4.1259

Holmström, K. M., & Finkel, T. (2014). Cellular mechanisms and physiological consequences of redox-dependent signalling. *Nature Reviews. Molecular Cell Biology*, *15*(6), 411–421. https://doi.org/10.1038/nrm3801

Honkoop, H., de Bakker, D. E., Aharonov, A., Kruse, F., Shakked, A., Nguyen, P. D., de Heus, C., Garric, L., Muraro, M. J., Shoffner, A., Tessadori, F., Peterson, J. C., Noort, W., Bertozzi, A., Weidinger, G., Posthuma, G., Grün, D., van der Laarse, W. J., Klumperman, J., et al. (2019). Single-cell analysis uncovers that metabolic reprogramming by ErbB2 signaling is essential for cardiomyocyte proliferation in the regenerating heart. *eLife*, *8*, 98. https://doi.org/10.7554/eLife.50163

Houghton, F. D., Thompson, J. G., Kennedy, C. J., & Leese, H. J. (1996). Oxygen consumption and energy metabolism of the early mouse embryo. *Molecular Reproduction and Development*, *44*(4), 476–485. https://doi.org/10.1002/(SICI)1098-2795(199608)44:4<476::AID-MRD7>3.0.CO;2-I

Howe, K., Clark, M. D., Torroja, C. F., Torrance, J., Berthelot, C., Muffato, M., Collins, J. E., Humphray, S., McLaren, K., Matthews, L., McLaren, S., Sealy, I., Caccamo, M., Churcher, C., Scott, C., Barrett, J. C., Koch, R., Rauch, G.-J., White, S., et al. (2013). The zebrafish reference genome sequence and its relationship to the human genome. *Nature*, *496*(7446), 498–503. https://doi.org/10.1038/nature12111

Kaneuchi, T., Sartain, C. V., Takeo, S., Horner, V. L., Buehner, N. A., Aigaki, T., & Wolfner, M. F. (2015). Calcium waves occur as Drosophila oocytes activate. *Proceedings of the National Academy of Sciences of the United States of America*, *112*(3), 791–796. https://doi.org/10.1073/pnas.1420589112

Kaur, A., Kolanowski, J. L., & New, E. J. (2016). Reversible Fluorescent Probes for Biological Redox States. *Angewandte Chemie (International Ed. in English)*, *55*(5), 1602–1613. https://doi.org/10.1002/anie.201506353

Kelly, B., & O'Neill, L. A. J. (2015). Metabolic reprogramming in macrophages and dendritic cells in innate immunity. *Cell Research*, *25*(7), 771–784. https://doi.org/10.1038/cr.2015.68

Kilburn, D. G., Lilly, M. D., & Webb, F. C. (1969). The energetics of mammalian cell growth. *Journal of Cell Science*, *4*(3), 645–654.

Kimmel, C. B., Ballard, W. W., Kimmel, S. R., Ullmann, B., & Schilling, T. F. (1995). Stages of embryonic development of the zebrafish. *Developmental Dynamics, 203*(3), 253–310. https://doi.org/10.1002/aja.1002030302

Kostyuk, A. I., Demidovich, A. D., Kotova, D. A., Belousov, V. V., & Bilan, D. S. (2019). Circularly Permuted Fluorescent Protein-Based Indicators: History, Principles, and Classification. *International Journal of Molecular Sciences*, *20*(17), 4200. https://doi.org/10.3390/ijms20174200

Krebs, H. A., & Johnson, W. A. (1937). Metabolism of ketonic acids in animal tissues. *The Biochemical Journal*, *31*(4), 645–660. https://doi.org/10.1042/bj0310645

Kuehne, A., Emmert, H., Soehle, J., Winnefeld, M., Fischer, F., Wenck, H., Gallinat, S., Terstegen, L., Lucius, R., Hildebrand, J., & Zamboni, N. (2015). Acute Activation of Oxidative Pentose Phosphate Pathway as First-Line Response to Oxidative Stress in Human Skin Cells. *Molecular Cell*, *59*(3), 359–371. https://doi.org/10.1016/j.molcel.2015.06.017

Lambeth, J. D. (2004). NOX enzymes and the biology of reactive oxygen. *Nature Reviews Immunology*, *4*(3), 181–189. https://doi.org/10.1038/nri1312

Lee, K. W., Webb, S. E., & Miller, A. L. (1999). A wave of free cytosolic calcium traverses zebrafish eggs on activation. *Developmental Biology*, *214*(1), 168–180. https://doi.org/10.1006/dbio.1999.9396

Liberti, M. V., & Locasale, J. W. (2016). The Warburg Effect: How Does it Benefit Cancer Cells? *Trends in Biochemical Sciences*, *41*(3), 211–218. https://doi.org/10.1016/j.tibs.2015.12.001

Liemburg-Apers, D. C., Willems, P. H. G. M., Koopman, W. J. H., & Grefte, S. (2015). Interactions between mitochondrial reactive oxygen species and cellular glucose metabolism. *Archives of Toxicology*, *89*(8), 1209–1226. https://doi.org/10.1007/s00204-015-1520-y

Link, B. A., & Megason, S. G. (2008). Zebrafish as a Model for Development. In P. M. Conn (Ed.), *Sourcebook of Models for Biomedical Research* (pp. 103–112). Humana Press.

Love, N. R., Chen, Y., Ishibashi, S., Kritsiligkou, P., Lea, R., Koh, Y., Gallop, J. L., Dorey, K., & Amaya, E. (2013). Amputation-induced reactive oxygen species are required for successful Xenopus tadpole tail regeneration. *Nature Cell Biology*, *15*(2), 222–228. https://doi.org/10.1038/ncb2659

Love, N. R., Ziegler, M., Chen, Y., & Amaya, E. (2014). Carbohydrate metabolism during vertebrate appendage regeneration: what is its role? How is it regulated?: A postulation that regenerating vertebrate appendages facilitate glycolytic and pentose phosphate pathways to fuel macromolecule biosynthesis. *BioEssays*, *36*(1), 27–33. https://doi.org/10.1002/bies.201300110

Lunt, S. Y., & Vander Heiden, M. G. (2011). Aerobic glycolysis: meeting the metabolic requirements of cell proliferation. *Annual Review of Cell and Developmental Biology*, *27*(1), 441–464. https://doi.org/10.1146/annurev-cellbio-092910-154237

Luo, W., Hu, H., Chang, R., Zhong, J., Knabel, M., O'Meally, R., Cole, R. N., Pandey, A., & Semenza, G. L. (2011). Pyruvate kinase M2 is a PHD3-stimulated coactivator for hypoxia-inducible factor 1. *Cell*, *145*(5), 732–744. https://doi.org/10.1016/j.cell.2011.03.054

Magadum, A., Singh, N., Kurian, A. A., Munir, I., Mehmood, T., Brown, K., Sharkar, M. T. K., Chepurko, E., Sassi, Y., Oh, J. G., Lee, P., Santos, C. X. C., Gaziel-Sovran, A., Zhang, G., Cai, C.-L., Kho, C., Mayr, M., Shah, A. M., Hajjar, R. J., & Zangi, L. (2020). Pkm2 Regulates Cardiomyocyte Cell Cycle and Promotes Cardiac Regeneration. *Circulation*, *141*(15), 1249–1265. https://doi.org/10.1161/CIRCULATIONAHA.119.043067

Maianski, N. A., Geissler, J., Srinivasula, S. M., Alnemri, E. S., Roos, D., & Kuijpers, T. W. (2004). Functional characterization of mitochondria in neutrophils: a role restricted to apoptosis. *Cell Death and Differentiation*, *11*(2), 143–153. https://doi.org/10.1038/sj.cdd.4401320

Massudi, H., Grant, R., Guillemin, G. J., & Braidy, N. (2012). NAD+ metabolism and oxidative stress: the golden nucleotide on a crown of thorns. *Redox Report: Communications in Free Radical Research*, *17*(1), 28–46. https://doi.org/10.1179/1351000212Y.0000000001

Mathieu, J., Zhou, W., Xing, Y., Sperber, H., Ferreccio, A., Agoston, Z., Kuppusamy, K. T., Moon, R. T., & Ruohola-Baker, H. (2014). Hypoxia-inducible factors have distinct and stage-specific roles during reprogramming of human cells to pluripotency. *Cell Stem Cell*, *14*(5), 592–605. https://doi.org/10.1016/j.stem.2014.02.012

Molavian, H. R., Kohandel, M., & Sivaloganathan, S. (2016). High Concentrations of H2O2 Make Aerobic Glycolysis Energetically More Favorable for Cellular Respiration. *Frontiers in Physiology*, *7*, 362. https://doi.org/10.3389/fphys.2016.00362

Movafagh, S., Crook, S., & Vo, K. (2015). Regulation of hypoxia-inducible factor-1a by reactive oxygen species: new developments in an old debate. *Journal of Cellular Biochemistry*, *116*(5), 696–703. https://doi.org/10.1002/jcb.25074

Mullarky, E., & Cantley, L. C. (2015). *Diverting Glycolysis to Combat Oxidative Stress* (K. Nakao, N. Minato, & S. Uemoto, Eds.; pp. 3–23). Springer Japan.

Murphy, M. P. (2009). How mitochondria produce reactive oxygen species. *The Biochemical Journal*, *417*(1), 1–13.

Muto, A., Kume, S., Inoue, T., Okano, H., & Mikoshiba, K. (1996). Calcium waves along the cleavage furrows in cleavage-stage Xenopus embryos and its inhibition by heparin. *The Journal of Cell Biology*, *135*(1), 181–190.

Nagao, A., Kobayashi, M., Koyasu, S., Chow, C. C. T., & Harada, H. (2019). HIF-1-Dependent Reprogramming of Glucose Metabolic Pathway of Cancer Cells and Its Therapeutic Significance. *International Journal of Molecular Sciences*, *20*(2), 238. https://doi.org/10.3390/ijms20020238

Newsholme, P., Curi, R., Gordon, S., & Newsholme, E. A. (1986). Metabolism of glucose, glutamine, long-chain fatty acids and ketone bodies by murine macrophages. *The Biochemical Journal*, *239*(1), 121–125.

Niethammer, P., Grabher, C., Look, A. T., & Mitchison, T. J. (2009). A tissue-scale gradient of hydrogen peroxide mediates rapid wound detection in zebrafish. *Nature*, *459*(7249), 996–999. https://doi.org/10.1038/nature08119

Noguchi, T., & Mabuchi, I. (2002). Localized Calcium Signals along the Cleavage Furrow of the Xenopus Egg Are Not Involved in Cytokinesis. *Molecular Biology of the Cell*, *13*(4), 1263–1273. https://doi.org/10.1091/mbc.01-10-0501

Noguchi, T., Inoue, H., & Tanaka, T. (1986). The M1- and M2-type isozymes of rat pyruvate kinase are produced from the same gene by alternative RNA splicing. *The Journal of Biological Chemistry*, *261*(29), 13807–13812.

Nulton-Persson, A. C., & Szweda, L. I. (2001). Modulation of mitochondrial function by hydrogen peroxide. *The Journal of Biological Chemistry*, *276*(26), 23357–23361. https://doi.org/10.1074/jbc.M100320200

Okabe, K., Yaku, K., Tobe, K., & Nakagawa, T. (2019). Implications of altered NAD metabolism in metabolic disorders. *Journal of Biomedical Science*, *26*(1), 34–13. https://doi.org/10.1186/s12929-019-0527-8

Pak, V. V., Ezeriņa, D., Lyublinskaya, O. G., Pedre, B., Tyurin-Kuzmin, P. A., Mishina, N. M., Thauvin, M., Young, D., Wahni, K., Martínez Gache, S. A., Demidovich, A. D., Ermakova, Y. G., Maslova, Y. D., Shokhina, A. G., Eroglu, E., Bilan, D. S., Bogeski, I., Michel, T., Vriz, S., et al. (2020). Ultrasensitive Genetically Encoded Indicator for Hydrogen Peroxide Identifies Roles for the Oxidant in Cell Migration and Mitochondrial Function. *Cell Metabolism*, *31*(3), 642–653.e646. https://doi.org/10.1016/j.cmet.2020.02.003

Palsson-McDermott, E. M., Curtis, A. M., Goel, G., Lauterbach, M. A. R., Sheedy, F. J., Gleeson, L. E., van den Bosch, M. W. M., Quinn, S. R., Domingo-Fernandez, R., Johnston, D. G. W., Jiang, J.-K., Jiang, J.-K., Israelsen, W. J., Keane, J., Thomas, C., Clish, C., Vander Heiden, M., Vanden Heiden, M., Xavier, R. J., & O'Neill, L. A. J. (2015). Pyruvate kinase M2 regulates Hif-1α activity and IL-1β induction and is a critical determinant of the warburg effect in LPS-activated macrophages. *Cell Metabolism*, *21*(1), 65–80. https://doi.org/10.1016/j.cmet.2014.12.005

Paudel, S., Sindelar, R., & Saha, M. (2018). Calcium Signaling in Vertebrate Development and Its Role in Disease. *International Journal of Molecular Sciences*, *19*(11), 3390. https://doi.org/10.3390/ijms19113390

Pearce, E. L., & Pearce, E. J. (2013). Metabolic Pathways in Immune Cell Activation and Quiescence. *Immunity*, *38*(4), 633–643. https://doi.org/10.1016/j.immuni.2013.04.005

Pendin, D., Greotti, E., Lefkimmiatis, K., & Pozzan, T. (2017). Exploring cells with targeted biosensors. *The Journal of General Physiology*, *149*(1), 1–36. https://doi.org/10.1085/jgp.201611654

Podor, B., Hu, Y.-L., Ohkura, M., Nakai, J., Croll, R., & Fine, A. (2015). Comparison of genetically encoded calcium indicators for monitoring action potentials in mammalian brain by two-photon excitation fluorescence microscopy. *Neurophotonics*, *2*(2), 021014. https://doi.org/10.1117/1.NPh.2.2.021014

Pollak, N., Dölle, C., & Ziegler, M. (2007). The power to reduce: pyridine nucleotides--small molecules with a multitude of functions. *The Biochemical Journal*, *402*(2), 205–218. https://doi.org/10.1042/BJ20061638

Prakasam, G., Iqbal, M. A., Bamezai, R. N. K., & Mazurek, S. (2018). Posttranslational Modifications of Pyruvate Kinase M2: Tweaks that Benefit Cancer. *Frontiers in Oncology*, *8*, 22. https://doi.org/10.3389/fonc.2018.00022

Prigione, A., Rohwer, N., Hoffmann, S., Mlody, B., Drews, K., Bukowiecki, R., Blümlein, K., Wanker, E. E., Ralser, M., Cramer, T., & Adjaye, J. (2014). HIF1α modulates cell fate reprogramming through early glycolytic shift and upregulation of PDK1-3 and PKM2. *Stem Cells (Dayton, Ohio)*, *32*(2), 364–376. https://doi.org/10.1002/stem.1552

Rahman Khan, F., & Sulaiman Alhewairini, S. (2019). Zebrafish (*Danio rerio*) as a Model Organism. In L. Streba, D. I. Gheonea, & M. Schenker (Eds.), *Current Trends in Cancer Management* (Number Chapter 1). IntechOpen. https://doi.org/10.5772/intechopen.81517

Rhee, S. G., Bae, Y. S., Lee, S. R., & Kwon, J. (2000). Hydrogen peroxide: a key messenger that modulates protein phosphorylation through cysteine oxidation. *Science's STKE : Signal Transduction Knowledge Environment*, *2000*(53), pe1–pe1. https://doi.org/10.1126/stke.2000.53.pe1

Ridgway, E. B., Gilkey, J. C., & Jaffe, L. F. (1977). Free calcium increases explosively in activating medaka eggs. *Proceedings of the National Academy of Sciences of the United States of America*, *74*(2), 623–627. https://doi.org/10.1073/pnas.74.2.623

Romero, M. M. G., McCathie, G., Jankun, P., & Roehl, H. H. (2018). Damage-induced reactive oxygen species enable zebrafish tail regeneration by repositioning of Hedgehog expressing cells. *Nature Communications*, *9*(1), 4010–4011. https://doi.org/10.1038/s41467-018-06460-2

Roos, D., & Loos, J. A. (1970). Changes in the carbohydrate metabolism of mitogenicellay stimulated human peripheral lymphocytes I. Stimulation by phytohaemagglutinin. 222(3), 565–582. https://doi.org/10.1016/0304-4165(70)90182-0

San Martín, A., Ceballo, S., Baeza-Lehnert, F., Lerchundi, R., Valdebenito, R., Contreras-Baeza, Y., Alegría, K., & Barros, L. F. (2014). Imaging mitochondrial flux in single cells with a FRET sensor for pyruvate. *PLoS ONE*, *9*(1), e85780. https://doi.org/10.1371/journal.pone.0085780

San Martín, A., Ceballo, S., Ruminot, I., Lerchundi, R., Frommer, W. B., & Barros, L. F. (2013). A genetically encoded FRET lactate sensor and its use to detect the Warburg effect in single cancer cells. *PLoS ONE*, *8*(2), e57712. https://doi.org/10.1371/journal.pone.0057712

Sauer, H., Wartenberg, M., & Hescheler, J. (2001). Reactive Oxygen Species as Intracellular Messengers During Cell Growth and Differentiation. *Cellular Physiology and Biochemistry*, *11*(4), 173–186. https://doi.org/10.1159/000047804

Schieber, M., & Chandel, N. S. (2014). ROS function in redox signaling and oxidative stress. *Current Biology : CB*, *24*(10), R453–R462. https://doi.org/10.1016/j.cub.2014.03.034

Sena, L. A., Li, S., Jairaman, A., Prakriya, M., Ezponda, T., Hildeman, D. A., Wang, C.-R., Schumacker, P. T., Licht, J. D., Perlman, H., Bryce, P. J., & Chandel, N. S. (2013). Mitochondria are required for antigen-specific T cell activation through reactive oxygen species signaling. *Immunity*, *38*(2), 225–236. https://doi.org/10.1016/j.immuni.2012.10.020

Shi, D.-Y., Xie, F.-Z., Zhai, C., Stern, J. S., Liu, Y., & Liu, S.-L. (2009). The role of cellular oxidative stress in regulating glycolysis energy metabolism in hepatoma cells. *Molecular Cancer*, *8*(1), 32–15. https://doi.org/10.1186/1476-4598-8-32

Sinclair, J. W., Hoying, D. R., Bresciani, E., Nogare, D. D., Needle, C. D., Wu, W., Bishop, K., Elkahloun, A. G., Chitnis, A., Liu, P., & Burgess, S. M. (2020). A metabolic shift to glycolysis promotes zebrafish tail regeneration through TGF–β dependent dedifferentiation of notochord cells to form the blastema. *bioRxiv*, *21*(1), 2020.03.03.975318. https://doi.org/10.1101/2020.03.03.975318

Steinhardt, R., Zucker, R., & Schatten, G. (1977). Intracellular calcium release at fertilization in the sea urchin egg. *Developmental Biology*, *58*(1), 185–196. https://doi.org/10.1016/0012-1606(77)90084-7

Tantama, M., Martínez-François, J. R., Mongeon, R., & Yellen, G. (2013). Imaging energy status in live cells with a fluorescent biosensor of the intracellular ATP-to-ADP ratio. *Nature Communications*, *4*(1), 1–11. https://doi.org/10.1038/ncomms3550

Tu, M. K., & Borodinsky, L. N. (2014). Spontaneous calcium transients manifest in the regenerating muscle and are necessary for skeletal muscle replenishment. *Cell Calcium*, *56*(1), 34–41. https://doi.org/10.1016/j.ceca.2014.04.004

van Raam, B. J., Sluiter, W., de Wit, E., Roos, D., Verhoeven, A. J., & Kuijpers, T. W. (2008). Mitochondrial membrane potential in human neutrophils is maintained by complex III activity in the absence of supercomplex organisation. *PLoS ONE*, *3*(4), e2013. https://doi.org/10.1371/journal.pone.0002013

Vander Heiden, M. G., Cantley, L. C., Thompson, C. B., Mammalian, P., Exhibit, C., & Metabolism, A. (2009). *Understanding the Warburg Effect: The Metabolic Requirements of Cell Proliferation*. *324*(5930), 1029–1033. https://doi.org/10.1126/science.1160809

Wang, Qi, Shui, B., Kotlikoff, M. I., & Sondermann, H. (2008). Structural basis for calcium sensing by GCaMP2. *Structure (London, England : 1993)*, *16*(12), 1817–1827. https://doi.org/10.1016/j.str.2008.10.008

Wang, Ting, Liu, H., Lian, G., Zhang, S.-Y., Wang, X., & Jiang, C. (2017). HIF1α-Induced Glycolysis Metabolism Is Essential to the Activation of Inflammatory Macrophages. *Mediators of Inflammation*, *2017*(11), 9029327–10. https://doi.org/10.1155/2017/9029327

Wang, Tingchung, Marquardt, C., & Foker, J. (1976). Aerobic glycolysis during lymphocyte proliferation. *Nature*, *261*(5562), 702–705. https://doi.org/10.1038/261702a0

Warburg, O. (1925). The Metabolism of Carcinoma Cells. *The Journal of Cancer Research*, *9*(1), 148–163. https://doi.org/10.1158/jcr.1925.148

Webb, S. E., & Miller, A. L. (2003a). Imaging intercellular calcium waves during late epiboly in intact zebrafish embryos. *Zygote (Cambridge, England)*, *11*(2), 175–182. https://doi.org/10.1017/s0967199403002211

Webb, S. E., & Miller, A. L. (2003b). Calcium: Calcium signalling during embryonic development. *Nature Reviews. Molecular Cell Biology*, *4*(7), 539–551. https://doi.org/10.1038/nrm1149

Webb, S. E., Li, W. M., & Miller, A. L. (2008). Calcium signalling during the cleavage period of zebrafish development. *Philosophical Transactions of the Royal Society B: Biological Sciences*, *363*(1495), 1363–1369. https://doi.org/10.1098/rstb.2007.2253

Williams, A. L., Khadka, V., Tang, M., Avelar, A., Schunke, K. J., Menor, M., & Shohet, R. V. (2018). HIF1 mediates a switch in pyruvate kinase isoforms after myocardial infarction. *Physiological Genomics*, *50*(7), 479–494. https://doi.org/10.1152/physiolgenomics.00130.2017

Xiao, W., Wang, R.-S., Handy, D. E., & Loscalzo, J. (2018). NAD(H) and NADP(H) Redox Couples and Cellular Energy Metabolism. *Antioxidants & Redox Signaling*, *28*(3), 251–272. https://doi.org/10.1089/ars.2017.7216

Xu, S., & Chisholm, A. D. (2011). A Gαq-Ca^{2+} signaling pathway promotes actin-mediated epidermal wound closure in C. elegans. *Current Biology : CB*, *21*(23), 1960–1967. https://doi.org/10.1016/j.cub.2011.10.050

Xu, Z., Kopf, G. S., & Schultz, R. M. (1994). Involvement of inositol 1,4,5-trisphosphate-mediated Ca2+ release in early and late events of mouse egg activation. *Development (Cambridge, England)*, *120*(7), 1851–1859.

Yang, W., Xia, Y., Ji, H., Zheng, Y., Liang, J., Huang, W., Gao, X., Aldape, K., & Lu, Z. (2011). Nuclear PKM2 regulates β-catenin transactivation upon EGFR activation. *Nature*, *480*(7375), 118–122. https://doi.org/10.1038/nature10598

Yoo, S. K., Freisinger, C. M., LeBert, D. C., & Huttenlocher, A. (2012). Early redox, Src family kinase, and calcium signaling integrate wound responses and tissue regeneration in zebrafish. *The Journal of Cell Biology*, *199*(2), 225–234. https://doi.org/10.1083/jcb.201203154

Yu, P., Cai, X., Liang, Y., Wang, M., & Yang, W. (2020). Roles of NAD+ and Its Metabolites Regulated Calcium Channels in Cancer. *Molecules (Basel, Switzerland)*, *25*(20), 4826. https://doi.org/10.3390/molecules25204826

Zadran, S., Standley, S., Wong, K., Otiniano, E., Amighi, A., & Baudry, M. (2012). Fluorescence resonance energy transfer (FRET)-based biosensors: visualizing cellular dynamics and bioenergetics. *Applied Microbiology and Biotechnology*, *96*(4), 895–902. https://doi.org/10.1007/s00253-012-4449-6

Zhang, J., Wang, X., Vikash, V., Ye, Q., Wu, D., Liu, Y., & Dong, W. (2016). ROS and ROS-Mediated Cellular Signaling. *Oxidative Medicine and Cellular Longevity*, *2016*(5782), 4350965–4350918. https://doi.org/10.1155/2016/4350965

Zhang, Q., Wang, Y., Man, L., Zhu, Z., Bai, X., Wei, S., Liu, Y., Liu, M., Wang, X., Gu, X., & Wang, Y. (2016). Reactive oxygen species generated from skeletal muscles are required for gecko tail regeneration. *Scientific Reports*, *6*(1), 20752. https://doi.org/10.1038/srep20752

Zhang, W., & Liu, H. T. (2002). MAPK signal pathways in the regulation of cell proliferation in mammalian cells. *Cell Research*, *12*(1), 9–18. https://doi.org/10.1038/sj.cr.7290105

Zhao, Y., Yang, Y., Zhao, Y., Hu, Q., Loscalzo, J., Correspondence, Y. Y., Su, N., Cheng, F., Zou, Y., Wang, A., Hu, H., Chen, X., Zhou, H.-M., Yang, K., Huang, X., Yi, J., Zhu, Q., Zhu, L., Wang, X., et al. (2015). SoNar, a Highly Responsive NAD+/NADH Sensor, Allows High-Throughput Metabolic Screening of Anti-tumor Agents. *Cell Metabolism*, *21*(5), 777–789. https://doi.org/10.1016/j.cmet.2015.04.009

Zhong, H., De Marzo, A. M., Laughner, E., Lim, M., Hilton, D. A., Zagzag, D., Buechler, P., Isaacs, W. B., Semenza, G. L., & Simons, J. W. (1999). Overexpression of hypoxia-inducible factor 1alpha in common human cancers and their metastases. *Cancer Research*, *59*(22), 5830–5835. https://pubmed.ncbi.nlm.nih.gov/10582706/

Zhou, W., Choi, M., Margineantu, D., Margaretha, L., Hesson, J., Cavanaugh, C., Blau, C. A., Horwitz, M. S., Hockenbery, D., Ware, C., & Ruohola-Baker, H. (2012). HIF1α induced switch from bivalent to exclusively glycolytic metabolism during ESC-to-EpiSC/hESC transition. *The EMBO Journal*, *31*(9), 2103–2116. https://doi.org/10.1038/emboj.2012.71

2: Generating Tools for Imaging Metabolism in Zebrafish

Abstract

Metabolic research has been recently growing in the context of broader areas of biology, in particular development and regeneration, as opposed to its traditionally considered role simply in anabolic and catabolic pathways. This growth has been greatly aided by the development of new tools such as genetically encoded sensors, allowing real time monitoring of metabolites with temporal and spatial resolution. These tools thus far have been primarily utilised on cells in culture, and as such in this chapter I aim to progress the use of these sensors into an *in vivo* model, the zebrafish. Using mRNA injections and chemical treatments to alter metabolism as positive controls, I show that the sensors Laconic and SoNar, detecting lactate and NADH/NAD+ ratio, respectively, function similarly *in vivo* as reported *in vitro*. I then go on to generate several transgenic lines via the Tol2 system for these two sensors and additionally HyPer, detecting hydrogen peroxide, under ubiquitous promoters, which also perform as expected during positive control experiments. I conclude that these genetically encoded sensors will be of use in studying early embryogenesis and for regeneration and wound healing experiments.

2.1 Introduction

In the early twentieth century, metabolism research was in its prime, with the discoveries of key metabolic pathways such as the citric acid cycle being made (reviewed in Wilson et al., 2010). During this time, the biochemical aspect was the main focus of experiments, and metabolism was largely considered a basic housekeeping function of all cells. In 1911 Charles Manning Child pioneered a new approach to metabolism when he published his preliminary theory of metabolic gradients (Child, 1911). His research between 1910 and 1915 led to the suggestion that more metabolically active tissues in development sequestered nutrients and this activity defined the resulting structures that developed (Child, 1941; reviewed in Blackstone, 2006). Child was the first to link metabolism with a biological system, however, experimental tools at the time were limited, impeding further expansion on Child's theories. Owing to the lack of experimental options and the rise of genetics by Child's contemporary, Thomas Hunt Morgan, the interest in metabolism was somewhat obscured for some time. More recently, with the implementation of new technologies, we are increasingly returning to Child's original ideas considering metabolism in the wider context of biological systems such as development, particularly with regards to redox signalling and the importance of reactive oxygen species (ROS) (reviewed in Schieber & Chandel, 2014).

The relatively new emergence of genetically encoded sensors for various metabolites has increased the ability of researchers to study the role of metabolism within other processes (see 1: General Introduction, section 1.7). Most notably there have been studies into the occurrance of aerobic glycolysis, also known as the Warburg effect, in systems during proliferative states (reviewed in Vander Heiden et al., 2009). Laconic is a biological sensor that is particularly useful for the identification of the Warburg effect, its ratiometric fluorescent signal indicating levels of lactate present in the cytoplasm (San Martín et al., 2013). An additional sensor, SoNar, which reports NADH/NAD+ ratio (Zhao et al., 2015), may be able to report on the overall redox balance of the cell. HyPer is a well-documented sensor for hydrogen peroxide (H_2O_2) (Belousov et al., 2006; Niethammer et al., 2009; Love et al., 2013; Gauron et al., 2016; reviewed in Bilan & Belousov, 2016), and can be used as a readout for mitochondrial respiration due to its production from the superoxide generated in the electron transport chain. However, mitochondria are not the only source of H_2O_2; another notable source is NADP oxidases (see 1: General Introduction, section 1.2.1), in particular dual oxidase (DUOX) (Nasr-Esfahani & Johnson, 1991), which can be regulated by calcium (Dupuy et al., 1988), linking these two metabolites together as has been implied previously in regeneration and fertilisation (Y. Han et al., 2018; see 1: General Introduction, section 1.3.1 and 1.3.2). It has been suggested that reactive oxygen species (ROS) have several functions and are not simply by-products from mitochondria (reviewed in Zhang et al., 2016), for instance playing a role in phenomena such as wound healing and regeneration (Niethammer et al., 2009; Love et al., 2013; Gauron et al., 2013; Razzell et al., 2013; P. Han et al., 2014), influencing the activity of glycolysis or the pentose phosphate pathway (PPP) (Molavian et al., 2016; Kuehne et al., 2015; Mullarky & Cantley, 2015; Colussi et al., 2000; Nulton-Persson & Szweda, 2001; Shi et al., 2009), or acting as a second messenger in symmetry breaking in *C. elegans* (De Henau et al., 2020).

Furthermore, metabolic switching has been shown to be involved in cell signalling and regulation of several cellular processes. A switch in carbohydrate metabolism from oxidative phosphorylation (OXPHOS) to glycolysis has been suggested to support epithelial to mesenchyme transitions, particularly in cancer (reviewed in Morandi et al., 2017). Work in *C. elegans* has shown that reduction of mitochondrial activity has positive effects on ageing (reviewed in Wang & Hekimi, 2015), and multiple studies have linked a switch to glycolytic metabolism with the proliferative potential of stem cells (Folmes et al., 2011; Kondoh et al., 2007; reviewed in Mathieu & Ruohola-Baker, 2017). Metabolism further plays an important part in cell identity and differentiation in a variety of settings, including immune cells and neurons (Buck et al., 2016; Zheng et al., 2016).

The process in which metabolism regulates these cellular processes is not clear in all cases, but it is known that metabolites can influence the epigenetic landscape to alter gene expression (reviewed in Harvey et al., 2016), for example the regulation of histone acetylation by acetyl-CoA (Wellen et al., 2009). As such, metabolism is becoming an increasingly significant area of research, and generation of tools to better examine metabolic changes in various systems will be beneficial for the field. The advent of genetically encoded sensors for various metabolites is particularly advantageous due to their capacity to permit *in vivo* study of dynamic changes with

temporal and spatial resolution. Thus, in this chapter, I endeavour to determine whether these tools are suitable for use in the zebrafish model and to generate stable transgenic lines to utilise these tools *in vivo*.

2.1.1 Laconic

The Warburg effect tends to transform glucose into lactose, despite aerobic conditions (Warburg, 1925; reviewed in Vander Heiden et al., 2009; see 1: General Introduction, section 1.1). Thus, imaging changes in lactate may indicate the stimulation of glycolysis as expected from the Warburg effect.

Förster resonance energy transfer (FRET) describes the energy transfer between two chromophores. Laconic, a lactate-specific FRET-based sensor, has been used to calculate lactate concentration and movement, and estimate the occurrence of the Warburg Effect (San Martín et al., 2013; Mächler et al., 2016). The donor chromophore mTFP (monomeric teal fluorescent protein) is bound to a DNA-binding domain and transfers energy to the acceptor chromophore Venus, which is fused to the bacterial transcription factor Lldr, and LldR lactate-binding domain (FIG 2.1A). Laconic utilises a full length E. coli LldR with no linkers between domains and fluorescent proteins; both mTFP and Venus are reportedly brighter and less pH-sensitive than CFP and YFP. Indeed, the authors of the original paper conclude the sensor is not significantly affected by pH in the physiological or pathological range (San Martín et al., 2013). Upon conformational change due to lactate binding, the FRET efficiency of electron transfer from mTFP to Venus is reduced, thus changing the intensities of each fluorescent protein (FIG 2.1B).

FRET-based sensors hence utilise one excitation wavelength and two emission wavelengths. In the case of Laconic, the emission peaks are measured at 492nm and 526nm for mTFP and Venus, respectively, with excitation at 430nm. The ratio between emission spectra—fluorescence intensity at 492nm divided by that at 526nm—calculates FRET efficiency, which decreases when binding lactate. Conversely, ratio thus increases in the presence of lactate, and can be used to calculate its concentration (San Martín et al., 2013).

2.1.2 SoNar

Reduction and oxidation of nicotinamide adenine dinucleotide (NAD) is a key component of the mitochondrial electron transport chain and in glycolysis (see 1: General Introduction, section 1.4). Informally considered the "housekeeping electron donors/acceptors" of the cell, NADH/NAD+ ratio therefore may provide an indication of the general redox state of the system. Furthermore, as both reduction and oxidation of NAD are involved in respiration and generation of energy, this ratio is also a gauge of the energy balance of the cell (reviewed in Cantó et al., 2015). NAD redox also plays a role in calcium regulation, gene expression, and as an enzyme cofactor, in addition to its links with various metabolic disorder such as diabetes (Okabe et al., 2019), making monitoring of its status significant for the aims of this project in regard to depicting the occurrence and potential significance of metabolic change for development and regeneration.

There have been multiple sensors generated to measure NAD redox ratio, currently based on cyclically permuted fluorescent proteins (cpFPs) (reviewed in Kyere-Yeboah et al., 2019). cpFPs describe a protein with its original termini fused and new termini formed near the chromophore. SoNar is a ratiometric indicator developed from the NADH-binding T-Rex protein fused with an altered version of cpYFP (FIG 2.1C), and, unlike the sensors preceding it, uniquely also responds to NAD+, by increasing fluorescence when excited with 485nm. The second excitation wavelength, 420nm, increases in the presence of NADH while the 485nm peak decreases proportionally (FIG 2.1D). Emission is measured at 530nm, and fluorescence signal is interpreted from the ratio between the signal obtained when exciting at the two aforementioned wavelengths (Zhao et al., 2015). Due to its response in both directions, SoNar possesses a wide dynamic range which, combined with its resistance to alteration by pH and high selectivity, suggests it to be the preferred approach to imaging changes in NADH/NAD+ levels.

2.1.3 HyPer

Reactive oxygen species (ROS) and H_2O_2 are of particular interest for a number of reasons, including a potential role in regulating or maintaining a switch to Warburg metabolism (see 1: General Introduction, section 1.2.2).

HyPer is formed of a yellow cpFP bound within the regulatory domain of the H_2O_2 sensitive Escherichia coli transcription factor, OxyR (FIG 2.1E). H_2O_2 oxidises one of OxyR's two cysteine residues, causing a reversible conformational change that allows the formation of a disulphide bridge and binding of OxyR to DNA, and altering the construct's excitation spectrum. Upon exposure to H_2O_2, the excitation peak at 420nm decreases in proportion to the increase of its 500nm peak (FIG 2.1F), and the ratio between these two peaks, imaged with a 516nm emission peak (Belousov et al., 2006), generates an indicator of H_2O_2 levels. Conformational changes are rapid, allowing dynamic imaging in live samples.

HyPer-2 differs to the original sensor by a single point mutation and has an expanded range and greater ratio response, using the same excitation peaks (Markvicheva et al., 2011). A couple of years later, this version was mutated and improved once again to produce HyPer-3. A mutation in the wild-type OxyR dimer interface that causes it to be constitutively active generated a construct that has an enhanced dynamic range and faster response rate (Bilan et al., 2013).

2.2 Materials and Methods

Cloning

Simple restriction digest and sticky end recombination was utilised for the majority of cloned constructs. In some cases, complimentary primers were designed and annealed to produce short sticky end fragments that were inserted into constructs in order to generate additional complementary restriction sites.

For specific restriction enzymes, inserts, and buffers used, see Table 2.

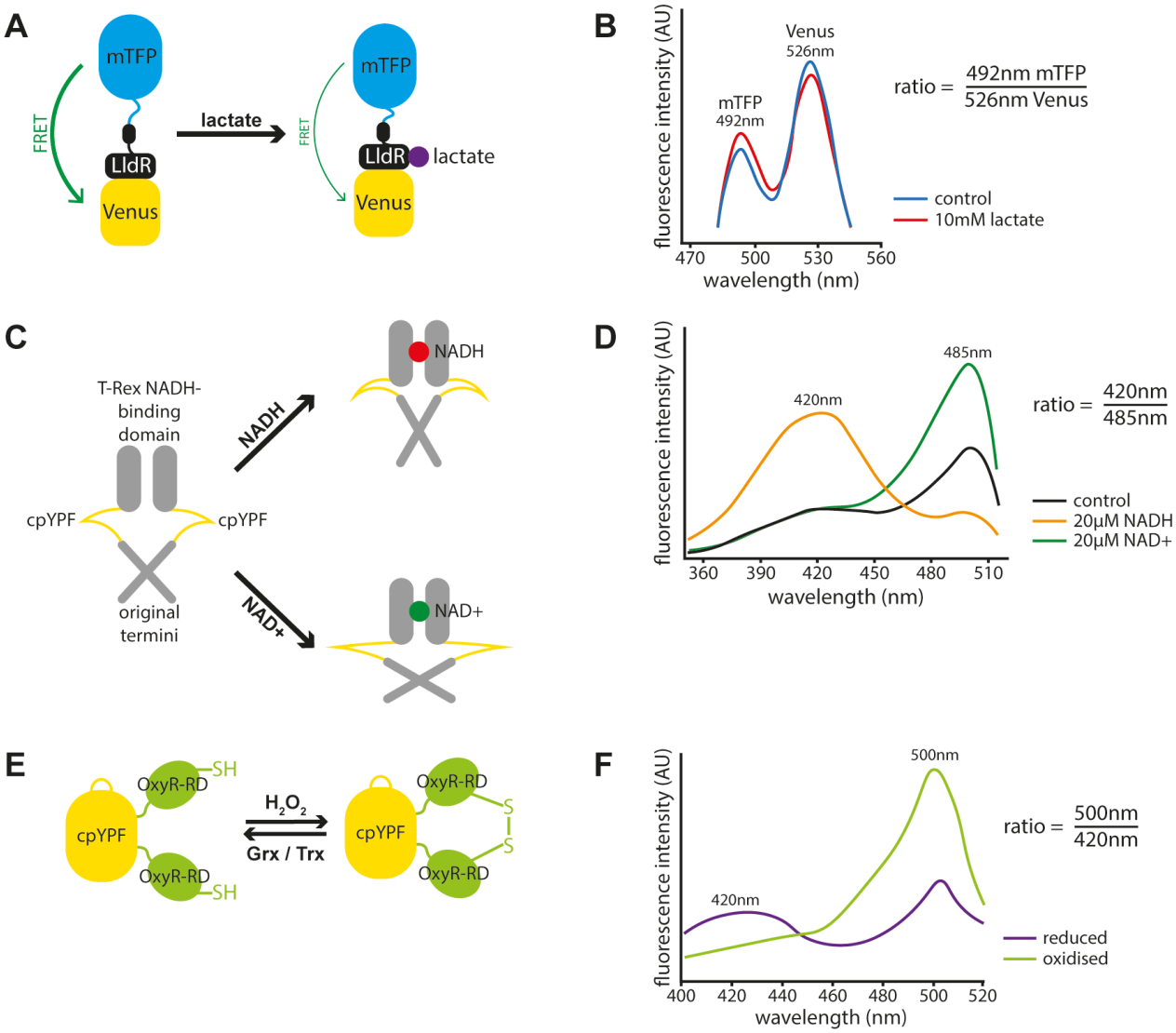

G

sensor	detects	emission (nm)	excitation (nm)	fluorescent protein(s)	↑ratio	publication	source
Laconic	lactate	485 / 528	430	mTFP/ Venus	↑*lactate*	*San Martín, A. et al., 2013.*	*F.Barros, Addgene #44238*
SoNar	NADH: NAD+	530	420 / 485	cpYFP	↑*NADH: NAD+*	*Zhao, Y. et al., 2015.*	*V.Belousov*
HyPer2	H_2O_2	516	500 / 420	cpYFP	↑H_2O_2	*Markvicheva, K.N. et al., 2011.*	*V.Belousov*

Figure 2.1. **Schematic diagrams of chosen genetically encoded sensors** (A) Schematic of the Laconic genetically encoded FRET-based sensor. A conformational change upon lactate binding to the LIdR lactate binding region fused to the Venus chromophore induces a change in energy transfer efficiency from mTFP to Venus. (Adapted from San Martín, A. et al., 2013. Figure 1B) (B) Graph depicting emission spectra of Laconic. When bound to lactate, fluorescence intensity detected in the range of mTFP increases and that of Venus decreases due to reduced FRET efficiency, thereby increasing the Laconic ratio as calculated by mTFP/ Venus. (Adapted from San Martín, A. et al., 2013. Figure 2A). (C) Schematic of the SoNar genetically encoded sensor. Conformational change upon binding of NADH or NAD+ alters fluorescence. (Adapted from Zhao, Y. et al., 2015. Figure 1A) (D) Graph depicting excitation spectra of SoNar in the presence of NADH and NAD+ compared to a control, emission measured at 530nm. (Adapted from Zhao, Y. et al., 2015. Figure 1B) (E) Schematic of the HyPer genetically encoded sensor. Upon oxidation by H_2O_2 a conformational change, formation of a disulphide bond between the two cysteine residues in the OxyR regulatory domain (OxyR-RD) alters structure and fluorescence. The conformational change is reversible, with oxidation by H_2O_2 and reduced by cellular glutaredoxins (Grxs) and thioredoxins (Trxs). (Adapted from Bilan, D.S. & Belousov, V.V., 2016. Figure 1A) (F) Graph depicting excitation spectra of HyPer in its oxidised and reduced states, emission measured at 530nm. (Adapted from Bilan, D.S. & Belousov, V.V., 2016. Figure 1B) (G) Table of details for chosen sensors, including excitation and emission peaks, constituent fluorescent protein(s), substrate level corresponding to ratio change, and source citations.

In brief: original plasmids and destination vectors were digested with the desired restriction enzymes and buffers (Roche) in a double digest or sequential digest with intermediate purification by phenol:chloroform and ethanol precipitation. Product was run on a 1% agarose electrophoresis gel and desired band was stained using diluted methylene blue in 1XTAE buffer and isolated with a QIAquick Gel Extraction Kit (Qiagen). In the case of digestion with a single restriction enzyme (see Table 2), dephosphorylation of the 5'-ends was achieved by incubating with alkaline phosphatase (CIP, M0290, NEB) at 37˚C for one hour. In instances where blunt ends were required (see Table 2), one unit of Klenow DNA polymerase (NEB) per microgram of DNA in 1XT4 DNA ligase buffer (NEB) supplemented with 33 μM each dNTP was incubated for 15 minutes at 25˚C. Ligation was performed overnight at 16˚C with T4 DNA ligase (NEB) and a 3:1 insert-to-vector ratio. In cases where a new restriction site was added via short oligos (see Table 2), complementary single stranded primers were designed and ordered from Sigma-Aldrich and equal amounts annealed in a microcentrifuge tube with 1X T4 DNA ligase buffer (NEB) for 5 minutes at 95˚C. Primers were allowed to cool naturally at room temperature and 5ng was used in ligation per 50ng vector. 5μL of ligation reactions were transformed into 50μL chemically competent DH5α *E. coli* cells (Invitrogen), grown on a suitable antibiotic inoculated LB agar plate at 37˚C overnight, and 6-12 colonies picked the following day for culture and plasmid preparation with PureLink Quick Plasmid Miniprep Kit (Invitrogen). Identification of positive clones was conducted via restriction enzyme digest.

For the transgene cassettes, the modular cloning systems pTransgenesis (Love et al., 2011) or Tol2 kit (Kawakami, 2007) based on the Gateway system of cloning (Hartley et al., 2000) were used (FIG 2.2), and recombination was facilitated with the Gateway LR Clonase II Enzyme Mix (Invitrogen, 11791) according to manufacturer instructions: incubated overnight with the LR clonase enzyme at 23˚C, followed by inactivation by addition of 0.5μL Proteinase K at 37˚C for 10 minutes. 3μL of the reaction was transformed into 30-50μL chemically competent DH5α *E. coli* cells (Invitrogen) as detailed previously. See Table 3 for the modular compositions and constructs generated.

mRNA microinjection

Wild type strain AB zebrafish embryos were injected at the one cell stage into the cell cytoplasm with 1ng sensor mRNA in nuclease free water with phenol red. Sensor mRNA was synthesised from pCS2+ plasmids linearised with NotI (NEB), with mMESSAGE mMACHINE SP6 Transcription Kit (Ambion) and purified with lithium chloride (LiCl) extraction.

Zebrafish husbandry

Adult zebrafish (*Danio rerio)* were maintained at 28 °C with a 14 hour light/10 hour dark cycle. Embryos collected from crosses were staged as described in (Kimmel et al., 1995). All animal experiments were performed in compliance with NACLAR Guidelines of Singapore overseen by the Biological Resource Centre of A*STAR (IACUC Protocol Number 140924), and Home Office guidelines UK. Wild type zebrafish are of the AB strain, and

transgenic embryos are made using the wild type AB background. In all cases, embryos were raised in 1X E3 embryo medium as described in Cold Spring Harbor Protocols, or 1X egg water consisting of 60 µg/ml sea salts (Sigma Aldrich S9883), supplemented with 0.1% Methylene Blue.

Generation of transgenic lines

Wild type strain AB zebrafish embryos were injected at the one cell stage into the cell cytoplasm with 25pg *tol2* mRNA and 25pg circular plasmid in 1nL. *tol2* mRNA was synthesised from pT3-Tol2 linearised with SmaI (NEB) with mMESSAGE mMACHINE T3 Transcription Kit (Ambion) and purified with LiCl extraction. Injected embryos with strongest expression of mosaic GFP were grown to adults and screened for germline transmission.

Pharmacological treatment

Embryos were maintained in 0.5X E2 medium (half strength modification of the E2 embryo medium described in Cunliffe (2003) in place of 1X E3 embryo medium. Stock concentrations of the drugs were added to the embryo media and incubated at room temperature for one hour unless otherwise stated.

Antimycin A (AA, Sigma Aldrich A8674) was dissolved to make a stock solution of 5mM in dimethyl sulfoxide (DMSO, Sigma Aldrich D8418) and diluted 1:1000 in E2 medium for a working concentration of 5µM with a final concentration of 0.1% DMSO.

Sodium azide (NaN_3, Sigma Aldrich S2002) was dissolved in 1X phosphate buffered saline (PBS, Sigma Aldrich P5493) fresh for each use at a stock concentration of 100X (eg. 5M for a working concentration of 50mM).

Hydrogen peroxide (H_2O_2, Sigma Aldrich H1009) in its commercially bought form of 30% w/w (9.8M) was added directly to the E2 media. Embryos were imaged pre-treatment and immediately after the addition of H_2O_2 to the media.

Biochemical lactate assay

A commercially available colorimetric lactate assay kit (MAK064, Sigma Aldrich) was used and protocol adapted for embryonic samples. Lactate in the sample reacts with the enzyme mix provided in the kit, the product of which interacts with the supplied lactate probe to produce colour (A_{570}) and fluorescence (excitation/emission = 535/587nm). Lactate concentration was measured by the colorimetric product of the enzymatic reaction with lactate at an absorbance of 570nm.

Samples were prepared by flash freezing on dry ice and macerating 25 dechorionated eggs or embryos with a plastic micropestle in 45µL 2:2:1 acetonitrile:methanol:dH_2O at -20˚C or pre-chilled on dry ice. Samples were then centrifuged at 4˚C at 15000rcf for 10 minutes, the supernatant collected into a new tube and stored at -20˚C until use in the assay. 5µL of the embryo supernatant was used per reaction.

A standard curve was set up using known concentrations of a lactate standard (0, 2, 4, 6, 8 and 10nM per reaction) with the addition of 5µL 2:2:1 to each reaction in order to control for any background or change in enzyme activity caused by the buffer.

Triplicate reactions were set up otherwise according to manufacturer instructions, with a minimum of three biological repeats. Reaction incubation time was extended to 3 hours, and absorbance at 570nm (A_{570}) was read on a microplate reader (BioTek Synergy H1) in triplicate to give a total of nine readings per sample, per experiment.

Microscopy

Sample preparation: Embryos were manually dechorionated and imaged in an agarose coated 35mm dish with small bored wells for individual embryos (Singapore) or in a 96-well plate (Corning) in separate wells (Manchester) surrounded by media supplemented with 0.04% MS-222 (tricaine, Sigma Aldrich E10521).

Images acquired on an AxioImager.M2 upright microscope (Zeiss) used a 5X/0.16 EC Plan-Neofluar, 10X/0.3 EC Plan-Neofluar, or 20X/0.4 Corr LD Plan-Neofluar objective as specified. Zeiss filter sets for CFP (BS455) and FITC/mCherry (DBS525/50 + 650/100) were utilised for Laconic imaging, and FITC/mCherry (DBS525/50 + 650/100) for SoNar and HyPer imaging. Excitation was from a Colibri 7 LED fluorescent light source, Violet (430nm) used for Laconic imaging and Violet (430nm) and Blue (475nm) used for SoNar and HyPer imaging. Imaging software: Zen Blue 2.3 Pro. The images were collected using a 2.8 Megapixels (Axiocam 503) colour camera at 14-bit on the black-and-white setting at room temperature.

Images for Laconic and SoNar imaging acquired on an Eclipse Ti inverted microscope (Nikon) used a 4X/0.13 Plan Fluor PhL DL or 20x/0.75 SFluor DIC M/N2 objective as specified. Semrock filter sets for eCFP (480/30) and eYFP (535/30) emission were used, and excited with Blue (440/20) from a SpectraX light engine (Lumencor). The images were collected using a Retiga R6 (Q-Imaging) CCD camera at 14-bit. Imaging software: NIS Elements AR.46.00.0. Mechanised point visiting was used to allow multiple positions to be imaged within the same time-course and environment was maintained at 28˚C.

Images for HyPer imaging were acquired on an Olympus IX83 inverted microscope using a 10X/0.30 UPlanFL N or 20X/0.85 UPlanSApo (Oil) objective as specified. Semrock filter set for YFP (544/25) emission was used, with excitation by Blue (440/20) and Teal (510/25) from a SpectraX light engine (Lumencor). The images were collected using a Retiga R6 (Q-Imaging) CCD camera at 16-bit. Imaging software: Metamorph v7.8.4.0 (Molecular Devices). Mechanised point visiting was used to allow multiple positions to be imaged within the same time-course.

Image analysis

All processing of images for calculating ratio and measuring fluorescence or ratio was conducted in Fiji (Fiji Is Just ImageJ, version 2.0.0). Average background was subtracted and threshold applied to remove remaining

background, then respective channels divided by one another as required using the Image Calculator function. Pseudocolouring was applied using Lookup Table "16 colors".

Statistical analysis

GraphPad Prism 8 was used for statistical testing, with sample numbers exceeding 6 in all experiments. Column or grouped statistics and analyses of differences between means were implemented for all data sets. For column statistics, two-tailed unpaired t-tests with assumed Gaussian distribution were used. Two-way ANOVA was used with Sidak's multiple comparisons test to compare means between groups. Differences were considered significant to * at $P<0.05$, ** at $P<0.01$, *** at $P<0.001$, and **** at $P<0.0001$. Not significant (ns) was considered $P\geq0.05$, 95% confidence interval.

2.3 Results

2.3.1 Generation of constructs

A number of genetically encoded sensors were obtained from Addgene in their original cell culture vectors, however I elected to optimise only Laconic and SoNar for use (see FIG 2.1G for full information, references, and sources for constructs). As such, it was required that the sensors be sub-cloned into vectors appropriate for use in zebrafish and allowing for the *in vitro* transcription of mRNA, either pCS2+ or pCS107, which possess SP6 sites for *in vitro* mRNA transcription. Note that in some cases an additional cloning step to add a novel restriction site was required, utilising appropriate linker primers (Table 2.1). FIG 2.3 shows examples of positive ligations for one of the chosen biosensors, Laconic, revealed by electrophoresis of restriction digest of minipreps.

To then generate transgenic lines, the sensor gene sequences were cloned into the 3' modular plasmid component of the Gateway system (Hartley et al., 2000) (see Table 2). These constructs were then combined with complementary modular plasmids from either the pTransgenesis (Love et al., 2011) or Tol2 kit (Kawakami, 2007) systems and inserted between Tol2 recognition sites on a destination vector using the LR recombinase method (FIG 2.1) (see Table 2.2 for details of the modular components). I realised there was an undesired upstream ATG site in the beta-actin constructs, and additionally performed a digest with BamHI and self-ligation to excise the sequence.

I successfully sub-cloned as described above into pCS2 and p3 for Laconic and SoNar, and into transgene cassettes under the beta-actin (actb2) and ubiquitin (ubb) promoters. We already possessed HyPer in the pCS2 and p3 vectors, and under the ubiquitin promoter for transgenesis, but I additionally generated a transgene construct with HyPer under the actb2 promoter.

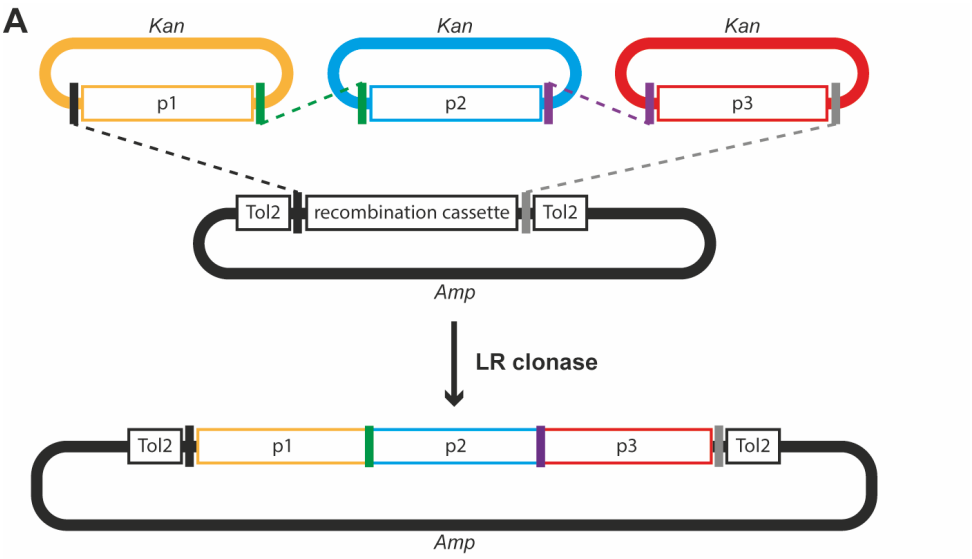

B

	pTransgenesis	Tol2kit
p1	selection marker	promoter
p2	promoter	coding sequence
p3	coding sequence+polyA tail	polyA tail
p4	desination vector with transgenesis facilitation sequence (Tol2)	

Figure 2.2. **Schematic diagrams of the Gateway cloning system** (A) Schematic depiction of the modular plasmids used in the Gateway cloning system. Coloured vertical bars represent attL and attR sites for recombination by LR clonase. Antibiotic selection markers shown in italics, kanamycin (Kan) for entry vectors and ampicillin (Amp) for the destination vector. Incubation overnight at room temperature with LR clonase results in recombination in a sequential and predictable order, as shown by dotted lines. The four entry vectors, p1, p2 and p3, correspond to different components for generating a transgenesis construct depending on whether they are sourced from the pTransgenesis system or Tol2kit (B). In both systems the destination vector contains Tol2 recognition sites either side of the att recombination sites between which the modular components will be inserted. (Adapted from Love, N.R. et al., 2011. Figure 1A,B and Kwan, K.M. et al., 2007. Figure 1A)

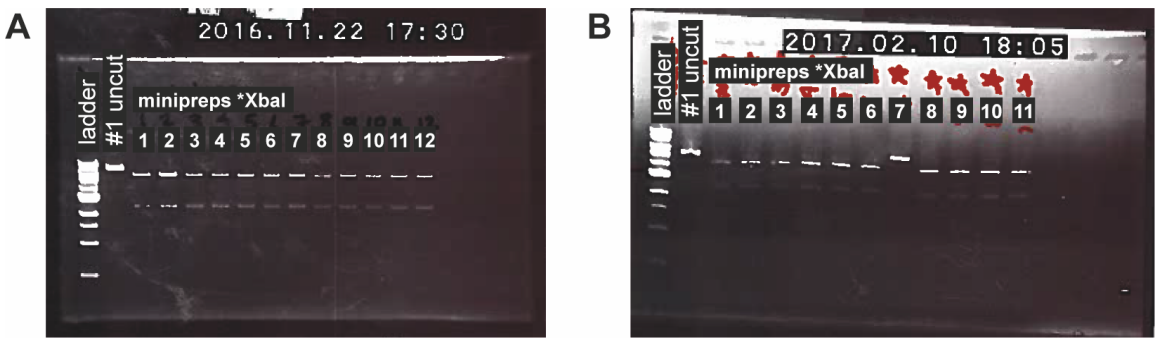

Figure 2.3. **Electrophoresis gel images of control digests to identify positive miniprep clones.** (A) pcDNA3.1-Laconic ligation with linker primer to add an XbaI recognition site, transformed, and colonies picked and mini prepped. Digested with XbaI to give two bands (construct also contains an endogenous XbaI site 72bp upstream from the gene), 5347bp and 2301bp, if ligation was successful, and a single band of 7648bp if unsuccessful. In this instance, all 12 colonies picked were positive. (B) pcDNA3.1-Laconic+XbaI ligation with pCS2. Digested with EcoRI and XbaI to give two bands, 4083bp (pCS2) and 2274bp (Laconic), if ligation was successful. In this instance, all colonies except #7 were positive.

sensor	original vector	new vector	restriction enzyme 5'	restriction enzyme 3'	double digest conditions	new construct	notes
Laconic	pcDNA3.1(-)	pCS2+	EcoRI	XbaI (site added from HindIII site via short oligos)	Roche buffer H, 37˚C	pCS2-Laconic	1. *digest pcDNA3.1-Laconic with HindIII (Roche buffer B, 37˚C), XbaI site added by ligation with primers** 2. *digest new pcDNA3.1-Laconic with EcoRI and XbaI (2262bp)* 3. *digest pCS2 with EcoRI and XbaI (4074bp) (will create extra 40bp fragment)* * *5'-AGCTGTCTAGACCCA-3'* *5'-AGCTTGGGTCTAGAC-3'*
SoNar	pcDNA3.1(-)	pCS2+	BamHI	XbaI	Roche buffer A, 37˚C	pCS2-SoNar	1. *digest pCS2 with BamHI and XbaI (4059bp)* 2. *digest SoNar with BamHI and XbaI (1177bp)*
Laconic	pcDNA3.1(-)	p3-HyPer	BamHI	HindIII	Roche buffer B, 37˚C	p3-Laconic	1. *digest Laconic with BamHI and HindIII (2239bp)* 2. *digest p3-HyPer with BamHI and HindIII (2967bp)*
SoNar	pcDNA3.1(-)	p3-mCherry	BamHI	XhoI	Roche buffer B, 37˚C	p3-SoNar	1. *digest SoNar with BamHI and XhoI (1171bp)* 2. *digest p3-mCherry with BamHI and XhoI (2914bp)*

Table 2.1. **Cloning information for Laconic and SoNar.**

p1	p2	p3	p4	resulting construct
p1-blank	p2-ubb	p3-laconic	pDEST-Tol2-ISceI	ubb:laconic
p1-blank	p2-ubb	p3-sonar	pDEST-Tol2-ISceI	ubb:sonar
p5E-bactin2	pME-MCS	p3-laconic	pDEST-Tol2-ISceI	actb2:laconic
p5E-bactin2	pME-MCS	p3-sonar	pDEST-Tol2-ISceI	actb2:sonar
p5E-bactin2	pME-MCS	p3-hyper2	pDEST-Tol2-ISceI	actb2:hyper

Note: MCS is multiple cloning site, ie. empty

Table 2.2. **Gateway modules for generation of transgenesis constructs.**

2.3.2 Transgenic lines

Though injections of sensor mRNA are useful for initial tests to determine the suitability of the constructs in the zebrafish model organism, due to their quick and easy application, in order to examine early development, mRNA injections are unsuitable due to the delayed translation of the sensor protein. Any later experiments, such as required for embryo fin fold and tail amputations, require expression to be maintained robustly until at least seven days post amputation, by which point mRNA expression will have been exhausted. Thus, the creation of transgenic lines with the sensors expressed under appropriate promotors was the best method for using these as a tool for investigating metabolism in early development and regeneration.

The beta-actin promoter (actb2) results in maternal expression with deposits of the protein products into the oocyte resulting in expression from even the one cell stage (Higashijima et al., 1997; Yoshinari et al., 2012), thus making it ideal for experiments on fertilisation until at least 48hpf. However, after this point expression becomes weaker, therefore for experiments regarding regeneration of the fin, the ubiquitin promotor (ubb) is most suitable, which gains intensity by 24hpf and is maintained throughout the rest of embryogenesis (Mosimann et al., 2011). Both actb2 and ubb are ubiquitous promotors, and the sensors would be expressed in the cytoplasm of all cell types.

The most common and well-documented method for generating zebrafish transgenic lines are using the Tol2 transposon system (Kawakami et al., 2004). Other methods are also viable, including meganuclease insertion such as ISce-I (Thermes et al., 2002), and more recently knock-in using the CAS9-CRISPR system (reviewed in Liu et al., 2019).

There are several existing genetic sensor transgenic lines, including *Tg[ubb:hyper]* (Gauron et al., 2016; Amaya lab, unpublished) and *Tg[βactin2:GCaMP6s]* (Chen et al., 2017), which measures calcium, however neither Laconic nor SoNar have been published in the zebrafish model organism, and as such this project aims to pioneer their use. I therefore aimed to make two lines for each sensor, one under the ubb promotor and one under actb2.

Injections into the cell cytoplasm of wild type embryos at the one cell stage were conducted as described in the Materials and Methods for the following plasmids: pTol2-actb2:laconic, pTol2-ubb:laconic, pTol2-actb2:sonar, pTol2-ubb:sonar, pTol2-actb2:hyper. Mosaic expressing injected embryos were raised to identify F0 founders with germline transmission, which were out-crossed with wild type to produce F1 adults. The F1 generation were then in-crossed in order to generate embryos for use in experiments.

Founders were identified for all lines with the exception of actb2:sonar.

2.3.3 Laconic positive controls

Due to the lack of published literature on the use of the Laconic in the zebrafish model organism, it was first necessary to ensure the sensor was operational *in vivo*. To this end, I generated mRNA from the sub-cloned construct pCS2-Laconic and injected this into one cell stage wild type embryos. The positive controls derived involved the use of mitochondrial inhibitors in order to stimulate the activity of glycolysis, thus promoting lactate

production. As described in the introduction, an increase in lactate concentration within the cytoplasm should cause an increase in Laconic ratio, as lactate binding decreases FRET efficiency. Therefore, if the positive control experiments are successful, increasing lactate levels with mitochondrial inhibitors should drive a corresponding increase in Laconic ratio.

The first inhibitor I chose to use was antimycin A (AA), which acts on complex III of the electron transport chain in mitochondria by binding to cytochrome C reductase (Slater, 1973), thereby preventing oxidative phosphorylation and causing the cells to up-regulate glycolysis activity as compensation (FIG 1.6A). The second inhibitor, sodium azide (NaN_3), inhibits complex IV of the electron transport chain, cytochrome oxidase (Bennett et al., 1996), similarly blocking oxidative phosphorylation and driving the cell towards anaerobic respiration. As with AA treatment, NaN_3 should induce an elevation in lactate levels and therefore Laconic ratio (FIG 1.6A). Unlike AA, NaN_3 is a reversible inhibitor, and thus an extra element was included in these experiments to show lactate returning to control levels after washing out of the drug, further supporting the conclusion Laconic ratio represents lactate levels.

Embryos were screened and those displaying the brightest fluorescence were selected and individually imaged before treatment and followed throughout the one hour treatment with AA. Laconic ratios of individual embryos were compared to minimise effects of any variability of expression within the clutch, though theoretically the ratiometric nature of the sensor should negate this problem regardless.

As expected, Laconic ratio significantly increased in mRNA injected embryos with AA treatment compared to controls treated with DMSO (FIG 2.5), showing the sensor is indeed viable *in vivo*. These experiments were conducted and successful in two locations (Manchester and Singapore) with two separate imaging set-ups, further supporting the repeatability of the experiment.

Having seen a positive outcome in mRNA injected embryos, I moved on to address my final aim and determine whether these sensors are transferable to and functional in the form of a stable transgene. After generating the transgenic lines *Tg[actb2:laconic]* and *Tg[ubb:laconic]*, I repeated the positive control experiments with AA, again in two locations, and additionally with NaN_3 to confirm the sensor functions in the same way as an endogenously expressed transgene. The positive controls on transgenic embryos were conducted at stages of development to most closely resemble the age of the embryos during the intended experiments—in the case of *Tg[actb2:laconic]*, earlier in development to coincide with imaging early embryogenesis, and for *Tg[ubb:laconic]*, 2 days post fertilisation (dpf) as would be used in amputation experiments—and imaging the same area with the same magnification. A small number of embryos in each condition were imaged every five minutes for the course of the one hour treatment to produce a timelapse, while most were simply imaged before and after incubation with the drug or control at 28˚C for one hour, in order to increase sample number. Pre- and post-treatment ratios of individual embryos were compared.

A significant increase in Laconic ratio was seen in *Tg[ubb:laconic]* embryos after treatment with AA, with a significant difference between the post-treatment ratios of AA and DMSO controls, while pre-treatment values

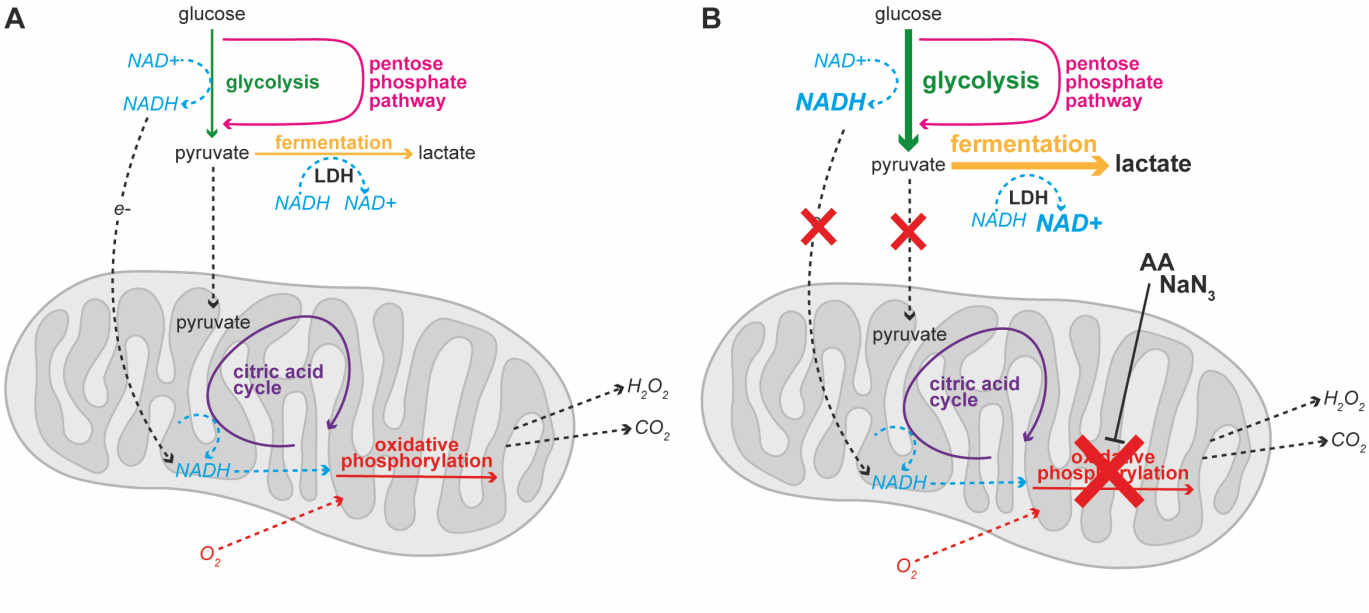

Figure 2.4. **Chemical induction of aerobic glycolysis** (A) Simple schematic depiction of the major metabolic pathways under normal aerobic cellular conditions. (B) Schematic showing the action of antimycin A (AA) and sodium azide (NaN_3): inhibition of oxidative phosphorylation in the mitochondria, leading to up-regulation of glycolysis activity and increased fermentation, as shown by larger, bold typeface.

were not significantly different between DMSO control and AA treated embryos (FIG 2.6A-B' and E-F'). Treatment with NaN_3 also resulted in significantly elevated Laconic ratios, which returned to levels not significantly different to controls after NaN_3 washout and 24 hours of recovery (FIG 2.6C-D').

Similarly for *Tg[actb2:laconic]* embryos, Laconic ratio significantly increased with AA treatment and NaN_3 treatment, but not with DMSO or PBS controls (FIG 2.7). Laconic ratio returned to control levels after washing out NaN_3 and allowing 24 hours for recovery (FIG 2.7D), as seen in experiments with mRNA injected and *Tg[ubb:laconic]* embryos.

To further support the conclusion that Laconic ratio corresponds to lactate level, I conducted a similar AA treatment on embryos and measured their lactate levels with a biochemical assay as a separate positive control. As the assay cannot be conducted on live embryos, a "pre-treatment" sample was taken to compare to samples of embryos treated for 10 minutes (from the timelapses in FIG 2.5B it is evident a significant increase in lactate is seen as early as after 10 minutes of treatment) with either 5μM AA or 0.1% DMSO control.

With three repeats of the experiment, each outcome confirmed the expectation that AA treatment would increase the levels of lactate in the embryos significantly, while there was no significant increase in measured lactate levels after treating with DMSO (FIG 2.8A). This supports the conclusion that the rise in Laconic ratio does indeed corroborate with and indicate a change in lactate level.

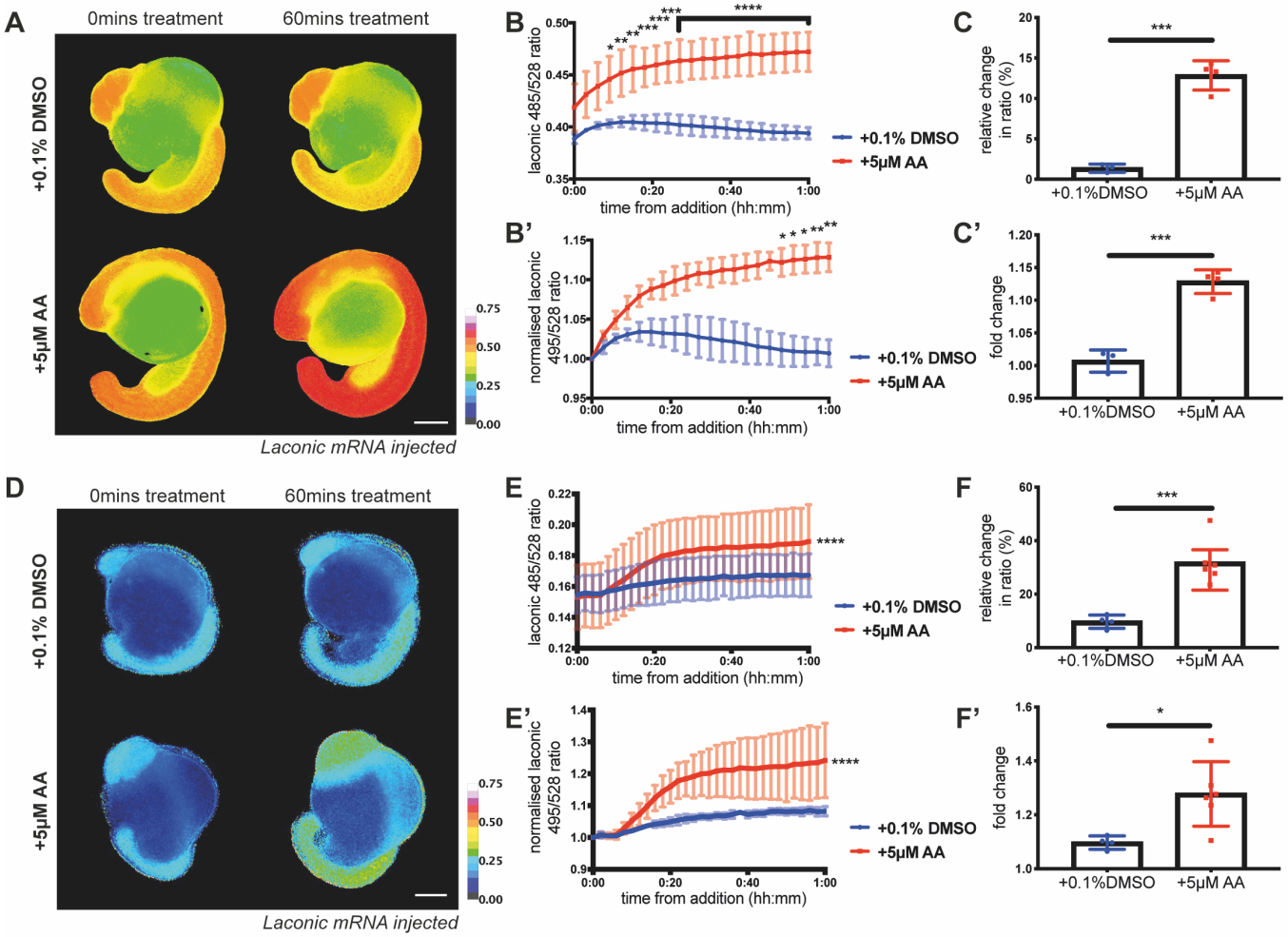

Figure 2.5. **Positive controls for Laconic mRNA with antimycin A (AA)** (A-C') show data obtained with Zeiss AxioImager.M2 widefield microscope (5X), (D-F') show data obtained with Nikon Ti Eclipse widefield microscope (4X). All scale bars represent 200µm. Differences were considered significant to * P<0.05, ** P<0.01, *** P<0.001, **** P<0.0001, and ns P≥0.05. (A) and (D) Representative ~19hpf wild type embryos injected with laconic mRNA at the one cell stage before and after 60mins of treatment with 0.1% DMSO or 5µM AA, pseudocoloured to show Laconic ratio calculated by dividing the 485nm emission channel by the 528nm emission channel. (B) and (E) Graphs showing raw Laconic ratios over time during treatment with 0.1% DMSO or 5µM AA. Two-way ANOVA to calculate significance, (B) n=4, (E) n=6. (B') and (E') Graphs showing Laconic ratios over time normalised to pre-treatment value. Two-way ANOVA to calculate significance, (B') n=4, (E') n=6. (C) and (F) Graphs showing quantification of ratio change as a percentage of individual pre-treatment ratio. Students' t-test to calculate significance, (C) n=4, (F) n=6. (C') and (F') Graphs showing quantification of ratio change as fold change (post treatment ratio divided by pre treatment ratio). Students' t-test to calculate significance, (C') n=4, (F') n=6.

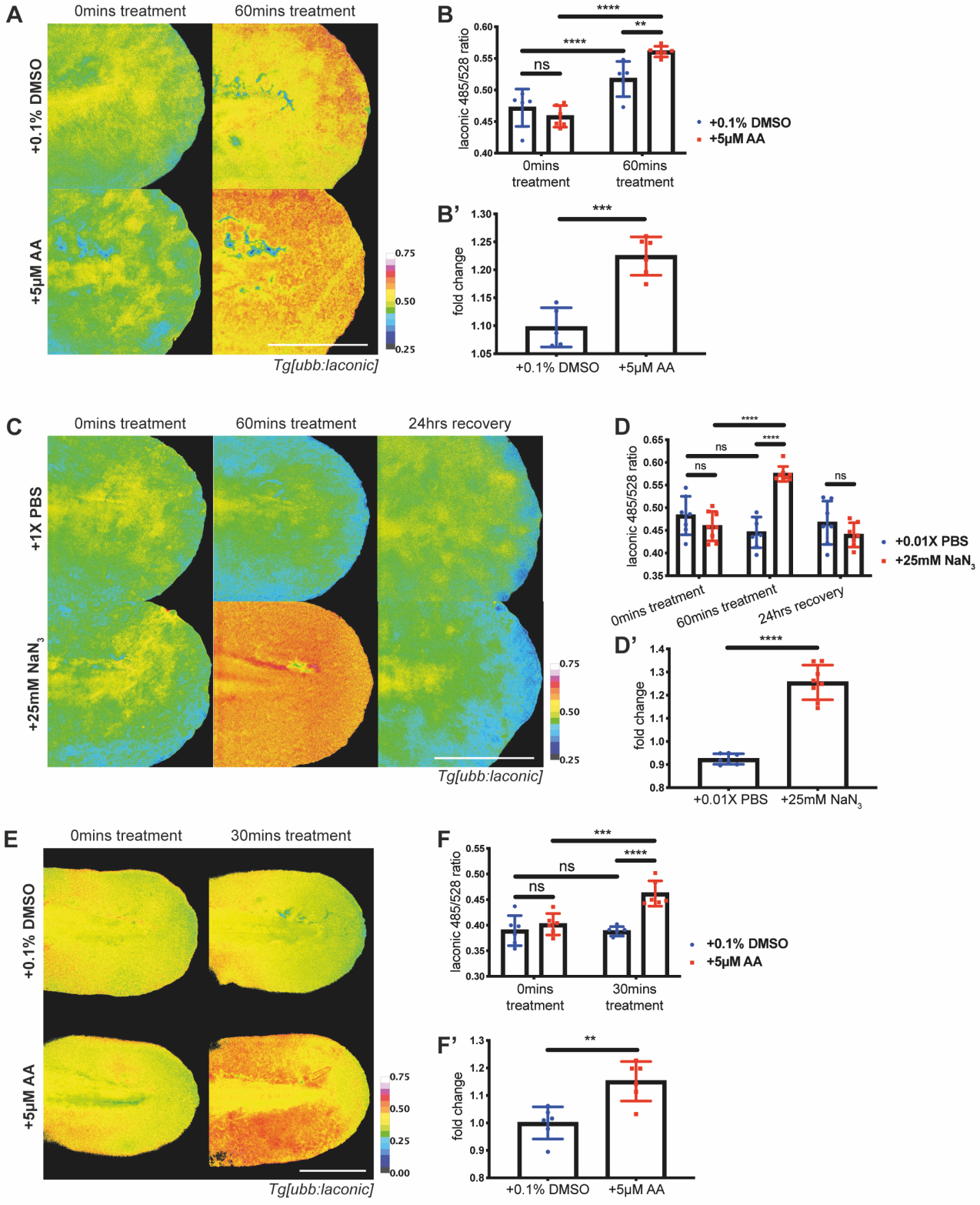

Figure 2.6. **Positive controls for transgenic line of Laconic under the ubiquitin promoter.** (A-D) show data obtained with Zeiss AxioImager.M2 upright widefield microscope (20X), (E) and (F) show data obtained with the Nikon Eclipse Ti inverted widefield microscope (20X). All scale bars represent 200μm. Differences were considered significant to * P<0.05, ** P<0.01, *** P<0.001, **** P<0.0001, and ns P≥0.05. (A) and (E) Representative transgenic embryos at 48hpf before and after treatment with 0.1% DMSO or 5μM AA, pseudocoloured to show Laconic ratio calculated by dividing the 428nm emission channel by the 485nm emission channel. (B) and (F) Graphs showing raw Laconic ratios pre-treatment and after treatment with 0.1% DMSO or 5μM AA. Two-way ANOVA to calculate significance, (B) n=6, (F) n=6. (B') and (F') Graphs showing quantification of ratio change after 60 minutes of treatment with 0.1% DMSO or 5μM AA as fold change (ratio after treatment divided by pre-treatment value). Students' t-test to calculate significance, (B') n=6, (F') n=6. (C) Representative transgenic embryos at 48hpf before and after 60 minutes of treatment with 0.01X PBS or 25mM NaN_3, and after 24 hours recovery post wash out of drug, pseudocoloured to show Laconic ratio calculated by dividing the 428nm emission channel by the 485nm emission channel. *(continued on next page)*

(Figure 2.6. cont.) (D) Graph showing raw Laconic ratios pre-treatment, after 60 minutes of treatment with 0.01X PBS or 25mM NaN_3, and after 24 hours of recovery after drug wash out. Two-way ANOVA used to calculate significance, n=8. (D') Graph showing quantification of ratio change after 60 minutes of treatment with 0.01X PBS or 25mM NaN_3 as fold change (ratio after treatment divided by pre-treatment value). Students' t-tests used to calculate significance, n=8.

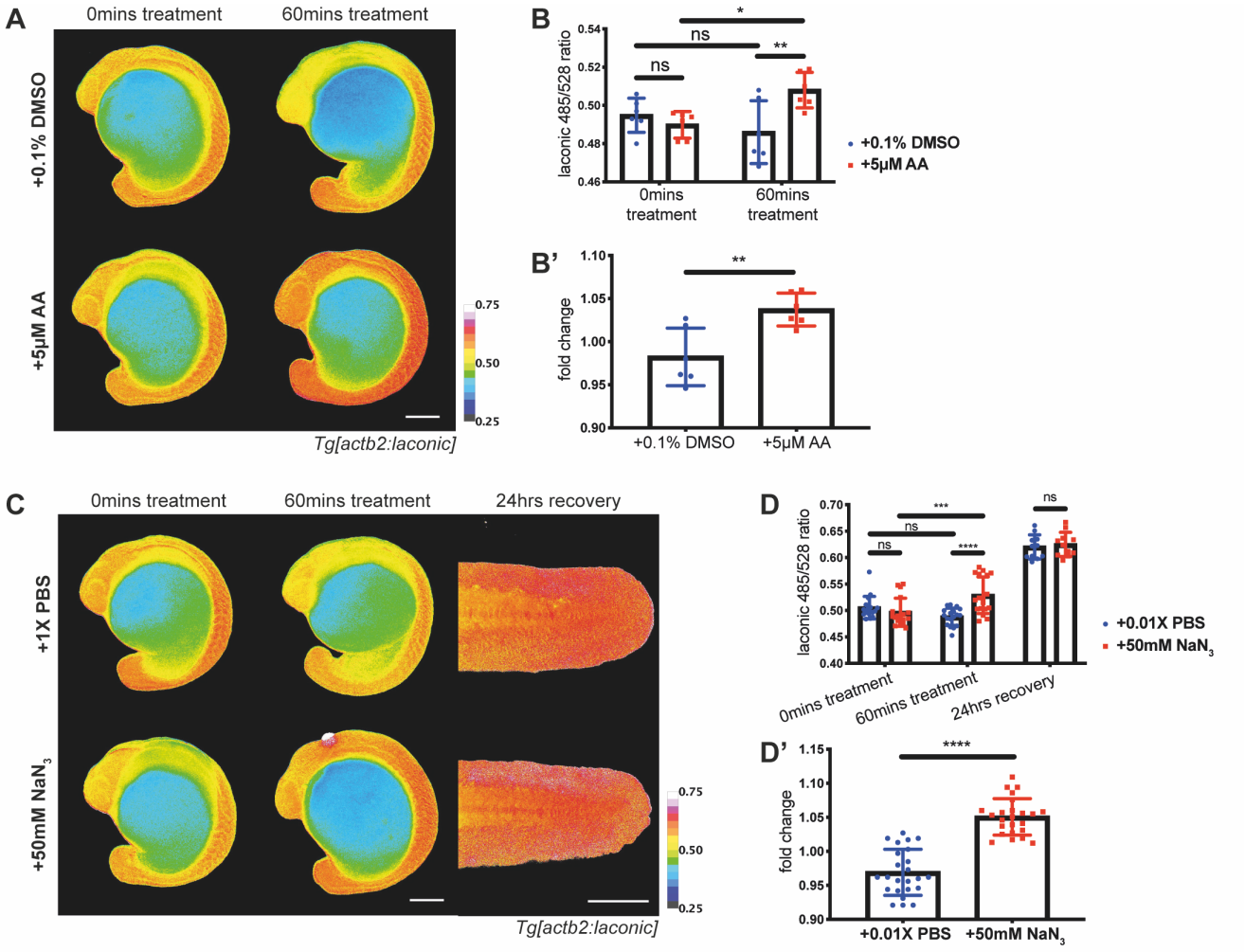

Figure 2.7. **Positive controls for transgenic line of Laconic under the beta-actin promoter.** All panels show data obtained with Zeiss AxioImager.M2 upright widefield microscope (5X, 10X). All scale bars represent 200µm. Differences were considered significant to * P<0.05, ** P<0.01, *** P<0.001, **** P<0.0001, and ns P≥0.05. (A) Representative transgenic embryos at ~17hpf before and after 60 minutes of treatment with 0.1% DMSO or 5µM AA, pseudocoloured to show Laconic ratio calculated by dividing the 428nm emission channel by the 485nm emission channel. (B) Graph showing raw Laconic ratios pre- and post-treatment. Two-way ANOVA to calculate significance, n=6. (B') Graph showing quantification of ratio change as fold change (ratio after 60 minutes of treatment with 0.1% DMSO or 5µM AA divided by individual pre-treatment values). Students' t-test to calculate significance, n=6. (C) Representative panels transgenic embryos at ~17hpf before and after 60 minutes of treatment with 0.01X PBS or 50mM NaN_3, and after 24 hours recovery post wash out of drug, pseudocoloured to show Laconic ratio calculated by dividing the 428nm emission channel by the 485nm emission channel. (D) Graph showing raw Laconic ratios pre-treatment, after 60 minutes of treatment with 0.01X PBS or 50mM NaN_3, and after 24 hours of recovery after drug wash out. Two-way ANOVA used to calculate significance, n=18. (D') Graph showing quantification of ratio change after 60 minutes of treatment with 0.01X PBS or 50mM NaN_3 as fold change (dividing post-treatment by pre-treatment value). Students' t-tests used to calculate significance, n=24.

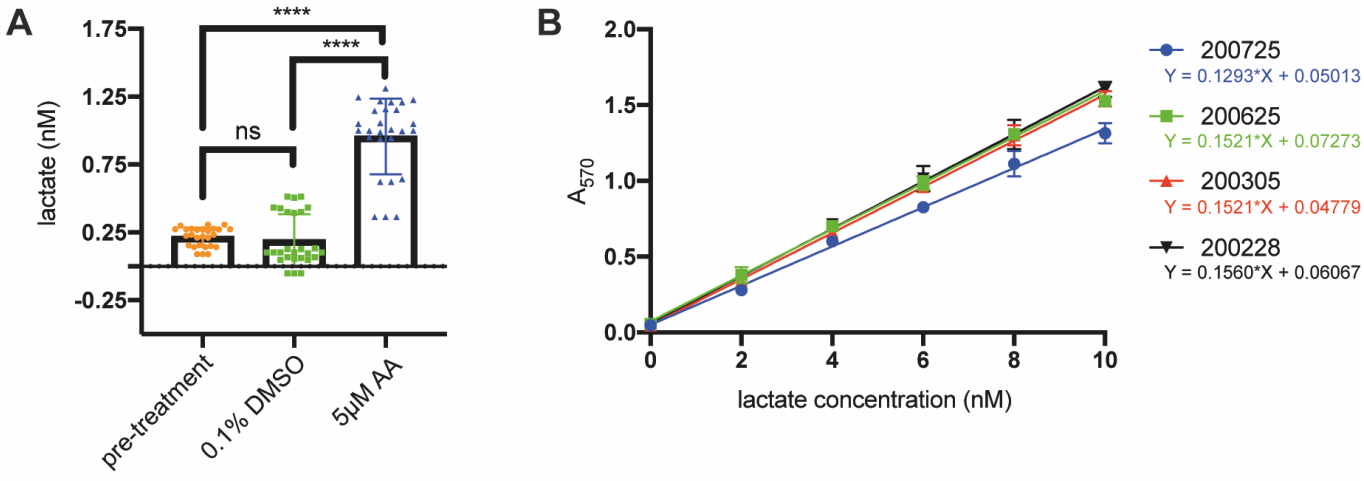

Figure 2.8. **Positive controls for lactate levels with antimycin A (AA) treatment measured by biochemical lactate assay** (A) Graph of lactate levels in 2dpf embryos (calculated using a standard curve) after 10 minutes treatment with 0.1% DMSO or 5μM AA compared to a pre-treatment baseline level. Data is a combination of three biological repeats, with three technical repeats read in triplicate. One-way ANOVA to calculate significance. ns $P \geq 0.05$, **** $P < 0.0001$, n=36. (B) Examples of standard curves for individual biological repeats generated by known concentrations of lactate with the addition of sample buffer as used in embryo samples. Legend shows date of experiment and equation calculated by simple linear regression.

2.3.4 SoNar positive controls

The situation regarding published literature on SoNar use in zebrafish is as with Laconic. It was therefore necessary for positive controls to also be conducted for my chosen NADH to NAD+ ratio (NADH/NAD+) sensor. Using the same strategies as for Laconic, I sub-cloned the SoNar sequence into the pCS2 plasmid so as to be able to synthesise mRNA for initial injection before generating transgenic lines, and treated mRNA injected embryos with mitochondrial inhibitors. I used the same inhibitors for testing SoNar as Laconic: antimycin A (AA), an inhibitor of complex III of the mitochondrial electron transport chain (Slater, 1973), and sodium azide (NaN_3), an inhibitor of complex IV of the electron transport chain (Bennett et al., 1996).

NADH is produced during glycolysis, however the fermentation reaction that produces lactate from pyruvate regenerates NAD+. Depending on the speed of each reaction, NADH/NAD+ and therefore SoNar ratio should increase with the up-regulation of glycolysis activity, and potentially even out when the fermentation reaction replenishes NAD+. Thus, a successful positive control experiment would show treatment with mitochondrial inhibitors causing an increase in SoNar ratio, at least initially, to indicate the correspondence between NADH/NAD+ and SoNar ratio.

In the same manner as the Laconic positive control experiments, embryos were screened for brightest SoNar expression (either from mRNA injection or transgenic expression), and individual embryos were imaged and followed during or after one hour of treatment. By following individual embryos I was able to directly compare the pre- and post-treatment ratios without concern about variability within the clutch. However, in theory, differences in brightness should not have an effect due to the ratiometric nature of the sensor.

Indeed, a significant increase in SoNar ratio was evident when treating mRNA injected embryos with AA but not DMSO controls (FIG 2.9). Since I was not able to produce a *Tg[actb2:sonar]* line, I repeated the positive controls on *Tg[ubb:sonar]* embryos only. As with Laconic, these experiments were conducted in two locations (Manchester and Singapore) to provide stronger evidence of repeatability and to ensure the imaging setups were comparable, and experiments on *Tg[ubb:sonar]* transgenic embryos were performed on 2dpf embryos at the same magnification and location as would be used for amputation experiments. As expected, significant increases in SoNar ratio were seen with AA and NaN_3 treatment but not DMSO or PBS controls (FIG 2.10), with a return to control levels after NaN_3 washout and 24 hours of recovery (FIG 2.10D).

2.3.5 HyPer positive controls

HyPer as a H_2O_2 sensor has been well documented in zebrafish (Niethammer et al., 2009; P. Han et al., 2014; Gauron et al., 2016; Jelcic et al., 2017), however, it was prudent to conduct positive controls to confirm the imaging setup was suitable. Addition of AA and inhibition of the mitochondria (Slater, 1973)—a source of H_2O_2 in the cells—is expected to decrease H_2O_2 levels and therefore the HyPer ratio, to act as a negative control. Conversely, addition of H_2O_2 itself should increase H_2O_2 levels and HyPer ratio. It has also been shown that H_2O_2 levels rise in zebrafish larvae fin fold amputation (Niethammer et al., 2009), and this experiment was also used an as additional confirmation that HyPer is working correctly in my hands.

Initially, mRNA injected embryos were used, as with Laconic and SoNar. Wild type embryos were injected at the one cell stage with HyPer mRNA generated *in vitro* and screened at the appropriate stage of development for brightest fluorescence. In each case, HyPer ratio followed expectations. That is, addition of AA significantly decreased HyPer ratio (FIG 2.11A-C'), addition of H_2O_2 increased HyPer ratio (FIG 2.11D-E'), and HyPer ratio was elevated at the wound upon amputation (FIG 2.11F-G').

My next intention was to produce transgenic lines with HyPer expressed under a ubiquitous promoter. We already possess a ubb:hyper transgenic line, and thus aimed only to generate an actb2:hyper line for strong expression as early as the one cell stage, in which I was successful. I proceeded to repeat a positive and negative control on these transgenic embryos, resulting in similar significant expected changes to HyPer ratio: treatment with AA significantly decreased HyPer ratios in treated compared to control embryos (FIG 2.12A-D'), and addition of H_2O_2 significantly increased HyPer ratios but not in controls (FIG 2.12E-F'). It is notable that the control condition of DMSO addition alone also significantly decreases HyPer ratio (FIG 2.12C and D), likely due to its mild antioxidant properties (Bektaşoğlu et al., 2006; Sanmartín-Suárez et al., 2011), thereby also following anticipations. Experiments were performed on younger embryos in order to mimic the experiments with which I intended to study early embryogenesis, and in the case of the AA negative control, the experiment was repeated in two locations with separate microscope set-ups in order to confirm repeatability. In both the results were alike and I could confirm the confidence in my imaging set-ups.

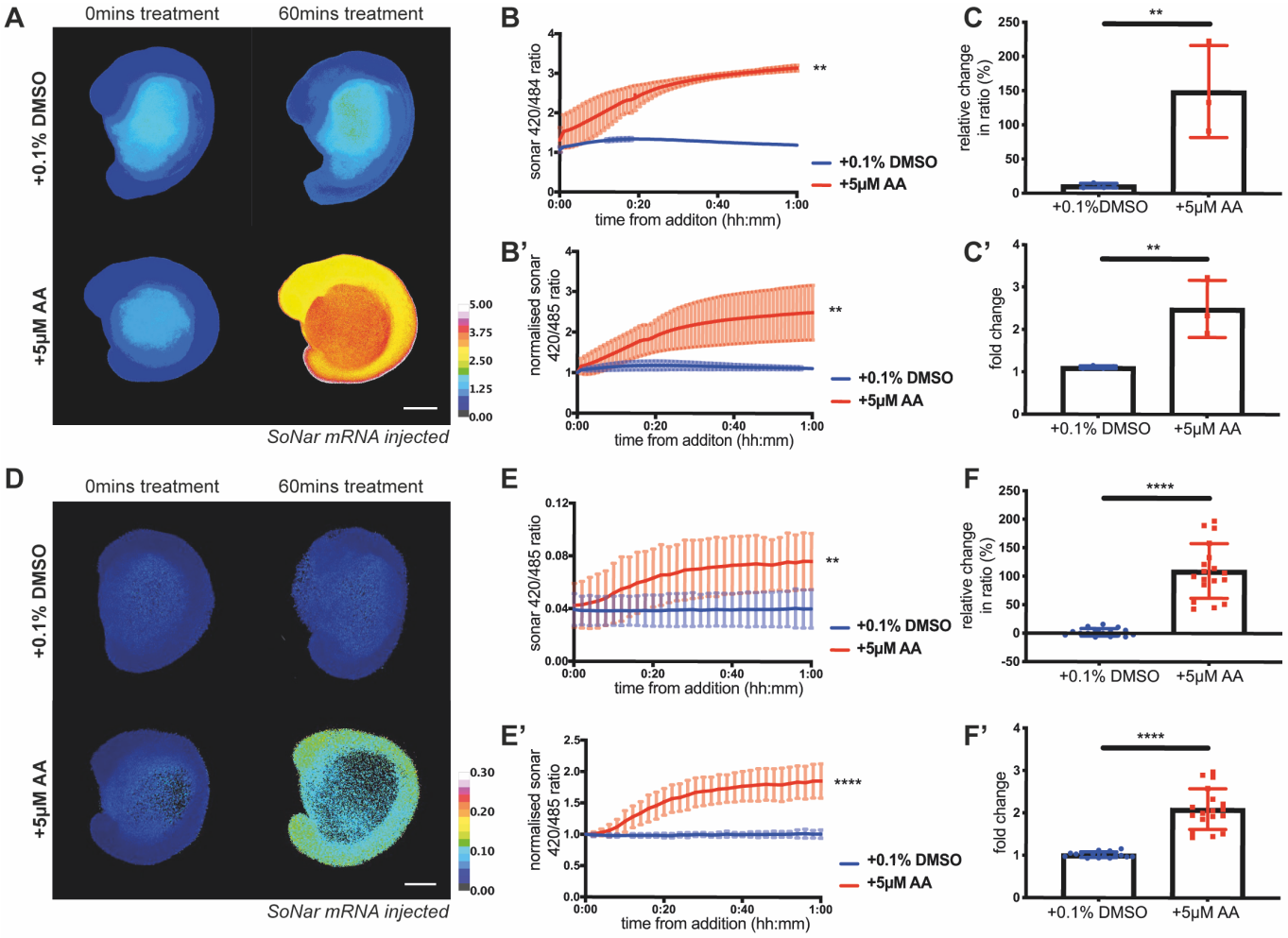

Figure 2.9. **Positive controls for SoNar mRNA with antimycin A (AA).** (A-C) show data obtained with Zeiss AxioImager.M2 upright widefield microscope (5X), (D-F) show data obtained with Nikon Ti Eclipse inverted widefield microscope (4X). All scale bars represent 200μm. Differences were considered significant to * P<0.05, ** P<0.01, *** P<0.001, **** P<0.0001, and ns P≥0.05. (A) and (D) Representative ~17hpf wild type embryos injected with SoNar mRNA at the one cell stage before and after 60mins of treatment with 0.1% DMSO or 5μM AA, pseudocoloured to show SoNar ratio calculated by dividing the 485nm excitation channel by the 528nm excitation channel. (B) and (E) Graphs showing raw SoNar ratios over time during treatment with 0.1% DMSO or 5μM AA. Two-way ANOVA to calculate significance, (B) n=3, (E) n=12. (B') and (E') Graphs showing SoNar ratios over time during treatment with 0.1% DMSO or 5μM AA normalised to pre-treatment values. Two-way ANOVA to calculate significance, (B') n=4, (E') n=12. (C) and (F) Graphs showing quantification of ratio change as a percentage of individual pre-treatment ratio. Students' t-test to calculate significance, (C) n=4, (F) n=16. (C') and (F') Graphs showing quantification of ratio change as fold change (post treatment ratio divided by pre-treatment value). Students' t-test to calculate significance, (C') n=4, (F') n=16.

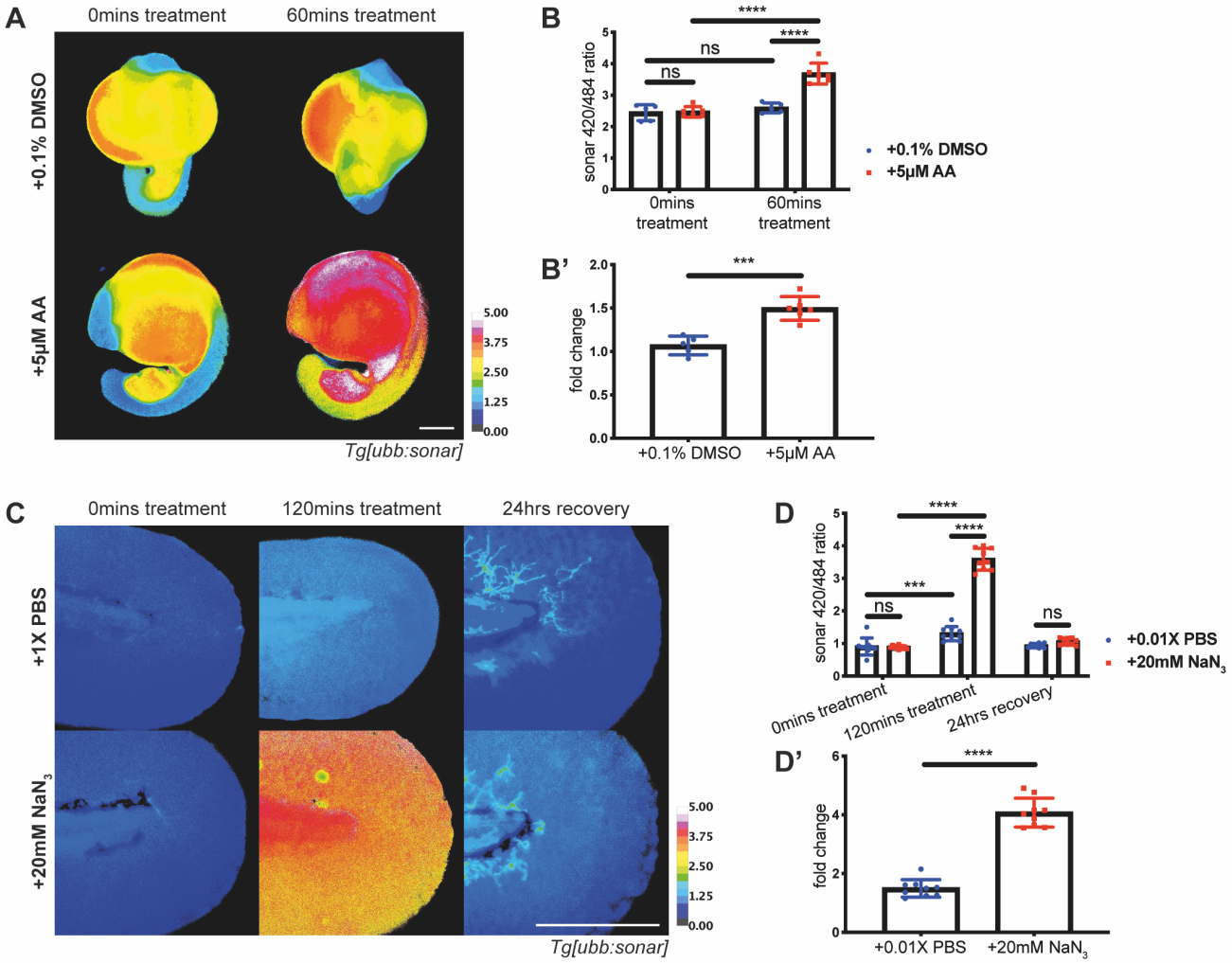

Figure 2.10. **Positive controls for transgenic line of SoNar under the ubiquitin promoter.** All panels show data obtained with Zeiss AxioImager.M2 upright widefield microscope (5X, 20X). All scale bars represent 200µm. Differences were considered significant to * P<0.05, ** P<0.01, *** P<0.001, **** P<0.0001, and ns P≥0.05. (A) Representative transgenic embryos at ~18hpf before and after 60 minutes of treatment with 0.1% DMSO or 5µM AA, pseudocoloured to show SoNar ratio calculated by dividing the 485nm excitation channel by the 528nm excitation channel. Images taken at 5X. (B) Graph showing raw SoNar ratios pre- and post-treatment with 0.1% DMSO or 5µM AA. Two-way ANOVA to calculate significance, n=6. (B') Graph showing quantification of ratio change as fold change (ratio after 60 minutes of treatment divided by individual pre-treatment values). Students' t-test to calculate to calculate significance, n=6. (C) Representative transgenic embryos at 48hpf before and after 120 minutes of treatment with 0.01X PBS or 20mM NaN_3, and after 24 hours recovery post wash out of drug, pseudocoloured to show SoNar ratio calculated by dividing the 485nm excitation channel by the 528nm excitation channel. Images taken at 20X. (D) Graph showing raw SoNar ratios pre-treatment, after 120 minutes of treatment with 0.01X PBS or 20mM NaN_3, and after 24 hours of recovery after drug wash out. Two-way ANOVA used to calculate significance, n=9. (D') Graph showing quantification of ratio change as fold change (ratio after 120 minutes of treatment with 0.01X PBS or 20mM NaN_3 divided by pre-treatment value). Students' t-test to calculate significance, n=9.

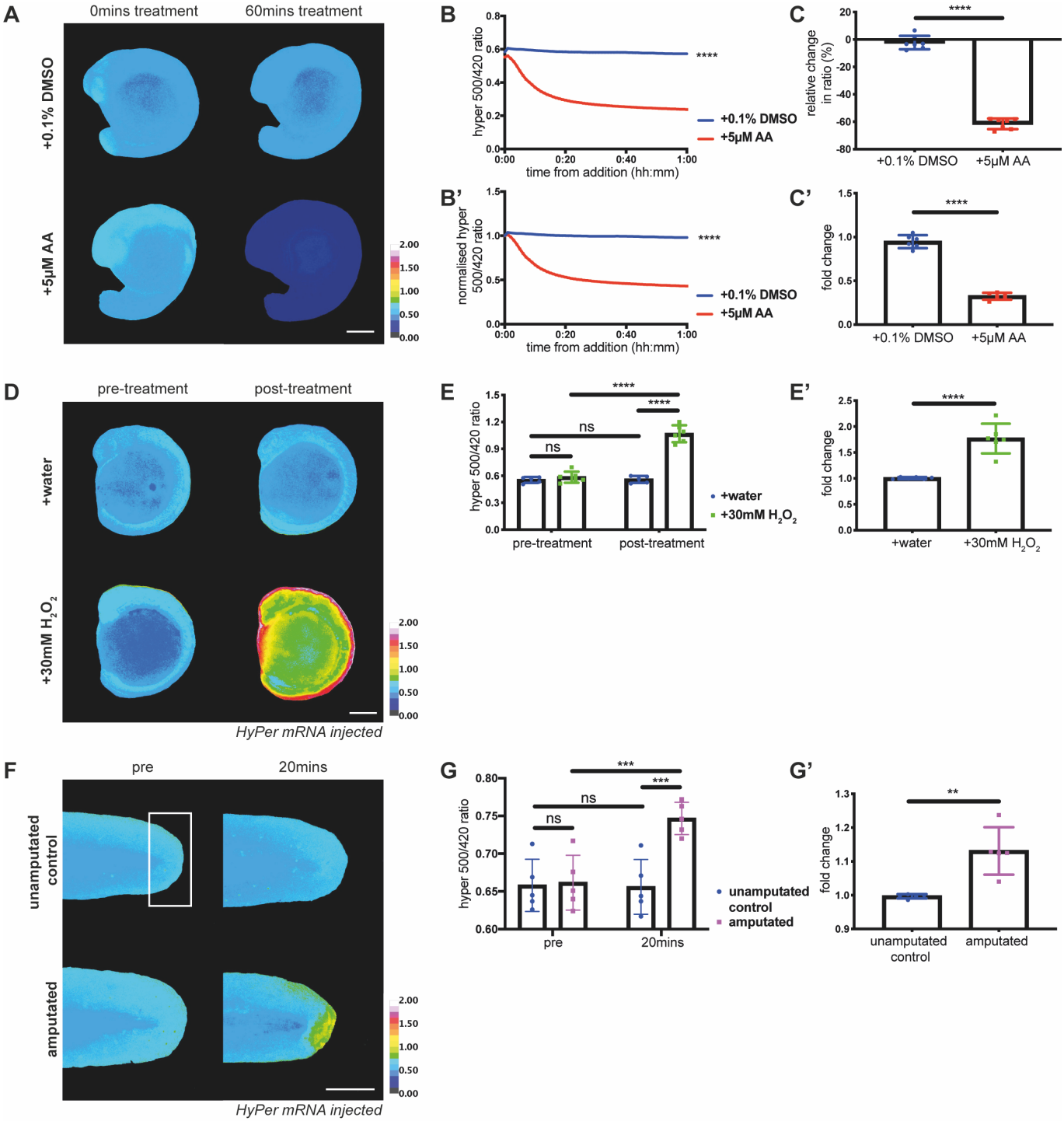

Figure 2.11. **Positive and negative controls for HyPerYFP mRNA.** All data was obtained with Zeiss AxioImager.M2 upright widefield microscope (5X, 10X). All scale bars represent 200μm. Differences were considered significant to * P<0.05, ** P<0.01, *** P<0.001, **** P<0.0001, and ns P ≥0.05. (A) Representative wild type embryos injected with HyPerYFP mRNA at the one cell stage ~17hpf before and after 60mins of treatment with 0.1% DMSO or 5μM antimycin A (AA), pseudocoloured to show Hyper ratio calculated by dividing the 500nm excitation channel by the 420nm emission channel. (B) Graph showing raw HyPer ratios over time during treatment with 0.1% DMSO or 5μM AA. Students' paired t-test to calculate significance, n=1. (B') Graph showing HyPer ratios normalised to individual pre-treatment ratios over time during treatment with 0.1% DMSO or 5μM AA. Students' paired t-test to calculate significance, n=1. (C) Graph showing quantification of ratio change after treatment with 0.1% DMSO or 5μM AA as a percentage of individual pre-treatment ratio. Students' t-test to calculate significance, n=7. (C') Graph showing quantification of ratio change after treatment with 0.1% DMSO or 5μM AA as fold change (ratios after 60 minutes treatment divided by individual pre-treatment values). Students' t-test to calculate significance, n=6. (D) Representative wild type embryos injected with HyPerYFP mRNA at the one cell stage ~15hpf before and immediately post addition of 30% stock hydrogen peroxide (H_2O_2) to a final concentration of 30mM H_2O_2, pseudocoloured to show Hyper ratio. (E) Graph comparing raw ratios pre-treatment and immediately post treatment. Students' t-test to calculate significance, n=6.

(continued on next page)

(*Figure 2.11. cont.)* (E') Graph showing quantification of ratio change as fold change (ratios immediately post treatment divided by individual pre-treatment values). Students' t-test to calculate significance, n=6. (F) Representative stage 48hpf embryos injected with HyPerYFP mRNA at the one cell before and 20 minutes post amputation, pseudocoloured to show Hyper ratio. White box indicates area measured for quantification. (G) Graph showing raw HyPer ratios pre-amputation and 20minspa. Two-way ANOVA to calculate significance, n=5. (G') Graph showing quantification of ratio change as fold change (20minspa ratio divided by individual pre-amputation value) Students' t-test to calculate significance, n=5.

2.4 Discussion

In this chapter I have shown that two genetically encoded fluorescent sensors for metabolites are operational in zebrafish, a system in which these tools had not previously been used. In addition to confirming the functionality, I went on to produce several transgenic lines under two ubiquitous promoters for experiments examining early embryogenesis, and regeneration and wound healing in embryos later in development. It is worth noting that despite being unpublished in zebrafish, Laconic and SoNar have previously been utilised *in vivo*, in the mouse (Zhao et al., 2016; Mächler et al., 2016), though neither involved the generation of transgenic lines.

There are many advantages of adding this tool to the repertoire of techniques available for use in zebrafish. For instance, metabolomics is able to analyse with precision and sensitivity the metabolites in a biological sample through a range of analytical technologies such as mass spectroscopy and NMR (nuclear magnetic resonance) (reviewed in Roessner & Bowne, 2009). However, this biochemistry-based approach is limited in its sample preparation requirements, resulting in analysis of a fixed time-point. Genetically encoded fluorescent sensors have the advantage of enabling the specimen to remain alive. Live imaging of sensors *in vivo* allows assessment of the dynamic changes of these metabolites in spatial resolution, a feat unachievable with biochemical methods. More refined temporal resolution can also be attained with such imaging, with short interval timelapse movies, and the expression of the sensor under tissue specific promoters additionally permits a higher degree of selectivity in the study of complex processes.

In vivo, it appears the sensors have a smaller dynamic range than originally in cell culture, though it is expected for there to be differences between use in cell culture and in whole organisms. The dimmer expression of the sensor may contribute to a reduction in sensitivity, as some changes in fluorescence may be very minor and go undetected. However, very high expression levels from multiple insertion sites are not advisable for the health and normal development of the embryo. The multi-cellular nature of organisms and potential interference from out of focus areas of the image may be a consideration, such as if out of focus wavelengths refract differently and therefore alter the ratio. Widefield microscopy can mask single cell data, and to overcome this concern one could instead inject mRNA at for instance the 16 cell stage, or transplant cells from donor transgenic embryos into wild type recipients, to generate mosaic embryos with identifiable single cells expressing the sensor. One may also consider confocal microscopy in addition to widefield imaging, which allows study through planes of the embryo to perhaps supplement spatial resolution, and has reduced background signal from out of focus areas of the

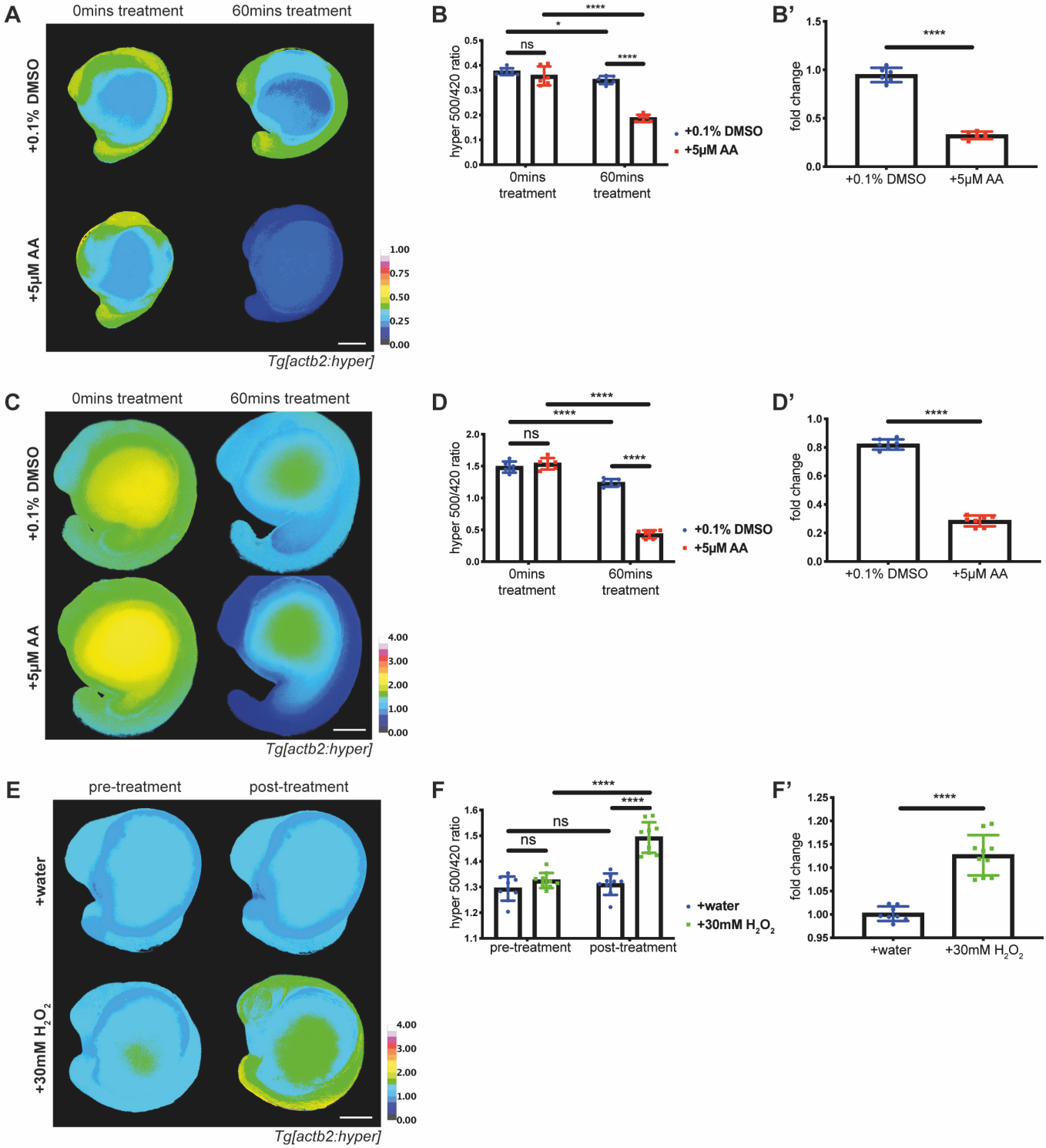

Figure 2.12. **Positive and negative controls for transgenic line of HyPerYFP under the beta-actin promoter.** (A) and (B) show data obtained with Zeiss AxioImager.M2 upright widefield microscope (5X), (C) to (F) show data obtained with Olympus IX83 inverted (10X). All scale bars represent 200µm. Differences were considered significant to * P<0.05, ** P<0.01, *** P<0.001, **** P<0.0001, and ns P≥0.05. (A and C) Representative transgenic embryos at ~15hpf (A) and ~18hpf (C) before and after 60 minutes of treatment with 0.1% DMSO or 5µM AA, pseudocoloured to show HyPerYFP ratio calculated by dividing the 500nm excitation channel by the 420nm excitation channel. (B) and (D) Graphs showing raw HyPer ratios pre-treatment and after 60 minutes of treatment with 0.1% DMSO or 5µM AA. Two-way ANOVA to calculate significance, (B) n=6, (D) n=6. (B') and (D') Graphs showing fold change in HyPer ratio after 60 minutes of treatment (post-treatment value divided by individual pre-treatment value. Students' t-test to calculate significance, (B') n=6, (D') n=7. (E) Representative transgenic embryos at ~15hpf before and immediately post addition of 30% stock hydrogen peroxide (H_2O_2) to a final concentration of 30mM H_2O_2, pseudocoloured to show Hyper ratio. (F) Graph showing raw HyPer ratios pre- and post-treatment with H_2O_2. Two-way ANOVA to calculate significance, n=10. (F') Graph showing quantification of HyPer ratio change as fold change (ratio immediately post treatment divided by individual pre-treatment value). Students' t-test to calculate significance, n=10.

image. Lastly, there could plausibly be disruption due to autofluorescence which may affect the usability of the sensor, especially in systems with high yolk content such as *Xenopus*.

In future, combining the techniques of metabolomics and imaging genetically encoded sensors for the same metabolites could produce a complementary array of data, with the sensors providing a broader depiction of the temporal and spatial changes in metabolism while metabolomic approaches supply more specific information.

Besides the two sensors I worked with and the existing sensors for H_2O_2 and calcium—HyPer (Belousov et al., 2006) and GECIs (reviewed in Zhong & Schleifenbaum, 2019), respectively—various other sensors have been developed in cell culture and could be optimised to create a more complete bank of tools *in vivo*. pH sensors such as SypHer (Matlashov et al., 2015) and pHRed (Tantama et al., 2011) may be useful as pH affects many cellular processes, including metabolism (Inoue & Kaneko, 1992). Furthermore, an alteration in pH levels due to the production of lactic acid from the fermentation reaction in anaerobic glycolysis or the Warburg effect (preferential aerobic glycolysis despite a reduced ATP yield and abundance of oxygen (Warburg, 1925), discussed in more detail in the Introduction and other chapters) may be detectable and indicative of the metabolic profile of cells or tissues. Another sensor that may be worth augmentation is the ATP:ADP ratio sensor, PercevalHR (Tantama et al., 2013), which could indicate the energy status of cells, or potentially a metabolic switch to the less ATP-productive glycolysis in the Warburg effect. Pyronic reports pyruvate levels (San Martín et al., 2014) and would also be a logical and complementary companion to its sister construct, the Laconic lactate sensor. Pyronic ratio could indicate the activity of the mitochondrial pyruvate carrier, a reduction in which would result in a increased concentration of pyruvate in the cytoplasm, or potentially low pyruvate levels with high lactate levels in aerobic conditions may indicate the Warburg effect. Finally, it is worth mentioning the variations of FLIPglu-Δ13V (Fehr et al., 2003), genetically encoded glucose reporters. Monitoring the uptake of glucose into cells may provide insight into the energetic needs of the cell. All these mentioned sensors are currently published only in cell culture (and in the case of FLIPglu-Δ13V, also in plants); for use *in vivo*, positive control experiments similar to those I conducted in this chapter would be compulsory to ensure their correct and comparable function in the context of whole organisms.

Overall, the results of this chapter present a promising beginning for a novel method of studying metabolism in a wider, more systems biology context. Specifically, in this case, to investigate the potential occurrence of a switch to a more glycolytic metabolism resulting in discernibly elevated lactate levels during early development or wound healing and regeneration of zebrafish embryos.

References

Bektaşoğlu, B., Esin Celik, S., Ozyürek, M., Güçlü, K., & Apak, R. (2006). Novel hydroxyl radical scavenging antioxidant activity assay for water-soluble antioxidants using a modified CUPRAC method. *Biochemical and Biophysical Research Communications*, *345*(3), 1194–1200. https://doi.org/10.1016/j.bbrc.2006.05.038

Belousov, V. V., Fradkov, A. F., Lukyanov, K. A., Staroverov, D. B., Shakhbazov, K. S., Terskikh, A. V., & Lukyanov, S. (2006). Genetically encoded fluorescent indicator for intracellular hydrogen peroxide. *Nature Methods*, *3*(4), 281–286. https://doi.org/10.1038/nmeth866

Bennett, M. C., Mlady, G. W., Kwon, Y. H., & Rose, G. M. (1996). Chronic in vivo sodium azide infusion induces selective and stable inhibition of cytochrome c oxidase. *Journal of Neurochemistry*, *66*(6), 2606–2611. https://doi.org/10.1046/j.1471-4159.1996.66062606.x

Bilan, D. S., & Belousov, V. V. (2016). HyPer Family Probes: State of the Art. *Antioxidants & Redox Signaling*, *24*(13), 731–751. https://doi.org/10.1089/ars.2015.6586

Bilan, D. S., Pase, L., Joosen, L., Gorokhovatsky, A. Y., Ermakova, Y. G., Gadella, T. W. J., Grabher, C., Schultz, C., Lukyanov, S., & Belousov, V. V. (2013). HyPer-3: A Genetically Encoded H_2O_2 Probe with Improved Performance for Ratiometric and Fluorescence Lifetime Imaging. *ACS Chemical Biology*, *8*(3), 535–542. https://doi.org/10.1021/cb300625g

Blackstone, N. W. (2006). Charles Manning Child (1869-1954): the past, present, and future of metabolic signaling. [Computer software]. In *Journal of experimental zoology. Part B, Molecular and developmental evolution* (Vol. 306, Number 1, pp. 1–7) [Computer software]. https://doi.org/10.1002/jez.b.21085

Buck, M. D., O'Sullivan, D., Klein Geltink, R. I., Curtis, J. D., Chang, C.-H., Sanin, D. E., Qiu, J., Kretz, O., Braas, D., van der Windt, G. J. W., Chen, Q., Huang, S. C.-C., O'Neill, C. M., Edelson, B. T., Pearce, E. J., Sesaki, H., Huber, T. B., Rambold, A. S., & Pearce, E. L. (2016). Mitochondrial Dynamics Controls T Cell Fate through Metabolic Programming. *Cell*, *166*(1), 63–76. https://doi.org/10.1016/j.cell.2016.05.035

Cantó, C., Menzies, K. J., & Auwerx, J. (2015). NAD(+) Metabolism and the Control of Energy Homeostasis: A Balancing Act between Mitochondria and the Nucleus. *Cell Metabolism*, *22*(1), 31–53. https://doi.org/10.1016/j.cmet.2015.05.023

Chen, J., Xia, L., Bruchas, M. R., & Solnica-Krezel, L. (2017). Imaging early embryonic calcium activity with GCaMP6s transgenic zebrafish. *Developmental Biology*. https://doi.org/10.1016/j.ydbio.2017.03.010

Child, C. M. (1911). A study of senescence and rejuvenescence based on experiments with Planaria dorotocephala. *Archiv Für Entwicklungsmechanik Der Organismen*, *31*(4), 537–616.

Child, C. M. (1941). *Patterns and problems of development*. [Computer software]. Chicago, Ill., The University of Chicago Press. https://doi.org/10.5962/bhl.title.6415

Colussi, C., Albertini, M. C., Coppola, S., Rovidati, S., Galli, F., & Ghibelli, L. (2000). H_2O_2-induced block of glycolysis as an active ADP-ribosylation reaction protecting cells from apoptosis. *FASEB Journal : Official Publication of the Federation of American Societies for Experimental Biology*, *14*(14), 2266–2276. https://doi.org/10.1096/fj.00-0074com

Cunliffe, V. T. (2003). Zebrafish: A Practical Approach. Edited by C. NÜSSLEIN-VOLHARD and R. DAHM. Oxford University Press. 2002. 322 pages. ISBN 0 19 963808 X. Price £40.00 (paperback). ISBN 0 19 963809 8. Price £80.00 (hardback). *Genetical Research*, *82*(1), 79–79.

De Henau, S., Pagès-Gallego, M., Pannekoek, W.-J., & Dansen, T. B. (2020). Mitochondria-Derived H_2O_2 Promotes Symmetry Breaking of the C. elegans Zygote. *Developmental Cell*, *53*(3), 263–271.e266. https://doi.org/10.1016/j.devcel.2020.03.008

Dupuy, C., Dème, D., Kaniewski, J., Pommier, J., & Virion, A. (1988). Ca2+ regulation of thyroid NADPH-dependent H_2O_2 generation. *FEBS Letters*, *233*(1), 74–78. https://doi.org/10.1016/0014-5793(88)81358-9

Fehr, M., Lalonde, S., Lager, I., Wolff, M. W., & Frommer, W. B. (2003). In vivo imaging of the dynamics of glucose uptake in the cytosol of COS-7 cells by fluorescent nanosensors. *The Journal of Biological Chemistry*, *278*(21), 19127–19133. https://doi.org/10.1074/jbc.M301333200

Folmes, C. D. L., Nelson, T. J., Martinez-Fernandez, A., Arrell, D. K., Lindor, J. Z., Dzeja, P. P., Ikeda, Y., Perez-Terzic, C., & Terzic, A. (2011). Somatic oxidative bioenergetics transitions into pluripotency-dependent glycolysis to facilitate nuclear reprogramming. *Cell Metabolism*, *14*(2), 264–271. https://doi.org/10.1016/j.cmet.2011.06.011

Gauron, C., Meda, F., Dupont, E., Albadri, S., Quenech'Du, N., Ipendey, E., Volovitch, M., Del Bene, F., Joliot, A., Rampon, C., & Vriz, S. (2016). Hydrogen peroxide (H_2O_2) controls axon pathfinding during zebrafish development. *Developmental Biology*, *414*(2), 133–141. https://doi.org/10.1016/j.ydbio.2016.05.004

Gauron, C., Rampon, C., Bouzaffour, M., Ipendey, E., Teillon, J., Volovitch, M., & Vriz, S. (2013). Sustained production of ROS triggers compensatory proliferation and is required for regeneration to proceed. *Scientific Reports*, *3*(1), 2084. https://doi.org/10.1038/srep02084

Han, P., Zhou, X.-H., Chang, N., Xiao, C.-L., Yan, S., Ren, H., Yang, X.-Z., Zhang, M.-L., Wu, Q., Tang, B., Diao, J.-P., Zhu, X., Zhang, C., Li, C.-Y., Cheng, H., & Xiong, J.-W. (2014). Hydrogen peroxide primes heart regeneration with a derepression mechanism. *Cell Research*, *24*(9), 1091–1107. https://doi.org/10.1038/cr.2014.108

Han, Y., Ishibashi, S., Iglesias-Gonzalez, J., Chen, Y., Love, N. R., & Amaya, E. (2018). Ca2+-Induced Mitochondrial ROS Regulate the Early Embryonic Cell Cycle. *Cell Reports*, *22*(1), 218–231. https://doi.org/10.1016/j.celrep.2017.12.042

Hartley, J. L., Temple, G. F., & Brasch, M. A. (2000). DNA cloning using in vitro site-specific recombination. *Genome Research*, *10*(11), 1788–1795. https://doi.org/10.1101/gr.143000

Harvey, A. J., Rathjen, J., & Gardner, D. K. (2016). Metaboloepigenetic Regulation of Pluripotent Stem Cells. *Stem Cells International*, *2016*(3215), 1816525–15. https://doi.org/10.1155/2016/1816525

Higashijima, S., Okamoto, H., Ueno, N., Hotta, Y., & Eguchi, G. (1997). High-frequency generation of transgenic zebrafish which reliably express GFP in whole muscles or the whole body by using promoters of zebrafish origin. *Developmental Biology*, *192*(2), 289–299. https://doi.org/10.1006/dbio.1997.8779

Inoue, Y., & Kaneko, T. (1992). Effects of pH on the endocrine system and metabolism. *Nihon Rinsho. Japanese Journal of Clinical Medicine*, *50*(9), 2124–2128.

Jelcic, M., Enyedi, B., Xavier, J. B., & Niethammer, P. (2017). Image-Based Measurement of H_2O_2 Reaction-Diffusion in Wounded Zebrafish Larvae. *Biophysical Journal*, *112*(9), 2011–2018. https://doi.org/10.1016/j.bpj.2017.03.021

Kawakami, K. (2007). Tol2: a versatile gene transfer vector in vertebrates. *Genome Biology*, *8 Suppl 1*(Suppl 1), S7. https://doi.org/10.1186/gb-2007-8-s1-s7

Kawakami, K., Takeda, H., Kawakami, N., Kobayashi, M., Matsuda, N., & Mishina, M. (2004). A transposon-mediated gene trap approach identifies developmentally regulated genes in zebrafish. *Developmental Cell*, *7*(1), 133–144. https://doi.org/10.1016/j.devcel.2004.06.005

Kimmel, C. B., Ballard, W. W., Kimmel, S. R., Ullmann, B., & Schilling, T. F. (1995). Stages of embryonic development of the zebrafish. *Developmental Dynamics, 203*(3), 253–310. https://doi.org/10.1002/aja.1002030302

Kondoh, H., Lleonart, M. E., Nakashima, Y., Yokode, M., Tanaka, M., Bernard, D., Gil, J., & Beach, D. (2007). A high glycolytic flux supports the proliferative potential of murine embryonic stem cells. *Antioxidants & Redox Signaling*, *9*(3), 293–299. https://doi.org/10.1089/ars.2006.1467

Kuehne, A., Emmert, H., Soehle, J., Winnefeld, M., Fischer, F., Wenck, H., Gallinat, S., Terstegen, L., Lucius, R., Hildebrand, J., & Zamboni, N. (2015). Acute Activation of Oxidative Pentose Phosphate Pathway as First-Line Response to Oxidative Stress in Human Skin Cells. *Molecular Cell*, *59*(3), 359–371. https://doi.org/10.1016/j.molcel.2015.06.017

Kyere-Yeboah, K., Denteh, J., Liu, K., Ye, P., & Gao, E.-B. (2019). Monitoring Nicotinamide Adenine Dinucleotide and its phosphorylated redox metabolism using genetically encoded fluorescent biosensors. *Sensing and Bio-Sensing Research*, *26*, 100307.

Liu, K., Petree, C., Requena, T., Varshney, P., & Varshney, G. K. (2019). Expanding the CRISPR Toolbox in Zebrafish for Studying Development and Disease. *Frontiers in Cell and Developmental Biology*, *7*, 13. https://doi.org/10.3389/fcell.2019.00013

Love, N. R., Chen, Y., Ishibashi, S., Kritsiligkou, P., Lea, R., Koh, Y., Gallop, J. L., Dorey, K., & Amaya, E. (2013). Amputation-induced reactive oxygen species are required for successful Xenopus tadpole tail regeneration. *Nature Cell Biology*, *15*(2), 222–228. https://doi.org/10.1038/ncb2659

Love, N. R., Thuret, R., Chen, Y., Ishibashi, S., Sabherwal, N., Paredes, R., Alves-Silva, J., Dorey, K., Noble, A. M., Guille, M. J., Sasai, Y., Papalopulu, N., & Amaya, E. (2011). pTransgenesis: a cross-species, modular transgenesis resource. *Development (Cambridge, England)*, *138*(24), 5451–5458. https://doi.org/10.1242/dev.066498

Mächler, P., Wyss, M. T., Elsayed, M., Stobart, J., Gutierrez, R., Faber-Castell, von, A., Kaelin, V., Zuend, M., Martín, A. S., Romero-Gómez, I., Baeza-Lehnert, F., Lengacher, S., Schneider, B. L., Aebischer, P., Magistretti, P. J., Barros, L. F., & Weber, B. (2016). In Vivo Evidence for a Lactate Gradient from Astrocytes to Neurons. *Cell Metabolism*, *23*(1), 94–102. https://doi.org/10.1016/j.cmet.2015.10.010

Markvicheva, K. N., Mishina, N. M., Belousov, V. V., Bilan, D. S., Lukyanov, S., Gorokhovatsky, A. Y., & Vinokurov, L. M. (2011). A genetically encoded sensor for H_2O_2 with expanded dynamic range. *Bioorganic and Medicinal Chemistry*, *19*(3), 1079–1084. https://doi.org/10.1016/j.bmc.2010.07.014

Mathieu, J., & Ruohola-Baker, H. (2017). Metabolic remodeling during the loss and acquisition of pluripotency. *Development (Cambridge, England)*, *144*(4), 541–551. https://doi.org/10.1242/dev.128389

Matlashov, M. E., Bogdanova, Y. A., Ermakova, G. V., Mishina, N. M., Ermakova, Y. G., Nikitin, E. S., Balaban, P. M., Okabe, S., Lukyanov, S., Enikolopov, G., Zaraisky, A. G., & Belousov, V. V. (2015). Fluorescent ratiometric pH indicator SypHer2: Applications in neuroscience and regenerative biology. *Biochimica Et Biophysica Acta (BBA) - General Subjects*, 1850(11), 2318–2328. https://doi.org/10.1016/j.bbagen.2015.08.002

Molavian, H. R., Kohandel, M., & Sivaloganathan, S. (2016). High Concentrations of H_2O_2 Make Aerobic Glycolysis Energetically More Favorable for Cellular Respiration. *Frontiers in Physiology*, *7*, 362. https://doi.org/10.3389/fphys.2016.00362

Morandi, A., Taddei, M. L., Chiarugi, P., & Giannoni, E. (2017). Targeting the Metabolic Reprogramming That Controls Epithelial-to-Mesenchymal Transition in Aggressive Tumors. *Frontiers in Oncology*, *7*(6), 40. https://doi.org/10.3389/fonc.2017.00040

Mosimann, C., Kaufman, C. K., Li, P., Pugach, E. K., Tamplin, O. J., & Zon, L. I. (2011). Ubiquitous transgene expression and Cre-based recombination driven by the ubiquitin promoter in zebrafish. *Development (Cambridge, England)*, *138*(1), 169–177. https://doi.org/10.1242/dev.059345

Mullarky, E., & Cantley, L. C. (2015). *Diverting Glycolysis to Combat Oxidative Stress* (K. Nakao, N. Minato, & S. Uemoto, Eds.; pp. 3–23). Springer Japan.

Nasr-Esfahani, M. M., & Johnson, M. H. (1991). The origin of reactive oxygen species in mouse embryos cultured in vitro. *Development (Cambridge, England)*, *113*(2), 551–560.

Niethammer, P., Grabher, C., Look, A. T., & Mitchison, T. J. (2009). A tissue-scale gradient of hydrogen peroxide mediates rapid wound detection in zebrafish. *Nature*, *459*(7249), 996–999. https://doi.org/10.1038/nature08119

Nulton-Persson, A. C., & Szweda, L. I. (2001). Modulation of mitochondrial function by hydrogen peroxide. *The Journal of Biological Chemistry*, *276*(26), 23357–23361. https://doi.org/10.1074/jbc.M100320200

Okabe, K., Yaku, K., Tobe, K., & Nakagawa, T. (2019). Implications of altered NAD metabolism in metabolic disorders. *Journal of Biomedical Science*, *26*(1), 34–13. https://doi.org/10.1186/s12929-019-0527-8

Razzell, W., Evans, I. R., Martin, P., & Wood, W. (2013). Calcium flashes orchestrate the wound inflammatory response through DUOX activation and hydrogen peroxide release. *Current Biology : CB*, *23*(5), 424–429. https://doi.org/10.1016/j.cub.2013.01.058

Roessner, U., & Bowne, J. (2009). What is metabolomics all about? *BioTechniques*, *46*(5), 363–365. https://doi.org/10.2144/000113133

San Martín, A., Ceballo, S., Baeza-Lehnert, F., Lerchundi, R., Valdebenito, R., Contreras-Baeza, Y., Alegría, K., & Barros, L. F. (2014). Imaging mitochondrial flux in single cells with a FRET sensor for pyruvate. *PLoS ONE*, *9*(1), e85780. https://doi.org/10.1371/journal.pone.0085780

San Martín, A., Ceballo, S., Ruminot, I., Lerchundi, R., Frommer, W. B., & Barros, L. F. (2013). A genetically encoded FRET lactate sensor and its use to detect the Warburg effect in single cancer cells. *PLoS ONE*, *8*(2), e57712. https://doi.org/10.1371/journal.pone.0057712

Sanmartín-Suárez, C., Soto-Otero, R., Sánchez-Sellero, I., & Méndez-Álvarez, E. (2011). Antioxidant properties of dimethyl sulfoxide and its viability as a solvent in the evaluation of neuroprotective antioxidants. *Journal of Pharmacological and Toxicological Methods*, *63*(2), 209–215. https://doi.org/10.1016/j.vascn.2010.10.004

Schieber, M., & Chandel, N. S. (2014). ROS function in redox signaling and oxidative stress. *Current Biology : CB*, *24*(10), R453–R462. https://doi.org/10.1016/j.cub.2014.03.034

Shi, D.-Y., Xie, F.-Z., Zhai, C., Stern, J. S., Liu, Y., & Liu, S.-L. (2009). The role of cellular oxidative stress in regulating glycolysis energy metabolism in hepatoma cells. *Molecular Cancer*, *8*(1), 32–15. https://doi.org/10.1186/1476-4598-8-32

Slater, E. C. (1973). The mechanism of action of the respiratory inhibitor, antimycin. *Biochimica Et Biophysica Acta (BBA) - Reviews on Bioenergetics*, *301*(2), 129–154.

Tantama, M., Hung, Y. P., & Yellen, G. (2011). Imaging intracellular pH in live cells with a genetically encoded red fluorescent protein sensor. *Journal of the American Chemical Society*, *133*(26), 10034–10037. https://doi.org/10.1021/ja202902d

Tantama, M., Martínez-François, J. R., Mongeon, R., & Yellen, G. (2013). Imaging energy status in live cells with a fluorescent biosensor of the intracellular ATP-to-ADP ratio. *Nature Communications*, *4*(1), 1–11. https://doi.org/10.1038/ncomms3550

Thermes, V., Grabher, C., Ristoratore, F., Bourrat, F., Choulika, A., Wittbrodt, J., & Joly, J.-S. (2002). I-SceI meganuclease mediates highly efficient transgenesis in fish. *Mechanisms of Development*, *118*(1-2), 91–98.

Vander Heiden, M. G., Cantley, L. C., Thompson, C. B., Mammalian, P., Exhibit, C., & Metabolism, A. (2009). *Understanding the Warburg Effect: The Metabolic Requirements of Cell Proliferation*. *324*(5930), 1029–1033. https://doi.org/10.1126/science.1160809

Wang, Y., & Hekimi, S. (2015). Mitochondrial dysfunction and longevity in animals: Untangling the knot. *Science*, *350*(6265), 1204–1207. https://doi.org/10.1126/science.aac4357

Warburg, O. (1925). The Metabolism of Carcinoma Cells. *The Journal of Cancer Research*, *9*(1), 148–163. https://doi.org/10.1158/jcr.1925.148

Wellen, K. E., Hatzivassiliou, G., Sachdeva, U. M., Bui, T. V., Cross, J. R., & Thompson, C. B. (2009). ATP-citrate lyase links cellular metabolism to histone acetylation. *Science*, *324*(5930), 1076–1080. https://doi.org/10.1126/science.1164097

Wilson, B. A., Schisler, J. C., & Willis, M. S. (2010). Sir Hans Adolf Krebs: Architect of Metabolic Cycles. *Laboratory Medicine*, *41*(6), 377–380.

Yoshinari, N., Ando, K., Kudo, A., Kinoshita, M., & Kawakami, A. (2012). Colored medaka and zebrafish: Transgenics with ubiquitous and strong transgene expression driven by the medaka β-actin promoter. *Development, Growth & Differentiation*, 54(9), 818–828. https://doi.org/10.1111/dgd.12013

Zhang, Q., Wang, Y., Man, L., Zhu, Z., Bai, X., Wei, S., Liu, Y., Liu, M., Wang, X., Gu, X., & Wang, Y. (2016). Reactive oxygen species generated from skeletal muscles are required for gecko tail regeneration. *Scientific Reports*, *6*(1), 20752. https://doi.org/10.1038/srep20752

Zhao, Y., Wang, A., Zou, Y., Su, N., Loscalzo, J., & Yang, Y. (2016). In vivo monitoring of cellular energy metabolism using SoNar, a highly responsive sensor for NAD+/NADH redox state. *Nature Protocols*, *11*(8), 1345–1359.

Zhao, Y., Yang, Y., Zhao, Y., Hu, Q., Loscalzo, J., Correspondence, Y. Y., Su, N., Cheng, F., Zou, Y., Wang, A., Hu, H., Chen, X., Zhou, H.-M., Yang, K., Huang, X., Yi, J., Zhu, Q., Zhu, L., Wang, X., et al. (2015). SoNar, a Highly Responsive NAD+/NADH Sensor, Allows High-Throughput Metabolic Screening of Anti-tumor Agents. *Cell Metabolism*, *21*(5), 777–789. https://doi.org/10.1016/j.cmet.2015.04.009

Zheng, X., Boyer, L., Jin, M., Mertens, J., Kim, Y., Ma, L., Hamm, M., Gage, F. H., & Hunter, T. (2016). Metabolic reprogramming during neuronal differentiation from aerobic glycolysis to neuronal oxidative phosphorylation. *eLife*, *5*, 859. https://doi.org/10.7554/eLife.13374

Zhong, C., & Schleifenbaum, J. (2019). Genetically Encoded Calcium Indicators: A New Tool in Renal Hypertension Research. *Frontiers in Medicine*, 6, 128. https://doi.org/10.3389/fmed.2019.00128

3: Metabolism in Early Zebrafish Development

Abstract

Regeneration can be considered a partial recapitulation of developmental programmes due to a number of similarities, including common signalling pathways and processes such as epithelial to mesenchyme transitions. Though a full reactivation of the developmental programme does not occur, the knowledge gathered from study of embryogenesis may provide insight into the underlying molecular workings of regeneration and potential therapeutic targets. An oscillating metabolism has been described in *Xenopus* embryos, and the discovery of heat oscillations in zebrafish lead us to question whether perhaps a similar metabolic fluctuation is conserved across species. I utilised transgenic lines for genetically encoded biosensors under the ubiquitous beta-actin promotor, allowing the imaging of changes in lactate and hydrogen peroxide (H_2O_2) levels in real time within live zebrafish embryos. Oscillations in H_2O_2 indeed do occur in zebrafish cleavage stages, suggesting dynamic mitochondrial activity that corresponds with the cell cycle. I additionally used pharmacological inhibitors to demonstrate the source of embryonic H_2O_2 is mitochondrial, and activity of the mitochondria or presence of mitochondrial reactive oxygen species (ROS) is necessary for the progression of the cell cycle. My initial findings of oscillating H_2O_2 levels suggest that the cell cycle-linked, phasic nature of metabolism in early cleavage stage embryos may be conserved across species. Furthermore, I establish that glycolysis activity increases shortly prior to gastrulation, coinciding with the midblastula transition and incorporation of cell growth into the cell cycle, potentially indicating a switch to Warburg metabolism. I thus provide a foundation for investigating the potential of ROS-mediated glycolysis, which may lead to applications in other situations where the Warburg effect is operative, such as cancer.

3.1 Introduction

At first glance, developmental biology could be considered an area of study pursued purely for academic curiosity. While it is certainly true that the processes by which a single-celled fertilised egg transforms into a complex organism is extremely fascinating, and a desire to understand this phenomenon would be reason enough to drive research, development is also consequential to wider applications and could arguably be one of the most important biological disciplines.

Congenital abnormality accounts for 14-42% of infant mortality (Boyle et al., 2018), and with insight into the underlying mechanisms of how an organism develops and precisely what occurs to produce defects, targets for treatment or prevention can be established. Furthermore, understanding such elemental aspects forms a basis for further research in modern biology, as many concepts in developmental biology—such as cell signalling, cell

migration, and morphogenesis to name a few—are relevant to other fields, such as regenerative and cancer biology. The field of developmental biology is multi-disciplinary, linking genetics, molecular biology and biochemistry, cell biology, evolutionary biology, and biophysics to explain phenomena across different levels of biology.

In the previous chapter, 2: Generating Tools for Imaging Metabolism in Zebrafish, I discuss the increasingly apparent role of metabolism in a wider context of biological systems and the development of genetically encoded sensors for metabolites, of which those for lactate and hydrogen peroxide (H_2O_2) I will make use of in this chapter.

3.1.1 Glucose metabolism in development

Glucose is metabolised by the cell first into pyruvate through glycolysis in the cytoplasm, and from there can be transported into the mitochondria by a pyruvate kinase isozyme for further processing via the citric acid cycle, to produce NADH that contributes electrons to the electron transport chain and oxidative phosphorylation (OXPHOS) (FIG 1.1A) (Alberts et al., 2002). Alternatively, pyruvate can be converted into lactate by the enzyme lactate dehydrogenase (LDH), thereby regenerating the NAD+ required for continued glycolysis. Ordinarily, under aerobic conditions, the cell predominantly utilises OXPHOS and efficiently generates large quantities of ATP for energy. In this situation, NAD+ is regenerated by the shuttling of electrons from the NADH produced in glycolysis into the mitochondria. However, in the absence of oxygen, OXPHOS and the mitochondria are restricted in their activity, and NAD+ must be replenished instead by the fermentation reaction by LDH, resulting in the additional production of lactate (FIG 1.1B), allowing glycolysis activity to continue even in anaerobic conditions (Alberts et al., 2002). Glycolysis is, in some instances, the preferred metabolism despite an abundance of oxygen (FIG 1.1C) (see 1: General Introduction, section 1.1). Termed the Warburg effect, aerobic glycolysis is often witnessed in biological systems with high rates of proliferation, notably cancer, activated immune cells, and development (reviewed in Lunt & Vander Heiden, 2011).

Epithelial to mesenchymal transitions (EMTs) occur frequently during embryogenesis; as just one example, during the formation of the neural crest cells that detach from the endoderm and migrate throughout the embryo to form a diverse number of tissues, including melanocytes, craniofacial skeletal elements, smooth muscle, and nervous cells (reviewed in Huang & Saint-Jeannet, 2004). A switch to glycolytic metabolism has now been shown to be important in EMT, downstream of various well known EMT-associated signalling cascades such as Wnt and transforming growth factor beta (TGF-β) (reviewed in Morandi et al., 2017). A positive correlation between TGF-β induction of EMT with a glycolytic switch and reduction in mitochondrial activity (Lee et al., 2015) suggests TGF-β drives EMT in conjunction with glycolysis activation, by up-regulation of expression of glucose transporters, LDH, and other hallmarks of aerobic glycolysis (Kondaveeti et al., 2015). Reactive oxygen species (ROS) have been described to modulate glycolysis activity (see 1: General Introduction, section 1.2.2), and there is also evidence of reciprocal regulation between ROS and TGF-β, with ROS mediating TGF-induced EMT (R.-M. Liu & Desai, 2015).

In the very early stages of mouse development, embryos switch from an almost exclusively oxidative metabolism to predominantly glycolytic activity. Glucose uptake is imperceptible until the blastocyst stage post-implantation, at which point lactate production accounts for upwards of 80% of the glucose consumed by the embryo (Houghton et al., 1996). The inner cell mass (ICM) cells of the blastocyst are in fact completely reliant on glycolysis, while the outer layer of the blastocyst, the trophectoderm cells, only convert 55% of their glucose into lactate (Hewitson & Leese, 1993). It is the ICM that will go on to give rise to the embryo proper, and therefore subject to considerable proliferation and requirements for generation of biomass. The demands of a dividing cell are better met by glycolysis rather than OXPHOS (see 1: General introduction, section 1.1), and thus a high prevalence of glycolysis and the Warburg effect would seem reasonable, if not expected, in such a highly proliferative cell type. Moreover, the Warburg effect is most commonly associated with cancer, and the gene profile of early mammalian embryos is similar to that of rapidly dividing cancer cells, most notably the expression of glycolytic enzyme hexokinase 2 and PKM2 (Redel et al., 2011).

Perturbation of glucose metabolism pre-implantation at the 8-cell stage of murine embryogenesis via inhibition of the malate-aspartate shuttle (MAS), which transfers electrons from the NADH produced in glycolysis into the mitochondria to contribute to the citric acid cycle and OXPHOS, results in reduced implantation rates and embryo viability (Mitchell et al., 2009). The MAS is responsible for the ability to use lactate as an energy substrate (Lane & Gardner, 2005), and the loss of this capability may lead to a reduction in ATP production and negatively affect cell signalling and result in reduced viability. Indeed, highly glycolytic pre-implantation mouse blastocysts are reported to have poor implantation success (Lane & Gardner, 1996).

At later developmental stages, mouse embryonic stem cells (ESC) show a stark contrast in metabolic states during the transition from the pluripotent pre-implantation ESCs to the post-implantation epiblast stem cells (EpiSC), with EpiSCs possessing a highly glycolytic metabolism and low cytochrome C oxidase expression (akin to the metabolic phenotype of cancer cells), and ESCs switching between glycolysis and mitochondrial metabolism dynamically. Hypoxia-inducible factor-1-alpha (HIF1α) signalling is responsible and sufficient for inducing the transition to glycolytic metabolism and converting ESCs into EpiSCs (W. Zhou et al., 2012), and has positive effects on glycolysis in cancer (reviewed in Nagao et al., 2019; see 1: General Introduction, section 1.2.2) and macrophages (Wang et al., 2017). Similar to TGF-β, HIF1α is inducible by H_2O_2, further linking metabolic reprogramming with ROS.

Progenitor cells in the developing embryo depend on glycolysis to maintain proliferation and their differential potency (Kondoh et al., 2007; Gu et al., 2016; reviewed in Mathieu & Ruohola-Baker, 2017). Kondoh et al. (2007) show that glycolytic rate correlates with proliferative potential, and the glycolytic flux of differentiating mouse ESCs dropped to less than half that of proliferating ESCs. Inhibiting glycolysis with low doses of 2-deoxy-D-glucose (2DG) reduced ESC proliferation drastically while not having a significant effect on cultured fibroblasts. Induced pluripotent stem cells (iPSCs) are similarly reliant on glycolysis for their proliferative ability, and this glycolytic switch occurs early in, and is required for, the process of dedifferentiation and return to pluripotency

(Folmes et al., 2011; Panopoulos et al., 2012; Prigione et al., 2014). Interestingly, there is also an accompanying burst of mitochondrial activity (Kida et al., 2015). This may be in order to produce a brief increase in ROS to activate a glycolytic programme via HIF1α (Bonello et al., 2007) or one of the other pathways through which ROS has been shown to stimulate glycolysis (see 1: General Introduction, section 1.2.2). A knockdown of HIF signalling has been shown to prevent human fibroblast cells from returning to pluripotency upon induction, meanwhile increasing HIF1α activation markedly improved iPSC stimulation (Mathieu et al., 2014; Prigione et al., 2014), implicating HIF1α and ROS in a metabolic switch to glycolysis.

In support of regeneration involving a partial recapitulation of developmental programmes, cardiomyocytes return to a dedifferentiated embryo-like state during zebrafish heart regeneration, down-regulating OXPHOS and mitochondrial activity while up-regulating glycolysis, a metabolic switch that is again imperative for proliferation (Honkoop et al., 2019). The requirements of a differentiated cell are distinguished from a highly proliferative pluripotent stem cell, and thus it seems logical that their metabolic needs may also change during differentiation or dedifferentiation. The importance is evident for an increase in glycolysis activity in encouraging a proliferative and pluripotent state in various systems such as development, cancer, and regeneration, and future research into the regulation of metabolism and metabolic switches may supply prospective routes for therapy and treatment.

3.1.2 Reactive oxygen species in development

ROS are generated by natural cellular processes and are fundamental to redox signalling (see 1: General Introduction, section 1.2). Many molecules integral to development are sensitive to ROS, and therefore ROS is able to modulate multiple aspects and processes within development, including proliferation, differentiation, apoptosis, and migration (reviewed in Covarrubias et al., 2008). For example, the tumour suppressor p53 regulates many genes in development, its loss contributing to developmental disorders in addition to its well known role in cancer (reviewed in Jain & Barton, 2018). p53 is redox sensitive and interacts with ROS both directly and indirectly via its action as an up-stream activation signal or a downstream factor that mediates apoptosis (reviewed in B. Liu et al., 2008 and Bowen & Attardi, 2019). In a similar fashion, ROS can act as a second messenger to activate or inhibit—depending on timeframe—Wnt and β-catenin signalling (reviewed in Korswagen, 2006), which are involved substantially during development (reviewed in Steinhart & Angers, 2018).

A more specific example of the involvement of ROS in development is in the axis formation of sea urchins, in which an asymmetric distribution and activity of mitochondria generates a redox gradient (similar to Charles Manning Child's proposition in his theory of metabolic gradients, see 2: Generating Tools for Imaging Metabolism in Zebrafish, section 2.1) to stimulate nodal activation and distinguish the future oral side of the embryo (Coffman et al., 2004). Mitochondrial H_2O_2 is also involved in *C. elegans* symmetry breaking, by a similar re-localisation of mitochondria, and reducing the production of H_2O_2 results in delayed symmetry breaking (De Henau et al., 2020).

More relevant to this project is the calcium-dependent burst of H_2O_2 that is released following fertilisation, seen in *Xenopus* (Han et al., 2018) and sea urchin (Heinecke & Shapiro, 1989). Antioxidant treatment in the early

Xenopus embryo causing a loss of ROS revealed impaired development, including truncated body axes and failed gastrulation, specifically affecting mesoderm formation, putatively due to loss of ROS-activated phosphatidylinositol 3-kinase/protein kinase B (PI3K/Akt) signalling. Adding exogenous H_2O_2 was able to partially rescue this phenotype, indicating the importance, but not irreversibility of its absence, of ROS and an oxidative environment (Han, 2015). ROS can generally be generated by the mitochondria or NADPH oxidases, and in the early embryo, the source in sea urchins is from an NADPH oxidase (Wong & Wessel, 2005). *Xenopus* embryonic ROS, however, is derived from the mitochondria (Han, 2015). Oscillations in mitochondrial H_2O_2 in phase with the cell cycle have been identified in cleaving *Xenopus* embryos (Han et al., 2018), very similar to the heat oscillations present in zebrafish cleavage stage embryos (Rodenfels et al., 2019), both of which are linked to the phosphorylation events of cell cycle oscillator complex cyclin-dependent kinase 1 (Cdk1)-cyclin B1. This could be indicative of fluctuating mitochondrial activity, and a dynamic energy requirement during early development.

The involvement, if not responsibility, of both ROS in several disease states attests to the importance of understanding their mechanisms of action in order to improve therapeutic techniques and provide potential targets for treatment.

3.2 Materials and Methods

Zebrafish husbandry

Adult AB strain wild type, *Tg[actb2:laconic]* and *Tg[actb2:hyper]* zebrafish (*Danio rerio)* were maintained at 28 °C with a 14 hour light/10 hour dark cycle. Embryos collected from in-crosses were staged as described in (Kimmel et al., 1995). All animal experiments were performed in compliance with NACLAR Guidelines of Singapore overseen by the Biological Resource Centre of A*STAR (IACUC Protocol Number 140924), and Home Office guidelines UK. In all cases, embryos were raised in 1X E3 embryo medium as described in Cold Spring Harbor Protocols, or 1X egg water consisting of 60 µg/ml sea salts (Sigma Aldrich S9883), supplemented with 0.1% Methylene Blue unless stated otherwise.

mRNA injections

AB strain wild type zebrafish embryos were injected at the one cell stage into the cell cytoplasm with 1ng sensor mRNA in nuclease free water with phenol red. Sensor mRNA was synthesised from pCS2+ plasmids linearised with NotI (NEB), with mMESSAGE mMACHINE SP6 Transcription Kit (Ambion) and purified with lithium chloride (LiCl) extraction.

Microscopy

Sample preparation: Embryos were visually screened using a fluorescent dissecting microscope for transgenic or mRNA expression and manually dechorionated very carefully in a glass dish with forceps. Embryos were mounted in 0.3% low melting agarose (Invitrogen 16520100) with a Vaseline spacer on a microscope slide and covered with a cover slip for imaging with an upright microscope (Singapore), or in a 35mm glass bottomed dish (Thermo Scientific Nunc) and covered with 1X egg water without the addition of Methylene Blue after one hour of imaging for imaging with an inverted microscope (Manchester).

Images acquired on an AxioImager.M2 upright microscope (Zeiss) used a 5X/0.16 EC Plan-Neofluar, 10X/0.3 EC Plan-Neofluar, or 20X/0.4 Corr LD Plan-Neofluar objective as specified. Zeiss filter sets for CFP (BS455) and FITC/mCherry (DBS525/50 + 650/100) were utilised for Laconic imaging, and FITC/mCherry (DBS525/50 + 650/100) for HyPer imaging. Excitation was from a Colibri 7 LED fluorescent light source, Violet (430nm) used for Laconic imaging and Violet (430nm) and Blue (475nm) used for HyPer imaging. Imaging software: Zen Blue 2.3 Pro. The images were collected using a 2.8 Megapixels (Axiocam 503) colour camera at 14-bit on the black-and-white setting at room temperature.

Images for HyPer imaging acquired on an Olympus IX83 inverted microscope used a 10X/0.30 UPlanFL N objective using a SpectraX light engine (Lumencor) with Semrock filter set for YFP (544/25) emission, and excitation with Blue (440/20) and Teal (510/25) LED fluorescent light source and filters. The images were collected using a Retiga R6 (Q-Imaging) CCD camera at 16-bit. Imaging software: Metamorph v7.8.4.0 (Molecular Devices). Mechanised point visiting was used to allow multiple positions to be imaged within the same time-course.

Image analysis

All processing of images for calculating ratio and measuring fluorescence or ratio was conducted in Fiji (Fiji Is Just ImageJ, version 2.0.0). Average background was subtracted and threshold applied to remove remaining background, then respective channels divided by one another as required using the Image Calculator function. Pseudocolouring was applied using Lookup Table "16 colors".

Pharmacological treatment

Embryos were maintained in 0.5X E2 medium (half strength modification of the E2 embryo medium described in Cunliffe, 2003) in place of 1X E3 embryo medium. A stock concentration of 625mM sodium azide (NaN_3, Sigma Aldrich S2002) was dissolved in 1X phosphate buffered saline (PBS, Sigma Aldrich P5493) fresh for each use and added to the agarose mounting medium or to the surrounding E2 media to a final concentration of 6.25mM (1 in 100 dilution). For treatments while mounted for timelapse imaging, embryos were dechorionated manually prior to mounting and incubated at room temperature (~22˚C) for the entirety of the timelapse. For treatment with recovery and static imaging, embryos were incubated within their chorions (dechorionated only if and when

required for imaging) at 28˚C for 1 or 2 hours as specified, before removal of the drug and rinsing twice with clean E2 media.

Biochemical lactate assay

A commercially available colorimetric lactate assay kit (Sigma Aldrich MAK064) was used and protocol adapted for embryonic samples. Samples were prepared by macerating 25 dechorionated eggs or embryos with a micropestle in 45µL 2:2:1 acetonitrile:methanol:dH_2O pre-chilled on dry ice. Samples were then centrifuged at 4˚C at 15000rcf for 10 minutes, the supernatant collected into a new tube and stored at -20˚C until use in the assay. 5µL of the embryo supernatant was used per reaction, and 5µL of 2:2:1 was added to each reaction for the standard curve in order to control for any background or change in enzyme activity caused by the buffer. Triplicate reactions were set up otherwise according to manufacturer instructions, with three biological repeats. Reaction incubation time was extended to 3 hours, and absorbance at 570nm (A_{570}) was read on a microplate reader (BioTek Synergy H1) in triplicate to give a total of nine readings per sample, per experiment.

Statistical analysis

GraphPad Prism 8 was used for statistical testing, with sample numbers exceeding 6 in all experiments. Grouped statistics and analyses of differences between means were implemented. Two-way ANOVA was used with Sidak's multiple comparisons test to compare means between groups. Differences were considered significant to * at $P<0.05$, ** at $P<0.01$, *** at $P<0.001$, and **** at $P<0.0001$. Not significant (ns) was considered $P\geq0.05$, 95% confidence interval.

3.3 Results

3.3.1 Lactate increases during gastrulation

Utilising the *Tg[actb2:laconic]* line, I observed an initial decrease in lactate levels during cleavage stages, followed by an increase beginning just prior to the onset of epiboly, and a later plateau around the time of somitogenesis (FIG 3.1A and B; Supplementary Movie 1). This matches with the general tendency seen with mRNA injections, which I imaged from roughly the sphere stage due to delay in protein production (FIG 3.1C). I also conducted biochemical lactate assays on systematic timepoints throughout development to compare the Laconic data with an alternative method of measurement, in order to confirm and increase confidence in the trend. It appears that a similar pattern is attained with this method, with a decrease during the cleavage stage proceeded by a less noticeable increase over gastrulation (FIG 3.2A and B). The assay data produced a more uneven graph which does not duplicate precisely the trend in Laconic ratio (FIG 3.1B), which could perhaps be a reflection of yolk autofluorescence interfering and reducing the quality of Laconic accuracy, or a difficulty relating

to the homogenisation process during assay sample preparation. Early stage embryos are very easy to macerate compared to the later stage post-gastrulation embryos which contain more residual debris, and therefore the relatively very high initial lactate concentration may result from more complete homogenisation and distort the axis, obscuring smaller changes in lactate level. Improvements to the experimental protocol could include a more controlled method of homogenisation, such as use of glass or zirconium beads or a mechanical homogeniser, or standardisation of the lactate concentration readout to total protein content or similar.

It is known that cleavage divisions do not incorporate growth into the cell cycle (Gilbert, 2000), therefore making the system more dissimilar to the criteria for the Warburg effect. However, at the midblastula transition (MBT), after roughly the tenth cleavage division, there is cell cycle remodelling as the zygotic genome is activated and cells begin to incorporate growth (Kane & Kimmel, 1993). The increase in Laconic ratio coincides roughly with this point (due to lack of temperature control, staging was done by observation only), potentially indicating that with the onset of cell growth and the increased level of proliferation at this stage, the Warburg effect may begin to occur. Proliferation is not the only process occurring during epiboly, and other factors such as convergence extension and cell migration are also important. Glycolysis has been shown to be necessary for cell migration (Shiraishi et al., 2015; Heiss et al., 2016), and this could be an alternate explanation for the rise in lactate during gastrulation.

The peak in Laconic ratio occurs later, after the end of gastrulation, around the 10-somite stage (FIG 3.1A). A published study of proliferation levels during early zebrafish suggests proliferation is highest at the 6- to 10-somite stages (Mendieta-Serrano et al., 2013); it appears that the general timing of high proliferation and lactate levels correspond. Stages 10- to 14-somites are not included, thus I cannot comment on proliferation in relation to Laconic ratio at the 12-somite stage, and it is difficult to comment definitively as the authors did not quantify proliferation in terms of nuclei number or mitotic index during segmentation. However, extension and cell migration are also conspicuous during this period, and as previously mentioned, this may alternatively suggest a potential role for glycolysis in migration resulting in elevated lactate levels.

3.3.2 Hydrogen peroxide oscillates with the cell cycle during cleavage

As discussed briefly in the introduction (section 3.1.2), there are oscillations of H_2O_2 in coordination with the cell cycle in *Xenopus laevis* cleavage stage embryos (Han et al., 2018). These oscillations can be ablated with chemical mitochondrial inhibition, suggesting the source of the H_2O_2 is from mitochondrial activity. This treatment additionally causes developmental arrest and cessation of cleavage divisions, proposing the necessity of OXPHOS in very early development. In zebrafish, heat oscillations that correspond to cyclin phosphorylation during the cell cycle have been shown, potentially indicating a dynamic energy requirement and production during this stage (Rodenfels et al., 2019). Indeed, both aforementioned studies in *Xenopus* and zebrafish link the oscillations with phosphorylation events of Cdk1-cyclin B1. Thus, utilising the *Tg[actb2:hyper]* line, similarly imaging from the one

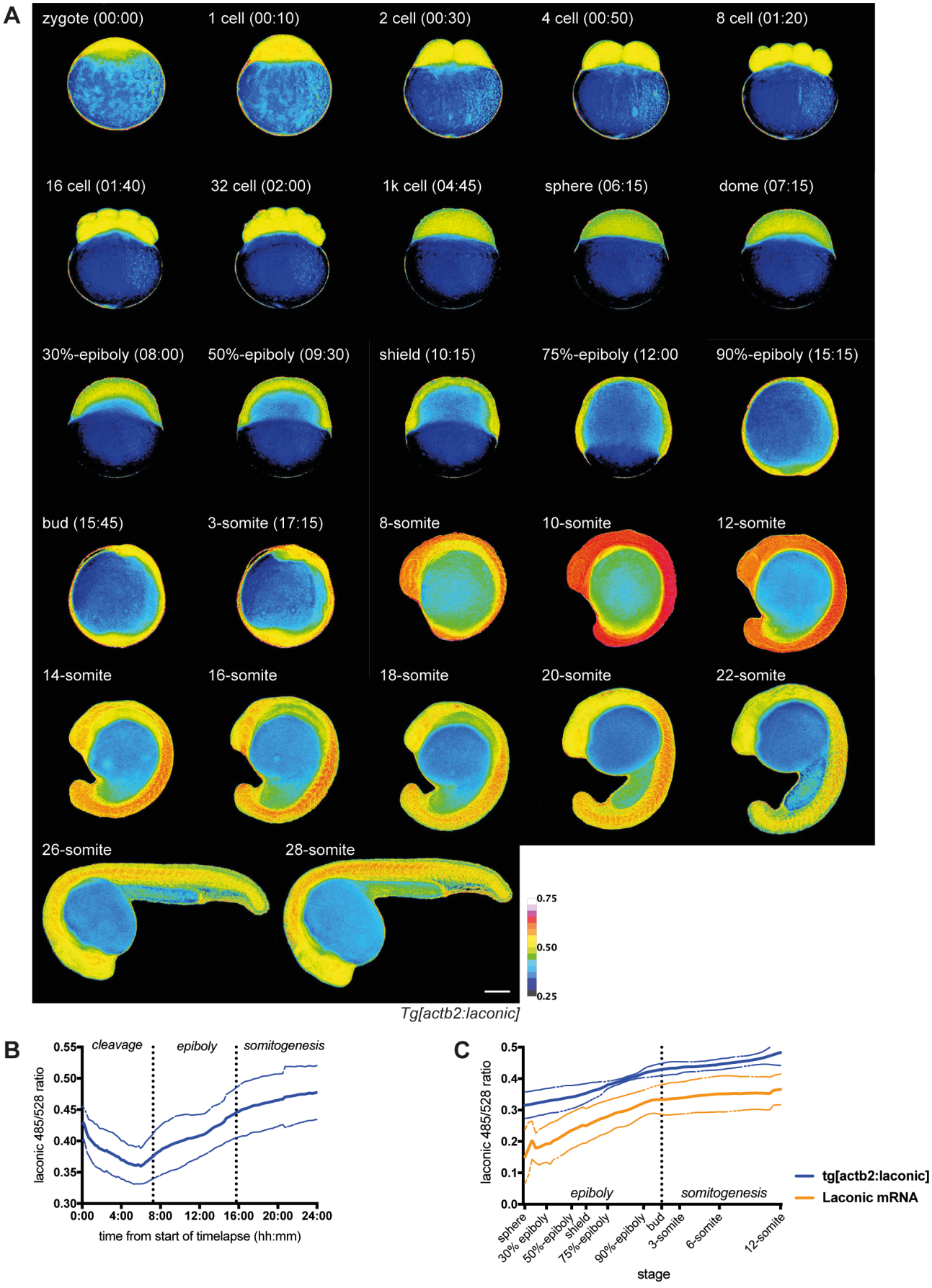

Figure 3.1. **Lactate levels during early embryogenesis.** All panels show data obtained with Zeiss AxioImager.M2 upright widefield microscope (5X). Scale bar represents 200µm. (A) Still images from a timelapse (see Supplementary Movie.1) of a single transgenic actb2:laconic embryo during development from fertilisation to the 3-somite stage from the lateral view, pseudocoloured to show Laconic ratio calculated by dividing the 428nm emission channel by the 485nm emission channel. Timings (hh:mm) correspond to timelapse duration. *(continued on next page)*

(Figure 3.1. cont.) Images of 8 somites onward are of different representative embryos, not from a timelapse. Hours post fertilisation correspond to stages described in Kimmel et al. (1995). (B) Graph showing quantification of Laconic ratio from timelapse imaging over the course of development. Trend shown is an average of separate embryos, dotted lines show error boundaries, n=5. Due to imaging being conducted at below 28˚C (~22˚C), development is delayed compared to traditional staging. (C) Graph showing quantification of Laconic ratio during gastrulation onwards, comparing results obtained with imaging the transgenic line and with injections of Laconic mRNA at the one cell stage. Imaging from the one cell stage not possible with mRNA injections due to time needed for translation, thus comparison starts at the onset of epiboly. n=3 (transgenic line), n=6 (mRNA injection).

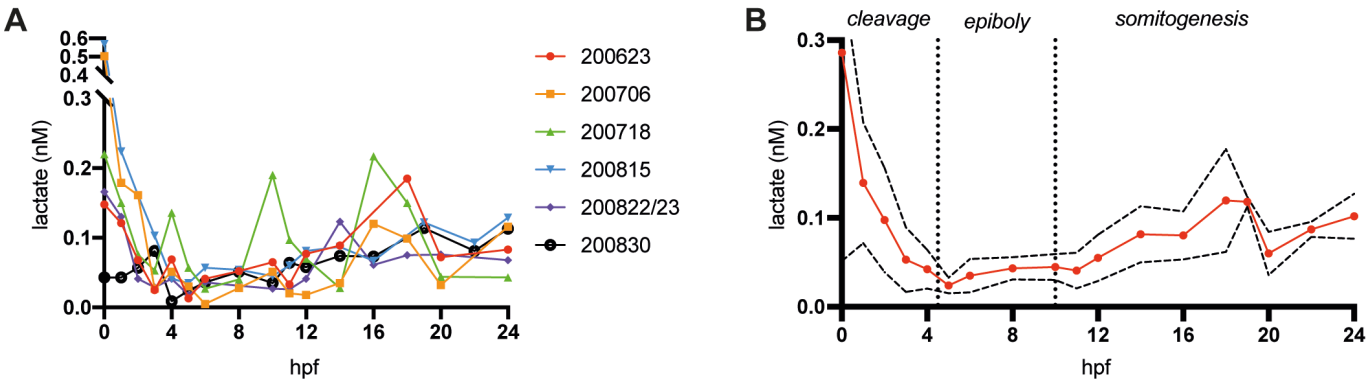

Figure 3.2. **Lactate levels during early zebrafish development assessed by biochemical lactate assay** (A) Graph of lactate levels calculated using a standard curve (specific for each data set) over the first 24 hours of development. Each data set corresponds to a separate biological repeat conducted on separate days (YYMMDD) and is a combination of three technical repeats, read in triplicate. (B) Graph showing average lactate level with error from panel (A), excluding 200718 (determined to be an outlier).

cell stage as I did with the Laconic transgenic line (FIG 3.3A, D and G; Supplementary Movie 2 and 4), I endeavoured to elucidate whether H_2O_2 oscillations were apparent in zebrafish embryos as they are in *Xenopus*.

I found that H_2O_2 oscillations appeared to be conserved between species, and HyPer ratio oscillated in phase with the cell cycle, with cleavage divisions occurring consistently at the points of lowest ratio (FIG 3.3C, E, and I; Supplementary Movie 3 and 5). (Due to the inability to control for temperature, divisions were identified visually from the timelapse images.) This was seen in two separate experimental set-ups, and also when imaging both from lateral and animal viewpoints, together forming a persuasive case for these oscillations being a genuine phenomenon rather than imaging artefact. To further confirm this, I compared the data from Laconic timelapses during cleavage with that of the HyPer timelapses, both normalised to t0, and showed that these oscillations occur in HyPer ratio alone (FIG 3.3F), thereby reducing the chance of the oscillations being due to focus changes during imaging or other extraneous causes.

Continuing to image throughout the rest of early development, until the beginnings of somitogenesis, I found that there was a slight increase in H_2O_2 during gastrulation, and more notably a drastic decrease in HyPer ratio at the start of segmentation. This was again confirmed with two microscope set-ups (FIG 3.3A, B, G and H; Supplementary Movie 2 and 4). Other work supports the requirement of H_2O_2 generated by NADPH oxidases at the leading edge for epiboly and cell migration (Mendieta-Serrano et al., 2019), which may explain the slight rise in HyPer ratio seen over the course of early gastrulation. However, HyPer may not be sensitive enough at these

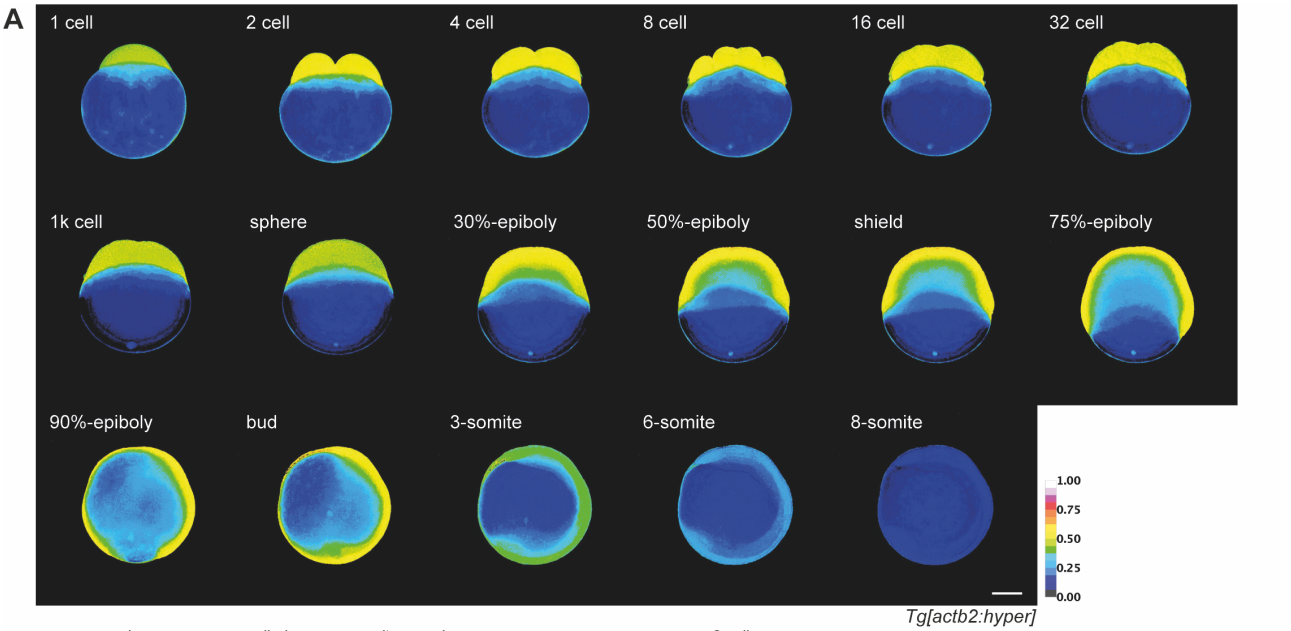

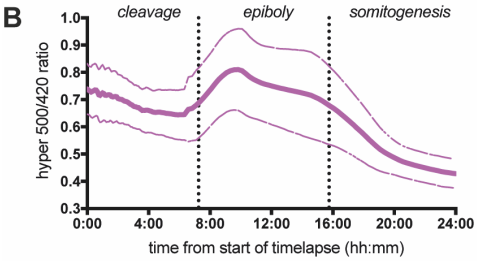

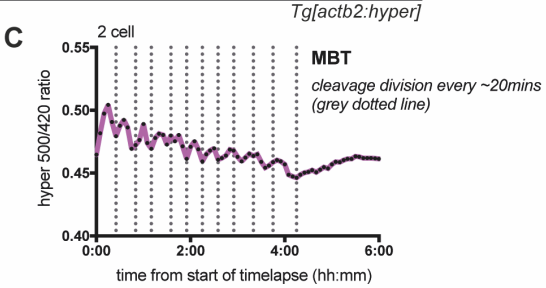

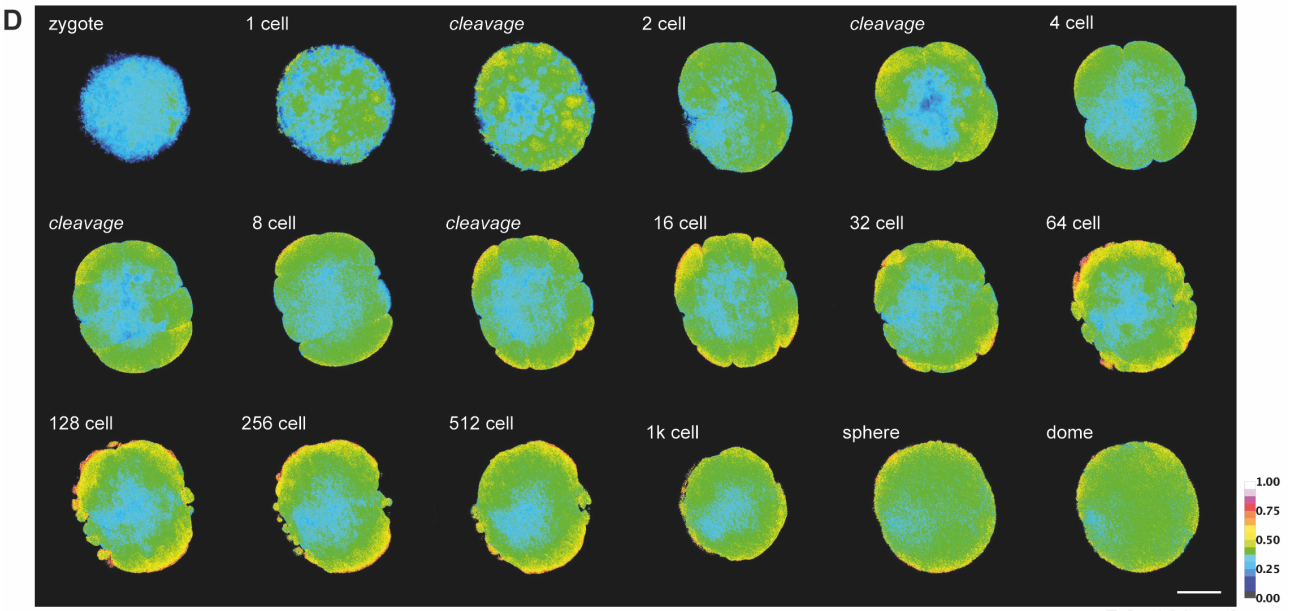

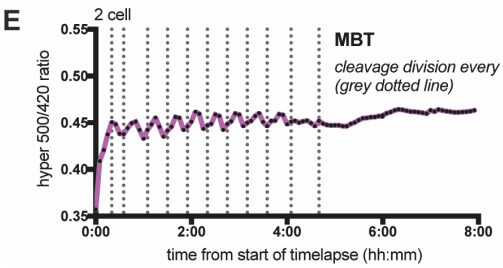

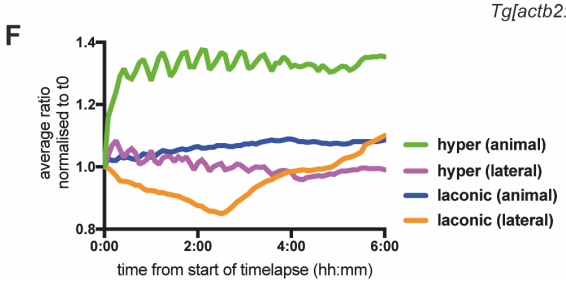

(continued on next page)

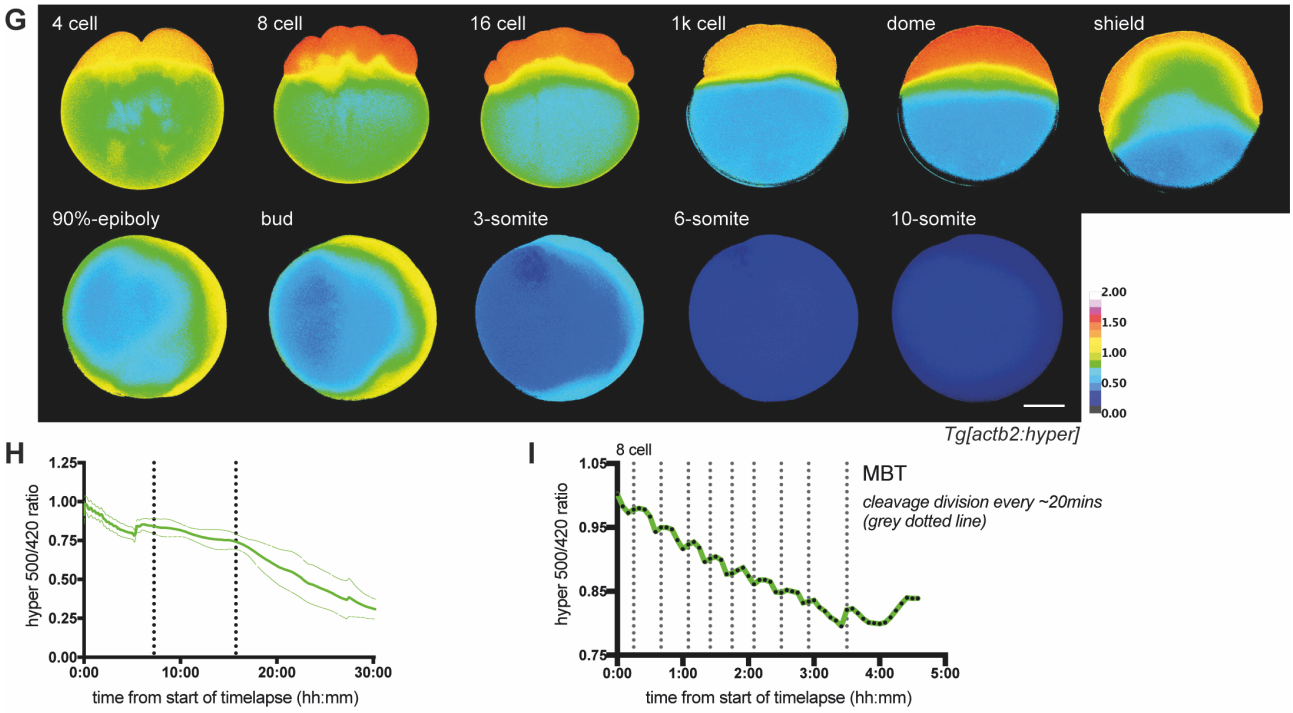

Figure 3.3. **Hydrogen peroxide levels during early embryogenesis.** Panels (A-F) show data obtained with Zeiss AxioImager.M2 upright widefield microscope (5X), panels (G-I) show data obtained with Olympus IX83 inverted (10X) to confirm repeatability. All scale bars represent 200µm. Due to imaging being conducted at uncontrolled temperatures below 28˚C (~22˚C), development is delayed compared to traditional staging and not necessarily consistent between experiments. (A) Still images from a timelapse (see Supplementary Movie.2) of a transgenic actb2:hyper embryo during development from fertilisation to the 8-somite stage from the lateral view, pseudocoloured to show HyPer ratio calculated by dividing the 500nm excitation channel by the 420nm excitation channel. (B) Graph showing quantification of HyPer ratio from lateral view timelapse imaging over the course of development. Trend shown is an average of separate embryos, dotted lines show error boundaries, n=5. (C) Graph showing quantification of HyPer ratio from the lateral view during cleavage of a single embryo to demonstrate H_2O_2 oscillations with the cell cycle. Dotted lines represent cleavage events, occurring every ~20 minutes. (D) Still images from a timelapse (see Supplementary Movie.3) of a transgenic actb2:hyper embryo during cleavage stages taken from the animal view, pseudocoloured to show HyPer ratio calculated by dividing the 500nm excitation channel by the 420nm excitation channel. (E) Graph showing quantification of HyPer ratio from the animal view during cleavage of a single embryo to demonstrate H_2O_2 oscillations with the cell cycle. Dotted lines represent cleavage events, occurring every ~20 minutes. (F) Graph comparing HyPer and Laconic ratios of individual embryos during cleavage normalised to the first timepoint (t0) measured from both lateral and animal view timelapses to show oscillations are specific to HyPer rather than due to an imaging or focus artefact. (G) Still images from a timelapse (see Supplementary Movie.4) of a transgenic actb2:hyper embryo during development from the 4-cell to the 10-somite stage from the lateral view, pseudocoloured to show HyPer ratio calculated by dividing the 500nm excitation channel by the 420nm excitation channel. (H) Graph showing quantification of HyPer ratio from lateral view timelapse imaging over the course of development. Trend shown is an average of separate embryos, dotted lines show error boundaries, n=10. (I) Graph showing quantification of HyPer ratio from the lateral view during cleavage of a single embryo to demonstrate H_2O_2 oscillations with the cell cycle (see Supplementary Movie.5). Dotted lines represent cleavage events, occurring every ~20 minutes.

magnifications and with the equipment I used to adequately spatially visualise the precise location of H_2O_2 elevation. Furthermore, the general decrease in H_2O_2 inversely correlates with the rise and peak in lactate I detected with Laconic imaging (FIG 3.1B and FIG 3.2), which may indicate a switch from oxidative to glycolytic metabolism during somitogenesis.

3.3.3 Early embryonic hydrogen peroxide is produced by the mitochondria

Since previous work in *Xenopus* has identified the source of oscillating H_2O_2 in cleavage stage embryos as the mitochondria, I sought to test whether the same held true in zebrafish. Using the mitochondrial inhibitor sodium azide (NaN_3), which inhibits complex IV of the electron transport chain and blocks OXPHOS, I treated early embryos and both measured H_2O_2 levels via HyPer imaging and observed whether development or the cell cycle were affected. I found that treatment with NaN_3 reduced HyPer ratio and eliminated oscillations, which resulted in developmental arrest and cell cycle cessation (FIG 3.4A and B, Supplementary Movie 6). As NaN_3 is a reversible inhibitor, I attempted to rescue development with simple removal of the drug. After washing out the drug and allowing the embryo to recover for three hours, I found that cell division resumed (FIG 3.4C). Furthermore, HyPer ratio returned to similar levels as controls (FIG 3.4D and E). Conjointly, these data suggest that, as with *Xenopus*, the source of H_2O_2 during early embryogenesis in zebrafish is the mitochondria, and mitochondrial activity is required for development.

3.4 Discussion

Mice use OXPHOS almost exclusively until implantation, at which point then increase their glucose consumption accompanied by a switch to glycolysis (Houghton et al., 1996). This event is imperative to the embryo, as perturbations causing altered glucose metabolism results in impaired viability and implantation capacity of the embryo (Lane & Gardner, 1998; Mitchell et al., 2009). The implantation stage roughly corresponds to the MBT in zebrafish, and a similar situation could explain the results I see (though it may be worth noting that mouse embryos lack a yolk, and therefore may utilise different energy sources which could impact metabolism). In early cleavage stages, embryos rely predominantly on OXPHOS and the mitochondria, the H_2O_2 oscillations potentially representing dynamic mitochondrial activity. The embryo expends considerable energy on regulation of the cell cycle, and this variable metabolic activity may be to supply energy for phosphorylation and de-phosphorylation of the Cdk1-cyclin B1 complex, a hypothesis that is supported by the observation of heat oscillations paired with the cell cycle oscillator (Rodenfels et al., 2019). Cleaving *Xenopus* embryos also show comparable ROS oscillations in phase with the cell cycle (Han et al., 2018), however more detailed work demonstrates oscillations not just of ROS, but also other metabolites, including ATP and lactate (Thomson, 2019).

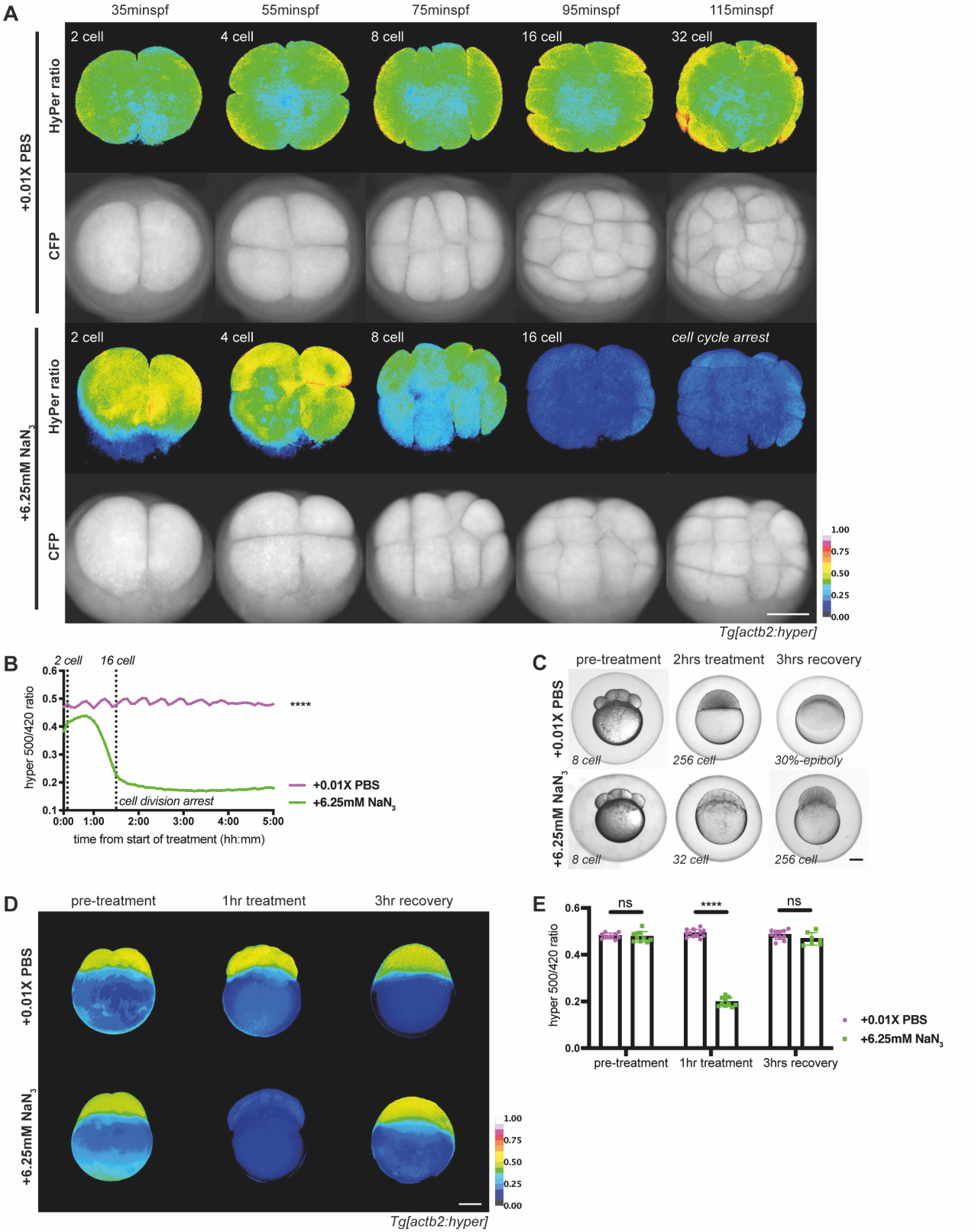

Figure 3.4. **Cell cycle arrest and abolishment of hydrogen peroxide oscillations with mitochondrial inhibition during early embryogenesis.** All panels show data obtained with Zeiss AxioImager.M2 upright widefield microscope (5X). All scale bars represent 200µm. Due to imaging being conducted at uncontrolled temperatures below 28˚C (~22˚C), development is delayed compared to traditional staging and not necessarily consistent between experiments. (A) Still images from a timelapse from the animal view (see Supplementary Movie.6) of a transgenic actb2:hyper embryo treated from the 2 cell stage with 6.25mM sodium azide (NaN_3) during development. Pseudocoloured images of HyPer ratio calculated by dividing the 500nm excitation channel by the 420nm excitation channel, and CFP channel to show cleavage divisions. (B) Graph comparing HyPer ratio of single control (treated with 0.01X PBS) and 6.25mM NaN_3 treated embryos during cleavage stages.

(continued on next page)

(Figure 3.4. cont.) Dotted lines mark the 2 cell stage, approximately when treatment is applied, and the 16 cell stage when cell cycle arrest in treated embryos occurs. Students' t-test to calculate significance, P<0.0001, n=1. (C) DIC images of AB strain wild type embryos pre-treatment with 0.01X PBS control or 6.25mM NaN_3, after 2 hours of treatment, and after 3 hours of recovery post washout of drug, showing recovery of the cell cycle when mitochondrial inhibition is removed. (D) Representative images of actb2:hyper embryos pre-treatment with 0.01X PBS control or 6.25mM NaN_3, after 1 hour of treatment, and after 3 hours of recovery post washout of drug, showing recovery of the cell cycle and H_2O_2 levels when mitochondrial inhibition is removed. (E) Quantification of HyPer ratio pre-treatment with 0.01X PBS control or 6.25mM NaN_3, after 1 hour of treatment, and after 3 hours of recovery post washout of drug, showing recovery of H_2O_2 levels. Two-way ANOVA to calculate significance, **** P<0.0001 and ns P≥0.05, n=12.

Moreover, using inhibitors of glycolysis and OXPHOS showed inverse patterns of ATP decrease, with glycolysis inhibition reducing ATP production at certain timepoints and OXPHOS inhibition reducing ATP production at contrasting timepoints within each cell cycle period (Thomson, 2019). It appears that the state of the cleaving embryo may fluctuate between Warburg and oxidative metabolism during the cell cycle, as opposed to an outright reliance on OXPHOS alone. More recently, murine pre-implantation embryos have also been shown to switch dynamically between glycolytic and mitochondrial metabolism (W. Zhou et al., 2012), suggesting a cyclic and oscillatory nature is conserved in cleavage stage embryos across species. In my work I did not witness oscillations in lactate, however this may be a consequence of insufficient sensitivity or temporal resolution. Future work could endeavour to improve on my study of lactate in cleavage stage zebrafish, for example using metabolomics techniques such as nuclear magnetic resonance with meticulous temporal sampling, to investigate whether an alternating metabolic state is apparent. In the context of wound healing, H_2O_2 production is more commonly documented as from NADPH oxidases as opposed to the mitochondria, and in this respect dissimilar to the embryonic programme. However, work in *Xenopus* tadpole tail amputations suggests mitochondrial ROS are also involved (Ng, 2019), and leads to the question of whether metabolic oscillations occur with the cell cycle in regeneration, but may be masked due to the lack of synchronisation that cleavage stages possess.

Following zygotic genome activation and the increased requirement for growth, the embryo seems to undergo a metabolic switch to glycolysis, maybe activating the Warburg effect, to compensate for the proliferative requirements. As discussed in the introduction, there are multiple links between carbohydrate metabolism and proliferation. A metabolic switch is required for maintaining the pluripotency and proliferative capacity of stem cells, both embryonic and induced (Kondoh et al., 2007; Folmes et al., 2011). It seems therefore plausible that a similar switch might occur in the embryo at the point of zygotic genome activation, when growth is incorporated into the cell cycle and the embryo enters a more canonical proliferative state. Cancer cells also incorporate the Warburg effect and a switch to aerobic glycolysis, and this mutual concept serves as a link between the two, suggesting that other findings may also be applicable to cancer cell systems. A switch to glycolytic metabolism may also be a feature of wound healing, as the requirement to replenish biomass renders regeneration a highly proliferative system. An alternative explanation for the rise in lactate may be a result of increased cell migration –

aerobic glycolysis is required for ATP production for migration of cancer cells (Shiraishi et al., 2015) and motility of activated vascular smooth muscle cells (Heiss et al., 2016).

I was unsuccessful in my attempt to manipulate the production of lactate during development with a number of chemical inhibitors in order to determine whether aerobic glycolysis was required for embryogenesis. 2DG, which inhibits hexokinase of the glycolysis pathway (FIG 1.6G) (Wick et al., 1957), possesses multiple hydroxyl groups (FIG 1.6H), making it polar and hydrophilic. Sodium oxamate, which inhibits LDH and the conversion of pyruvate to lactate (FIG 1.6D) (M. Zhou et al., 2010), is a salt and thus similarly charged and hydrophilic (FIG 1.6E). As such, these two compounds I tried are water soluble, and I hypothesised as such had no effect no matter the strength of concentration as they were unable to enter the cells. Aquatic embryos are required to be robust to foreign elements in the water, and a degree of lipophilicity is required to enable passage through the lipid membrane. I did attempt injections of oxamate, however the results were extremely variable, and it is likely the drug was not well distributed throughout the embryo during development. The other compound I used, 7-benzyl-2,3-dihydroxy-6-methyl-4-propyl-1-naphthoic acid (FX11) (Le et al., 2010), which also acts on LDH but is more lipid soluble due to its multiple carbon rings (FIG 1.6D and F), produced some interesting results, however I was unable to successfully perform positive controls to confirm the drug was acting as expected, and as such did not include the data. If a method of inhibition could be optimised, it would be very interesting to elucidate whether glycolysis is required throughout development, or if a dependence on glycolysis occurs at a certain point.

In both Laconic imaging and biochemical assay analysis, lactate levels at the one cell stage begin high before decreasing over the cleavage stage, during which potentially OXPHOS is the primary metabolism, as discussed above. The resumption of meiosis in mammalian oocyte nuclear maturation is accompanied by increased activity of glycolysis and the PPP (Tsutsumi et al., 1992; Cetica et al., 2002), and cytoplasmic maturation (that is, protein and mRNA production, cytoskeleton reorganisation) requires both glycolysis and the PPP, with inhibition of the PPP in murine oocytes resulting in an increase in oxidative stress, likely resulting from the lack of glutathione production to detoxify H_2O_2 (Xie et al., 2016). In equine oocytes, 95% of glucose consumption during *in vitro* maturation can be accounted for by lactate production (Lewis et al., 2020). Though corresponding work has not been conducted in fish, it is possible a similar profile exists, explaining the initial high levels of lactate I detect in the zygote. The reason lactate concentration in the early stages of embryogenesis when detected by biochemical assay is so much higher than as reported by Laconic may be due to the yolk possibly containing high levels of lactate. Laconic is not expressed within the yolk, and thus this would be detectable with the assay alone. Alternatively, there may be more complete extraction with early stage samples. With the nature of sample preparation for the biochemical assay, it is much easier to lyse and homogenise the younger embryos than those post gastrulation, at which point it becomes difficult to ascertain whether the embryo has been properly crushed with the micropestle, and more embryo debris remains in the homogenate.

The increase in H_2O_2 seen at the beginning of epiboly corresponds with the start of the rise in lactate. While lactate continues to slowly rise, the H_2O_2 levels appear to peak and then begin to fall much more rapidly. ROS has

been related to the promotion of glycolytic metabolism, for instance by inhibiting citric acid cycle enzymes (Nulton-Persson & Szweda, 2001) and PKM2 (Anastasiou et al., 2011), driving glucose away from being processed through the mitochondria. Additionally, mathematical models have shown that at high concentrations of H_2O_2 glycolysis is more efficient (Molavian et al., 2016), and therefore perhaps this initial production of H_2O_2 is involved in stimulating the switch to glycolysis. As mentioned in section 3.3.2, there is also evidence suggesting a requirement for ROS in cell migration during epiboly (Mendieta-Serrano et al., 2019), which may provide an alternate explanation for the increase in H_2O_2. In *Xenopus* gastrula, ROS are required for mesoderm formation (Han et al., 2017), and though this has not been investigated in the zebrafish, the rise in HyPer ratio and therefore H_2O_2 level during this stage may suggest a similar requirement.

Cdc25C is a ROS-sensitive phosphatase integral to cell cycle regulation for activating the Cdk1-cyclin B1 complex to promote cell cycle entry (Perdiguero & Nebreda, 2004). Work in *Xenopus* suggests that ROS potentially inactivates Cdc25C via its two redox-sensitive cysteine residues, which affects the phosphorylation state and thus its activity. Therefore H_2O_2 may play an additional role in for cell cycle progression rather than elevated only as a by-product of OXPHOS (Han et al., 2018). Future work could aim to elucidate whether ROS is similarly required for continuation of the cell cycle in zebrafish, or if it is the other products of mitochondrial activity that are important, such as ATP for kinase activity.

My work in this study provides a supporting basis for further investigation of the importance of glycolysis following the MBT and beginning of epiboly, and the potentially oscillating nature of metabolism during cleavage stages with possible regulatory interactions between ROS and glycolysis. The similarities I demonstrate in this study between regenerative and cancer systems and development, including the Warburg effect and ROS production, further support the concept of shared molecular programmes, and advocates the possibility for future discoveries regarding these elements to be applicable to treatment of cancer and in regenerative medicine.

References

Alberts, B., Johnson, A., Lewis, J., Raff, M., Roberts, K., & Walter, P. (2002). Chapter 2: Cell Chemistry and Biosynthesis. In *Molecular Biology of the Cell. 4th Edition* (4 ed., Number 2). https://doi.org/https://www.ncbi.nlm.nih.gov/books/NBK26838/

Anastasiou, D., Poulogiannis, G., Asara, J. M., Boxer, M. B., Jiang, J.-K., Shen, M., Bellinger, G., Sasaki, A. T., Locasale, J. W., Auld, D. S., Thomas, C. J., Vander Heiden, M. G., & Cantley, L. C. (2011). Inhibition of pyruvate kinase M2 by reactive oxygen species contributes to cellular antioxidant responses. *Science*, *334*(6060), 1278–1283. https://doi.org/10.1126/science.1211485

Bonello, S., Zähringer, C., BelAiba, R. S., Djordjevic, T., Hess, J., Michiels, C., Kietzmann, T., & Görlach, A. (2007). Reactive oxygen species activate the HIF-1alpha promoter via a functional NFkappaB site. *Arteriosclerosis, Thrombosis, and Vascular Biology*, *27*(4), 755–761. https://doi.org/10.1161/01.ATV.0000258979.92828.bc

Bowen, M. E., & Attardi, L. D. (2019). The role of p53 in developmental syndromes. *Journal of Molecular Cell Biology*, *11*(3), 200–211. https://doi.org/10.1093/jmcb/mjy087

Boyle, B., Addor, M.-C., Arriola, L., Barisic, I., Bianchi, F., Csáky-Szunyogh, M., de Walle, H. E. K., Dias, C. M., Draper, E., Gatt, M., Garne, E., Haeusler, M., Källén, K., Latos-Bielenska, A., McDonnell, B., Mullaney, C., Nelen, V., Neville, A. J., O'Mahony, M., et al. (2018). Estimating Global Burden of Disease due to congenital anomaly: an analysis of European data. *Archives of Disease in Childhood. Fetal and Neonatal Edition*, *103*(1), F22–F28. https://doi.org/10.1136/archdischild-2016-311845

Cetica, P., Pintos, L., Dalvit, G., & Beconi, M. (2002). Activity of key enzymes involved in glucose and triglyceride catabolism during bovine oocyte maturation in vitro. *Reproduction (Cambridge, England)*, *124*(5), 675–681.

Coffman, J. A., McCarthy, J. J., Dickey-Sims, C., & Robertson, A. J. (2004). Oral–aboral axis specification in the sea urchin embryo. *Developmental Biology*, *273*(1), 160–171. https://doi.org/10.1016/j.ydbio.2004.06.005

Covarrubias, L., Hernández-García, D., Schnabel, D., Salas-Vidal, E., & Castro-Obregón, S. (2008). Function of reactive oxygen species during animal development: passive or active? *Developmental Biology*, *320*(1), 1–11. https://doi.org/10.1016/j.ydbio.2008.04.041

De Henau, S., Pagès-Gallego, M., Pannekoek, W.-J., & Dansen, T. B. (2020). Mitochondria-Derived H2O2 Promotes Symmetry Breaking of the C. elegans Zygote. *Developmental Cell*, *53*(3), 263–271.e266. https://doi.org/10.1016/j.devcel.2020.03.008

Folmes, C. D. L., Nelson, T. J., Martinez-Fernandez, A., Arrell, D. K., Lindor, J. Z., Dzeja, P. P., Ikeda, Y., Perez-Terzic, C., & Terzic, A. (2011). Somatic oxidative bioenergetics transitions into pluripotency-dependent glycolysis to facilitate nuclear reprogramming. *Cell Metabolism*, *14*(2), 264–271. https://doi.org/10.1016/j.cmet.2011.06.011

Gu, W., Gaeta, X., Sahakyan, A., Chan, A. B., Hong, C. S., Kim, R., Braas, D., Plath, K., Lowry, W. E., & Christofk, H. R. (2016). Glycolytic Metabolism Plays a Functional Role in Regulating Human Pluripotent Stem Cell State. *Cell Stem Cell*, *19*(4), 476–490. https://doi.org/10.1016/j.stem.2016.08.008

Han, Y. (2015). The Role of Reactive Oxygen Species during Early Embryonic Development (E. Amaya, Ed.; pp. 1–162).

Han, Y., Chen, Y., Love, N. R., Ishibashi, S., & Amaya, E. (2017). Elevated and sustained reactive oxygen species levels facilitate mesoderm formation during early *Xenopus* development. *bioRxiv*, 223453.

Han, Y., Ishibashi, S., Iglesias-Gonzalez, J., Chen, Y., Love, N. R., & Amaya, E. (2018). Ca2+-Induced Mitochondrial ROS Regulate the Early Embryonic Cell Cycle. *Cell Reports*, *22*(1), 218–231. https://doi.org/10.1016/j.celrep.2017.12.042

Heinecke, J. W., & Shapiro, B. M. (1989). Respiratory burst oxidase of fertilization. *Proceedings of the National Academy of Sciences of the United States of America*, *86*(4), 1259–1263. https://doi.org/10.1073/pnas.86.4.1259

Heiss, E. H., Schachner, D., Donati, M., Grojer, C. S., & Dirsch, V. M. (2016). Increased aerobic glycolysis is important for the motility of activated VSMC and inhibited by indirubin-3'-monoxime. *Vascular Pharmacology*, *83*, 47–56. https://doi.org/10.1016/j.vph.2016.05.002

Hewitson, L. C., & Leese, H. J. (1993). Energy metabolism of the trophectoderm and inner cell mass of the mouse blastocyst. *The Journal of Experimental Zoology*, *267*(3), 337–343. https://doi.org/10.1002/jez.1402670310

Honkoop, H., de Bakker, D. E., Aharonov, A., Kruse, F., Shakked, A., Nguyen, P. D., de Heus, C., Garric, L., Muraro, M. J., Shoffner, A., Tessadori, F., Peterson, J. C., Noort, W., Bertozzi, A., Weidinger, G., Posthuma, G., Grün, D., van der Laarse, W. J., Klumperman, J., et al. (2019). Single-cell analysis uncovers that metabolic reprogramming by ErbB2 signaling is essential for cardiomyocyte proliferation in the regenerating heart. *eLife*, *8*, 98. https://doi.org/10.7554/eLife.50163

Houghton, F. D., Thompson, J. G., Kennedy, C. J., & Leese, H. J. (1996). Oxygen consumption and energy metabolism of the early mouse embryo. *Molecular Reproduction and Development*, *44*(4), 476–485. https://doi.org/10.1002/(SICI)1098-2795(199608)44:4<476::AID-MRD7>3.0.CO;2-I

Huang, X., & Saint-Jeannet, J.-P. (2004). Induction of the neural crest and the opportunities of life on the edge. *Developmental Biology*, *275*(1), 1–11. https://doi.org/10.1016/j.ydbio.2004.07.033

Jain, A. K., & Barton, M. C. (2018). p53: emerging roles in stem cells, development and beyond. *Development (Cambridge, England)*, *145*(8), dev158360. https://doi.org/10.1242/dev.158360

Kane, D. A., & Kimmel, C. B. (1993). The zebrafish midblastula transition. *Development (Cambridge, England)*, *119*(2), 447–456.

Kida, Y. S., Kawamura, T., Wei, Z., Sogo, T., Jacinto, S., Shigeno, A., Kushige, H., Yoshihara, E., Liddle, C., Ecker, J. R., Yu, R. T., Atkins, A. R., Downes, M., & Evans, R. M. (2015). ERRs Mediate a Metabolic Switch Required for Somatic Cell Reprogramming to Pluripotency. *Cell Stem Cell*, *16*(5), 547–555. https://doi.org/10.1016/j.stem.2015.03.001

Kimmel, C. B., Ballard, W. W., Kimmel, S. R., Ullmann, B., & Schilling, T. F. (1995). Stages of embryonic development of the zebrafish. *Developmental Dynamics, 203*(3), 253–310. https://doi.org/10.1002/aja.1002030302

Kondaveeti, Y., Guttilla Reed, I. K., & White, B. A. (2015). Epithelial-mesenchymal transition induces similar metabolic alterations in two independent breast cancer cell lines. *Cancer Letters*, *364*(1), 44–58. https://doi.org/10.1016/j.canlet.2015.04.025

Kondoh, H., Lleonart, M. E., Nakashima, Y., Yokode, M., Tanaka, M., Bernard, D., Gil, J., & Beach, D. (2007). A high glycolytic flux supports the proliferative potential of murine embryonic stem cells. *Antioxidants & Redox Signaling*, *9*(3), 293–299. https://doi.org/10.1089/ars.2006.1467

Korswagen, H. C. (2006). Regulation of the Wnt/beta-catenin pathway by redox signaling. *Developmental Cell*, *10*(6), 687–688. https://doi.org/10.1016/j.devcel.2006.05.007

Lane, M., & Gardner, D. K. (1998). Amino acids and vitamins prevent culture-induced metabolic perturbations and associated loss of viability of mouse blastocysts. *Human Reproduction (Oxford, England)*, *13*(4), 991–997. https://doi.org/10.1093/humrep/13.4.991

Lane, M., & Gardner, D. K. (1996). Selection of viable mouse blastocysts prior to transfer using a metabolic criterion. *Human Reproduction (Oxford, England)*, *11*(9), 1975–1978. https://doi.org/10.1093/oxfordjournals.humrep.a019527

Lane, M., & Gardner, D. K. (2005). Mitochondrial malate-aspartate shuttle regulates mouse embryo nutrient consumption. *The Journal of Biological Chemistry*, *280*(18), 18361–18367. https://doi.org/10.1074/jbc.M500174200

Le, A., Cooper, C. R., Gouw, A. M., Dinavahi, R., Maitra, A., Deck, L. M., Royer, R. E., Vander Jagt, D. L., Semenza, G. L., & Dang, C. V. (2010). Inhibition of lactate dehydrogenase A induces oxidative stress and inhibits tumor progression. *Proceedings of the National Academy of Sciences of the United States of America*, *107*(5), 2037–2042. https://doi.org/10.1073/pnas.0914433107

Lee, S. Y., Jeon, H. M., Ju, M. K., Jeong, E. K., Kim, C. H., Yoo, M.-A., Park, H. G., Han, S. I., & Kang, H. S. (2015). Dlx-2 is implicated in TGF-β- and Wnt-induced epithelial-mesenchymal, glycolytic switch, and mitochondrial repression by Snail activation. *International Journal of Oncology*, *46*(4), 1768–1780. https://doi.org/10.3892/ijo.2015.2874

Lewis, N., Hinrichs, K., Leese, H. J., McG Argo, C., Brison, D. R., & Sturmey, R. (2020). Energy metabolism of the equine cumulus oocyte complex during in vitro maturation. *Scientific Reports*, *10*(1), 3493–10. https://doi.org/10.1038/s41598-020-60624-z

Liu, B., Chen, Y., & St Clair, D. K. (2008). ROS and p53: a versatile partnership. *Free Radical Biology and Medicine*, *44*(8), 1529–1535. https://doi.org/10.1016/j.freeradbiomed.2008.01.011

Liu, R.-M., & Desai, L. P. (2015). Reciprocal regulation of TGF-β and reactive oxygen species: A perverse cycle for fibrosis. *Redox Biology*, *6*, 565–577. https://doi.org/10.1016/j.redox.2015.09.009

Lunt, S. Y., & Vander Heiden, M. G. (2011). Aerobic glycolysis: meeting the metabolic requirements of cell proliferation. *Annual Review of Cell and Developmental Biology*, *27*(1), 441–464. https://doi.org/10.1146/annurev-cellbio-092910-154237

Mathieu, J., & Ruohola-Baker, H. (2017). Metabolic remodeling during the loss and acquisition of pluripotency. *Development (Cambridge, England)*, *144*(4), 541–551. https://doi.org/10.1242/dev.128389

Mathieu, J., Zhou, W., Xing, Y., Sperber, H., Ferreccio, A., Agoston, Z., Kuppusamy, K. T., Moon, R. T., & Ruohola-Baker, H. (2014). Hypoxia-inducible factors have distinct and stage-specific roles during reprogramming of human cells to pluripotency. *Cell Stem Cell*, *14*(5), 592–605. https://doi.org/10.1016/j.stem.2014.02.012

Mendieta-Serrano, M. A., Mendez-Cruz, F. J., Antúnez-Mojica, M., Schnabel, D., Alvarez, L., Cárdenas, L., Lomelí, H., Ruiz-Santiesteban, J. A., & Salas-Vidal, E. (2019). NADPH-Oxidase-derived reactive oxygen species are required for cytoskeletal organization, proper localization of E-cadherin and cell motility during zebrafish epiboly. *Free Radical Biology and Medicine*, *130*, 82–98. https://doi.org/10.1016/j.freeradbiomed.2018.10.416

Mendieta-Serrano, M. A., Schnabel, D., Lomelí, H., & Salas-Vidal, E. (2013). Cell Proliferation Patterns in Early Zebrafish Development. *The Anatomical Record*, *296*(5), 759–773. https://doi.org/10.1002/ar.22692

Mitchell, M., Cashman, K. S., Gardner, D. K., Thompson, J. G., & Lane, M. (2009). Disruption of mitochondrial malate-aspartate shuttle activity in mouse blastocysts impairs viability and fetal growth. *Biology of Reproduction*, *80*(2), 295–301. https://doi.org/10.1095/biolreprod.108.069864

Molavian, H. R., Kohandel, M., & Sivaloganathan, S. (2016). High Concentrations of H2O2 Make Aerobic Glycolysis Energetically More Favorable for Cellular Respiration. *Frontiers in Physiology*, *7*, 362. https://doi.org/10.3389/fphys.2016.00362

Morandi, A., Taddei, M. L., Chiarugi, P., & Giannoni, E. (2017). Targeting the Metabolic Reprogramming That Controls Epithelial-to-Mesenchymal Transition in Aggressive Tumors. *Frontiers in Oncology*, *7*(6), 40. https://doi.org/10.3389/fonc.2017.00040

Nagao, A., Kobayashi, M., Koyasu, S., Chow, C. C. T., & Harada, H. (2019). HIF-1-Dependent Reprogramming of Glucose Metabolic Pathway of Cancer Cells and Its Therapeutic Significance. *International Journal of Molecular Sciences*, *20*(2), 238. https://doi.org/10.3390/ijms20020238

Ng, N. C. Y. (2019). Xenopus laevis Tail Regeneration: Investigating the Role of Aquaporins in

NADPH oxidase Signalling (E. Amaya, Ed.).

Panopoulos, A. D., Yanes, O., Ruiz, S., Kida, Y. S., Diep, D., Tautenhahn, R., Herrerías, A., Batchelder, E. M., Plongthongkum, N., Lutz, M., Berggren, W. T., Zhang, K., Evans, R. M., Siuzdak, G., & Izpisúa Belmonte, J. C. (2012). The metabolome of induced pluripotent stem cells reveals metabolic changes occurring in somatic cell reprogramming. *Cell Research*, *22*(1), 168–177. https://doi.org/10.1038/cr.2011.177

Perdiguero, E., & Nebreda, A. R. (2004). Regulation of Cdc25C activity during the meiotic G2/M transition. *Cell Cycle (Georgetown, Tex.)*, *3*(6), 733–737.

Prigione, A., Rohwer, N., Hoffmann, S., Mlody, B., Drews, K., Bukowiecki, R., Blümlein, K., Wanker, E. E., Ralser, M., Cramer, T., & Adjaye, J. (2014). HIF1α modulates cell fate reprogramming through early glycolytic shift and upregulation of PDK1-3 and PKM2. *Stem Cells (Dayton, Ohio)*, *32*(2), 364–376. https://doi.org/10.1002/stem.1552

Redel, B. K., Brown, A. N., Spate, L. D., Whitworth, K. M., Green, J. A., & Prather, R. S. (2011). Glycolysis in preimplantation development is partially controlled by the Warburg Effect. *Molecular Reproduction and Development*, *79*(4), 262–271. https://doi.org/10.1002/mrd.22017

Rodenfels, J., Neugebauer, K. M., & Howard, J. (2019). Heat Oscillations Driven by the Embryonic Cell Cycle Reveal the Energetic Costs of Signaling. *Developmental Cell*, *48*(5), 646–658.e646. https://doi.org/10.1016/j.devcel.2018.12.024

Shiraishi, T., Verdone, J. E., Huang, J., Kahlert, U. D., Hernandez, J. R., Torga, G., Zarif, J. C., Epstein, T., Gatenby, R., McCartney, A., Elisseeff, J. H., Mooney, S. M., An, S. S., & Pienta, K. J. (2015). Glycolysis is the primary bioenergetic pathway for cell motility and cytoskeletal remodeling in human prostate and breast cancer cells. *Oncotarget*, *6*(1), 130–143. https://doi.org/10.18632/oncotarget.2766

Steinhart, Z., & Angers, S. (2018). Wnt signaling in development and tissue homeostasis. *Development (Cambridge, England)*, *145*(11), dev146589. https://doi.org/10.1242/dev.146589

Thomson, C. (2019). Metabolic Patterning and Regulation During Early Embryo Development and Appendage Regeneration (E. Amaya, Ed.).

Tsutsumi, O., Satoh, K., Taketani, Y., & Kato, T. (1992). Determination of enzyme activities of energy metabolism in the maturing rat oocyte. *Molecular Reproduction and Development*, *33*(3), 333–337. https://doi.org/10.1002/mrd.1080330315

Wang, T., Liu, H., Lian, G., Zhang, S.-Y., Wang, X., & Jiang, C. (2017). HIF1α-Induced Glycolysis Metabolism Is Essential to the Activation of Inflammatory Macrophages. *Mediators of Inflammation*, *2017*(11), 9029327–10. https://doi.org/10.1155/2017/9029327

Wick, A. N., Drury, D. R., Nakada, H. I., & Wolfe, J. B. (1957). Localization of the primary metabolic block produced by 2-deoxyglucose. *The Journal of Biological Chemistry*, *224*(2), 963–969.

Wong, J. L., & Wessel, G. M. (2005). Reactive oxygen species and Udx1 during early sea urchin development. *Developmental Biology*, *288*(2), 317–333. https://doi.org/10.1016/j.ydbio.2005.07.004

Xie, H.-L., Wang, Y.-B., Jiao, G.-Z., Kong, D.-L., Li, Q., Li, H., Zheng, L.-L., & Tan, J.-H. (2016). Effects of glucose metabolism during in vitro maturation on cytoplasmic maturation of mouse oocytes. *Scientific Reports*, *6*(1), 20764–11. https://doi.org/10.1038/srep20764

Zhou, M., Zhao, Y., Ding, Y., Liu, H., Liu, Z., Fodstad, O., Riker, A. I., Kamarajugadda, S., Lu, J., Owen, L. B., Ledoux, S. P., & Tan, M. (2010). Warburg effect in chemosensitivity: targeting lactate dehydrogenase-A re-sensitizes taxol-resistant cancer cells to taxol. *Molecular Cancer*, *9*(1), 33–12. https://doi.org/10.1186/1476-4598-9-33

Zhou, W., Choi, M., Margineantu, D., Margaretha, L., Hesson, J., Cavanaugh, C., Blau, C. A., Horwitz, M. S., Hockenbery, D., Ware, C., & Ruohola-Baker, H. (2012). HIF1α induced switch from bivalent to exclusively glycolytic metabolism during ESC-to-EpiSC/hESC transition. *The EMBO Journal*, *31*(9), 2103–2116. https://doi.org/10.1038/emboj.2012.71

4: Metabolism in the Zebrafish Fin Amputation Model of Wound Healing and Regeneration

Abstract

Modern medicine has yet to answer why some organisms capable of regeneration and others inexplicably are not. Clear benefits would result from understanding the phenomenon of regeneration and being able to apply that knowledge and generate the same results in humans. Previous studies have suggested an importance for glycolysis in regenerating tissues and proliferation, and metabolism research is undergoing a relatively recent revitalisation, with new techniques allowing the study of metabolic activity with more broad-minded consideration outside of simply energy production. I utilise one such technique, genetically encoded biosensors, and chemical manipulation in the zebrafish larval fin and tail amputation model to show the importance of glycolysis at two stages of regeneration and wound healing: very initially, during wound closure, to facilitate the contraction of the actomyosin cable at the wound edge, and during the second phase, for the correct formation of the blastema and replacement of lost tissue. I find this latter effect is apparent only in the more severe tail amputations, in which a noticeable blastema-like structure is generated. Inhibition of glycolysis or lactate production attenuates wound contraction and regenerative outgrowth, depending on temporality of treatment. These results build on past data to implicate glycolysis and potentially the Warburg effect in successful regeneration, and induction of glycolysis or influencing its regulation may prove to be a target for future therapies.

4.1 Introduction

Certain organisms have the ability to heal scarlessly and regenerate fully functional tissues. Many organisms possess this ability as embryos or in earlier developmental stages, for example fingertip regeneration has been more commonly documented in human children (Vidal & Dickson, 1993; L. P. Lee et al., 1995), but this capability is gradually lost with ontogenesis. How some organisms are able to regenerate, while others are incapable, is a major question that remains to be answered and elucidation of which would have far-reaching implications for modern medicine. For instance, should the regenerative capacity of *Xenopus laevis* following larval tail amputation, which includes the regrowth of multiple tissues including the spinal cord, notochord, and muscle (reviewed in Beck et al., 2009), be replicated in humans, many currently incurable diseases and conditions such as paralysis after spinal cord injury and ageing-related degenerative conditions would have the potential to be addressed. Indeed, some endogenous proliferative capacity has been shown to be present in human hearts with

the discovery of myocardial stem cells in the mammalian heart (Beltrami et al., 2003), and perhaps study of the well-established zebrafish heart regeneration model (Poss et al., 2002; reviewed in Beffagna, 2019) may illuminate strategies to encourage emulation in human cells. Understanding the underlying cellular and molecular processes responsible for successful regeneration is the first step towards uncovering novel targets for therapeutic use.

One element of regeneration that has until relatively recently been understudied is the possible role of metabolism. Ever increasingly, metabolites such as hydrogen peroxide (H_2O_2) and lactate are being reported to act as second messengers, and a switch from oxidative phosphorylation (OXPHOS) to glycolysis has been suggested to be involved in epithelial to mesenchymal transitions (EMTs), particularly in cancer (S. Y. Lee et al., 2015; Kondaveeti et al., 2015; reviewed in Morandi et al., 2017). Work in *C. elegans* has shown that reduction of mitochondrial activity has positive effects on ageing (reviewed in Wang & Hekimi, 2015), and multiple studies have linked a switch to glycolytic metabolism with the proliferative potential of stem cells (Folmes et al., 2011; Kondoh et al., 2007; reviewed in Mathieu & Ruohola-Baker, 2017). Metabolism further plays an important part in cell identity and differentiation in a variety of settings, including immune cells and neurons (Buck et al., 2016; Zheng et al., 2016). Evidently, it is becoming progressively apparent that metabolism plays a wider role in physiology than simply energy production. The aforementioned examples, including EMTs and proliferation, are of relevance to and important for regeneration and wound healing, given the role of EMT for wound re-epithelialisation (reviewed in Barriere et al., 2015) and blastema formation in gecko tail regeneration (Gilbert et al., 2013), and need for proliferation to replace lost or wounded tissue. Comprehending the metabolic changes and how these are regulated, in addition to deciphering their potential importance during regeneration, may provide insight into how one may be able to manipulate cellular metabolism in order to facilitate regeneration in humans.

In this study, I utilise transgenic lines for genetically encoded biosensors for lactate, NADH/NAD+ ratio, and H_2O_2 (see 2: Generating Tools for Imaging Metabolism in Zebrafish), and chemical intervention (see 1: General Introduction, section 1.5), to examine the changes in metabolism following zebrafish larval fin amputation.

4.1.1 Glucose metabolism in wound healing and regeneration

The Warburg effect, also known as aerobic glycolysis, is characterised by the increased use of the glycolytic pathway in preference to oxidative phosphorylation and the mitochondria (see 1: General Introduction, section 1.1, FIG 1.1). The most commonly taken view presents the Warburg effect as a method of accommodating the requirements for the cellular growth and anabolism involved in rapid proliferation (reviewed in Lunt & Vander Heiden, 2011), and the importance of a switch to a primarily glycolytic metabolism, such as described in the Warburg effect, has been confirmed in various proliferative systems, including development (Houghton et al., 1996; Fiske & Vander Heiden, 2012), the immune response (reviewed in E. L. Pearce & Pearce, 2013), and cancer (Warburg, 1925). Given that regenerative outgrowth is a process that requires the generation of a significant amount of new biomass, it could be expected for regenerating cells to display up-regulated glycolysis activity.

Indeed, carbohydrate metabolism in regenerating *Xenopus* tadpole tails promotes entry into glycolysis and the PPP and away from the mitochondria (Love et al., 2014), and up-regulation of glycolysis genes is seen in zebrafish regeneration (Honkoop et al., 2019; Sinclair et al., 2020). Consistent with what is known regarding the essential role of glycolysis for proliferative ability in embryonic stem cells (reviewed in Mathieu & Ruohola-Baker, 2017), glycolytic activity is also imperative for the proliferation of regenerating cells: glycolysis inhibitor 2-deoxy-D-glucose (2DG) significantly attenuates cardiomyocyte proliferation (Honkoop et al., 2019) and levels of proliferating cells in the regenerating tail (Sinclair et al., 2020) of zebrafish. In the latter, the authors hypothesise a switch to glycolysis is necessary for blastema formation, rather than simply required for proliferation and re-entry into the cell cycle as has been previously suggested.

The lack of mammalian regenerative capacity is well known, however the MRL strain of mouse displays an abnormal ability to regenerate, for instance to completely heal though-and-through puncture wounds in the ear (Clark et al., 1998) and an elevated level of recovery with reduced scarring after heart injury (Leferovich et al., 2001). Interestingly, adults of this strain retain characteristically embryonic metabolism, sporting low mitochondrial activity and an emphasis on aerobic glycolysis (Naviaux et al., 2009), supporting the idea that regeneration involves partial recapitulation of developmental programmes and further substantiating the significance of glycolysis in regenerative potential.

Together, these data suggest a metabolic shift to glycolysis occurs in regenerating tissues to promote anabolic pathways, as is the proposed purpose of the Warburg effect, and possibly also non-proliferation-related roles such as might be involved in blastema formation.

4.1.2 Reactive oxygen species in wound healing and regeneration

H_2O_2 is generally considered a by-product metabolite due to its production by the electron transport chain of mitochondria (see 1: General Introduction, section 1.2), but has also been shown to be essential for regeneration. Notably, a sustained level of reactive oxygen species (ROS) is required for successful regeneration in both zebrafish larval and *Xenopus* tadpole tail amputations (Niethammer et al., 2009; Love et al., 2013). The source of this necessary H_2O_2 is dual oxidase (DUOX) of the NADPH oxidase family of enzymes, activated by calcium as shown in zebrafish fin regeneration (Yoo et al., 2012) and Drosophila epithelial wounds (Razzell et al., 2013). Inhibition of the production of H_2O_2 by DUOX by genetic or chemical means with diphenyleneiodonium (DPI), or by blocking calcium signalling, is sufficient to significantly impair the success of regeneration (Yoo et al., 2012; Romero et al., 2018; Love et al., 2013). In zebrafish, H_2O_2 appears to act as an early wound signal, required to trigger molecular events crucial for later regeneration, including the formation of a blastema-like structure (Romero et al., 2018). ROS is required at the wound border until minimally four hours post amputation; prevention of H_2O_2 production with DPI for just one hour from the time of amputation attenuates regeneration by 50% and results in decreased cell proliferation (Niethammer et al., 2009; Yoo et al., 2012; Romero et al., 2018). Furthermore, adding exogenous H_2O_2 promotes regeneration axons in zebrafish larval fin amputations, while

inhibition in *duox* morphants prevents axon regrowth (Rieger & Sagasti, 2011). This H_2O_2 is also responsible for recruitment of neutrophils to the injury site, stimulating the inflammatory immune response in zebrafish fin amputations via activation of nuclear factor kappa B (NF-κB) (Niethammer et al., 2009; de Oliveira et al., 2014), a major regulator of pro-inflammatory genes (reviewed in Kawai & Akira, 2007). In addition to its necessity in tail amputations, H_2O_2 is also crucial to zebrafish heart regeneration. Inhibition of DUOX significantly impairsregeneration, with fewer mitotic cardiac cells in treated hearts compared to controls at 14 days post amputation, indicating H_2O_2 is related to the proliferative function of regeneration. In the same experiment, addition of H_2O_2 was able to rescue the effects of DPI, demonstrating that presence of H_2O_2 is both required and sufficient to drive the regenerative process (Han et al., 2014).

In *Xenopus* tadpoles the role of H_2O_2 does not appear to be linked with the immune response, as the peaks of ROS and inflammatory cell accumulation do not coincide. Inhibition of the ROS-producing NOX complexes over the first 72 hours permanently impedes the regenerative response, and is not rescuable by removal of the inhibitors. Regenerating tail lengths are shorter and tissue bud formation is decreased, with reduced proliferation during the intermediate and late phases (Love et al., 2013), suggesting an early presence of ROS is consequential for subsequent regenerative responses including proliferation, similar to in zebrafish. Putatively downstream of ROS is hypoxia-inducible factor-1-alpha (HIF1α) signalling, which is directly regulated by ROS (Movafagh et al., 2015) and whose inhibition within two hours post amputation is able to prevent *Xenopus* tadpole tail regeneration, while its induction is sufficient to induce it (Ferreira et al., 2018).

Salamanders, with their somewhat extreme ability to regenerate that they retain throughout their lifespan, also produce ROS upon amputation. Inhibition with DPI similarly shows significant decrease in regenerated tissue and mitosis, indicating the conserved requirement of NOX-generated H_2O_2 for the proliferative response and regenerative outgrowth, particularly in the spinal cord (Haj Baddar et al., 2019).

4.1.3 Wound healing and regeneration models in zebrafish

Zebrafish possess a remarkable regenerative capacity, including the ability to regrow their fins both as adults or larvae (Morgan, 1900; reviewed in Poss et al., 2003; Kawakami et al., 2004; Mateus et al., 2012; Romero et al., 2018), and regenerate other organs including the spinal cord (Becker et al., 1997), retina (Vihtelic & Hyde, 2000), brain (Kroehne et al., 2011), and kidney (Diep et al., 2011). Zebrafish can also fully recover following heart injury (Poss et al., 2002; reviewed in Beffagna, 2019), while the fibrotic scarring that occurs in human patients as a result of myocardial infarction lowers the efficiency of the heart's contraction and can lead to congestive heart failure. However, the discovery of myocardial stem cells in the mammalian heart (Beltrami et al., 2003) suggests there may in fact be an extent of endogenous regenerative capacity in humans. Elucidating how the zebrafish achieves regeneration of its cardiac muscle or other structures could illuminate strategies for encouraging human tissue to do the same.

The heart and fin regeneration models are the most extensively used, and in this project I use larval fin amputations in order to take advantage of the expression of transgenic biosensors which, under the ubiquitous promoter ubiquitin (ubb), are expressed satisfactorily in embryos and larvae but are substantially dimmer in adults. A further advantage in this model is the faster regeneration time in larvae compared to adults, allowing experiments to be performed and analysed over a shorter period, and the availability of dual models of amputation allows comparison between two representations of regeneration (FIG 4.1).

Fin fold amputations, in which the amputation plane lies just distal to the tip of the notochord and only epidermal tissue is excised (Kawakami et al., 2004), serves more as a representation of wound healing. Tail amputations, which additionally sever the notochord and somitic muscle tissue (Romero et al., 2018), involves the regrowth of multiple tissue types and as such is more applicable for regeneration studies (FIG 4.1A,B). There are three established phases of regeneration in the zebrafish larval fin or tail: wound healing, blastema formation, and outgrowth (Kawakami et al., 2004). The initial stage involves the contraction of the epithelial cells surrounding the wound by an actomyosin cable, which then thickens to generate the wound epithelium before 24 hours post amputation (hpa) (Mateus et al., 2012). The second phase sees the formation of the "blastema" beneath the wound epithelium by 48hpa, a pluripotent and highly proliferative tissue important for replacing the lost cells during regeneration. In tail amputations, notochord cells extrude and contribute to the blastema-like structure, forming the "notochord bud" (Romero et al., 2018). In the final phase, there is an increase in proliferation and outgrowth, followed by differentiation and a scaling back of proliferation (Mateus et al., 2012) (FIG 4.1C,D). Similar stages occur, though over longer periods, during the regeneration of adult fins (Kawakami et al., 2004).

The conservation of genes and signalling pathways between zebrafish and other vertebrate animals, including humans (Howe et al., 2013), suggest insight made into regeneration in this model may be useful for transferring regenerative treatment to human medicine.

4.2 Materials and Methods

Zebrafish husbandry

Adult AB strain wild type and *Tg[ubb:laconic]* zebrafish (*Danio rerio*) were maintained at 28 °C with a 14 hour light/10 hour dark cycle. Embryos collected from in-crosses were staged as described in Kimmel et al., 1995. All animal experiments were performed in compliance with NACLAR Guidelines of Singapore overseen by the Biological Resource Centre of A*STAR (IACUC Protocol Number 140924), and Home Office guidelines UK. In all cases, embryos were raised in 1X E3 embryo medium as described in Cold Spring Harbor Protocols, or 1X egg water consisting of 60 µg/ml sea salts (Sigma Aldrich S9883), supplemented with 0.1% Methylene Blue unless stated otherwise.

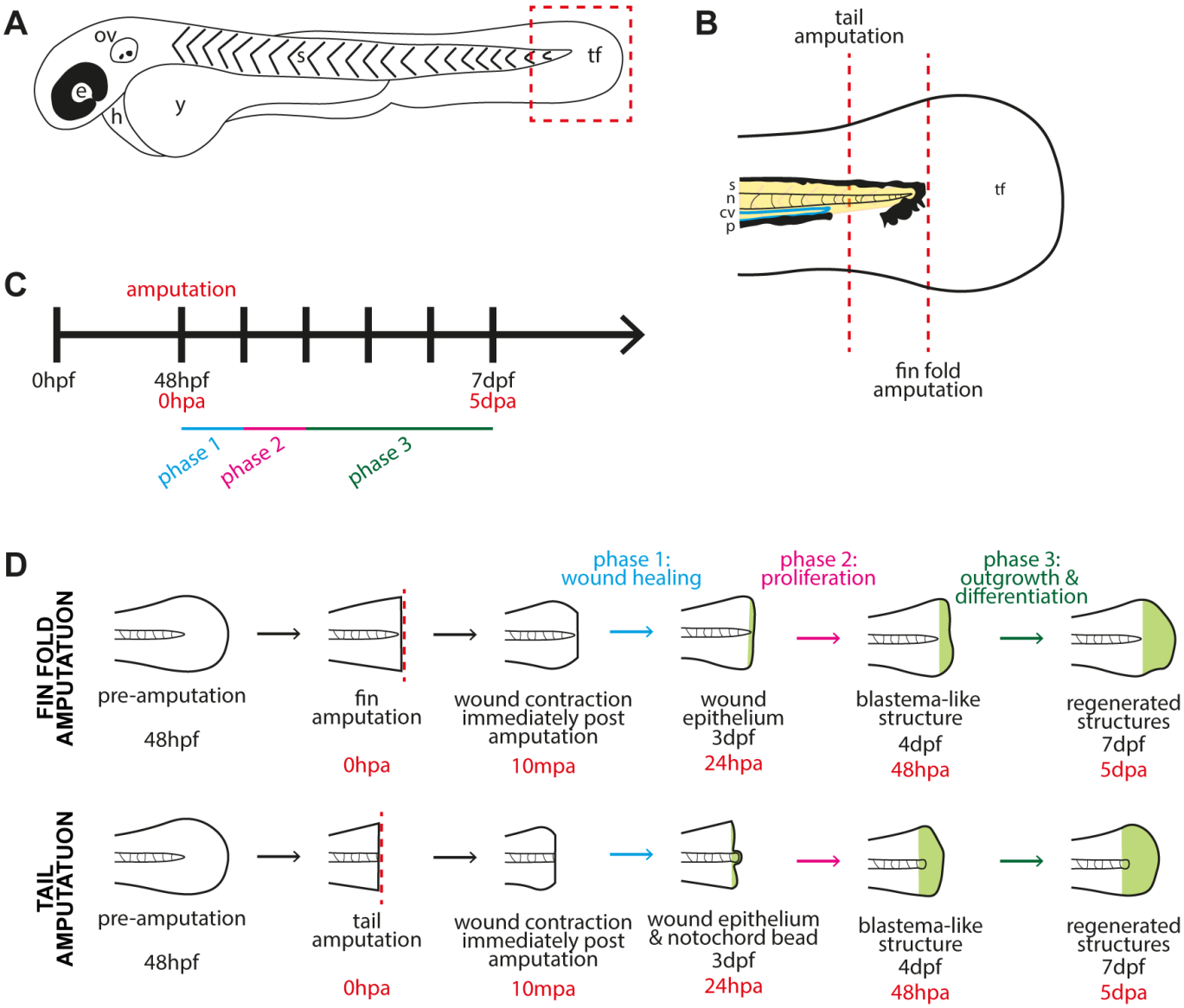

Figure 4.1. **Schematic diagrams of the fin and tail amputation models of zebrafish embryo regeneration** (A) Schematic drawing of a two day post fertilisation zebrafish embryo. e: eye, ov: otic vesicle, h: heart, y: yolk, s: somites, tf: tail fin. Red dashed box indicates the area shown in panel (B). (B) Tail region with amputation planes for fin fold and tail amputations (dashed red lines). A fin fold amputation site is positioned just distal to the tip of the notochord and excision is limited epithelial tissue and mesenchymal cells, while a tail amputation is oriented using the pigment gap and circulatory loop of the caudal vein, severing notochord, neural tube, and muscle in addition to epithelial tissue. s: somites (yellow), n: notochord (pink), cv: caudal vein (blue), p: pigment (black), tf: tail fin fold. (C) General timeline for amputation experiments. Embryos are imaged at various time points depending on the specific experiment between ten minutes post amputation (10minspa) and full regeneration at five days post amputation (5dpa). (D) Schematic depiction of the general timeline for amputation experiments. Embryos are amputated at 48hpf, following which the wound contracts and closes within ten minutes. Over the next five days the embryo regenerates the removed tissue. The events are equivalent in both fin fold and tail amputations.

Fin fold and tail amputations

2 days post fertilisation (dpf) embryos were mounted in 1% low melting agarose (Invitrogen 16520100) supplemented with 0.04% MS-222 (tricaine, Sigma Aldrich E10521) on a glass microscope slide for imaging with an upright microscope (Singapore) or in a 35mm glass bottomed dish (Thermo Scientific Nunc) for imaging with an inverted microscope (Manchester), and imaged pre-amputation. Amputations were made while embryos were mounted in agarose with either a size 10 or 15 scalpel blade, the agarose surrounding the fins excavated, and the embryos covered with media. Images were then taken at various timepoints post amputation with the embryos being de-mounted from the agarose and kept in 1X egg water or 1X E3 at 28˚C between imaging timepoints of longer than one hour.

For experiments where imaging immediately post amputation was not required, 2dpf embryos were not mounted in agarose, and instead amputated in a droplet of 1X egg water supplemented with 0.04% MS-222 on a glass microscope slide, transferred to 1X egg water with or without drug treatment within 5 minutes of amputation, and maintained at 28˚C.

Microscopy

Sample preparation: Embryos were visually screened using a fluorescent dissecting microscope for transgenic expression and dechorionated manually with forceps. Embryos were mounted in 1% low melting agarose (Invitrogen 16520100) supplemented with 0.04% MS-222 (tricaine, Sigma Aldrich E10521) on a microscope slide for imaging with an upright microscope, or in a 35mm glass bottomed dish (Thermo Scientific Nunc) for imaging with an inverted microscope.

Images acquired on an AxioImager.M2 upright microscope (Zeiss) used a 5X/0.16 EC Plan-Neofluar, 10X/0.3 EC Plan-Neofluar, or 20X/0.4 Corr LD Plan-Neofluar objective as specified. Zeiss filter sets for CFP (BS455) and FITC/mCherry (DBS525/50 + 650/100) were utilised for Laconic imaging, and FITC/mCherry (DBS525/50 + 650/100) for HyPer imaging. Excitation was from a Colibri 7 LED fluorescent light source, Violet (430nm) used for Laconic imaging and Violet (430nm) and Blue (475nm) used for HyPer imaging. Imaging software: Zen Blue 2.3 Pro. The images were collected using a 2.8 Megapixels (Axiocam 503) colour camera at 14-bit on the black-and-white setting at room temperature.

Images for immunohistochemistry and phalloidin staining were acquired on a LSM800 (Zeiss) upright confocal microscope using a 20X/0.5 N-Achroplan WD (water) objective. Emission was collected at 400-550nm with excitation laser 488nm for pNM-488, 561-700nm emission with 561nm excitation for rhodamine phalloidin, and 400-454nm emission with 405nm excitation for DAPI. Imaging software: Zen Blue 2.3 Pro. The images were collected using two-channel multi-alkali PMT detectors at 8-bit, pinhole 1AU, with Z-stacks of 2.44µm slice intervals.

Images for Laconic imaging acquired on an Eclipse Ti inverted microscope (Nikon) with a 4X/0.13 Plan Fluor PhL DL objective used a SpetraX light engine (Lumencore) with individual Semrock emission filters for eCFP

(480/30) and eYFP (535/30), and excitation with Blue (440/20) LED fluorescent light source and filter. The images were collected using a Retiga R6 (Q-Imaging) CCD camera at 14-bit. Imaging software: NIS Elements AR.46.00.0. Mechanised point visiting was used to allow multiple positions to be imaged and environment was maintained at 28˚C.

Images for HyPer imaging acquired on an Olympus IX83 inverted microscope used a 10X/0.30 UPlanFL N objective using a SpectraX light engine (Lumencor) with Semrock filter set for YFP (544/25) emission, and excitation with Blue (440/20) and Teal (510/25) LED fluorescent light source and filters. The images were collected using a Retiga R6 (Q-Imaging) CCD camera at 16-bit. Imaging software: Metamorph v7.8.4.0 (Molecular Devices). Mechanised point visiting was used to allow multiple positions to be imaged.

Image analysis

All processing of images for calculating ratio and measuring fluorescence or ratio was conducted in Fiji (Fiji Is Just ImageJ, version 2.0.0). Average background was subtracted and threshold applied to remove remaining background, then respective channels divided by one another as required using the Image Calculator function. Pseudocolouring was applied using Lookup Table "16 colors".

Pharmacological treatment

2dpf embryos were maintained in 0.5X E2 medium (half strength modification of the E2 embryo medium described in Cunliffe, 2003) in place of 1X E3 embryo medium. Drug treatments were maintained until one hour post amputation, with the exception of experiments in section 4.3.7.

A stock concentration of 500mM oxamate (Sigma Aldrich O2751) was dissolved in distilled water fresh for each use and diluted in E2 supplemented with 0.04% MS-222 (tricaine, Sigma Aldrich E10521) to a working concentration of 10, 150 or 200mM. For amputation experiments examining the initial hour of regeneration, embryos were amputated in media containing oxamate at a concentration of 150 or 200mM; for those regarding the whole of the regeneration process, embryos were placed into media containing 10mM oxamate immediately following amputation and kept in the drug until assessment at 120hpa.

For sodium azide (NaN_3, Sigma Aldrich S2002) treatment, powder form of the drug was dissolved in 1X phosphate buffered saline (PBS, Sigma Aldrich P5493) fresh for each use at a stock concentration of 1.5M and diluted in E2 supplemented with 0.04% MS-222 to a working concentration of 15mM.

Hydrogen peroxide (H_2O_2, Sigma Aldrich H1009) in its commercially bought form of 30% w/w (9.8M) was diluted in E2 media supplemented with 0.04% MS-222 to a working concentration of 20mM.

2-Deoxy-D-glucose (2DG, Sigma Aldrich D8375) was dissolved in distilled water to a stock solution of 250mM and diluted 1:10 in 1X egg water with methylene blue to produce a working concentration of 25mM. In amputation experiments, embryos were placed into media containing 2DG immediately following amputation and

2DG treatment was maintained from 0hpa until 72hpa, then washed out and the embryos placed in new 1X egg water with methylene blue, as longer treatment results in embryo mortality.

For Laconic imaging experiments of the first hour post amputation, 2dpf embryos were mounted in 1% low melting agarose (Invitrogen 16520100) supplemented with 0.04% tricaine on a glass microscope slide or in a 35mm glass bottomed dish (Thermo Scientific Nunc) and imaged pre-amputation. Amputations were made while embryos were mounted in agarose with either a size 10 or 15 scalpel blade. Agarose surrounding the fins was excavated and the embryos covered with the treatment solution. Images were then taken 10 minutes post amputation. For immunohistochemistry samples, 2dpf embryos were amputated in a droplet of the oxamate and tricaine solution on a glass microscope slide with a size 10 or 15 scalpel blade, incubated for 10 minutes at room temperature, then fixed as described below.

Immunohistochemistry

10 AB strain wild type embryos per condition per experiment were fixed in either 4% paraformaldehyde (PFA, Sigma Aldrich F8775) in 1X phosphate buffered saline (PBS, Sigma Aldrich P5493) at room temperature for 2 hours or 95% methanol (MeOH, Sigma Aldrich 34860)/5% glacial acetic acid (GAA, Sigma Aldrich A6283) at -20°C for 4 hours.

In brief: if fixed in 95% MeOH/5% GAA washes were done with PBDT (1XPBS/1%BSA/2%DMSO [dimethyl sulfoxide, Sigma Aldrich D8418]/0.5%Tween), if fixed in 4% PFA washes were in PBST (1XPBS/0.1%Tween or Triton). Samples were systematically rehydrated in methanol washes, then washed in PBDT or PBST as specified by the fixation method, followed by acetone cracking at -20˚C for 7 (PFA fix) or 14 (MeOH/GAA fix) minutes. Blocking was in 2% donkey serum for 2 hours at room temperature. Primary antibody, rabbit α-phosphomyosin light chain II (Cell Signalling Technology #3671), was added in fresh block at a dilution of 1:250 and incubated overnight at 4˚C. Secondary antibody, donkey α-rabbit Alexa Fluor 488 (Invitrogen R37118), was added in fresh block at a dilution of 1:500 and incubated overnight at 4˚C. DAPI (Invitrogen D1306) was added 1:1000 (10nM) during the first half an hour wash post-secondary antibody addition. Samples were transferred to 50% glycerol (Sigma Aldrich G5516) in 1X PBS and stored at 4˚C.

Phalloidin staining: rhodamine phalloidin (Invitrogen R415) was made up as 40X stock solution in methanol and added in a 1:40 dilution to 4% PFA fixed samples, either alone directly after fixation or in tandem with secondary antibody addition.

Statistical analysis

GraphPad Prism 8 was used for statistical testing, with sample numbers exceeding 6 in all experiments. Column or grouped statistics and analyses of differences between means were implemented for all data sets. For column statistics, two-tailed unpaired t-tests with assumed Gaussian distribution were used. Two-way ANOVA was used with Sidak's multiple comparisons test to compare means between groups. Differences were considered significant

to * at P<0.05, ** at P<0.01, *** at P<0.001, and **** at P<0.0001. Not significant (ns) was considered P≥0.05, 95% confidence interval.

4.3 Results

4.3.1 Lactate in fin fold and tail amputation

Upon amputation, most regenerative organisms form a highly proliferative structure termed the blastema. Since regeneration involves the regrowth of lost tissue, it would stand to reason that the system would have the requirements for generation of biomass. As such, regeneration is a good candidate for the Warburg effect. Thus, I aimed to utilise the *Tg[ubb:laconic]* line, which I generated and described in Results 1, ubiquitously expressing the genetically encoded cytoplasmic lactate sensor Laconic (San Martín et al., 2013), to image lactate levels over the regeneration of larval zebrafish fin fold and tail amputations. In the former, only the epidermis is wounded, whereas the latter incorporates a cut through other tissues including the notochord, and previous work has shown the formation of a "notochord bead" from extruding notochord sheath cells (Romero et al., 2018; Sinclair et al., 2020) that seems equivalent to a blastema-like structure.

In fin fold amputations, I found that Laconic ratio increases directly following amputation, rising significantly within the first five minutes post amputation (minspa) and returning to control levels by 20minspa (FIG 4.2A and C). Spatially, lactate was raised in a broad gradient from the wound border, where it was strongest, to approximately 80µm into the fin. For the rest of regeneration there was no difference between amputated and un-amputated controls (FIG 4.2B and D). In order to confirm the initial lactate production I saw within 10minspa, I repeated the experiment on the same transgenic line with a different microscope and imaging set-up. Again, I saw a comparable result, with Laconic ratio significantly increasing at 10minspa (FIG 4.2E and F) Together, this increases my confidence in there being a burst of lactate immediately ensuing amputation.

I then sought to determine whether the same pattern occurred in tail amputation, with the transection through more tissues and the formation of a blastema. Overall, the trends are very alike, with a near instant and rapid increase in Laconic ratio, proceeded by little change over the remaining course of regeneration (FIG 4.3A and B). The initial lactate increase takes longer to return to control levels in tail amputation (24 hours) and when specifically measuring Laconic ratio in the blastema region I find that Laconic ratio remains significantly higher until at least 48 hours post amputation (FIG 4.3C). The blastema begins formation at 12 hours post amputation and blastema genetic markers start to be lost after 48 hours post amputation (Kawakami et al., 2004; Romero et al., 2018), fitting with the lactate data I observe: that is, while the presence of the proliferative blastema-like structure persists there are higher lactate levels and, correspondingly, high glycolysis activity and therefore potentially the Warburg effect.

Though it is known that activated immune cells utilise the Warburg effect (reviewed in E. L. Pearce & Pearce, 2013 and Palsson-McDermott & O'Neill, 2013) and therefore might be expected to display elevated levels of

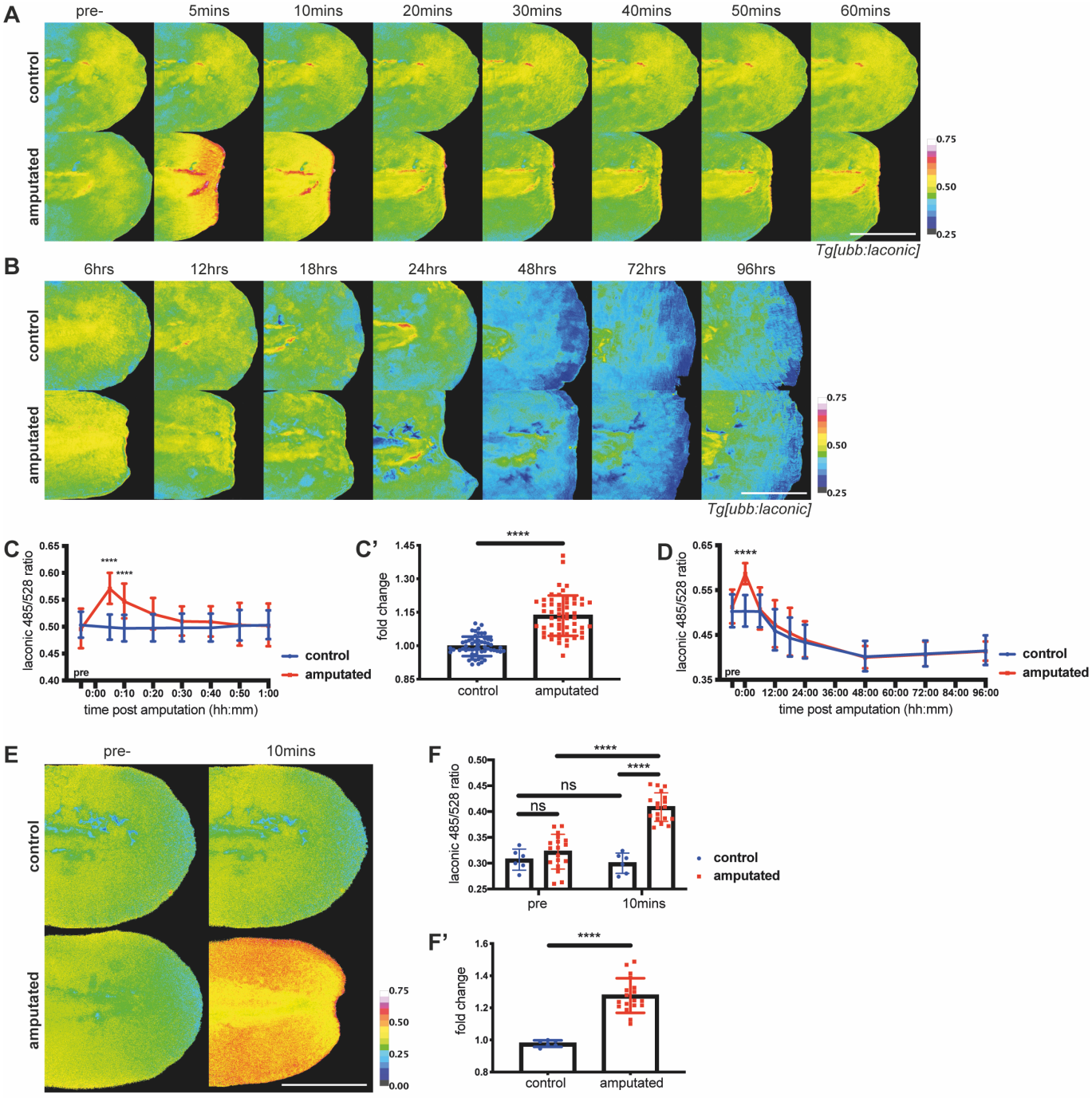

Figure 4.2. **Lactate levels during fin fold amputation.** (A-D) show data obtained with Zeiss AxioImager.M2 upright widefield microscope (20X), (E-F) show data obtained with Nikon Eclipse Ti inverted widefield microscope (20X). All scale bars represent 200µm. Differences were considered significant to * P<0.05, ** P<0.01, *** P<0.001, **** P<0.0001, and ns P≥0.05. (A) Representative transgenic ubb:laconic embryos at 48hpf imaged pre-amputation and the same individual embryo followed over the course of one hour post amputation, pseudocoloured to show Laconic ratio calculated by dividing the 428nm emission channel by the 485nm emission channel. (B) Representative transgenic ubb:laconic embryos (note not all images are the same embryo) amputated at 48hpf and imaged at various time-points over the course of regeneration, pseudocoloured to show Laconic ratio calculated by dividing the 428nm emission channel by the 485nm emission channel. (C) Graph showing quantification of raw Laconic ratios pre-treatment and over the course of one hour post amputation. Two-way ANOVA to calculate significance, n=18. (C') Graph showing fold change between pre-amputation ratio and 10 minutes post amputation. Students' t-test to calculate significance, n=56. (D) Graphs showing quantification of raw Laconic ratios pre-treatment and at various timepoints post amputation. Two-way ANOVA to calculate significance, n=18. (E) Representative transgenic ubb:laconic embryos at 48hpf imaged pre-amputation and 10 minutes post amputation to confirm repeatability of the result seen in (A) and (D), pseudocoloured to show Laconic ratio calculated by dividing the 428nm emission channel by the 485nm emission channel. (F) Graph showing raw Laconic ratios pre- and 10 minutes post-amputation. Two way ANOVA to calculate significance, n=6 (control), n=18 (amputated). (F') Graph showing quantification of ratio change 10 minutes post amputation as fold change (ratio at 10minspa divided by pre-amputation ratio). Students' t-test used to calculate significance, n=6 (control), n=18 (amputated).

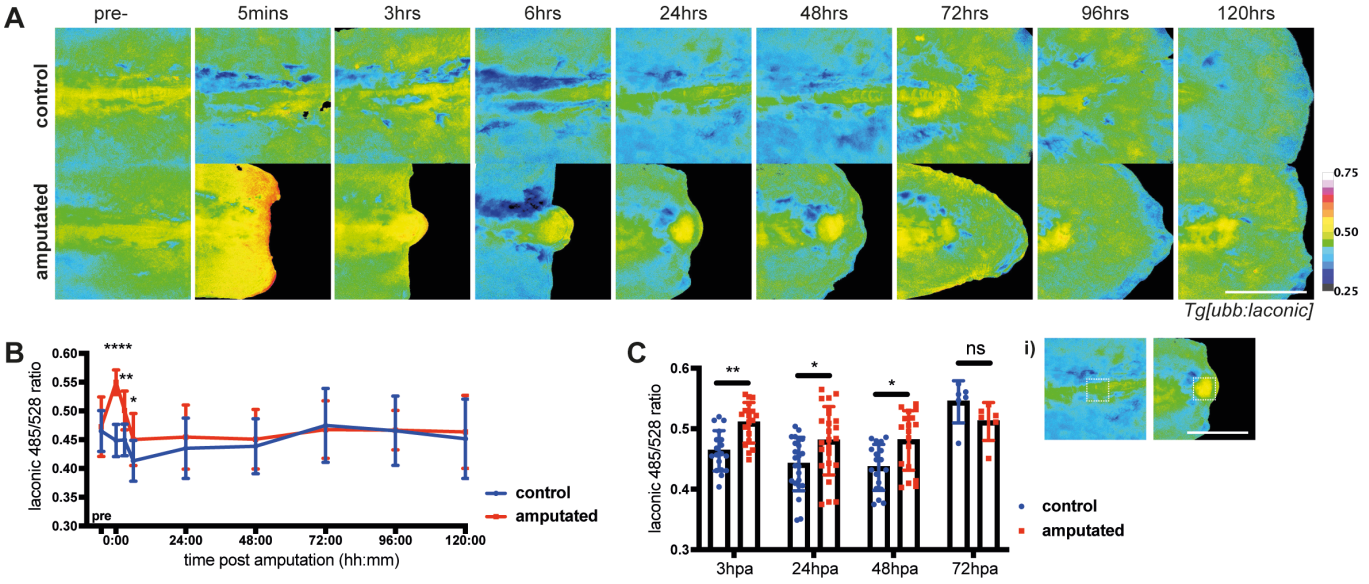

Figure 4.3. **Lactate levels during tail amputation.** All panels show data obtained with Zeiss AxioImager.M2 upright widefield microscope (20X). Scale bar represents 200µm. Differences were considered significant to * P<0.05, ** P<0.01, *** P<0.001, **** P<0.0001, and ns P≥0.05. (A) Representative transgenic ubb:laconic embryos at 48hpf imaged pre-amputation and at various time-points over the course of regeneration (note that images show representative embryos rather than following an individual embryo), pseudocoloured to show Laconic ratio calculated by dividing the 428nm emission channel by the 485nm emission channel. (B) Graphs showing quantification of raw Laconic ratios pre-treatment and at various timepoints post amputation. Two-way ANOVA to calculate significance, n=24. (C) Graph showing quantification of raw Laconic ratios specifically in the blastema/notochord bead region (as indicated in (i)). Students' t-test to calculate significance, n=24.

lactate, I did not detect increased Laconic ratio specifically in any cells that resembled neutrophils in either fin fold or tail regeneration. Potentially this suggests that the widefield imaging approach is unable to discern lactate levels at the single cell level, or movement of the cells is interfering with the imaging, or that in this instance the Warburg effect is not occurring.

In both models, fin fold amputation and tail amputation in the zebrafish larva, Laconic ratio is significantly higher directly following amputation. The first event in both is a wound healing phase, in which the wound closes by the mechanism of an actomyosin cable (Mateus et al., 2012). Glycolysis is able to produce more ATP rapidly in a short space of time than OXPHOS, which is why the fastest contracting muscle fibres, which are also actomyosin based, are purely glycolysis-based in their metabolism (reviewed in Schiaffino & Reggiani, 2011). I hypothesised that perhaps this was an explanation for the transient burst of lactate and glycolysis activity after amputation, as a strategy for swiftly producing large quantities of energy to fuel the contraction of the actomyosin cable in wound closure.

4.3.2 NADH/NAD+ ratio in fin fold and tail amputation

With a similar strategy to imaging lactate throughout regeneration, I employed the *Tg[ubb:sonar]* line that I generated and described in 2: Generating Tools for Imaging Metabolism in Zebrafish, expressing the genetically encoded sensor for NADH/NAD+ ratio, SoNar (Zhao et al., 2015), in the cytoplasm under the ubiquitous ubiquitin

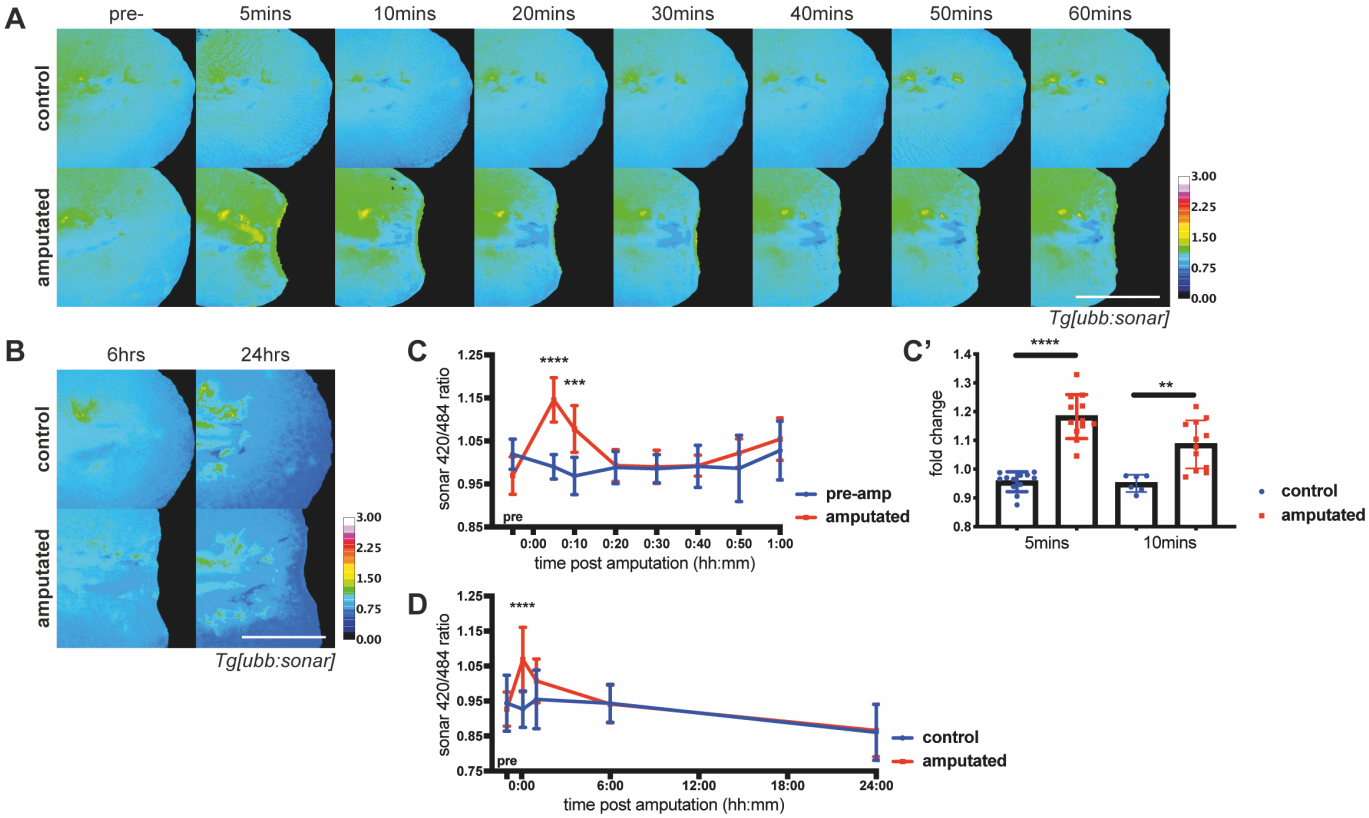

Figure 4.4. **NADH/NAD+ ratio during fin fold amputation.** All panels show data obtained with Zeiss AxioImager.M2 upright widefield microscope (20X). All scale bars represent 200µm. Differences were considered significant to * P<0.05, ** P<0.01, *** P<0.001, **** P<0.0001, and ns P≥0.05. (A) Representative transgenic ubb:sonar embryos at 48hpf imaged pre-amputation and the same individual embryo followed over the course of one hour post amputation, pseudocoloured to show SoNar ratio calculated by dividing the 420nm excitation channel by the 484nm excitation channel. (B) Representative transgenic ubb:sonar embryos (note not all images are the same embryo) at 48hpf imaged pre-amputation and at various time-points over the course of regeneration, pseudocoloured to show SoNar ratio calculated by dividing the 420nm excitation channel by the 484nm excitation channel. (C) Graph showing quantification of raw SoNar ratios pre-treatment and over the course of one hour post amputation. Two-way ANOVA to calculate significance, n=6. (C') Graph showing fold change between pre-amputation ratio and 5 and 10 minutes post amputation. Students' t-tests to calculate significance, n=12. (D) Graphs showing quantification of raw SoNar ratios pre-treatment and at various timepoints post amputation. Two-way ANOVA to calculate significance, n=6.

promotor. NAD(H) (FIG 1.5A) can provide information on the energy balance of the cell, due to its involvement in glycolysis and OXPHOS (reviewed in Cantó et al., 2015).

I found that in fin fold amputations there was very little to no change in SoNar ratio over the course of regeneration (FIG 4.4). There was however an initial peak in NADH/NAD+ ratio as seen with lactate, which was lost after 10minspa. An increase in H_2O_2 from activity of the NADPH oxidase DUOX following amputation is well documented (Niethammer et al., 2009), however NADPH and NADH are not interchangeable. Though the phosphate group in NADPH does not affect the redox activity of the molecule, it does alter the shape and thus allows enzymes to distinguish between the two. NAD(H) and NADP(H) have distinct roles within the cell (Alberts et al., 2002): the NADH/NAD+ redox couple is known as a regulator of cellular energy metabolism (ie. involved in glycolysis and OXPHOS), whereas NADPH/NADP+ are involved in maintaining redox balance and biosynthesis, such as in the PPP (reviewed in Xiao et al., 2018). Thus, NADPH oxidase activity cannot explain the initial

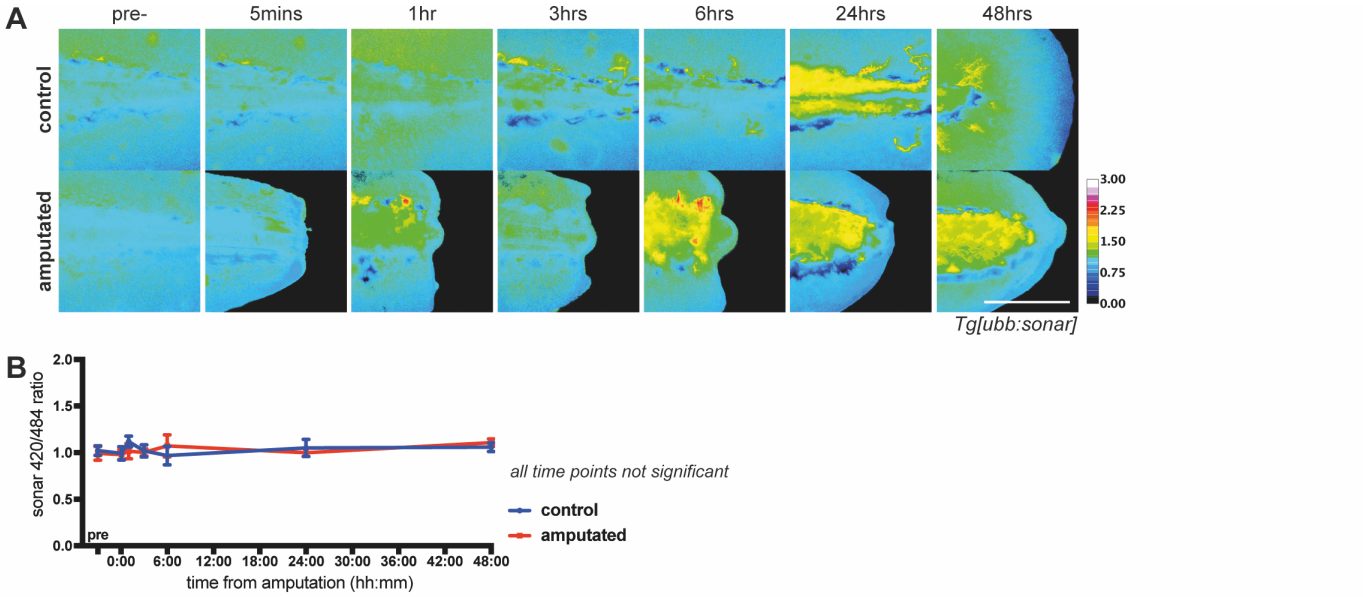

Figure 4.5. **NADH/NAD+ ratio during tail amputation.** All panels show data obtained with Zeiss AxioImager.M2 upright widefield microscope (20X). All scale bars represent 200μm. Differences were considered not significant at P≥0.05. (A) Representative transgenic ubb:sonar embryos at 48hpf imaged pre-amputation and at various time-points over the course of regeneration, pseudocoloured to show SoNar ratio calculated by dividing the 420nm excitation channel by the 484nm excitation channel. (B) Graph showing quantification of raw SoNar ratios pre-treatment and over the course of one hour post amputation, and fold change between pre-amputation ratio and 5 and 10 minutes post amputation. Two-way ANOVA to calculate significance, n=6.

imbalance of NADH/NAD+ ratio measured by SoNar ratio. In the cytoplasm, interconversion between NADH and NAD+ is mediated by GAPDH (producing NADH) and lactate dehydrogenase (LDH) or the malate-aspartate shuttle (MAS) (producing NAD+) (FIG 1.5B,C) (reviewed in Xiao et al., 2018). There would appear to be neither an expected net gain or loss regardless of the employment of the Warburg effect or mitochondrial metabolism, and NADH/NAD+ ratio depends on speed of each reaction/pathway. Thus, perhaps the early rise in SoNar ratio shows an excess of NADH due to increased glycolysis activity, whose rate exceeds LDH activity in fermentation or MAS activity to regenerate NAD+.

In tail amputation no significant change in NADH/NAD+ ratio was seen at any point during regeneration or wound healing, including directly post amputation, which contrasts with that seen in fin fold amputation and imaging lactate levels (FIG 4.5). Possibly equilibrium was restored more rapidly in the tail amputation model or LDH is activated more promptly, though these solutions seem unlikely. As NAD(H) is involved in many reactions and multiple pathways may result in simply cancelling one another out, it is difficult to predict or properly explain the data. Lactate levels behave similarly in both fin fold and tail amputations, leading me to believe the SoNar data do not appear to fit the same model of increased glycolysis.

4.3.3 Inhibition of lactate production in fin fold amputation

I hypothesised in 4.3.1 that the burst in lactate production was due to an up-regulation of glycolysis activity to rapidly provide energy for actomyosin cable contraction in wound closure. The SoNar data for fin fold amputation

also displayed an early imbalance of NADH to NAD+, hinting at a higher rate of glycolysis compared with fermentation or OXPHOS. Therefore, I endeavoured to inhibit the production of lactate, and thus the regeneration of NAD+ for the continued activity of glycolysis, to determine whether expeditious glycolysis was required for wound contraction. To do this I utilised the chemical inhibitor oxamate, which competes with pyruvate to bind with LDH (FIG 1.6D) (Zhou et al., 2010). Unlike pyruvate, oxamate is not processed by the enzyme and effectively blocks its activity.

Initially I conducted a positive control to ensure oxamate treatment was effective in preventing the increase in lactate post amputation. I found that treatment was successful and also dose dependent. When measuring both Laconic ratio and fin width, I found that oxamate treatment during amputation prevented the expected increase in Laconic ratio and the wound remained significantly wider 10minspa (FIG 4.6A-D). Incubating the embryos continuously in oxamate at a concentration sufficient to prevent the initial burst in lactate following amputation caused death, hence I only sustained treatment up to one hour post amputation (hpa) before washing out the drug. This one hour treatment did not affect overall regeneration, and fins appeared as like controls in terms of Laconic ratio and fin length (FIG 4.6A-D), which was measured from the tip of the notochord to the distal edge of the regenerated fin fold. For further confidence in my data, I repeated the same experiment with a different microscope and imaging set-up in Manchester, and attained the same results (FIG 4.6E-G). Together, these data suggests that rapid glycolysis activity is required for correct contraction of the wound post amputation, but the larva is able to recover following temporary inhibition and this is not detrimental to long-term regeneration, complementing the previous Laconic data in 4.3.1.

In order to further investigate the theory of importance to actomyosin activity, I stained for phosphorylated non-muscle myosin (pNM) and actin on treated and control amputated embryos, using immunohistochemistry and phalloidin, respectively. I found that myosin is largely still able to be activated and is only significantly reduced with the higher concentration of oxamate. However, actin at the wound border is significantly diminished with both concentrations of oxamate treatment (FIG 4.7). This may be attributed to the fact myosin phosphorylation requires only a single ATP to donate the phosphate group for each myosin, and therefore is not the most energetically demanding process. Activated myosin is not necessarily *actively contracting*, which requires one molecule of ATP for each myosin stroke cycle. Therefore, the process likely to be consuming the most ATP is contraction itself, and it is this contraction that requires the use of glycolysis. It may be that actin stabilisation and condensation at the site of action requires activity of myosin, and the lack of actin remodelling may indicate a loss of active contraction.

4.3.4 Fin fold amputation with mitochondrial inhibition and prolonged lactate production

Since lactate production seemed to be important for the early wound healing phase of regeneration, I attempted to perpetuate lactate production to see what effect this may have on wound healing. To do this, I

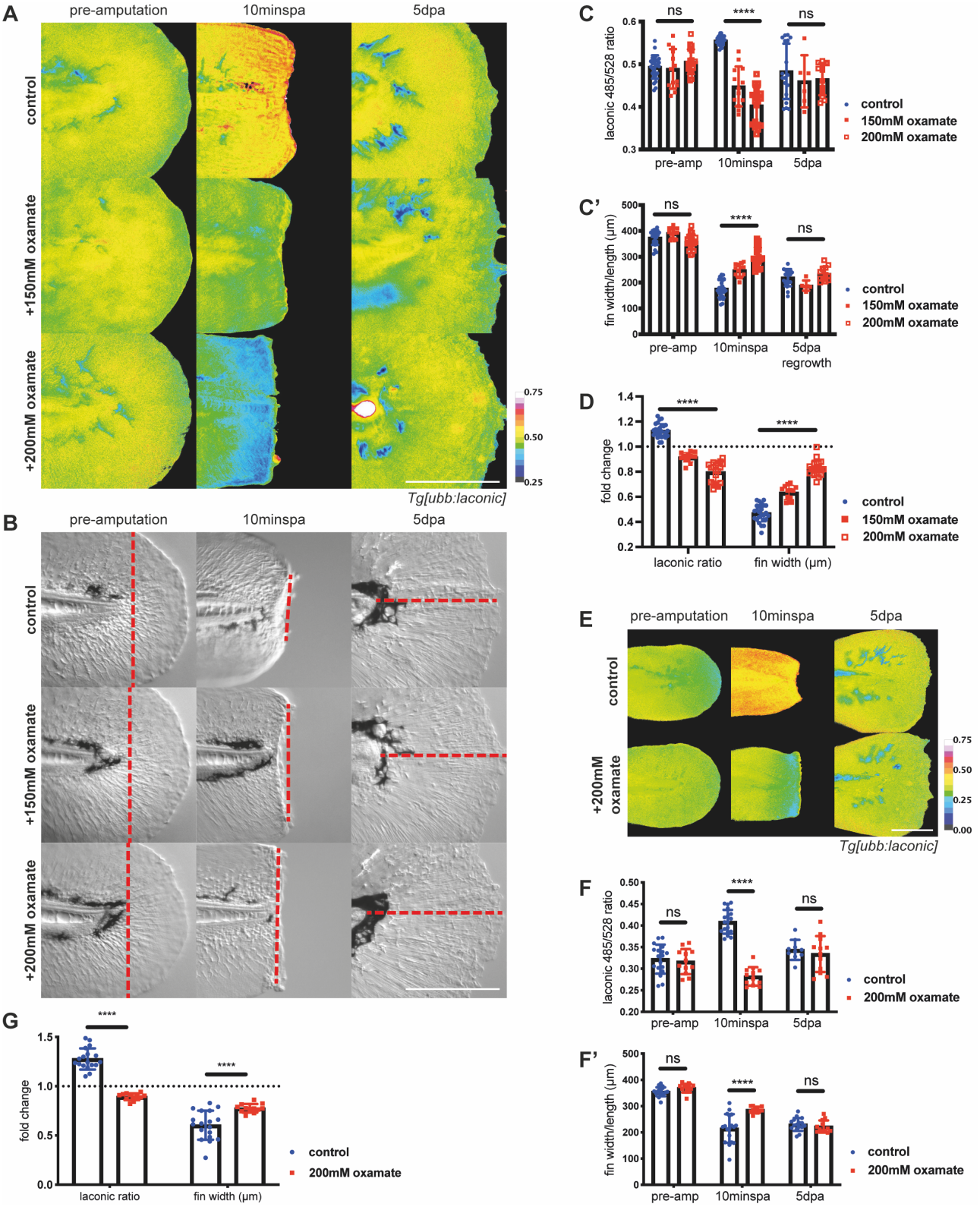

Figure 4.6. **Inhibition of lactate production during fin fold amputation.** (A-D) show data obtained with Zeiss AxioImager.M2 upright widefield microscope (20X), (E-G) show data obtained with Nikon Eclipse Ti inverted widefield microscope (20X). All scale bars represent 200μm. Differences were considered significant to * P<0.05, ** P<0.01, *** P<0.001, **** P<0.0001, and ns P≥0.05. (A) Representative transgenic ubb:laconic embryos at 48hpf imaged pre-amputation, 10 minutes post amputation with treatment with oxamate or water control, and five days post amputation, pseudocoloured to show Laconic ratio calculated by dividing the 428nm emission channel by the 485nm emission channel. (B) DIC images of representative transgenic ubb:laconic embryos as in (A) with examples of measurements (red dashed line) taken for fin width and length quantification. Pre-amputation and wound width taken to be from edge to edge of the fin fold just distal to the notochord along the amputation plane; regrowth taken from the end of the notochord to the most distal edge of the fin fold.

(continued on next page)

(*Figure 4.6. cont.)* (C) Graph showing quantification of raw Laconic ratios pre-, 10 minutes post-, and 5 days post-amputation. Two-way ANOVA to calculate significance, n=25 (control), n=13 (150mM oxamate), n=19 (200mM oxamate). (C') Graph showing measured fin widths/length in micrometres pre-, 10 minutes post-, and 5 days post-amputation. Fin length measured from the tip of the notochord to the distal edge of the fin fold. Two-way ANOVA to calculate significance, n=25 (control), n=13 (150mM oxamate), n=19 (200mM oxamate). (D) Graph showing fold change (10minspa value divided by pre-amputation value) of Laconic ratio and fin width in micrometres in the first 10 minutes of amputation with treatment with oxamate or water control. Dotted line on the Y axis marks a fold change of 1 (no change). Two-way ANOVA to calculate significance, n=25 (control), n=13 (150mM oxamate), n=19 (200mM oxamate). (E) Representative transgenic ubb:laconic embryos at 48hpf imaged pre-amputation,10 minutes post amputation with treatment with 200mM oxamate or water control, and five days post amputation, to confirm repeatability of the results seen in (A-D), pseudocoloured to show Laconic ratio calculated by dividing the 428nm emission channel by the 485nm emission channel. (F) Graph showing raw Laconic ratios pre-, 10 minutes post-, and 5 days post-amputation. Two way ANOVA to calculate significance, n=18 (control), n=18 (200mM oxamate). (F') Graph showing measured fin widths/length in micrometres pre-, 10 minutes post-, and 5 days post-amputation. Fin length measured from the tip of the notochord to the distal edge of the fin fold. Two way ANOVA to calculate significance, n=18 (control), n=18 (200mM oxamate). (G) Graph showing fold change (10minspa value divided by pre-ampuation value) of Laconic ratio and wound contraction 10 minutes post amputation. Two-way ANOVA to calculate significance, n=18 (control), n=18 (200mM oxamate).

treated amputated fins with the reversible mitochondrial inhibitor sodium azide (NaN_3), which acts on cytochrome oxidase to block the final step of oxidative phosphorylation and drive the cell towards anaerobic respiration (ie. glycolysis), or a PBS control. Furthermore, this treatment would indicate whether the process involves OXPHOS or is entirely dependent on glycolysis. Since mitochondrial inhibitors are potent and embryos do not survive prolonged treatment, I treated only until 1hpa.

I performed fin fold amputations on 2dpf *Tg[ubb:laconic]* embryos and immersed them immediately in NaN_3 treatment, finding that within 10minspa Laconic ratios were not significantly different in treated and control embryos, even if NaN_3 embryos tended to have higher levels of lactate (FIG 4.8A, B and C). Additionally, there was no difference in fin widths and wound contraction (FIG 4.8B' and C), thus a reduction of mitochondrial activity does not appear to induce accelerated wound healing or prevent actomyosin contraction. Wound widths trend slightly wider in NaN_3 treated embryos compared to controls, suggesting OXPHOS is active and possibly contributes at a low level, but is not inherent for the process. By 1hpa control embryos have reduced in Laconic ratio, while NaN_3 treated embryos continued producing lactate (FIG 4.8A and B). After washing out the drug and allowing embryos to regenerate their fin folds, I imaged both conditions and found that there was no difference in Laconic ratio or fin regrowth (defined as the distance from the tip of the notochord to the distal edge of the fin fold) five days post amputation (FIG 4.8A, B and B'). This suggests an abundance of lactate in the wound has no effect on overall regeneration, while a reduction in lactate and glycolysis activity negatively impacts early wound healing. Moreover, a requirement of OXPHOS for wound contraction is not apparent, since inhibiting the mitochondria has no consequence on amputated fin widths, suggesting the process is reliant on glycolysis.

4.3.5 Fin fold amputation with hydrogen peroxide treatment

As discussed in section 4.1.2, ROS and glycolysis appear to have the potential to be linked, with H_2O_2 acting as a regulator or activator of glycolytic activity. Therefore, I suspected an impact of H_2O_2 on the lactate production

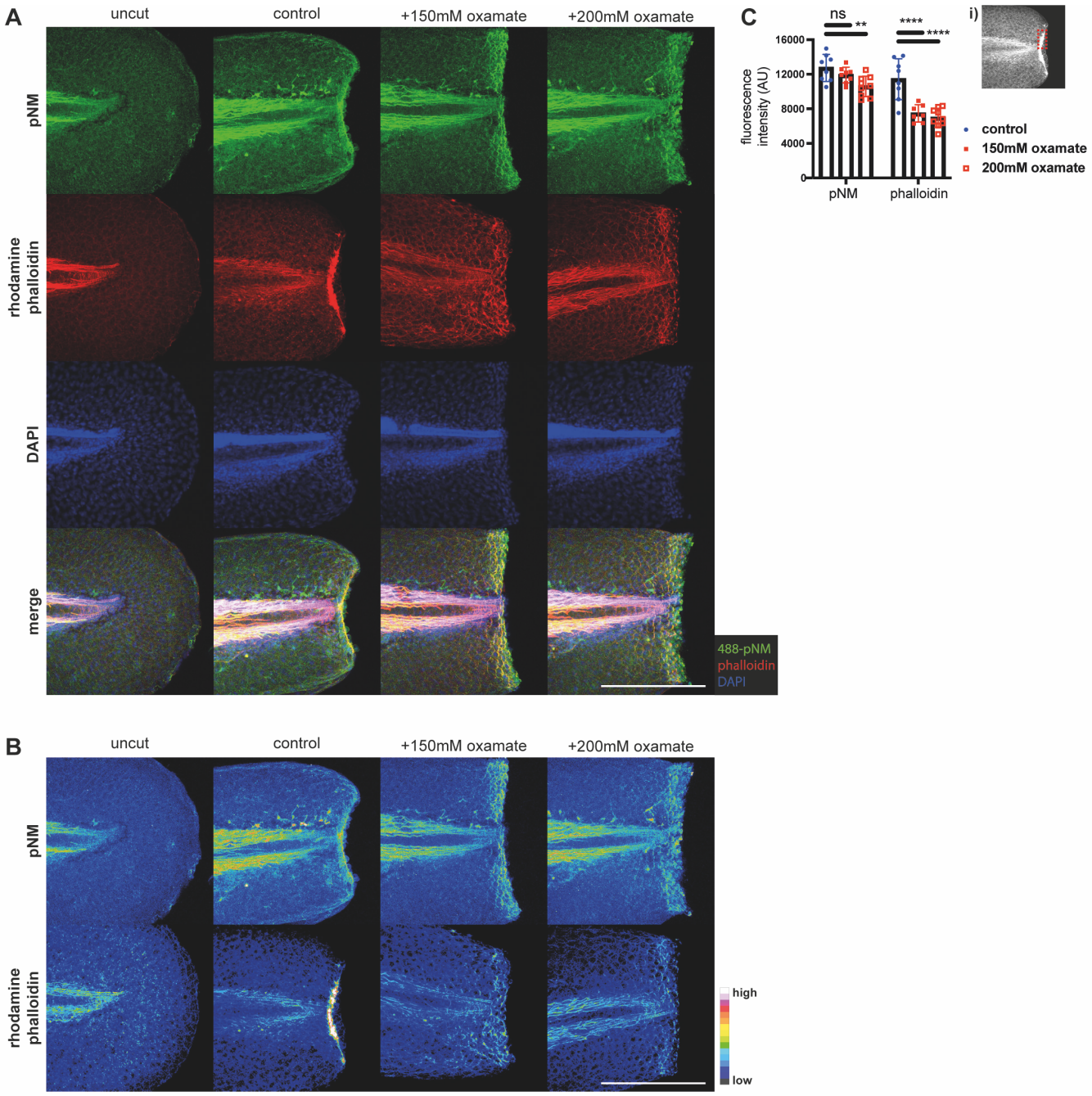

Figure 4.7. **Effect of inhibition of lactate production during fin fold amputation on the actomyosin cable involved in wound contraction.** All panels show data obtained with Zeiss LSM800 confocal microscope (20X, 2.44µm slices). All scale bars represent 200µm. (A) Maximal intensity projections of representative embryos at 48hpf fixed and stained for phospho-non muscle myosin light chain II (pNM) or actin at 10 minutes post amputation. (B) As (A), pseudocoloured to show fluorescence intensity. (C) Graphs showing quantification of fluorescence intensity at the wound border of phalloidin actin staining and immunofluorescent pNM staining. Inset (i) denotes example of region measured. Two-way ANOVAs used to calculate significance, ** $P<0.01$, **** $P<0.0001$, ns $P\geq0.05$, n=8.

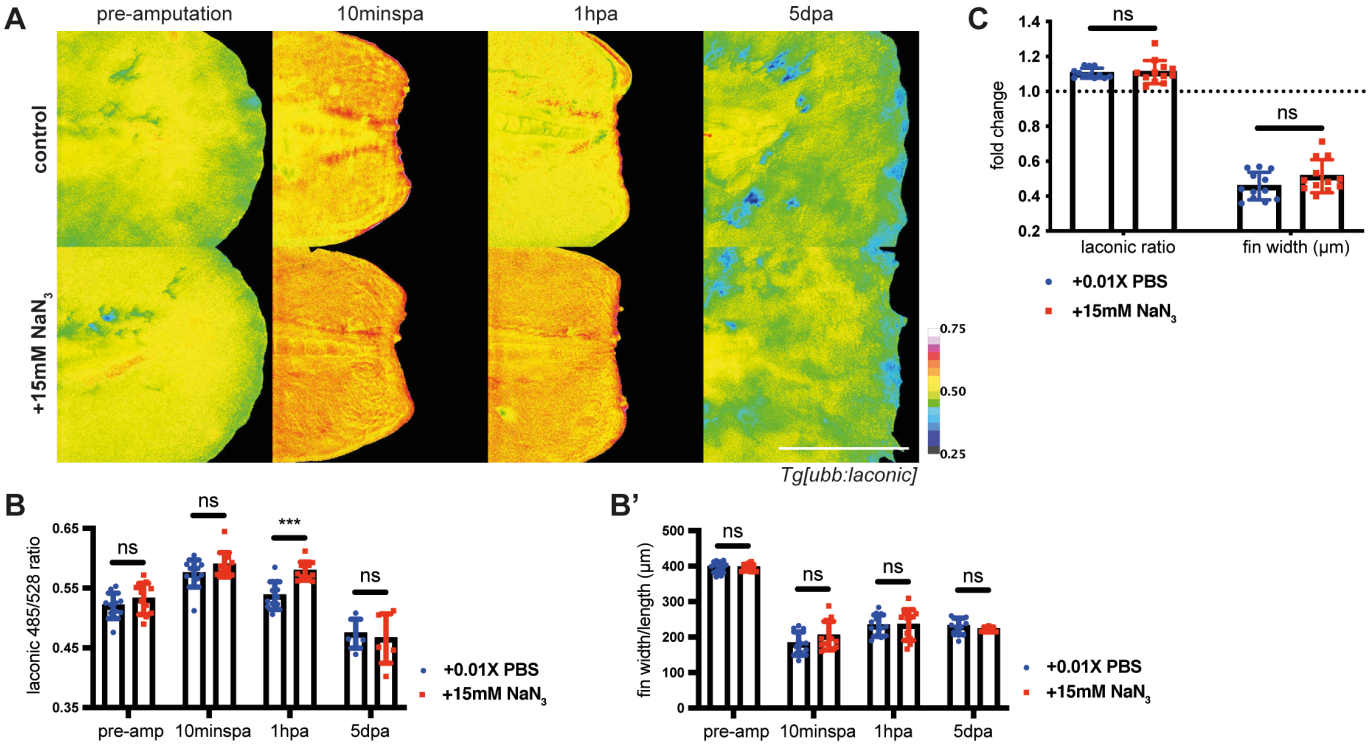

Figure 4.8. **Effect of mitochondrial inhibition and prolonged lactate production during fin fold amputation.** All panels show data obtained with Zeiss AxioImager.M2 upright widefield microscope (20X). All scale bars represent 200μm. Differences were considered significant to * P<0.05, ** P<0.01, *** P<0.001, **** P<0.0001, and ns P≥0.05. (A) Representative transgenic ubb:laconic embryos at 48hpf imaged pre-amputation, 10 minutes and 1 hour post amputation with treatment with 15mM sodium azide (NaN_3) to induce prolonged glycolysis and lactate production or PBS control, and five days post amputation, pseudocoloured to show Laconic ratio calculated by dividing the 428nm emission channel by the 485nm emission channel. (B) Graph showing quantification of raw Laconic ratios pre-, 10 minutes post-, and 5 days post-amputation. Two-way ANOVAs to calculate significance, n=12. (B') Graph showing measured fin widths/length in micrometres pre-, 10 minutes post-, and 5 days post-amputation. Fin length measured from the tip of the notochord to the distal edge of the fin fold. Two-way ANOVA to calculate significance, n=12. (C) Graph showing fold change (10minspa value divided by pre-amputation value) of Laconic ratio and fin width in micrometres in the first 10 minutes of amputation with treatment with 15mM NaN_3 or PBS control. Dotted line on the Y axis marks a fold change of 1 (no change). Two-way ANOVA to calculate significance, n=12.

during zebrafish fin fold amputation, though in which direction I was not certain due to conflicting ideas in the literature suggesting both a role for H_2O_2 in inhibiting glycolytic enzymes to drive PPP activity (Colussi et al., 2000) and stimulating glycolysis while decreasing mitochondrial activity (Shi et al., 2009; Martinez-Outschoorn et al., 2011; Molavian et al., 2016; Nulton-Persson & Szweda, 2001).

In order to assess this notion, I added 10mM H_2O_2 to freshly amputated fin folds and imaged Laconic ratio and wound contraction. I found that treatment with H_2O_2 prevented both the lactate increase within 10minspa and significant contraction of the wound border (FIG 4.9). Again, maintaining embryos in H_2O_2 was not conducive for survival, thus treatment was not continued past 1hpa. As with the experiments with lactate production inhibition and sustainment, I found the effects of H_2O_2 on regeneration were not long term, and fin folds regenerated as normal and possessed Laconic ratios not significantly different to controls at five days post amputation (FIG 4.9B and B').

Together, these data suggest H_2O_2 is able to prevent the activation of glycolysis occurring immediately post amputation, as its inhibitory action on certain glycolytic enzymes would advocate, and support my hypothesis that rapid glycolysis is necessary for wound closure by actomyosin cable contraction, but this temporary block is not important for long term regeneration.

4.3.6 Effect of inhibition of lactate production in fin fold amputation on hydrogen peroxide

H_2O_2 has been linked to regulation of glycolysis, as explored in section 4.1.2, and in the previous section I established that treatment of H_2O_2 at the time of amputation appears to reduce lactate production. To investigate the inverse situation, I performed fin fold amputations on the transgenic HyPer line and treated with oxamate, in the same manner as in section 4.3.3. I saw the significant lack of wound contraction as with the experiments with Laconic, and though H_2O_2 increase is expected and required in fin amputations (Niethammer et al., 2009; Yoo et al., 2012; Romero et al., 2018), I witnessed a significantly greater increase in HyPer ratio with oxamate treatment compared to controls (FIG 4.10). H_2O_2 produced by NADPH oxidases are important for regeneration in several instances, including zebrafish fins (Niethammer et al., 2009; Yoo et al., 2012; Romero et al., 2018), zebrafish hearts (Han et al., 2014), and *Xenopus* tails (Love et al., 2013). However, H_2O_2 is also produced within the electron transport chain of mitochondria (reviewed in Murphy, 2009), and as such could provide an indication of mitochondrial respiration. Therefore, this elevated increase in H_2O_2 I witnessed may arguably be due to the prevention of rapid glycolysis causing an increase in mitochondrial activity and OXPHOS to compensate.

4.3.7 Inhibition of glycolysis during regeneration

An up-regulation in expression of genes for glycolytic enzymes with an accompanying reduction in mitochondrial activity occurs in proliferating cardiomyocytes of regenerating zebrafish hearts (Honkoop et al., 2019), and a similar promotion of carbohydrate metabolism through glycolysis and the PPP is witnessed in *Xenopus* tail amputations (Love et al., 2014). Recently, Sinclair et al. (2020) have shown glycolysis is required for blastema formation in zebrafish larval tail amputation, fitting with my data in section 4.3.1 (FIG 4.3C.), and regeneration can be attenuated using 2-deoxy-D-glucose (2DG) (Sinclair et al., 2020), which inhibits hexokinase of the glycolysis pathway (Wick et al., 1957) (FIG 1.6G). I sought to recapitulate these results, and also investigate the impact of 2DG on fin fold amputation, in which no notochord bead is formed. In all experiments, embryos were amputated at 2dpf in 1X egg water with methylene blue supplemented with 0.04% tricaine and transferred to control, 25mM 2DG, or 10mM oxamate media within five minutes of amputation, and maintained in these solutions for 120 hours until imaged for oxamate treatment, or for 72 hours in the case of 2DG as longer treatment results in death of the embryos. I found that the concentration of 2DG used by Sinclair et al. (2020) was too high and caused 100% embryo death, and thus used a much lower dose in my experiments (25mM as opposed to 100mM, titration data not shown).

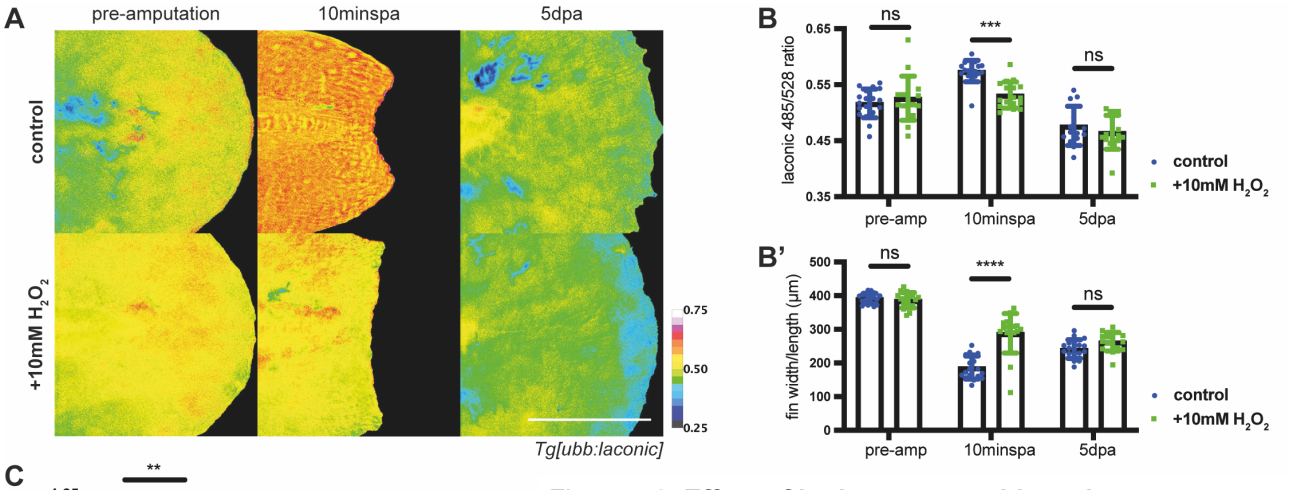

Figure 4.9. **Effect of hydrogen peroxide on lactate production during fin fold amputation.** All panels show data obtained with Zeiss AxioImager.M2 upright widefield microscope (20X). All scale bars represent 200µm. Differences were considered significant to * P<0.05, ** P<0.01, *** P<0.001, **** P<0.0001, and ns P≥0.05. (A) Representative transgenic ubb:laconic embryos at 48hpf imaged pre-amputation, 10 minutes post amputation with treatment with 10mM hydrogen peroxide (H_2O_2) or water control, and five days post amputation, pseudocoloured to show Laconic ratio calculated by dividing the 428nm emission channel by the 485nm emission channel. (B) Graph showing quantification of raw Laconic ratios pre-, 10 minutes post-, and 5 days post-amputation. Two-way ANOVA to calculate significance, n=18. (B') Graph showing quantification of measured fin widths/length in micrometres pre-, 10 minutes post-, and 5 days post-amputation. Fin length measured from the tip of the notochord to the distal edge of the fin fold. Two-way ANOVA to calculate significance, n=18. (C) Graph showing fold change (10minspa value divided by pre-amputation value) of Laconic ratio and fin width in micrometres in the first 10 minutes of amputation with treatment with 10mM H_2O_2 or water control. Dotted line on the Y axis marks a fold change of 1 (no change). Two-way ANOVA to calculate significance, n=18.

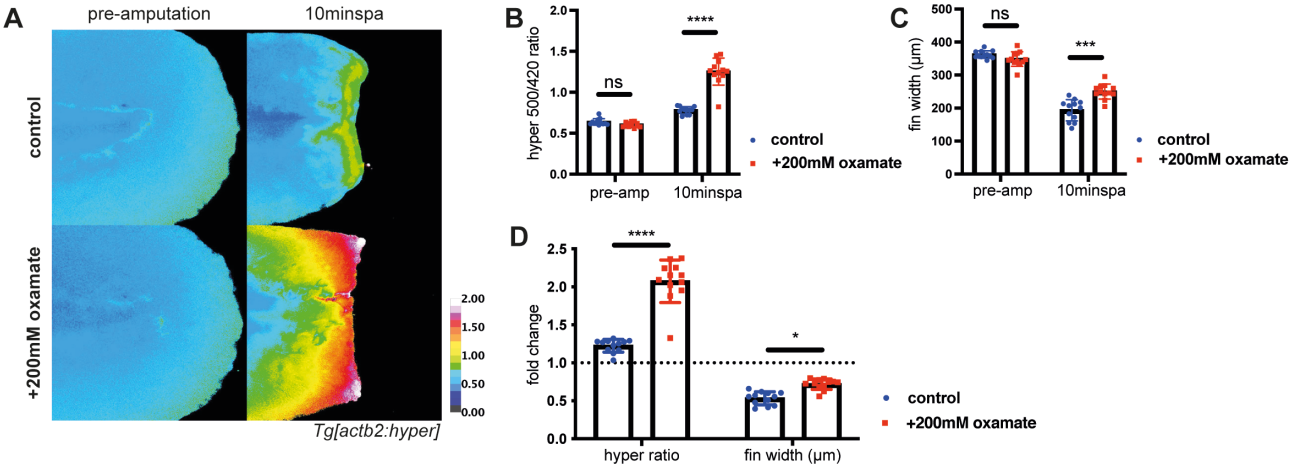

Figure 4.10. **Effect of lactate production inhibition on hydrogen peroxide levels during fin fold amputation.** All panels show data obtained with Zeiss AxioImager.M2 upright widefield microscope (20X). All scale bars represent 200µm. Differences were considered significant to * P<0.05, ** P<0.01, *** P<0.001, **** P<0.0001, and ns P≥0.05. (A) Representative transgenic actb2:hyper embryos at 48hpf imaged pre-amputation and 10 minutes post amputation with treatment with 200mM oxamate or water control, pseudocoloured to show HyPer ratio calculated by dividing the 500nm excitation channel by the 420nm excitation channel. (B) Graph showing quantification of raw HyPer ratios pre- and 10 minutes post-amputation treated with 200mM oxamate or control. Two-way ANOVAs to calculate significance, n=12. (C) Graph showing quantification of measured fin widths/regrowth in micrometres pre- and 10 minutes post-amputation treated with 200mM oxamate or water control. Two-way ANOVAs to calculate significance, n=12. (D) Graph showing fold change (10minspa value divided by pre-amputation value) of HyPer ratio and fin width in micrometres in the first 10 minutes of amputation with treatment with 200mM oxamate or water control. Dotted line on the Y axis marks a fold change of 1 (no change). Two-way ANOVA to calculate significance, n=12.

Tail amputated embryos did not regenerate when treated with 2DG, in support of the data from Sinclair et al. (2020), with a significantly shorter tail length at 120hpa. Fin fold amputations, though averaging a shorter regrowth than controls, were not significantly affected (FIG 4.11A and B). This is fitting with my expectations, in that increased Laconic ratios and therefore lactate levels are seen only in the notochord bead of tail amputations, while fin amputations lack the formation of a similar blastema-like structure and show no significant difference in Laconic ratio through the duration of regeneration, aside from the rapid burst of lactate production seen immediately post amputation during wound closure (section 4.3.1). Thus, the importance of glycolysis is likely related to the formation of the notochord bead. There was no difference between 2DG treated and control unamputated embryo fin lengths (FIG 4.11A and B), suggesting glycolysis is not imperative for normal embryo fin development.

In order to confirm the efficacy of the drug on lactate production, I measured lactate levels at 120hpa after treatment for the first 72 hours post amputation and verified that 2DG caused a significant decrease in Laconic ratio, and therefore lactate level, in both amputation conditions at 120hpa and in 7dpf unamputated controls (FIG 4.11D and E). I can therefore assert that 2DG is operating as expected to inhibit glycolysis, and the effects seen are likely due to this action.

In Chapter 3, I attempted to treat embryos with 2DG over development, but was unsuccessful. Given my hypothesis that the hydrophilic nature of the compound due to its polar hydroxyl groups (FIG) prevents its passing through the lipid membrane, I suspect that the drug enters only via the open wound following amputation, or after 5dpf in unamputated controls, at which point the larvae's mouths have formed and thus the drug can potentially enter via ingestion. Other studies have furthermore shown a need for reducing drug concentrations for use in older embryos compared to early stages (Stackley et al., 2011), so perhaps embryos become more sensitive and susceptible with age. An alternative explanation for this discrepancy may be length of treatment, as treatment during development was shorter (24 hours) than over regeneration (3-5 days). However, no matter the concentration I used during development (as high as 200mM 2DG or oxamate), I saw no effect, whereas with 24 hours treatment of 100mM 2DG in amputated 2dpf embryos resulted in death, suggesting treatment length was not a critical element.

To support the findings with 2DG, I additionally utilised oxamate, an inhibitor of LDH used previously in section 4.3.3, in a similar manner to examine whether aerobic glycolysis is important for regeneration. As mentioned in section 4.3.3, the concentration required to ablate the initial lactate increase is too high to allow embryo survival. Such a high concentration is needed most likely to allow inhibitory maximum to be reached rapidly enough to prevent the initial peak in lactate immediately following amputation, however this concentration results in embryo death within 24 hours of treatment. Hence, for experiments examining the effect of lactate production inhibition on overall regeneration, I titrated the concentration down to a low enough level that the drug was still effective, but permitted embryo survival (though at this concentration oxamate is unable to inhibit the initial contraction). A visible effect of the drug was the embryos would "twitch" instead of actively swimming as early as after 24 hours

of treatment, suggesting the fast muscle fibres used in larval swimming were not able to function ordinarily. Since the fastest contracting muscle fibres utilise glycolysis as their method of energy production (reviewed in Schiaffino & Reggiani, 2011), this is an acceptable outcome from blocking the regeneration of NAD+ for use in rapid glycolysis. Similar to the experiments with 2DG, oxamate treatment over the entirety of regeneration at this lower concentration prevented the regeneration following tail amputation, while allowing fin fold amputated larvae to reach regrowth lengths comparable to control amputees. Likewise, oxamate treated embryos showed no difference in fin lengths to unamputated controls (FIG 4.11A and C), supporting the speculation that rapid or aerobic glycolysis is not critical to the normal fin formation of the larva.

It is interesting that about 70% of oxamate treated embryos failed to form or inflate their swimbladders (data not shown). Swimbladder inflation, the final phase of swimbladder development, requires "swim-up behaviour" (Lindsey et al., 2010), in which larvae swim to the surface of the water to gulp air for initial inflation. Perhaps the lack of active swimming seen in the oxamate treated embryos resulted in the larvae being unable to swim to the water surface. Swimbladder formation also requires normal blood circulation (Winata et al., 2010), and though an aberrant heartbeat was not visually apparent in treated embryos, it is possible the drug also had some effect on the heart given just under 30% of embryos presented with heart oedemas (data not shown).

Figure 4.11D and F demonstrate the significantly reduced lactate levels in tail amputated embryos treated with 10mM oxamate from 2dpf until imaging at 120hpa to assess regeneration. I suggest the same reasons as for 2DG as to why oxamate appears to work in amputated larvae but not in treatment during early embryogenesis in 3: Metabolism in Early Zebrafish Development. However, this reduction was not seen in fin amputated or unamputated embryos, and despite significant attenuation of regeneration being seen only in tail amputations (FIG 4.11A and C), I cannot entirely rule out the possibility that lactate production does not affect fin fold regeneration, due to the failure of oxamate to reduce Laconic ratios in any condition aside from tail amputations. Potentially this suggests that, at this concentration, either a difficulty for the drug to enter the embryo through a less extreme wound or without entry via a wound entirely (less likely given the visible disturbances to the larvae), or oxamate has a weaker effect than 2DG. 2DG inhibits glycolysis itself—a much more severe action—and therefore may have a more drastic effect. Indeed, embryos survive treatment in oxamate over the full 120 hours of regeneration, whereas those in 2DG are unable to survive past 72 hours. Alternately, the lack of change may stem from an already low level of LDH activity, making the inhibition too minor to be noticeable, though the results with 2DG seem to suggest that it is at least possible to attenuate lactate levels. Oxamate is likely to deliver off-target effects, as is a concern with many chemical compounds, further supported by the observation of heart oedemas in many oxamate treated embryos, which may be the reason for needing to drastically reduce the concentration, and at this level oxamate may be considerably less effective and provides incomplete inhibition of LDH. The variability in the effects of oxamate on tail regeneration additionally suggests a lower and more erratic quality of inhibition.

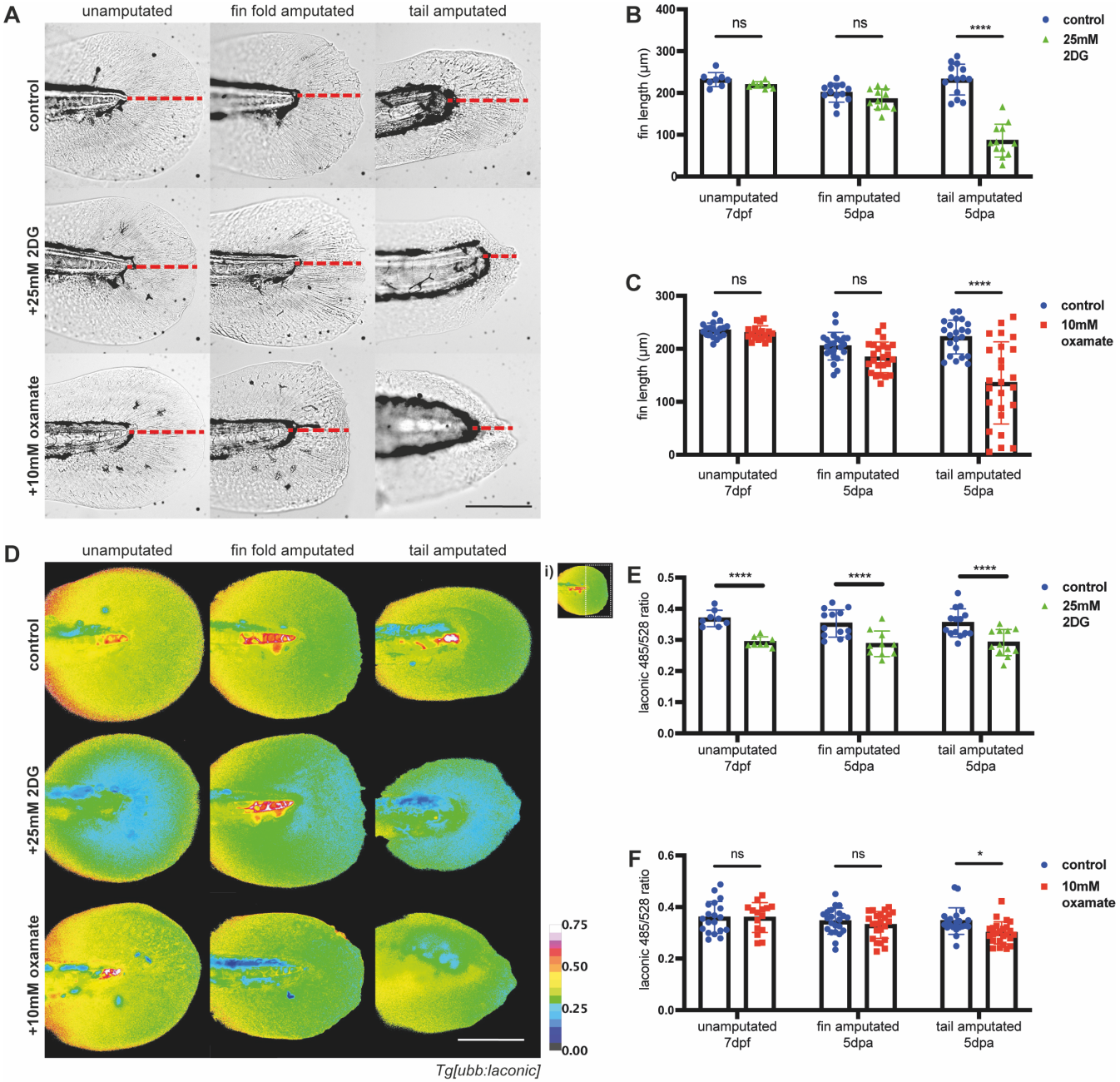

Figure 4.11. **Inhibition of lactate production over the whole of regeneration.** (A-D) show data obtained with Nikon Eclipse Ti inverted widefield microscope (20X). All scale bars represent 200µm. Differences were considered significant to * P<0.05, ** P<0.01, *** P<0.001, **** P<0.0001, and ns P ≥0.05. (A) Brightfield images of representative transgenic ubb:laconic embryos at 7dpf or 120hpa when amputated at 48hpf, treated for the first 72 hours post amputation with 25mM 2DG, for the full 120 hours of regeneration with 10mM oxamate, or with a vehicle control. Red dashed line indicates measurement taken for fin length. (B) Graph showing fin length measurements taken at 7dpf or 120hpa when amputated at 48hpf and treated for the first 72 hours post amputation with 25mM 2DG or with a vehicle control. Two-way ANOVA to calculate significance, n=13. (C) Graph showing fin length measurements taken at 7dpf or 120hpa when amputated at 48hpf and treated for the full 120 hours of regeneration with 10mM oxamate or with a vehicle control. Two-way ANOVA to calculate significance, n=25. (D) Representative transgenic ubb:laconic embryos, pseudocoloured to show Laconic ratio calculated by dividing the 428nm emission channel by the 485nm emission channel. Imaged at 7dpf or 120hpa when amputated at 48hpf, treated for the first 72 hours post amputation with 25mM 2DG, for the full 120 hours of regeneration with 10mM oxamate, or with a vehicle control. White dashed box in inset (i) shows example of area measured for quantification of Laconic ratio in (E) and (F). (E) Graph showing quantification of raw Laconic ratios at 7dpf or 120hpa when amputated at 48hpf and treated for the first 72 hours post amputation with 25mM 2DG or with a vehicle control. Two-way ANOVA to calculate significance, n=13. (F) Graph showing quantification of raw Laconic ratios at 7dpf or 120hpa when amputated at 48hpf and treated for the full 120 hours of regeneration with 10mM oxamate or with a vehicle control. Two-way ANOVA to calculate significance, n=25.

4.4 Discussion

The Warburg effect is applicable to any highly proliferative or growing system, and thus the regrowth of tissue following amputation is a logical candidate for this metabolic strategy. Indeed, as discussed in section 4.1.2, increased expression of glycolytic genes have been described in multiple regeneration models, including zebrafish larval fins (Sinclair et al., 2020), adult zebrafish hearts (Honkoop et al., 2019), and *Xenopus* tadpole tails (Love et al., 2014).

The most overt difference between fin fold and tail amputation is the formation of the "notochord bead" in the latter but not the former. Fin fold amputation, in which only epithelial tissue is lost, is more appropriate as a wound healing model, whereas tail amputation is more similar to a regenerative response, in that multiple tissues are affected and replenished, additionally including the notochord and somitic muscle (FIG 4.1A,B). Despite the formation of a supposed blastema-like structure in both models, marked by the expression of *msx* genes (Akimenko et al., 1995; Kawakami et al., 2004; Romero et al., 2018) and elevated proliferation, it appears that the larval blastema does not play a specific role in proliferation as it does in adult fin regeneration, and instead proliferation occurs in a more spatially global manner (Mateus et al., 2012; Romero et al., 2018). However, the blastema in tail amputations is partly also made up of extruded notochord cells in a visually noticeable structure, the "notochord bead". My data show no significant increase in lactate levels in fin fold regeneration via Laconic imaging during the phase in which proliferation should be significantly increased, but instead during tail regeneration in a spatially restricted manner, specifically in the notochord bead from as early as 3hpa until 48hpa. The raised lactate levels correlate temporally with the blastema, returning to control levels after 48hpa as the wound enters the third phase of regeneration, characterised by differentiation and progressive scaling back of proliferation (Kawakami et al., 2004; Mateus et al., 2012). Different signalling mechanisms have been described between fin fold and tail regeneration, for instance Hedgehog signalling is necessary for tail regeneration but is not crucial to fin fold regeneration (Romero et al., 2018). Thus, glycolysis may be involved in notochord bead formation or signalling, with lactate acting as a second messenger rather than in a Warburg-associated role to provide for proliferation, thus explaining the lack of effect on fin fold regeneration by glycolysis inhibition, despite a previously reported increase in proliferation. Regrowth in regeneration is additionally reliant on cell movement rather than solely proliferation (Poleo et al., 2001), and EMTs are required for gecko and zebrafish blastema formation (Gilbert et al., 2013; Sinclair et al., 2020). Glycolysis has been found to be an important factor for both cell motility and EMT (Shiraishi et al., 2015; Heiss et al., 2016; reviewed in Morandi et al., 2017), thus this may be an alternative purpose for metabolic reprogramming in regeneration.

It is known that the immune response utilises the Warburg effect (reviewed in E. L. Pearce & Pearce, 2013 and Palsson-McDermott & O'Neill, 2013), and attenuation of macrophages inhibits blastema formation (reviewed in Abnave & Ghigo, 2019). However, I did not witness specific cells bearing resemblance to inflammatory immune cells displaying elevated Laconic ratios. Furthermore, the immune response occurs following both fin fold and tail

amputation, but inhibition of glycolysis prevents tail regeneration alone. Thus, it is unlikely that the importance of glycolysis can be attributed to the immune response involved in wound healing.

Regardless of this disparity between the two amputation models, both consistently showed a swift and transient burst of lactate production immediately after injury. By chemically inhibiting this peak of lactate with oxamate treatment to inhibit LDH and the conversion of pyruvate to lactate, I showed this rapid glycolysis activity is likely to fuel wound contraction by actomyosin cable. Past studies have demonstrated the use of actomyosin cables in wound closures and repair (reviewed in Abreu-Blanco et al., 2012), including specifically in zebrafish larval fin amputation in which wound contraction occurs in the first phase of regeneration within the first 8minspa (Mateus et al., 2012). Actin and myosin are accumulated at the wound edge as early as 5minspa, however with oxamate treatment I detected a lack of actin at the wound border at 10minspa. Immunostainings for activated (phosphorylated) non-muscle myosin show a more diffuse localisation but significant reduction only with the highest concentration of treatment. This may be explained by the fact phosphorylation of myosin requires only a single ATP molecule per myosin, whereas contraction is the more energetically consuming process. The fastest contracting muscle fibres are purely glycolytic in their energy production, as—though unsustainable for long periods—glycolysis is able to produce ATP at a more rapid rate than OXPHOS (reviewed in Schiaffino & Reggiani, 2011). Therefore, I suspect that the increased production of lactate is indicative of NAD+ replenishment for rapid aerobic glycolysis in order to fuel actomyosin cable contraction at the wound border. I also found that mitochondrial inhibition does not disrupt wound contraction, supporting the emphasis on glycolysis within this process.

I noted that I encountered some difficulties with the pharmacological treatments: when attempting to recapitulate the results with oxamate on wound contraction, I found that no concentration of 2DG was able to prevent the increase in Laconic ratio within 10minspa. I surmised that 2DG is unable to enter the cells and reach inhibitory maximum rapidly enough, and while this is possible with oxamate, very high concentrations are required. I also suspected that, as both inhibitors are water soluble, entry into the larva occurs only via the open wound, or after 5dpf when the mouth has developed and the larvae can ingest the drug through the water, since the epidermis of water-dwelling embryos tends to be very resilient to foreign molecules in the environment.

The increased lactate level during early regeneration does not have a lasting consequence on overall regeneration, as larvae recover from both sustained and inhibited lactate production induced from amputation to 1hpa. It is likely that the process is simply delayed for one hour, and following removal of the drug the system recovers and proceeds as normal. It is only with less toxic, lower concentrations, that do not prevent wound contraction but instead impair the function of the blastema, that an effect on overall regeneration is seen, with glycolysis or lactate production inhibition reducing the length of fin regrowth.

The data obtained with SoNar is difficult to interpret, given its role in numerous reactions within the cell, and apparent balancing of production of NADH from glycolysis with either LDH or MAS activity (reviewed in Xiao et al., 2018). The initial elevated SoNar ratio in fin fold amputation, similar to that seen with Laconic, suggests an

imbalance between glycolysis and LDH or the MAS, with glycolysis proceeding more rapidly to generate an excess of NADH. This conclusion would fit with the hypothesis proposing elevated glycolysis to supply ATP for actomyosin contraction in wound closure. However, the same correspondence between SoNar and Laconic data is not evident in tail amputations. Thus, I cannot be confident that the NADH/NAD+ ratio is representing glycolysis activity in a similar model to lactate.

H_2O_2 has been linked to having important roles in both regeneration (Niethammer et al., 2009; Yoo et al., 2012; Love et al., 2013; Han et al., 2014; Romero et al., 2018) and regulating glycolysis (see section 4.1.2 for more detail). ROS is required for the formation of the notochord bead in tail amputations, with DPI treatment significantly reducing the size at 4hpa (Romero et al., 2018) and indicating H_2O_2 contributes positively to regeneration, but I found adding H_2O_2 to freshly amputated fin folds lessened the production of lactate and wound contraction. It is not known whether the lactate levels of the notochord bead are attenuated along with the size, however this may suggest different roles for H_2O_2 at these two timepoints within the regenerative response: a negative effect on wound closure, but a positive effect on blastema formation. H_2O_2 has been reported to inhibit the glycolytic enzyme glyceraldehyde-3-phosphate dehydrogenase (Colussi et al., 2000), and this inhibition of glycolysis is in fact considered promotive of the Warburg effect, in that it drives a shunt towards the PPP, which provides multiple intermediates for use in biosynthesis. The blastema is a proliferative structure and the notochord bead displays elevated lactate levels, possibly suggesting the Warburg effect and emphasis on the PPP rather than glycolysis alone, or a role for lactate as a second messenger, and thus H_2O_2 may have a positive effect in the context of the blastema, while having an inhibitory action on the rapid glycolysis required for swift actomyosin contraction.

Taken in combination, my findings advocate an importance for glycolysis at two points of regeneration. Firstly, required directly following amputation to generate energy for the actomyosin cable responsible for wound closure. Secondly, consequential only in tail amputations, required for overall regeneration and regrowth of the amputated tissue. Though the elevated lactate levels are localised to the repositioned notochord cells in the stump of the wound that contribute to the blastema, inhibition of lactate production or glycolysis does not prevent the formation of the notochord bead. This is feasibly due to the contribution of mechanical factors and pressure experienced by the cells upon amputation (Romero et al., 2018).

Future work may be directed at the blastema and the effects of H_2O_2 on glycolysis in the blastema, perhaps whether increasing ROS at the site of injury may be able to encourage blastema formation and the Warburg effect, as its inhibition appears to have a reductive effect and both H_2O_2 and up-regulation of glycolytic genes have been demonstrated to be requisite for proliferation (Yoo et al., 2012; Honkoop et al., 2019). It would also be interesting to examine the effect of glycolysis inhibition on proliferation in fin fold amputations, as glycolysis gene expression has been previously linked to proliferation in zebrafish heart regeneration (Honkoop et al., 2019) and proliferative capacity of embryonic stem cells (reviewed in Mathieu & Ruohola-Baker, 2017), and it would be worth knowing whether this association is conserved between models. If inhibition of glycolysis impacts proliferation levels in fin

fold amputation, despite my detecting no significant increase in lactate, this would suggest either an inadequate sensitivity of my lactate imaging, or perhaps a greater importance of the PPP rather than glycolysis, rendering rapid regeneration of mitochondrial-independent NAD+ unnecessary. An alternate line of investigation could aim to elucidate whether inducing glycolysis through different means can stimulate blastema formation, and if this could be applied to a traditionally non-regenerative organism to improve regenerative capacity.

References

Abnave, P., & Ghigo, E. (2019). Role of the immune system in regeneration and its dynamic interplay with adult stem cells. *Seminars in Cell & Developmental Biology*, *87*, 160–168. https://doi.org/10.1016/j.semcdb.2018.04.002

Abreu-Blanco, M. T., Watts, J. J., Verboon, J. M., & Parkhurst, S. M. (2012). Cytoskeleton responses in wound repair. *Cellular and Molecular Life Sciences : CMLS*, *69*(15), 2469–2483. https://doi.org/10.1007/s00018-012-0928-2

Akimenko, M. A., Johnson, S. L., Westerfield, M., & Ekker, M. (1995). Differential induction of four msx homeobox genes during fin development and regeneration in zebrafish. *Development (Cambridge, England)*, *121*(2), 347–357.

Alberts, B., Johnson, A., Lewis, J., Raff, M., Roberts, K., & Walter, P. (2002). Chapter 2: Cell Chemistry and Biosynthesis. In *Molecular Biology of the Cell. 4th Edition* (4 ed., Number 2). https://doi.org/https://www.ncbi.nlm.nih.gov/books/NBK26838/

Barriere, G., Fici, P., Gallerani, G., Fabbri, F., & Rigaud, M. (2015). Epithelial Mesenchymal Transition: a double-edged sword. Clinical and Translational Medicine, 4(1), 14. https://doi.org/10.1186/s40169-015-0055-4

Beck, C. W., Izpisúa Belmonte, J. C., & Christen, B. (2009). Beyond early development: Xenopus as an emerging model for the study of regenerative mechanisms. *Developmental Dynamics : an Official Publication of the American Association of Anatomists*, *238*(6), 1226–1248. https://doi.org/10.1002/dvdy.21890

Becker, T., Wullimann, M. F., Becker, C. G., Bernhardt, R. R., & Schachner, M. (1997). Axonal regrowth after spinal cord transection in adult zebrafish. *The Journal of Comparative Neurology*, *377*(4), 577–595. https://doi.org/10.1002/(sici)1096-9861(19970127)377:4<577::aid-cne8>3.0.co;2-#

Beffagna, G. (2019). Zebrafish as a Smart Model to Understand Regeneration After Heart Injury: How Fish Could Help Humans. *Frontiers in Cardiovascular Medicine*, *6*, 107. https://doi.org/10.3389/fcvm.2019.00107

Beltrami, A. P., Barlucchi, L., Torella, D., Baker, M., Limana, F., Chimenti, S., Kasahara, H., Rota, M., Musso, E., Urbanek, K., Leri, A., Kajstura, J., Nadal-Ginard, B., & Anversa, P. (2003). Adult Cardiac Stem Cells Are Multipotent and Support Myocardial Regeneration. *Cell*, *114*(6), 763–776. https://doi.org/10.1016/S0092-8674(03)00687-1

Buck, M. D., O'Sullivan, D., Klein Geltink, R. I., Curtis, J. D., Chang, C.-H., Sanin, D. E., Qiu, J., Kretz, O., Braas, D., van der Windt, G. J. W., Chen, Q., Huang, S. C.-C., O'Neill, C. M., Edelson, B. T., Pearce, E. J., Sesaki, H., Huber, T. B., Rambold, A. S., & Pearce, E. L. (2016). Mitochondrial Dynamics Controls T Cell Fate through Metabolic Programming. *Cell*, *166*(1), 63–76. https://doi.org/10.1016/j.cell.2016.05.035

Cantó, C., Menzies, K. J., & Auwerx, J. (2015). NAD(+) Metabolism and the Control of Energy Homeostasis: A Balancing Act between Mitochondria and the Nucleus. *Cell Metabolism*, *22*(1), 31–53. https://doi.org/10.1016/j.cmet.2015.05.023

Clark, L. D., Clark, R. K., & Heber-Katz, E. (1998). A new murine model for mammalian wound repair and regeneration. *Clinical Immunology and Immunopathology*, *88*(1), 35–45. https://doi.org/10.1006/clin.1998.4519

Colussi, C., Albertini, M. C., Coppola, S., Rovidati, S., Galli, F., & Ghibelli, L. (2000). H2O2-induced block of glycolysis as an active ADP-ribosylation reaction protecting cells from apoptosis. *FASEB Journal : Official Publication of the Federation of American Societies for Experimental Biology*, *14*(14), 2266–2276. https://doi.org/10.1096/fj.00-0074com

Cunliffe, V. T. (2003). Zebrafish: A Practical Approach. Edited by C. NÜSSLEIN-VOLHARD and R. DAHM. Oxford University Press. 2002. 322 pages. ISBN 0 19 963808 X. Price £40.00 (paperback). ISBN 0 19 963809 8. Price £80.00 (hardback). *Genetical Research*, *82*(1), 79–79.

de Oliveira, S., López-Muñoz, A., Candel, S., Pelegrín, P., Calado, Â., & Mulero, V. (2014). ATP modulates acute inflammation in vivo through dual oxidase 1-derived H2O2 production and NF-κB activation. *Journal of Immunology (Baltimore, Md. : 1950)*, *192*(12), 5710–5719. https://doi.org/10.4049/jimmunol.1302902

Diep, C. Q., Ma, D., Deo, R. C., Holm, T. M., Naylor, R. W., Arora, N., Wingert, R. A., Bollig, F., Djordjevic, G., Lichman, B., Zhu, H., Ikenaga, T., Ono, F., Englert, C., Cowan, C. A., Hukriede, N. A., Handin, R. I., & Davidson, A. J. (2011). Identification of adult nephron progenitors capable of kidney regeneration in zebrafish. *Nature*, *470*(7332), 95–100. https://doi.org/10.1038/nature09669

Ferreira, F., Raghunathan, V., Luxardi, G., Zhu, K., & Zhao, M. (2018). Early redox activities modulate Xenopus tail regeneration. *Nature Communications*, *9*(1), 4296–15. https://doi.org/10.1038/s41467-018-06614-2

Fiske, B. P., & Vander Heiden, M. G. (2012, August). Seeing the Warburg effect in the developing retina. *Nature Cell Biology*, *14*(8), 790–791. https://doi.org/10.1038/ncb2554

Folmes, C. D. L., Nelson, T. J., Martinez-Fernandez, A., Arrell, D. K., Lindor, J. Z., Dzeja, P. P., Ikeda, Y., Perez-Terzic, C., & Terzic, A. (2011). Somatic oxidative bioenergetics transitions into pluripotency-dependent glycolysis to facilitate nuclear reprogramming. *Cell Metabolism*, *14*(2), 264–271. https://doi.org/10.1016/j.cmet.2011.06.011

Gilbert, R. W. D., Vickaryous, M. K., & Viloria-Petit, A. M. (2013). Characterization of TGFβ signaling during tail regeneration in the leopard Gecko (Eublepharis macularius). *Developmental Dynamics : an Official Publication of the American Association of Anatomists*, *242*(7), 886–896. https://doi.org/10.1002/dvdy.23977

Haj Baddar, Al, N. W., Chithrala, A., & Voss, S. R. (2019). Amputation-induced reactive oxygen species signaling is required for axolotl tail regeneration. *Developmental Dynamics : an Official Publication of the American Association of Anatomists*, *248*(2), 189–196. https://doi.org/10.1002/dvdy.5

Han, P., Zhou, X.-H., Chang, N., Xiao, C.-L., Yan, S., Ren, H., Yang, X.-Z., Zhang, M.-L., Wu, Q., Tang, B., Diao, J.-P., Zhu, X., Zhang, C., Li, C.-Y., Cheng, H., & Xiong, J.-W. (2014). Hydrogen peroxide primes heart regeneration with a derepression mechanism. *Cell Research*, *24*(9), 1091–1107. https://doi.org/10.1038/cr.2014.108

Heiss, E. H., Schachner, D., Donati, M., Grojer, C. S., & Dirsch, V. M. (2016). Increased aerobic glycolysis is important for the motility of activated VSMC and inhibited by indirubin-3'-monoxime. *Vascular Pharmacology*, *83*, 47–56. https://doi.org/10.1016/j.vph.2016.05.002

Honkoop, H., de Bakker, D. E., Aharonov, A., Kruse, F., Shakked, A., Nguyen, P. D., de Heus, C., Garric, L., Muraro, M. J., Shoffner, A., Tessadori, F., Peterson, J. C., Noort, W., Bertozzi, A., Weidinger, G., Posthuma, G., Grün, D., van der Laarse, W. J., Klumperman, J., et al. (2019). Single-cell analysis uncovers that metabolic reprogramming by ErbB2 signaling is essential for cardiomyocyte proliferation in the regenerating heart. *eLife*, *8*, 98. https://doi.org/10.7554/eLife.50163

Houghton, F. D., Thompson, J. G., Kennedy, C. J., & Leese, H. J. (1996). Oxygen consumption and energy metabolism of the early mouse embryo. *Molecular Reproduction and Development*, *44*(4), 476–485. https://doi.org/10.1002/(SICI)1098-2795(199608)44:4<476::AID-MRD7>3.0.CO;2-I

Howe, K., Clark, M. D., Torroja, C. F., Torrance, J., Berthelot, C., Muffato, M., Collins, J. E., Humphray, S., McLaren, K., Matthews, L., McLaren, S., Sealy, I., Caccamo, M., Churcher, C., Scott, C., Barrett, J. C., Koch, R., Rauch, G.-J., White, S., et al. (2013). The zebrafish reference genome sequence and its relationship to the human genome. *Nature*, *496*(7446), 498–503. https://doi.org/10.1038/nature12111

Kawai, T., & Akira, S. (2007). Signaling to NF-kappaB by Toll-like receptors. *Trends in Molecular Medicine*, *13*(11), 460–469. https://doi.org/10.1016/j.molmed.2007.09.002

Kawakami, A., Fukazawa, T., & Takeda, H. (2004). Early fin primordia of zebrafish larvae regenerate by a similar growth control mechanism with adult regeneration. 231(4), 693–699. https://doi.org/10.1002/dvdy.20181

Kimmel, C. B., Ballard, W. W., Kimmel, S. R., Ullmann, B., & Schilling, T. F. (1995). Stages of embryonic development of the zebrafish. *Developmental Dynamics, 203*(3), 253–310. https://doi.org/10.1002/aja.1002030302

Kondaveeti, Y., Guttilla Reed, I. K., & White, B. A. (2015). Epithelial-mesenchymal transition induces similar metabolic alterations in two independent breast cancer cell lines. *Cancer Letters*, *364*(1), 44–58. https://doi.org/10.1016/j.canlet.2015.04.025

Kondoh, H., Lleonart, M. E., Nakashima, Y., Yokode, M., Tanaka, M., Bernard, D., Gil, J., & Beach, D. (2007). A high glycolytic flux supports the proliferative potential of murine embryonic stem cells. *Antioxidants & Redox Signaling*, *9*(3), 293–299. https://doi.org/10.1089/ars.2006.1467

Kroehne, V., Freudenreich, D., Hans, S., Kaslin, J., & Brand, M. (2011). Regeneration of the adult zebrafish brain from neurogenic radial glia-type progenitors. *Development (Cambridge, England)*, *138*(22), 4831–4841. https://doi.org/10.1242/dev.072587

Lee, L. P., Lau, P. Y., & Chan, C. W. (1995). A simple and efficient treatment for fingertip injuries. *Journal of Hand Surgery (Edinburgh, Scotland)*, *20*(1), 63–71. https://doi.org/10.1016/s0266-7681(05)80019-1

Lee, S. Y., Jeon, H. M., Ju, M. K., Jeong, E. K., Kim, C. H., Yoo, M.-A., Park, H. G., Han, S. I., & Kang, H. S. (2015). Dlx-2 is implicated in TGF-β- and Wnt-induced epithelial-mesenchymal, glycolytic switch, and mitochondrial repression by Snail activation. *International Journal of Oncology*, *46*(4), 1768–1780. https://doi.org/10.3892/ijo.2015.2874

Leferovich, J. M., Bedelbaeva, K., Samulewicz, S., Zhang, X. M., Zwas, D., Lankford, E. B., & Heber-Katz, E. (2001). Heart regeneration in adult MRL mice. *Proceedings of the National Academy of Sciences of the United States of America*, *98*(17), 9830–9835. https://doi.org/10.1073/pnas.181329398

Lindsey, B. W., Smith, F. M., & Croll, R. P. (2010). From inflation to flotation: contribution of the swimbladder to whole-body density and swimming depth during development of the zebrafish (Danio rerio). *Zebrafish*, *7*(1), 85–96. https://doi.org/10.1089/zeb.2009.0616

Love, N. R., Chen, Y., Ishibashi, S., Kritsiligkou, P., Lea, R., Koh, Y., Gallop, J. L., Dorey, K., & Amaya, E. (2013). Amputation-induced reactive oxygen species are required for successful Xenopus tadpole tail regeneration. *Nature Cell Biology*, *15*(2), 222–228. https://doi.org/10.1038/ncb2659

Love, N. R., Ziegler, M., Chen, Y., & Amaya, E. (2014). Carbohydrate metabolism during vertebrate appendage regeneration: what is its role? How is it regulated?: A postulation that regenerating vertebrate appendages facilitate glycolytic and pentose phosphate pathways to fuel macromolecule biosynthesis. *BioEssays*, *36*(1), 27–33. https://doi.org/10.1002/bies.201300110

Lunt, S. Y., & Vander Heiden, M. G. (2011). Aerobic glycolysis: meeting the metabolic requirements of cell proliferation. *Annual Review of Cell and Developmental Biology*, *27*(1), 441–464. https://doi.org/10.1146/annurev-cellbio-092910-154237

Martinez-Outschoorn, U. E., Lin, Z., Trimmer, C., Flomenberg, N., Wang, C., Pavlides, S., Pestell, R. G., Howell, A., Sotgia, F., & Lisanti, M. P. (2011). Cancer cells metabolically "fertilize" the tumor microenvironment with hydrogen peroxide, driving the Warburg effect: implications for PET imaging of human tumors. *Cell Cycle (Georgetown, Tex.)*, *10*(15), 2504–2520. https://doi.org/10.4161/cc.10.15.16585

Mateus, R., Pereira, T., Sousa, S., de Lima, J. E., Pascoal, S., Saúde, L., & Jacinto, A. (2012). In vivo cell and tissue dynamics underlying zebrafish fin fold regeneration. *PLoS ONE*, *7*(12), e51766. https://doi.org/10.1371/journal.pone.0051766

Mathieu, J., & Ruohola-Baker, H. (2017). Metabolic remodeling during the loss and acquisition of pluripotency. *Development (Cambridge, England)*, *144*(4), 541–551. https://doi.org/10.1242/dev.128389

Molavian, H. R., Kohandel, M., & Sivaloganathan, S. (2016). High Concentrations of H2O2 Make Aerobic Glycolysis Energetically More Favorable for Cellular Respiration. *Frontiers in Physiology*, *7*, 362. https://doi.org/10.3389/fphys.2016.00362

Morandi, A., Taddei, M. L., Chiarugi, P., & Giannoni, E. (2017). Targeting the Metabolic Reprogramming That Controls Epithelial-to-Mesenchymal Transition in Aggressive Tumors. *Frontiers in Oncology*, *7*(6), 40. https://doi.org/10.3389/fonc.2017.00040

Morgan, T. H. (1900). Regeneration in teleosts. *Archiv Für Mikroskopische Anatomie*, *10*(1), 120–134. https://doi.org/https://doi.org/10.1007/BF02156348

Movafagh, S., Crook, S., & Vo, K. (2015). Regulation of hypoxia-inducible factor-1a by reactive oxygen species: new developments in an old debate. *Journal of Cellular Biochemistry*, *116*(5), 696–703. https://doi.org/10.1002/jcb.25074

Murphy, M. P. (2009). How mitochondria produce reactive oxygen species. *The Biochemical Journal*, *417*(1), 1–13.

Naviaux, R. K., Le, T. P., Bedelbaeva, K., Leferovich, J., Gourevitch, D., Sachadyn, P., Zhang, X.-M., Clark, L., & Heber-Katz, E. (2009). Retained features of embryonic metabolism in the adult MRL mouse. *Molecular Genetics and Metabolism*, *96*(3), 133–144. https://doi.org/10.1016/j.ymgme.2008.11.164

Niethammer, P., Grabher, C., Look, A. T., & Mitchison, T. J. (2009). A tissue-scale gradient of hydrogen peroxide mediates rapid wound detection in zebrafish. *Nature*, *459*(7249), 996–999. https://doi.org/10.1038/nature08119

Nulton-Persson, A. C., & Szweda, L. I. (2001). Modulation of mitochondrial function by hydrogen peroxide. *The Journal of Biological Chemistry*, *276*(26), 23357–23361. https://doi.org/10.1074/jbc.M100320200

Palsson-McDermott, E. M., & O'Neill, L. A. J. (2013). The Warburg effect then and now: From cancer to inflammatory diseases. *BioEssays*, *35*(11), 965–973. https://doi.org/10.1002/bies.201300084

Pearce, E. L., & Pearce, E. J. (2013). Metabolic Pathways in Immune Cell Activation and Quiescence. *Immunity*, *38*(4), 633–643. https://doi.org/10.1016/j.immuni.2013.04.005

Poleo, G., Brown, C. W., Laforest, L., & Akimenko, M. A. (2001). Cell proliferation and movement during early fin regeneration in zebrafish. *Developmental Dynamics : an Official Publication of the American Association of Anatomists*, *221*(4), 380–390. https://doi.org/10.1002/dvdy.1152

Poss, K. D., Keating, M. T., & Nechiporuk, A. (2003). *Tales of regeneration in zebrafish*. *226*(2), 202–210. https://doi.org/10.1002/dvdy.10220

Poss, K. D., Wilson, L. G., & Keating, M. T. (2002). Heart regeneration in zebrafish. *Science*, *298*(5601), 2188–2190. https://doi.org/10.1126/science.1077857

Razzell, W., Evans, I. R., Martin, P., & Wood, W. (2013). Calcium flashes orchestrate the wound inflammatory response through DUOX activation and hydrogen peroxide release. *Current Biology : CB*, *23*(5), 424–429. https://doi.org/10.1016/j.cub.2013.01.058

Rieger, S., & Sagasti, A. (2011). Hydrogen peroxide promotes injury-induced peripheral sensory axon regeneration in the zebrafish skin. *PLoS Biology*, *9*(5), e1000621. https://doi.org/10.1371/journal.pbio.1000621

Romero, M. M. G., McCathie, G., Jankun, P., & Roehl, H. H. (2018). Damage-induced reactive oxygen species enable zebrafish tail regeneration by repositioning of Hedgehog expressing cells. *Nature Communications*, *9*(1), 4010–4011. https://doi.org/10.1038/s41467-018-06460-2

San Martín, A., Ceballo, S., Ruminot, I., Lerchundi, R., Frommer, W. B., & Barros, L. F. (2013). A genetically encoded FRET lactate sensor and its use to detect the Warburg effect in single cancer cells. *PLoS ONE*, *8*(2), e57712. https://doi.org/10.1371/journal.pone.0057712

Schiaffino, S., & Reggiani, C. (2011). Fiber types in mammalian skeletal muscles. *Physiological Reviews*, *91*(4), 1447–1531. https://doi.org/10.1152/physrev.00031.2010

Shi, D.-Y., Xie, F.-Z., Zhai, C., Stern, J. S., Liu, Y., & Liu, S.-L. (2009). The role of cellular oxidative stress in regulating glycolysis energy metabolism in hepatoma cells. *Molecular Cancer*, *8*(1), 32–15. https://doi.org/10.1186/1476-4598-8-32

Shiraishi, T., Verdone, J. E., Huang, J., Kahlert, U. D., Hernandez, J. R., Torga, G., Zarif, J. C., Epstein, T., Gatenby, R., McCartney, A., Elisseeff, J. H., Mooney, S. M., An, S. S., & Pienta, K. J. (2015). Glycolysis is the primary bioenergetic pathway for cell motility and cytoskeletal remodeling in human prostate and breast cancer cells. *Oncotarget*, *6*(1), 130–143. https://doi.org/10.18632/oncotarget.2766

Sinclair, J. W., Hoying, D. R., Bresciani, E., Nogare, D. D., Needle, C. D., Wu, W., Bishop, K., Elkahloun, A. G., Chitnis, A., Liu, P., & Burgess, S. M. (2020). A metabolic shift to glycolysis promotes zebrafish tail regeneration through TGF–β dependent dedifferentiation of notochord cells to form the blastema. *bioRxiv*, *21*(1), 2020.03.03.975318. https://doi.org/10.1101/2020.03.03.975318

Stackley, K. D., Beeson, C. C., Rahn, J. J., & Chan, S. S. L. (2011). Bioenergetic profiling of zebrafish embryonic development. *PLoS ONE*, *6*(9), e25652. https://doi.org/10.1371/journal.pone.0025652

Vidal, P., & Dickson, M. G. (1993). Regeneration of the distal phalanx. A case report. *Journal of Hand Surgery (Edinburgh, Scotland)*, *18*(2), 230–233. https://doi.org/10.1016/0266-7681(93)90116-w

Vihtelic, T. S., & Hyde, D. R. (2000). Light-induced rod and cone cell death and regeneration in the adult albino zebrafish (Danio rerio) retina. *Journal of Neurobiology*, *44*(3), 289–307. https://doi.org/10.1002/1097-4695(20000905)44:3<289::aid-neu1>3.0.co;2-h

Wang, Y., & Hekimi, S. (2015). Mitochondrial dysfunction and longevity in animals: Untangling the knot. *Science*, *350*(6265), 1204–1207. https://doi.org/10.1126/science.aac4357

Warburg, O. (1925). The Metabolism of Carcinoma Cells. *The Journal of Cancer Research*, *9*(1), 148–163. https://doi.org/10.1158/jcr.1925.148

Wick, A. N., Drury, D. R., Nakada, H. I., & Wolfe, J. B. (1957). Localization of the primary metabolic block produced by 2-deoxyglucose. *The Journal of Biological Chemistry*, *224*(2), 963–969.

Winata, C. L., Korzh, S., Kondrychyn, I., Korzh, V., & Gong, Z. (2010). The role of vasculature and blood circulation in zebrafish swimbladder development. *BMC Developmental Biology*, *10*(1), 3–9. https://doi.org/10.1186/1471-213X-10-3

Xiao, W., Wang, R.-S., Handy, D. E., & Loscalzo, J. (2018). NAD(H) and NADP(H) Redox Couples and Cellular Energy Metabolism. *Antioxidants & Redox Signaling*, *28*(3), 251–272. https://doi.org/10.1089/ars.2017.7216

Yoo, S. K., Freisinger, C. M., LeBert, D. C., & Huttenlocher, A. (2012). Early redox, Src family kinase, and calcium signaling integrate wound responses and tissue regeneration in zebrafish. *The Journal of Cell Biology*, *199*(2), 225–234. https://doi.org/10.1083/jcb.201203154

Zhao, Y., Wang, A., Zou, Y., Su, N., Loscalzo, J., & Yang, Y. (2016). In vivo monitoring of cellular energy metabolism using SoNar, a highly responsive sensor for NAD + /NADH redox state. *Nature Protocols*, *11*(8), 1345–1359. https://doi.org/10.1038/nprot.2016.074

Zheng, X., Boyer, L., Jin, M., Mertens, J., Kim, Y., Ma, L., Hamm, M., Gage, F. H., & Hunter, T. (2016). Metabolic reprogramming during neuronal differentiation from aerobic glycolysis to neuronal oxidative phosphorylation. 5, 859. https://doi.org/10.7554/eLife.13374

Zhou, M., Zhao, Y., Ding, Y., Liu, H., Liu, Z., Fodstad, O., Riker, A. I., Kamarajugadda, S., Lu, J., Owen, L. B., Ledoux, S. P., & Tan, M. (2010). Warburg effect in chemosensitivity: targeting lactate dehydrogenase-A re-sensitizes taxol-resistant cancer cells to taxol. *Molecular Cancer*, *9*(1), 33–12. https://doi.org/10.1186/1476-4598-9-33

5: Metabolism in the *hai1a* Mutant as a Chronic Epithelial Wound

Abstract

Chronic and unhealing wounds are an aspect of modern medicine that remain to be addressed. Diabetic patients commonly suffer from chronic wounds such as foot ulcers, and cancer has long been likened to a wound that is unable to heal. Understanding the molecular biology underlying these processes could provide insight for improving the current therapies available in modern medicine, and it is becoming increasingly apparent that metabolism plays an important role in both cancer and wound healing, for example hydrogen peroxide (H_2O_2) as a attractant for neutrophils in the immune response and a metabolic switch to glycolysis. In this study I utilise the zebrafish *hai1a* mutant and propose it as a model for unhealing wounds, showing it possesses similarities consistent with those seen in cancer and wound healing via live imaging of genetically encoded biosensors and fluorescent probes, and the employment of chemical inhibitors. Previous work has demonstrated the mutant to be a result of unrestricted Matriptase1a activity, which causes keratinocyte motility in a partial epithelial to mesenchymal transition and a sterile inflammatory response. I demonstrate that neutrophils are recruited due to release of H_2O_2, the source of which is the enzyme dual oxidase (DUOX) when activated by calcium signalling, as occurs in wound healing. I further establish that abolition of either the calcium release or production of H_2O_2 by chemical inhibition of IP_3 receptors or DUOX, respectively, is sufficient to rescue the inflammation phenotype but does not affect the loss of epithelial integrity. I instead determine the epithelial motility to be a function of elevated protein kinase C signalling, which has been also linked to cancer tumourigenesis and metastasis. Looking further into the potential aberrance in metabolism, it appears that the mutant displays aerobic glycolysis, a metabolic strategy commonly taken by cancer cells. From this data I conclude that the zebrafish *hai1a* mutant is a promising model for use into further elucidating the molecular pathways that may prove valuable targets for treating chronic wounds or in cancer therapies.

5.1 Introduction

The *hai1a* gene encodes an inhibitor for the serine protease Matriptase1a. Matriptase is membrane-bound and expressed in a variety of epithelial cells (Oberst et al., 2003), with its over-expression implicated in the progression and metastasis of several cancer types (reviewed in Martin & List, 2019). Existing work suggests the oncogenic activity of Matriptase is prevented by *Hai1a*, which inhibits Matriptase1a from cleaving and activating the G-protein coupled transmembrane protein protease activated receptor 2 (Par2), leading to activation of downstream targets such as extracellular signal-regulated kinase (ERK) and protein kinase C (PKC) (Sales et al., 2015; Schepis et

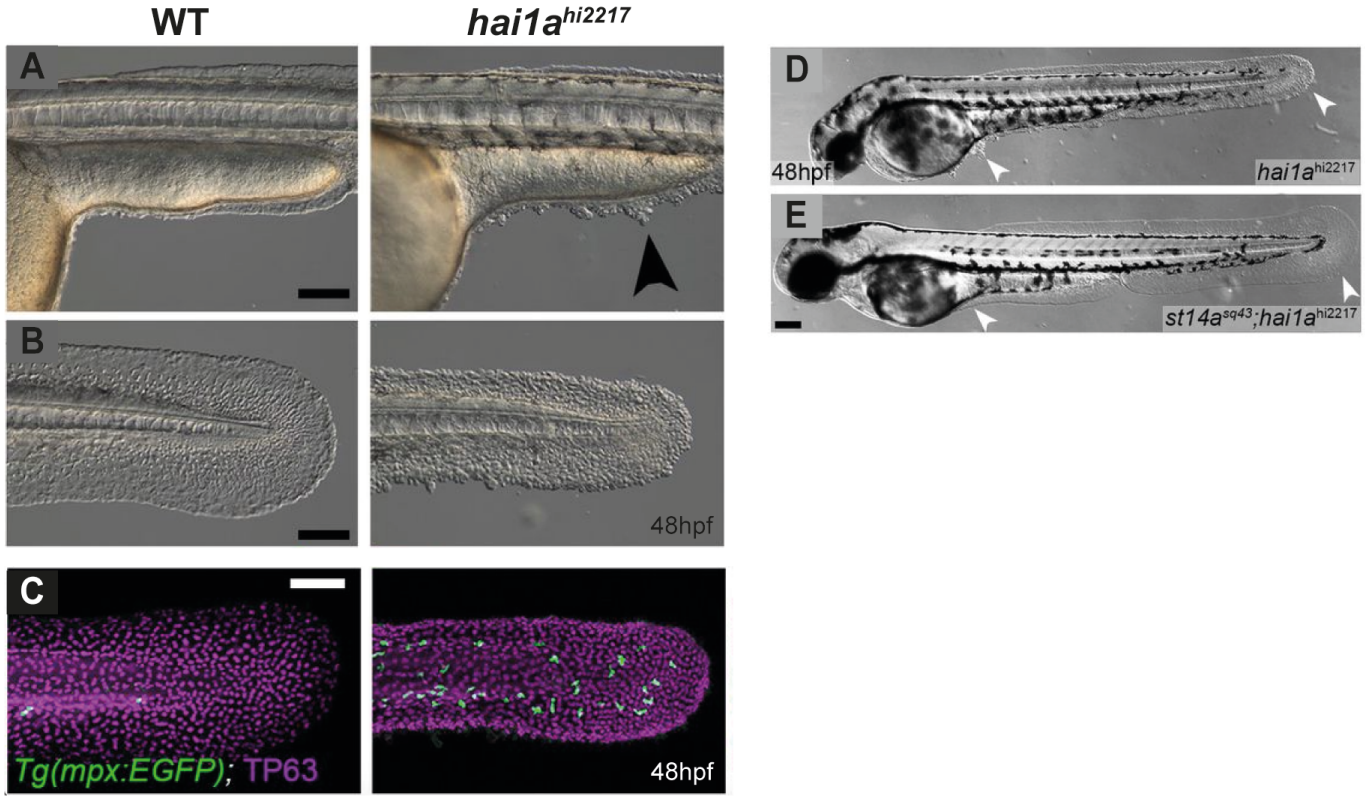

Figure 5.1. **The zebrafish *hai1a* phenotype.** All scale bars represent 100μM. (A-B) DIC images of epidermal aggregates (black arrowhead) at the trunk (A) and fin fold (B) areas of the mutant compared to wild type controls, 48hpf. (C) 24hpf Tg[mpx:EGFP] embryos immunostained for basal keratinocytes (TP63, magenta) and eGFP (green). (D-E) DIC images of 48hpf hai1a mutant compared with hai1a (D) and matriptase1a double mutant (E), showing rescue of epidermal aggregate phenotype (white arrowheads). (A-C) adapted from Ma et al., 2021. Figure 5, (D-E) adapted from Ma et al., 2021. Figure 3.

al., 2018). Par2 has been shown to be involved in the metastasis of ovarian cancer cells (Jiang et al., 2021), and higher Matriptase:Hai1 ratios are displayed in tumours (reviewed in Martin & List, 2019), with *matriptase1a* over-expression in mouse keratinocytes causing carcinoma (List et al., 2005). Cancer cells are well documented for exhibiting disrupted metabolism, including the Warburg effect (DeBerardinis & Chandel, 2016), thus presenting the zebrafish orthologue *hai1a* mutant as an interesting study.

5.1.1 The zebrafish *hai1a* mutant phenotype

The zebrafish *hai1a* mutant was discovered in a large scale mutagenesis screen (Amsterdam et al., 1999). Mutation in this gene causes a visible epidermal phenotype in zebrafish embryos, in which basal keratinocytes appear to take on mesenchymal-like characteristics and increase in motility, forming aggregates on the skin surface (FIG 5.1A,B) as early as 20hpf, and displaying elevated levels of proliferation after 48hpf (Carney et al., 2007). The compromised integrity of the epidermis is a result of a partial epithelial to mesenchymal transition (EMT) (Carney et al., 2007), bearing a striking similarity to cancer and metastasis. A metabolic switch to glycolysis is involved in EMT (reviewed in Morandi et al., 2017), suggesting an up-regulation of glycolytic metabolism may be occurring in the mutant.

In addition to an epidermal motility phenotype, the zebrafish *hai1a* mutation also displays a sterile immune response (Mathias et al., 2007) (FIG 5.1C), characteristic of over-activity of Matriptase and Par2 (Heuberger & Schuepbach, 2019). Indeed, both the epidermal and inflammation phenotypes can be rescued by knockdown of matriptase expression (Carney et al., 2007; Mathias et al., 2007) (FIG 5.1D,E), suggesting conservation of the pathway. Early inflammation, a hallmark of wound healing, with a later increase in proliferation is comparable to the phases of regeneration (FIG 4.1D), thus posing the possibility for using the mutant as a model for chronic, unhealing wounds.

5.1.2 Chronic wounds and metabolism

Humans are incapable of scarless wound healing or regenerating tissues following a loss such as amputation. In addition to these deficits in acute wound healing, chronic wounds also pose a significant area of concern, particularly in diabetic patients. Poor healing is a recognised difficulty experienced by those with diabetes, in that they heal slower, which can leave them prone to infection and in particular susceptible to foot ulceration (reviewed in Kidman, 2008 and Patel et al., 2019), greatly diminishing their quality of life. This impaired healing has been linked to high glucose levels (Endara et al., 2013), which in turn impedes the activity of lymphocytes (Moura et al., 2017). An elevated inflammatory response has also been associated with diabetes (reviewed in Wellen & Hotamisligil, 2005), and metabolic shifts are closely related to the immune response (reviewed in Kominsky et al., 2010). Moreover, type 2 diabetes has been characterised as an immuno-metabolic disorder (Hameed et al., 2015), and multiple mechanisms influencing diabetic wounds, such as protein kinase C (PKC) pathways, have been shown to be stimulated by oxidative stress from overproduction of reactive oxygen species (ROS) by the mitochondria (reviewed in Patel et al., 2019).

Cancer has also long been likened to a chronic, unhealing wound (Dvorak, 1986; reviewed in MacCarthy-Morrogh & Martin, 2020). Cancer cells possess similar metabolic reprogramming, including up-regulation of glycolysis (Warburg, 1925), an inflammatory response (reviewed in Coussens & Werb, 2002), and higher levels of ROS (reviewed in Kumari et al., 2018), all of which are also involved in wound healing. These similarities pose the question of whether chronic wounds also share the metabolic hallmarks of cancer.

5.1.3 The *hai1a* mutant as a tool for studying chronic wound healing

The *hai1a* mutant, though bearing many similarities to cancer, has not previously been utilised as a disease model. Cancer cells, healing wounds, and the *hai1a* phenotype all exhibit an inflammatory immune response and elevated levels of proliferation. This comparability generates an interest to explore the potential metabolic disruption in the mutant phenotype, both to clarify the molecular pathway of the mutant and potentially provide insight into how metabolism may be important in chronic wound healing.

ROS and glycolysis are particularly implicated in regeneration, and inflammation is already known to display Warburg metabolism and require ROS for activation (Sena et al., 2013; Martínez-Navarro et al., 2020). To address

the question of how metabolism is altered in the mutant, with a focus on these elements, I will utilise genetically encoded sensors to image levels of various metabolites, specifically Laconic (San Martín et al., 2013) for lactate levels, SoNar (Zhao et al., 2015) for NADH/NAD+ ratio, and GCaMP6s (Wang et al., 2008) for calcium. In addition, I will make use of the fluorescent probe pentafluorobenzenesulfonyl fluorescein (PFBSF) to image levels of hydrogen peroxide (H_2O_2) (Maeda et al., 2004).

Following these observational experiments, should there be dysregulation in any of these metabolites in the mutant, I will then introduce chemical perturbations to further elucidate possible links and molecular pathways, in particular between H_2O_2 and calcium.

5.2 Materials and Methods

Zebrafish husbandry

Adult heterozygous mutant *hai1a*^{fr26} zebrafish and AB strain wild type zebrafish (*Danio rerio)* were maintained at 28 °C with a 14 hour light/10 hour dark cycle. Embryos collected from crosses were staged as described in Kimmel et al., 1995. All animal experiments were performed in compliance with NACLAR Guidelines of Singapore overseen by the Biological Resource Centre of A*STAR (IACUC Protocol Number 140924). In all cases, embryos were raised in 1X E3 embryo medium as described in Cold Spring Harbor Protocols, supplemented with 0.1% Methylene Blue. For imaging neutrophils and keratinocytes, the offspring from crossing the transgenic lines *Tg[mpx:EGFP]*^{i114} (Renshaw et al., 2006) and *Tg[krtt1c19e:lyn-tdTomato]*^{sq16} (R. T. H. Lee et al., 2014) were used.

Genotyping

To identify heterozygous mutant *hai1a*^{fr26} adults, genomic DNA was extracted from fin clips in lysis buffer supplemented with proteinase K at 55˚C for 4 hours and then 95˚C for 10 minutes. PCR reaction was performed using GoTaq Green Master Mix (Promega, M712) with the primer pair: forward 5'-TGCAATTCCCAGTGTCTTTG-3' and reverse 5'-CACCGTCATTACAGCAGACG-3'. PCR conditions were as follows: 35 cycles of 95˚C for 20 seconds, 61˚C for 30 seconds, 72˚C for 30 seconds. Samples were then commercially Sanger sequenced (1st Base) with the same primer pair and analysed with SeqMan Pro sequence alignment against a reference to determine the presence of the mutated allele 445C>T Q149*.

mRNA injections

Heterozygous mutant *hai1a*^{fr26} adult zebrafish were in-crossed and the resulting embryos were injected at the one cell stage into the cell cytoplasm with 1ng sensor mRNA in 1nL in nuclease free water with phenol red. Sensor mRNA was synthesised from pCS2 plasmids linearised with NotI (NEB), with mMESSAGE mMACHINE SP6

Transcription Kit (Ambion) and purified with lithium chloride (LiCl) extraction. The plasmid for generation of GCaMP-6s mRNA was kindly gifted by the Solnica-Krezel lab (Chen et al., 2017).

Microscopy

Sample preparation: Embryos were visually screened using a fluorescent dissecting microscope for phenotype and mRNA expression and manually dechorionated if not already hatched. Embryos were then anaesthetised with 0.04% MS-222 (tricaine, Sigma Aldrich E10521) in 0.5X E2 media before mounting on 35mm glass bottomed dishes (Thermo Scientific Nunc) in 0.7% low melting agarose (Invitrogen 16520100) supplemented with 0.04% tricaine.

For metabolic sensor imaging: Images were acquired on an AxioImager.M2 upright microscope (Zeiss) using a EC Plan-Neofluar 40x/0.75 W N-Achroplan (water) objective as specified. Zeiss filter sets for CFP (BS455) and FITC/mCherry (DBS525/50 + 650/100) were utilised for Laconic imaging, and FITC/mCherry (DBS525/50 + 650/100) for SoNar imaging. Excitation was from a Colibri 7 LED fluorescent light source, Violet (430nm) used for Laconic imaging and Violet (430nm) and Blue (475nm) used for SoNar imaging. Imaging software: Zen Blue 2.3 Pro. The images were collected using a 2.8 Megapixels (Axiocam 503) colour camera at 14-bit on the black-and-white setting at room temperature.

For calcium and H_2O_2 imaging: Images were acquired on a LSM800 (Zeiss) upright confocal microscope using a 40X/0.75 N-Achroplan WD (water) objective with a 0.5X scan area. Emission was collected at 495-700nm with excitation laser 488nm. Imaging software: Zen Blue 2.3 Pro. The images were collected using two-channel multi-alkali PMT detectors at 8-bit and room temperature, pinhole 1AU.

For lightsheet imaging: Images were acquired on a Lightsheet Z.1 (Zeiss), every 20 seconds for a total timelapse length of 30 minutes.

Image analysis

All processing of images for calculating ratio and measuring fluorescence or ratio was conducted in Fiji (Fiji Is Just ImageJ, version 2.0.0). Average background was subtracted and threshold applied to remove remaining background, then respective channels divided by one another as required using the Image Calculator function. Pseudocolouring was applied using Lookup Table "16 colors".

Cell tracking for neutrophils was achieved using the TrackMate plugin in Fiji, blob diameter 12μm with threshold 2.0.

PFBSF

Pentafluorobenzenesulfonyl fluorescein (PFBSF, Cayman 10005983) was dissolved in DMSO treated with argon gas to make a 10mM stock which was aliquoted, protected from light, and kept at -20˚C until used. Working

solutions of 12.5μM were made in 0.5X E2 medium (half strength modification of the E2 embryo medium described in Cunliffe, 2003) and embryos were incubated for 1hr at room temperature protected from light before mounting in 0.7% low-melting agarose on a glass-bottomed dish (Nunc) for imaging.

Pharmacological treatment

Embryos were maintained in 0.5X E2 medium (half strength modification of the E2 embryo medium described in Cunliffe, 2003) in place of 1X E3 embryo medium.

2-Aminoethyl diphenylborinate (2-APB, Sigma-Aldrich D9754) treatment for calcium inhibition: stock concentration of 100μM was made in dimethyl sulfoxide (DMSO, Sigma Aldrich D8418) and diluted in 0.5X E2 medium to a working concentration of 3μM. Treatment was added to embryos with chorions intact at 8-9hpf and incubated at 28˚C overnight and imaged at 24hpf.

Phorbol 12-myristate 13-acetate (PMA, Sigma-Aldrich P8139) treatment for protein kinase C (PKC) activation: stock concentrations of 10mg/mL was made in DMSO and diluted in 0.5X E2 medium to a working concentration of 100ng/mL or 37.5ng/mL, as specified. Treatment was added to embryos with chorions intact at 19hpf and incubated at 28˚C for 5 hours, or to dechorionated 2dpf embryos and incubated at 28˚C overnight, as specified. A lower concentration was required for older embryos as they are more sensitive to the drug and susceptible to death.

Statistical analysis

GraphPad Prism 8 was used for statistical testing, with sample numbers exceeding 6 in all experiments. Grouped statistics and analyses of differences between means were implemented for all data sets. Two-way ANOVA was used with Sidak's multiple comparisons test to compare means between groups. Differences were considered significant to * at $P<0.05$, ** at $P<0.01$, *** at $P<0.001$, and **** at $P<0.0001$. Not significant (ns) was considered $P\geq0.05$, 95% confidence interval.

5.3 Results

5.3.1 Hydrogen peroxide and calcium signalling are up-regulated in *hai1a* mutants

The *hai1a*^{fr26} mutant displays sterile inflammation in the epidermis (Carney et al., 2007). In zebrafish, it has been shown that H_2O_2 mediates neutrophil recruitment to a wound (Niethammer et al., 2009; reviewed in Martínez-Navarro et al., 2020), and thus I sought to determine whether H_2O_2 levels were elevated in homozygous mutants compared to wild-type or heterozygous sibling controls. Using the selective fluorescent dye PFBSF to visualise static levels of H_2O_2 in live embryos, I found H_2O_2 was significantly elevated in mutant embryos at both 24hpf and

48hpf (FIG 5.2A-D). It was apparent when obtaining the confocal Z-stack images that PFBSF intensity was highest in the skin cells, particularly the aggregates. H_2O_2 levels were highest in areas with more severe aggregates and disrupted epidermal integrity, for instance at 24hpf aggregates are more noticeable at the yolk extension, and PFBSF staining in this area is more intense than that in the fin fold (FIG 5.2A-B). Similarly, at 48hpf the phenotype has progressed and both the fin fold and skin over the yolk extension display acute aggregations of keratinocytes, and H_2O_2 levels are correspondingly higher (FIG 5.2C-D).

The main sources of H_2O_2 in cells are the mitochondria, as a by-product of oxidative phosphorylation (OXPHOS) (Murphy, 2009), and from NADPH oxidases (NOXs) or dual oxidase (DUOX) (reviewed in Bedard & Krause, 2007). DUOX derived H_2O_2 has been implicated in tumourigenesis of multiple cancers (reviewed in Little et al., 2017), and in zebrafish the production of H_2O_2 during wounding has been shown to be generated by DUOX, which in turn is activated by calcium (Niethammer et al., 2009). Calcium signalling is also responsible for triggering H_2O_2 production by DUOX in *Drosophila* wounds (Razzell et al., 2013); I therefore endeavoured to resolve the status of calcium signalling in the *hai1a*^{fr26} mutant, particularly in conjunction with H_2O_2 presence.

GCaMP-6s is an established calcium indicator *in vivo* (Wang et al., 2008). One cell stage embryos injected with GCaMP-6s mRNA and imaged at 24hpf in the yolk extension and fin fold areas, every 2 minutes for a total of 10 minutes (Supplementary Movie.7), revealed significantly higher fluorescence in homozygous *hai1a*^{fr26} mutants compared to sibling controls in both areas (FIG 5.3A-C). In an alternative quantification method, number of signalling cells were counted (determined as any cell that changed fluorescence intensity during the duration of the timelapse); this parameter was also significantly higher in mutants (FIG 5.3D), suggesting up-regulated calcium signalling.

5.3.2 Calcium inhibition rescues hydrogen peroxide levels in *hai1a* mutants

To investigate whether the increased H_2O_2 and calcium levels are linked, I inhibited calcium signalling with 2-aminoethoxydiphenyl borate (2-APB), which acts on both IP_3 receptors and TRP channels (Maruyama et al., 1997). I injected GCaMP-6s mRNA into one cell stage embryos from *hai1a*^{fr26} heterozygote in-crosses, screened at 9hpf and treated the brightest mutants with 3μM 2-APB or DMSO control overnight at 28˚C. I then visualised H_2O_2 levels at 24hpf with PFBSF and found that calcium inhibition significantly reduces H_2O_2 (FIG 5.4A and B), as demonstrated by a lower PFBSF fluorescence. Notably, H_2O_2 is still elevated in the most severe keratinocyte aggregates.

I also verified in a control experiment that the drug acts to significantly decrease calcium signalling in mutant *hai1a*^{fr26} embryos, which was confirmed with GCaMP-6s mRNA injections in mutants treated with 3μM 2-APB or DMSO control as described previously. GCaMP-6s fluorescence intensity in treated embryos was indeed significantly lower than controls, indicating a reduced level of calcium in the presence of 2-APB (FIG 5.4C and D, Supplementary Movie.8).

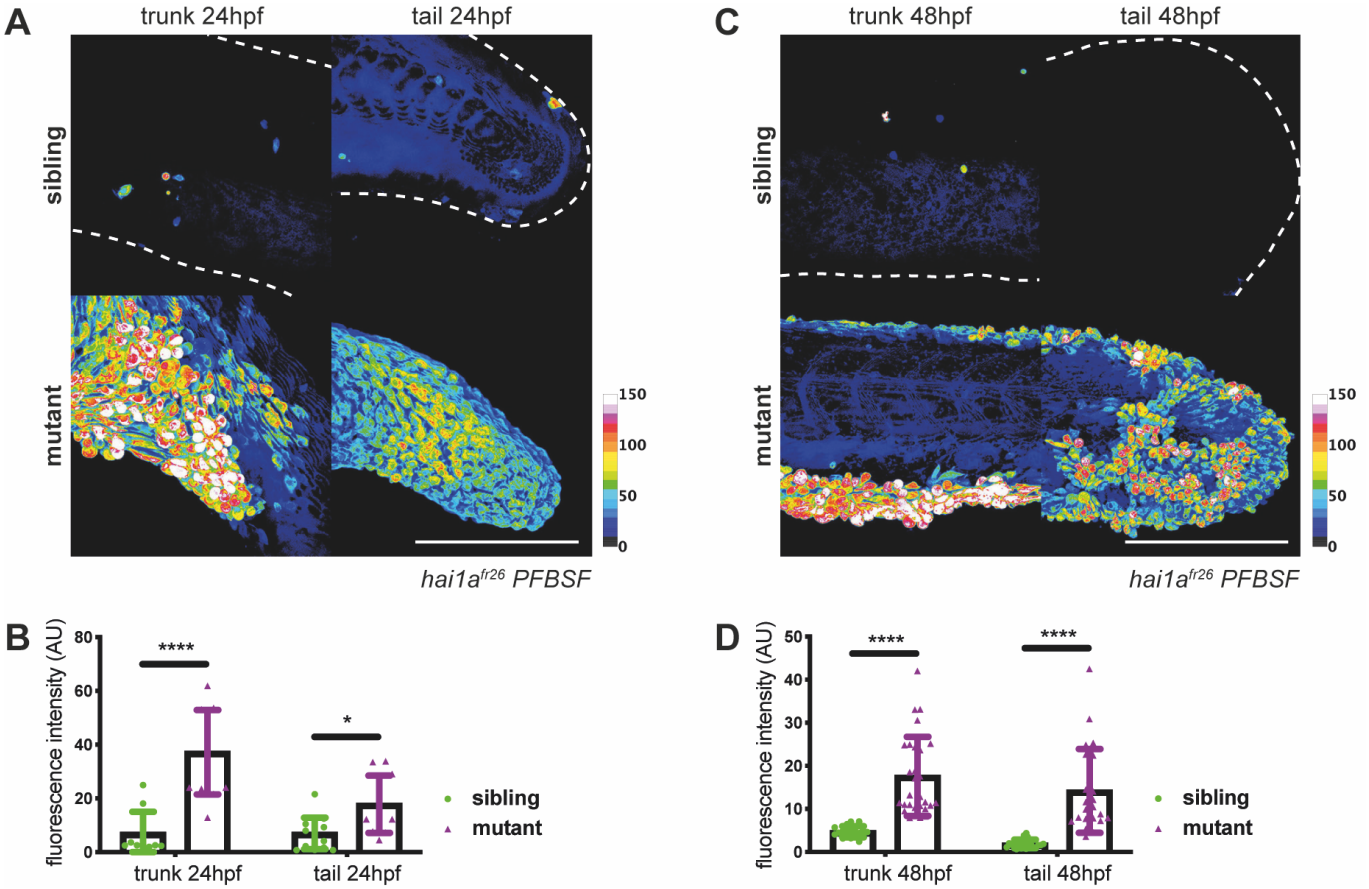

Figure 5.2. **Hydrogen peroxide levels in *hai1a*^{fr26} siblings and mutants.** All panels show data obtained with Zeiss LSM800 upright confocal microscope (20X). All scale bars represent 200μm. Differences were considered significant to * P<0.05, ** P<0.01, *** P<0.001, **** P<0.0001, and ns P≥0.05. Sibling genotype is *hai1a*$^{fr(+/+ \text{ or } +/-)}$, while mutant genotype is *hai1a*$^{fr26(-/-)}$. (A) Representative *hai1a*^{fr26} embryos stained with pentafluorobenzenesulfonyl fluorescein (PFBSF) to show hydrogen peroxide levels (H_2O_2) at 24hpf, pseudocoloured to show fluorescence intensity. White dashed line denotes outline of embryo where staining is too dim to discern. (B) Graph showing quantification of PFBSF fluorescence intensity in arbitrary units in the trunk and tail regions at 24hpf. Two-way ANOVA to calculate significance, n=15. (C) Representative *hai1a*^{fr26} embryos stained with PFBSF to show H_2O_2 levels at 48hpf, pseudocoloured to show fluorescence intensity. White dashed line denotes outline of embryo where staining is too dim to discern. (D) Graph showing quantification of PFBSF fluorescence intensity in arbitrary units in the trunk and tail regions at 48hpf. Two-way ANOVA to calculate significance, n=25.

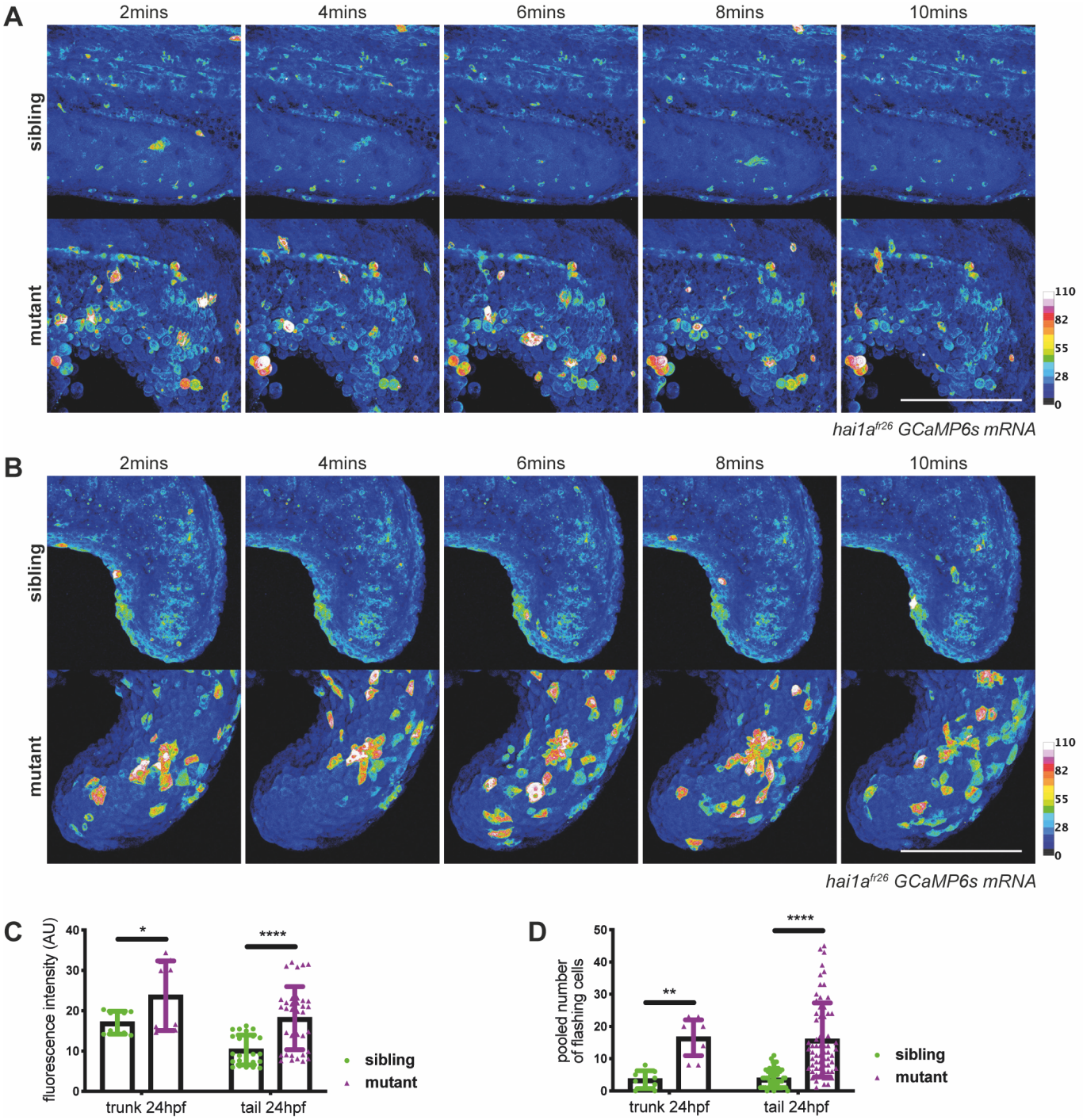

Figure 5.3. **Calcium levels in *hai1a*^{fr26} siblings and mutants.** All panels show data obtained with Zeiss LSM800 upright confocal microscope (20X). All scale bars represent 200µm. Differences were considered significant to * P<0.05, ** P<0.01, *** P<0.001, **** P<0.0001, and ns P≥0.05. Sibling genotype is *hai1a*$^{fr26(+/+ \text{ or } +/-)}$, while mutant genotype is *hai1a*$^{fr26(-/-)}$. (A) Still images of 10 minute timelapses (Supplementary Movie.7) of the trunk region of representative 24hpf *hai1a*^{fr26} embryos injected at the one cell stage with GCaMP-6s mRNA to show calcium signalling, pseudocoloured to show fluorescence intensity. (B) Still images of 10 minute timelapses (Supplementary Movie.7) of the tail region of representative 24hpf *hai1a*^{fr26} embryos injected at the one cell stage with GCaMP-6s mRNA to show calcium signalling, pseudocoloured to show fluorescence intensity. (C) Graph showing quantification of GCaMP-6s fluorescence intensity in arbitrary units in the trunk and tail regions at 24hpf. Each data point is the average intensity of one frame (5 data points per embryo). Two-way ANOVA to calculate significance, n=10 (trunk), n=25 (tail). (D) Graph showing number of cells actively signalling in the trunk and tail regions at 24hpf. Quantified as the number of cells per frame (5 data points per embryo) that alter in fluorescence throughout the timelapse. Two-way ANOVA to calculate significance, n=10 (trunk), n=55 (tail).

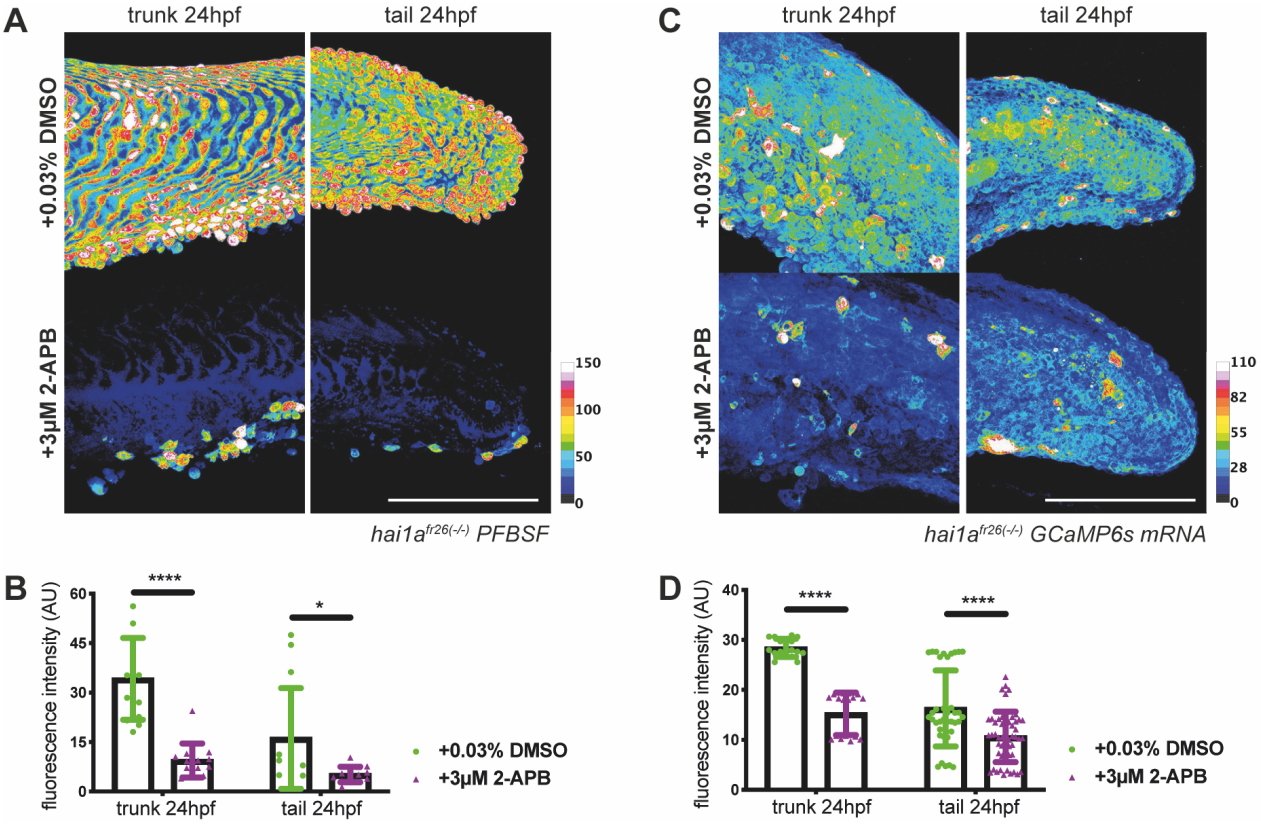

Figure 5.4. **Effect of calcium inhibition on hydrogen peroxide levels in *hai1a*^{fr26} mutants.** All panels show data obtained with Zeiss LSM800 upright confocal microscope (20X). All scale bars represent 200µm. Differences were considered significant to * P<0.05, ** P<0.01, *** P<0.001, **** P<0.0001, and ns P≥0.05. Mutant genotype is *hai1a*$^{fr26(-/-)}$. (A) Representative *hai1a*^{fr26} mutant embryos at 24hpf treated overnight (from 9hpf) at 28˚C with 3µM 2-APB to inhibit calcium signalling or DMSO control, then stained with pentafluorobenzenesulfonyl fluorescein (PFBSF) to show hydrogen peroxide (H_2O_2) levels, pseudocoloured to show fluorescence intensity. (B) Graph showing quantification of PFBSF fluorescence intensity in arbitrary units in the trunk and tail regions of DMSO and 2-APB treated *hai1a*^{fr26} mutant embryos at 24hpf. DMSO and untreated embryos not significantly different (data not shown). Two-way ANOVA to calculate significance, n=14. (C) Representative still images of 10 minute timelapses (Supplementary Movie.8) of the trunk and tail regions of 24hpf *hai1a*^{fr26} mutant embryos injected at the one cell stage with GCaMP-6s mRNA to show calcium signalling and treated overnight (from 9hpf) at 28 ˚C with 3µM 2-APB to inhibit calcium signalling or DMSO control, pseudocoloured to show fluorescence intensity. (D) Graph showing quantification of GCaMP-6s fluorescence intensity in arbitrary units in the trunk and tail regions at 24hpf after treatment overnight (from 9hpf) at 28˚C with 3µM 2-APB to inhibit calcium signalling or DMSO control. Each data point is the average fluorescence intensity per frame (5 per embryo). Two-way ANOVA to calculate significance, n=17.

5.3.3 PKC activation induces a *hai*-like phenotype

Putatively, Hai1a acts to inhibit Matriptase1a, which activates the G-protein-coupled receptor Par2 (Sales et al., 2015). Indeed, it has been found that the *hai1a*, *matriptase1a*, and *par2b* genes are co-expressed in zebrafish skin (Schepis et al., 2018). Par2 activates phospholipase C (PLC) (Schechter et al., 1998), catalysing the formation of diacylglycerol (DAG) and inositol 1,4,5-trisphosphate (IP_3) from phosphatidylinositol 4,5-bisphosphate (PIP_2) (reviewed in Putney & Tomita, 2012). IP_3 and its receptor are upstream of calcium release from the endoplasmic reticulum (Streb et al., 1983), and from the H_2O_2 and calcium work in the previous sections, it is apparent calcium activation of DUOX leading to H_2O_2 production is involved in the *hai1a* phenotype. DAG in this cascade remains attached to the membrane and activates protein kinase C (PKC), which can go on to phosphorylate and activate

further cytosolic proteins (reviewed in Newton, 2018). Since H_2O_2 and calcium appear to be responsible for the inflammatory phenotype, we proposed perhaps DAG and PKC activity produces the epidermal phenotype.

In order to investigate the potential involvement of PKC, I treated wild type embryos with the DAG analogue and activator of PKC, phorbol 12-myristate 13-acetate (PMA). I found activating PKC signalling in wild type larvae generated an epidermal phenotype resembling the *hai1a*^{fr26} mutant at 24hpf, with the formation of keratinocyte aggregates and significantly elevated H_2O_2 levels (FIG 5.5A and B). Similar treatment on 2dpf *Tg[mpx:EGFP;krtt1c19e:lyn-tdTomato]* (Renshaw et al., 2006; R. T. H. Lee et al., 2014) embryos produces a sterile inflammatory response with neutrophils increasing in number and motility (FIG 5.5C, Supplementary Movie.9) as is seen in the mutant. However, when examining calcium signalling, PMA treatment significantly decreases fluorescence intensity of GCaMP-6s at 24hpf (FIG 5.5D and E, Supplementary Movie.10). It is likely that PKC acts to produce H_2O_2 independently of calcium, via a currently unknown mechanism, potentially interacting with DUOX or other NADH oxidases (Rigutto et al., 2009; Schlam et al., 2013).

5.3.4 Lactate levels are increased in *hai1a* mutants

Previous work has shown that proliferation is increased in the *hai1a*^{fr26} mutant after 48hpf (Carney et al., 2007). As the Warburg effect is associated with proliferating cells (reviewed in Lunt & Vander Heiden, 2011), I hypothesised there may be elevated lactate production in the mutant, potentially only noticeably at 48hpf. By injecting Laconic mRNA into one cell embryos attained from in-crossing *hai1a*^{fr26} heterozygous adults, I was able to image real-time levels of lactate in mutants and sibling controls at 24hpf and 48hpf.

Despite the lack of increased proliferative activity at 24hpf (Carney et al., 2007), lactate was significantly higher in the aggregates over the yolk extension in mutants compared to controls. As a glycolytic switch is important for EMT (reviewed in Morandi et al., 2017), and mutant keratinocytes gain mesenchymal characteristics, this increase in glycolysis may be a result of aggregate formation. The fin fold did not show higher Laconic ratios, predictably due to the weaker nature of the epidermal phenotype at this earlier stage (FIG 5.6A and B). At 48hpf, however, Laconic ratio was significantly raised in both the trunk and fin fold regions (FIG 5.6C and D). As confocal imaging with my available set-up was not conducive to Laconic imaging, it was not easy to determine which cells precisely were expressing elevated Laconic ratio. Thus, as a control, I additionally imaged the trunk focussing on the notochord – the *hai1a* phenotype does not affect the notochord and as such would not be expected to show any variance. Indeed, this was the case at both 24hpf and 48hpf (FIG 5.6A-D), advocating the conclusion that lactate increase is caused by the *hai1a* epidermal phenotype and present only in the affected keratinocytes.

As mentioned in the introduction, the inflammatory immune response is known to display the Warburg effect (reviewed in Palsson-McDermott & O'Neill, 2013), however I did not observe any distinct immune cells in the mutant to be displaying elevated Laconic levels. Since I have confirmed that a sterile inflammation response is indeed occurring, perhaps the neutrophils are being obscured by the disorganisation of or interference from the epithelium, or are in this case not exhibiting aerobic glycolysis.

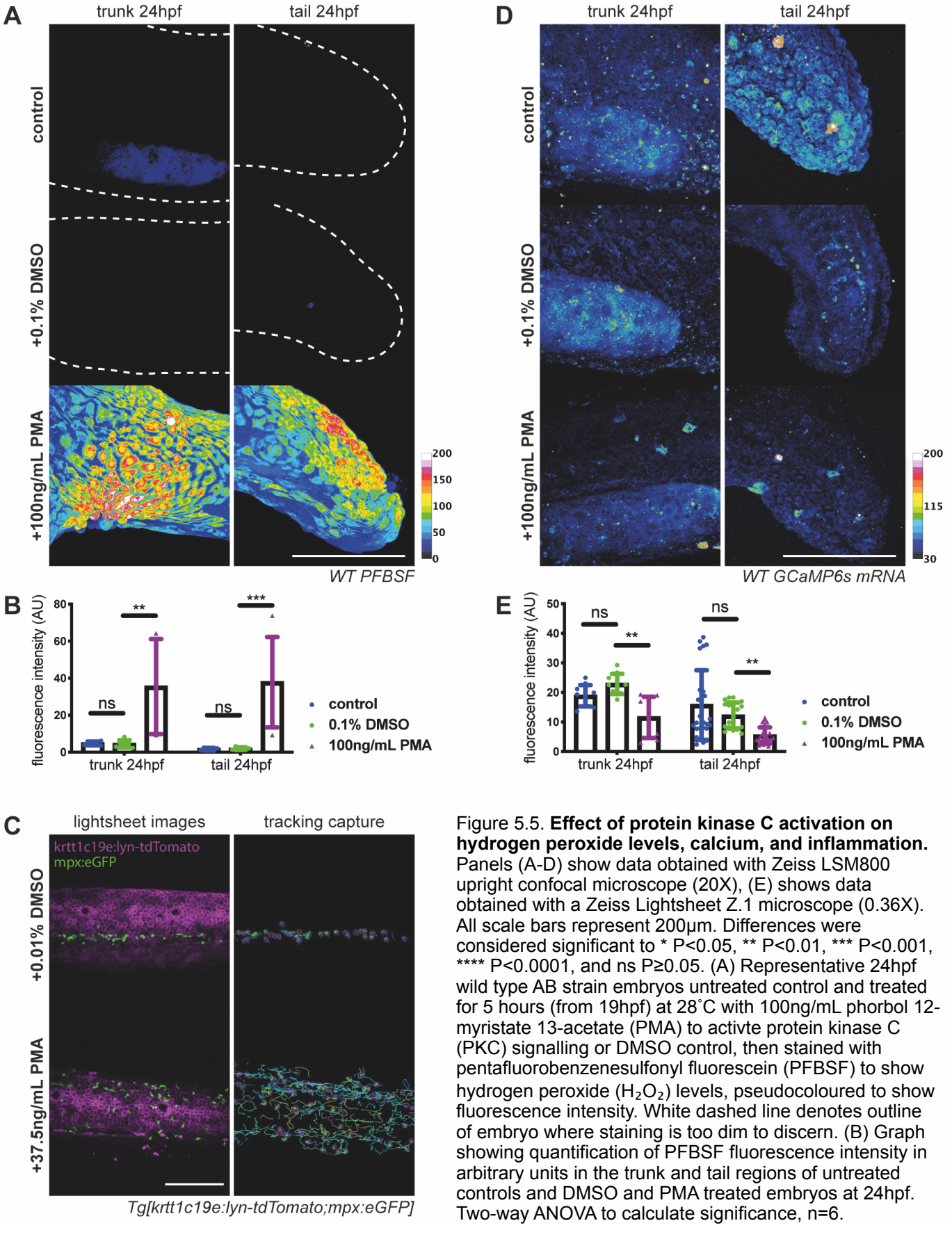

Figure 5.5. **Effect of protein kinase C activation on hydrogen peroxide levels, calcium, and inflammation.** Panels (A-D) show data obtained with Zeiss LSM800 upright confocal microscope (20X), (E) shows data obtained with a Zeiss Lightsheet Z.1 microscope (0.36X). All scale bars represent 200µm. Differences were considered significant to * P<0.05, ** P<0.01, *** P<0.001, **** P<0.0001, and ns P≥0.05. (A) Representative 24hpf wild type AB strain embryos untreated control and treated for 5 hours (from 19hpf) at 28˚C with 100ng/mL phorbol 12-myristate 13-acetate (PMA) to activte protein kinase C (PKC) signalling or DMSO control, then stained with pentafluorobenzenesulfonyl fluorescein (PFBSF) to show hydrogen peroxide (H_2O_2) levels, pseudocoloured to show fluorescence intensity. White dashed line denotes outline of embryo where staining is too dim to discern. (B) Graph showing quantification of PFBSF fluorescence intensity in arbitrary units in the trunk and tail regions of untreated controls and DMSO and PMA treated embryos at 24hpf. Two-way ANOVA to calculate significance, n=6.

(continued on next page)

(Figure 5.5. cont.) (C) Representative stills from 30 minute lightsheet timelapses (Supplementary Movie.9) and tracking capture of TrackMate (Tinevez et al., 2017) analysis of neutrophil migration of the trunk area of 3dpf *Tg[kmpx:EGFP;krtt1c19e:lyn-tdTomato]* embryos (Renshaw et al., 2006; Lee et al., 2014) treated at 2dpf with 37.5ng/mL PMA or 0.01% DMSO control. Track colour denotes mean velocity (dark blue 0.0 – red 0.2). (D) Representative still images from 10 minute timelapse movies (see Supplementary Movie.10) of 24hpf wild type AB strain embryos injected at the one cell stage with GCaMP-6s mRNA to show calcium signalling. Untreated controls and treated for 5 hours (from 19hpf) at 28˚C with 100ng/mL PMA to activate PKC signalling or DMSO control, pseudocoloured to show fluorescence intensity. (E) Graph showing quantification of GCaMP-6s fluorescence intensity in arbitrary units in the trunk and tail regions of untreated control and DMSO or PMA treated embryos at 24hpf. Each data point is the average fluorescence intensity per frame (5 per embryo). Two-way ANOVA to calculate significance, n=10 (trunk), n=25 (tail).

Together with the data evidencing increased proliferation, it suggests the presence of the Warburg effect in the *hai1a*^{fr26} mutant, at least after 48hpf.

To further investigate the possibility of the Warburg effect, I sought to chemically inhibit the mitochondria and measure Laconic ratio before and after treatment, to determine whether *hai1a* mutants showed a lesser change in lactate production and therefore a lower reliance on mitochondria. As before, Laconic mRNA was injected into one cell embryos from heterozygous *hai1a*^{fr26} in-crosses, and mutants and siblings were selected and imaged before and after a one hour treatment with the mitochondrial inhibitor antimycin A (AA), which acts on cytochrome C of the electron transport chain (Slater, 1973), effectively blocking the activity of oxidative phosphorylation. I found that AA treatment at 24hpf significantly increased lactate levels to the same extent in both mutants and sibling controls in the fin fold region, as expected due to the lack of difference without treatment and thus are likely to react in a similar manner. However, in the epidermis over the yolk extension, in which there is a significant difference pre-treatment between mutants and controls, Laconic ratio was significantly changed in the AA treated siblings only (FIG 5.7A-B'). Furthermore, there was no significant difference between post-treatment siblings and mutants (FIG 5.7B), suggesting the lactate level of sibling controls had been elevated to a comparable level as the mutants. An analogous situation is apparent with treatment at 48hpf. In the areas that show a significant difference in Laconic ratio pre-treatment—that is, the trunk and fin fold epidermis—mutants did not significantly change in response to AA treatment while the Laconic ratios of siblings rose to be no longer significantly different from those of mutants (FIG 5.7C-D'). The lesser response of mutants up-regulating glycolysis and lactate production to compensate for loss of mitochondrial function also suggests the potential occurrence of the Warburg effect, as they appear to have a reduced reliance on OXPHOS. It is noteworthy, however, that I cannot definitively eliminate the possibility that the Laconic sensor is simply saturated in the mutants, obscuring a true increase in response to mitochondrial inhibition as occurs in siblings.

5.3.5 NADH/NAD+ ratio is slightly elevated in *hai1a* mutants

NADH and NAD+ are important cofactors for redox reactions within the cell; the ratio between the reduced (NADH) and oxidised (NAD+) form can provide information on the metabolic activity of the cell (reviewed in Cantó et al., 2015). NAD+ is also used during glycolysis to facilitate the activity of glyceraldehyde-3-phosphate

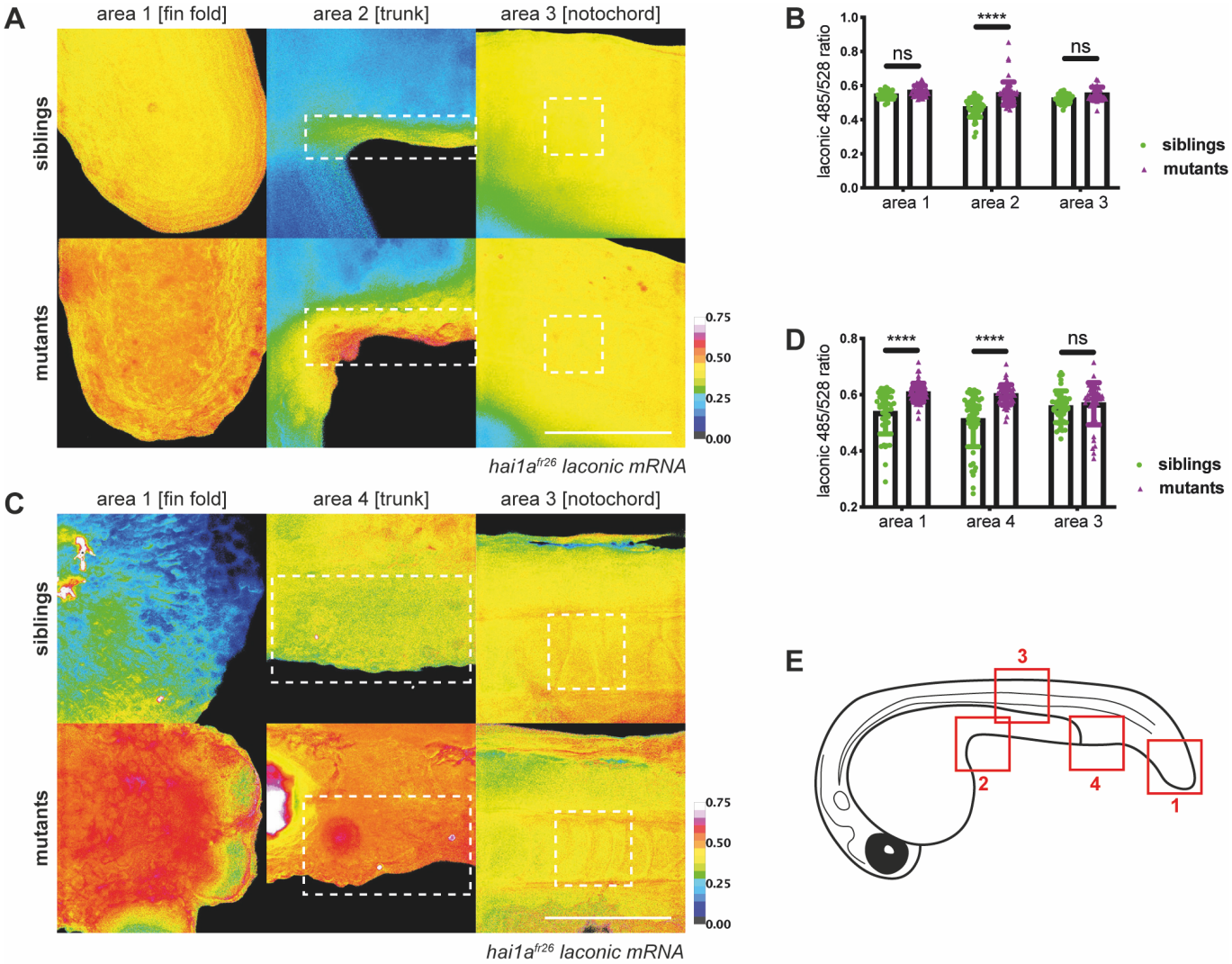

Figure 5.6. **Lactate levels in *hai1a*^{fr26} siblings and mutants.** All panels show data obtained with Zeiss AxioImager.M2 upright widefield microscope (40X). All scale bars represent 100µm. Differences were considered significant to * P<0.05, ** P<0.01, *** P<0.001, **** P<0.0001, and ns P≥0.05. Sibling genotype is *hai1a*$^{fr26(+/+ \text{ or } +/-)}$, while mutant genotype is *hai1a*$^{fr26(-/-)}$.(A) Representative images of 24hpf *hai1a*^{fr26} embryos injected at the one cell stage with Laconic mRNA, pseudocoloured to show Laconic ratio calculated by dividing the 428nm emission channel by the 485nm emission channel. Regions of the embryo imaged shown in panel (E). White dotted boxes denote regions of interest measured for quantification. (B) Graph showing quantification of Laconic ratio in each area at 24hpf, comparing siblings with mutants. Two-way ANOVA to calculate significance, n=30. (C) Representative images of 48hpf *hai1a*^{fr26} embryos injected at the one cell stage with Laconic mRNA, pseudocoloured to show Laconic ratio. White dotted boxes denote regions of interest measured for quantification. (D) Graph showing quantification of Laconic ratio in each area at 48hpf, comparing siblings with mutants. Two-way ANOVA to calculate significance, n=50. (E) Schematic of a 24hpf zebrafish embryo annotated with the regions imaged in panels (A) and (B). Area 1 is the fin fold, area 2 is the skin at the yolk/yolk extension where aggregates form in the mutant phenotype, area 3 focuses on the notochord, and area 4 is the skin of the post-anal fin fold (aggregates have formed in this area by 48hpf) and replaces area 2 at 48hpf due to increased autofluorescence of the yolk.

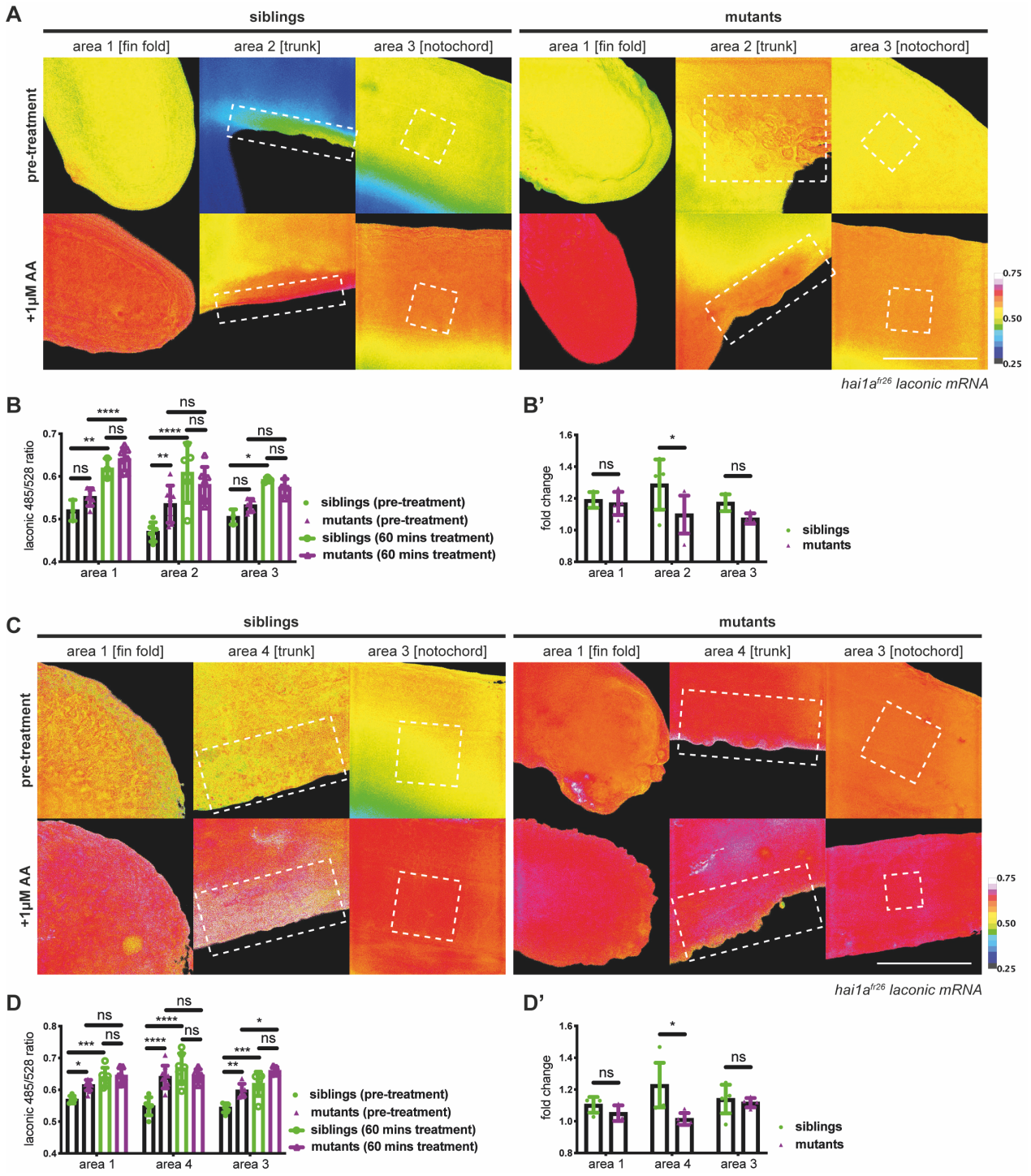

Figure 5.7. **Effect of mitochondrial inhibition on lactate levels in *hai1a*^{fr26} siblings and mutants.** All panels show data obtained with Zeiss AxioImager.M2 upright widefield microscope (40X). All scale bars represent 100µm. Differences were considered significant to * P<0.05, ** P<0.01, *** P<0.001, **** P<0.0001, and ns P≥0.05. Sibling genotype is *hai1a*$^{fr26(+/+ \text{ or } +/-)}$, while mutant genotype is *hai1a*$^{fr26(-/-)}$. (A) Representative images of 24hpf *hai1a*^{fr26} embryos injected at the one cell stage with Laconic mRNA, before and after treatment with 1µM antimycin A (AA) for 1 hour at 28˚C, pseudocoloured to show Laconic ratio calculated by dividing the 428nm emission channel by the 485nm emission channel. Regions of the embryo imaged shown in panel (E) of Figure 5.5. White dotted boxes denote regions of interest measured for quantification. (B) Graph showing raw Laconic ratios pre- and 60 mins post-addition of AA at 24hpf comparing siblings with mutants. Two-way ANOVA to calculate significance, n=6. (B') Graph showing fold change of Laconic ratio after treatment with AA at 24hpf comparing siblings with mutants. Two-way ANOVA to calculate significance, n=5. (C) Representative images of 48hpf *hai1a*^{fr26} embryos injected at the one cell stage with Laconic mRNA, before and after treatment with 1µM antimycin A (AA) for 1 hour at 28˚C, pseudocoloured to show Laconic ratio calculated by dividing the 428nm emission channel by the 485nm emission channel. Regions of the embryo imaged shown in panel (E) of Figure 5.5. White dotted boxes denote regions of interest measured for quantification.

(continued on next page)

(Figure 5.7. cont.) (D) Graph showing raw Laconic ratios pre- and 60 mins post-addition of AA at 48hpf comparing siblings with mutants. Two-way ANOVA to calculate significance, n=6. (D') Graph showing fold change of Laconic ratio after treatment with AA at 48hpf comparing siblings with mutants. Two-way ANOVA to calculate significance, n=6.

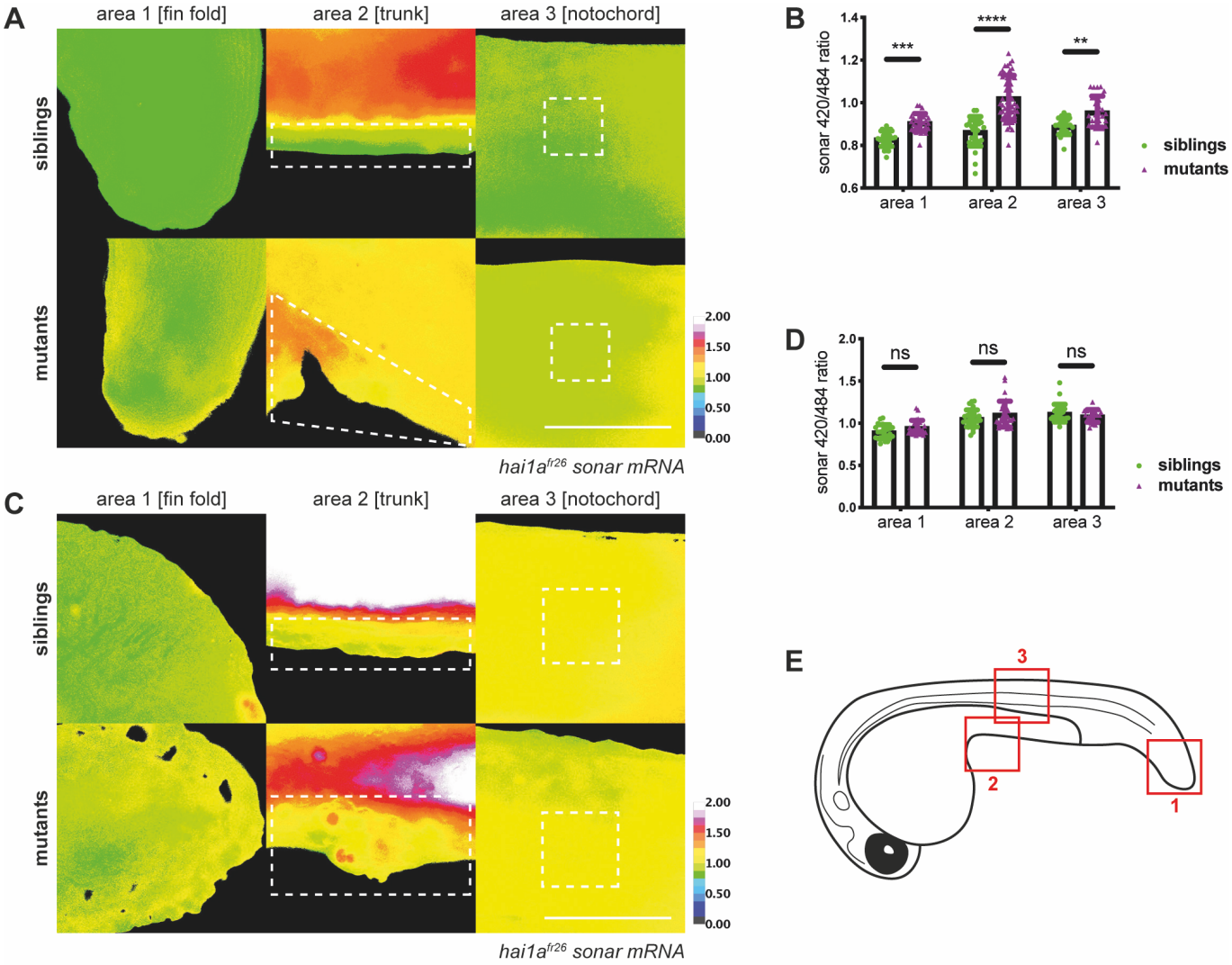

Figure 5.8. **NADH/NAD+ ratios in *hai1a*^{fr26} siblings and mutants.** All panels show data obtained with Zeiss AxioImager.M2 upright widefield microscope (40X). All scale bars represent 100µm. Differences were considered significant to * P<0.05, ** P<0.01, *** P<0.001, **** P<0.0001, and ns P≥0.05. Sibling genotype is *hai1a*$^{fr26(+/+ \text{ or } +/-)}$, while mutant genotype is *hai1a*$^{fr26(-/-)}$. (A) Representative images of 24hpf *hai1a*^{fr26} embryos injected at the one cell stage with SoNar mRNA, pseudocoloured to show SoNar ratio calculated by dividing the 485nm excitation channel by the 528nm excitation channel. Regions of the embryo imaged shown in panel (E). White dotted boxes denote regions of interest measured for quantification. (B) Graph showing quantification of SoNar ratio in each area at 24hpf, comparing siblings with mutants. Two-way ANOVA to calculate significance, n=30. (C) Representative images of 48hpf *hai1a*^{fr26} embryos injected at the one cell stage with SoNar mRNA, pseudocoloured to show SoNar ratio. White dotted boxes denote regions of interest measured for quantification. (D) Graph showing quantification of SoNar ratio in each area at 48hpf, comparing siblings with mutants. Two-way ANOVA to calculate significance, n=28. (E) Schematic of a 24hpf zebrafish embryo annotated with the regions imaged in panels (A) and (B). Area 1 is the fin fold, area 2 is the skin at the yolk/yolk extension where aggregates form in the mutant phenotype, and area 3 focuses on the notochord.

dehydrogenase (GAPDH), and in anaerobic conditions is regenerated by lactate dehydrogenase (LDH) during the conversion of pyruvate to lactate (reviewed in Akram, 2013). Under normal physiological conditions, concentration of free cytosolic NAD+ is higher than that of NADH (Williamson et al., 1967), translating to a low ratio of SoNar, my selected NADH/NAD+ ratiometric sensor. SoNar may be able to provide insight into an increase in glycolysis activity in the *hai1a* mutant; depending on the rate of fermentation producing lactate compared to that of glycolysis, SoNar ratio may increase in response to the Warburg effect.

As with Laconic, SoNar mRNA was injected into one cell embryos from clutches laid by heterozygous *hai1a*^{fr26} adults. At 24hpf and 48hpf, homozygous mutants identified by epidermal phenotype and sibling controls were imaged in three regions (fin fold, epidermis over the yolk extension, and notochord) and processed to generate SoNar ratios. I found at 24hpf all three regions showed significantly higher SoNar ratio in the mutant compared to controls (FIG 5.8A and B). However, by 48hpf NADH/NAD+ ratio in mutants was no longer elevated and was very similar to that of controls (FIG 5.8C and D). From the positive control experiments with mitochondrial inhibitors (see Results 1) I can hypothesise that glycolysis generally appears to proceed more rapidly than fermentation, at least initially, and thus potentially in the early stages of the phenotype glycolysis is highly active, out of balance with the fermentation reaction, and by the later stages an equilibrium has been reached to restore NADH/NAD+ balance.

5.4 Discussion

In this study I have tested the hypothesis that the zebrafish *hai1a* mutant can be presented as an unhealing wound, similar to cancer, particularly with respect to inflammation and epidermal cell motility, which are common to all three.

Figure 5.9 shows a simplified schematic of the proposed pathway involved in the *hai1a* inflammation and epithelial motility phenotypes. The *hai1a* mutant phenotype is a result of a loss of inhibition of the serine protease Matriptase1a (Carney et al., 2007) and subsequent overactivity of the G-protein coupled receptor, Par2, which is cleaved and activated by Matriptase1a (Sales et al., 2015; Ma et al., 2021). In section 5.3.3 I discuss the potential pathway in the *hai1a* mutant involving the activation of PKC downstream from Par2 to cause the keratinocyte motility, and I am able to phenocopy the epidermal phenotype by stimulating PKC signalling with the DAG analogue PMA. PKC has been implicated in the proliferation and motility of tumour growth (Haughian et al., 2009), potentially due to one of its downstream targets, the mitogen-activated protein kinase/extracellular signal-regulated kinase (MAPK/ERK) signalling pathway, which is responsible for the migration and proliferation of keratinocytes in the wound response (Lavoie et al., 1996; Robinson & Cobb, 1997; Matsubayashi et al., 2004) and implicated in the development of many cancers due to its mitogenic activity in promoting cell cycle entry and proliferation (reviewed in Guo et al., 2020). Indeed, Par2 has been shown to activate ERK to promote metastasis in breast cancer cells (Morris et al., 2006). Ma et al. (2021) demonstrate an up-regulation of phosphorylated ERK

(pERK) in the aggregates of *hai1a* mutants and PMA treated embryos, suggesting pERK is downstream of PKC. Mitogen-activated protein kinase (MEK) inhibition ablates the epidermal pERK levels and rescues the *hai1a* aggregate phenotype, further suggesting pERK is crucial for the keratinocyte motility and suggests the role of

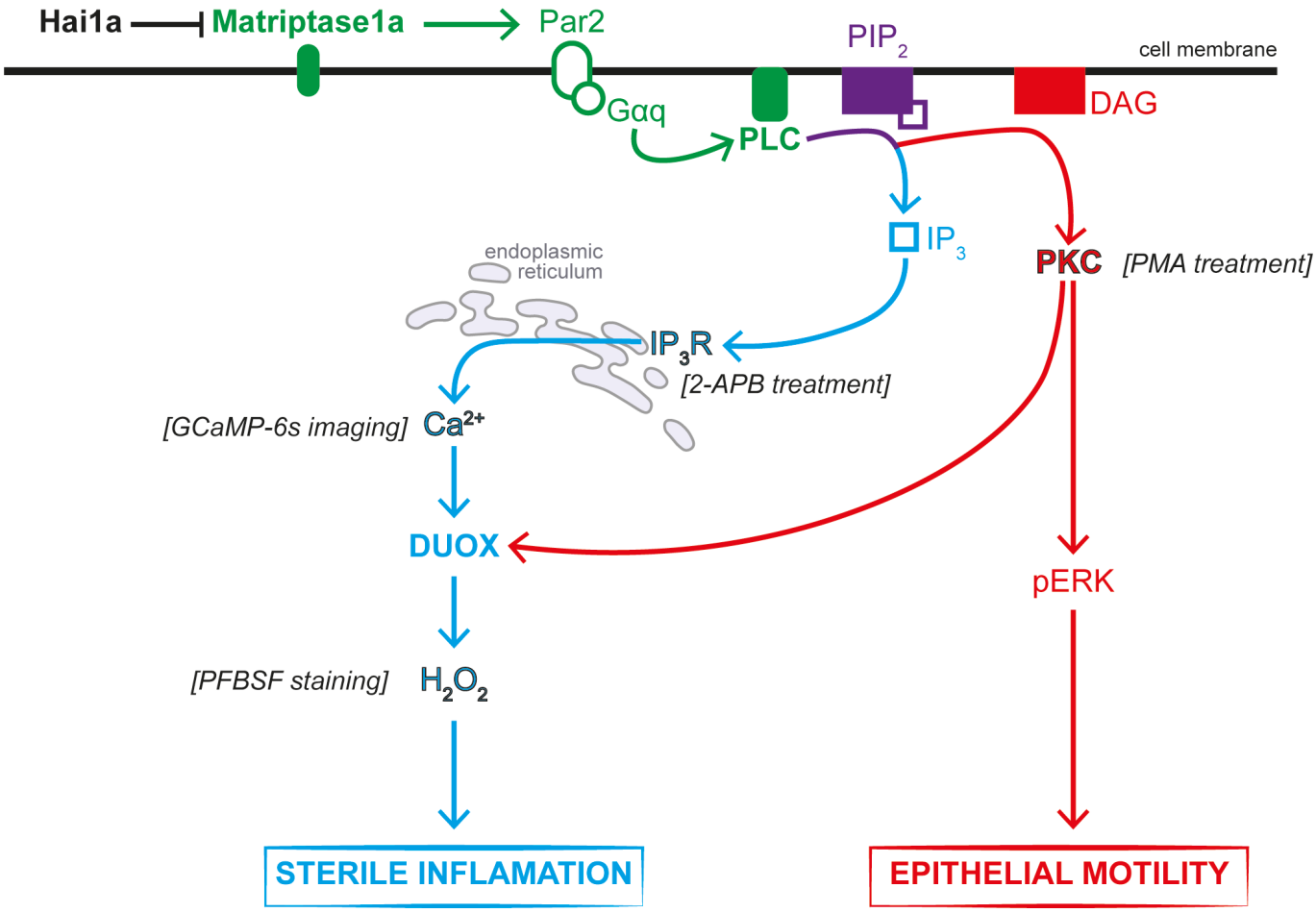

Figure 5.9. **Simplified schematic of the proposed pathway in the *hai1a* mutant.** Proposed model of the pathways activated downstream of Hai1a and Matriptase1a driving sterile inflammation (blue) and epithelial aggregates and motility (red). Hai1a acts to inhibit Matriptase1a, which in the mutant results in overactivation of Par2. Subsequently, phospholipse C (PLC) cleaves phospholipid phosphatidylinositol 4,5-bisphosphate (PIP_2) into diacyl glycerol (DAG) on the membrane and inositol 1,4,5-trisphosphate (IP_3) which is released into the cytosol. IP_3 interacts with its receptor on the endoplasmic reticulum to trigger the release of calcium, activating DUOX which generates H_2O_2, attracting neutrophils and giving rise to the inflammation phenotype. DAG activates protein kinase C (PKC), leading to the phosphorylation of extracellular signal-related kinase (pERK), involved in stimulating epithelial motility and partial epithelial to mesenchymal transition (EMT) of keratinocytes. Note that this is a simplified and incomplete schematic, other pathways downstream of Matriptase and potential intermediate signals not shown.
Contributions from experiments included in my thesis are highlighted in black outlined font and square bracketed italicised side notes. PMA, a DAG analogue, stimules PKC activity and results in increased pERK levels (Ma et al., 2021) and keratinocyte aggregates. I detected elevated calcium levels with GCaMP-6s imaging and increased H_2O_2 levels with PFBSF staining in the *hai1a*^{fr26} mutant, while treatment with 2-APB to inhibit IP_3 receptors results in reduced calcium, H_2O_2, and rescues the inflammatory phenotype.

pERK is similar in the mutant, cancer, and wound response.

My work also supports the parallel branch of the pathway, concerned with the sterile inflammation phenotype. I found H_2O_2 levels and calcium signalling are raised in the mutant, as is the case in zebrafish fin regeneration

(Niethammer et al., 2009; Yoo et al., 2012). Moreover, the H_2O_2 in zebrafish wounds is generated by the calcium-activated DUOX enzyme and responsible for attracting neutrophils to the site of injury (Niethammer et al., 2009; Yoo et al., 2012; de Oliveira et al., 2014), and the same mechanism is suggested in the *hai1a* mutant. Morpholinos against *duox* rescue the inflammation and H_2O_2 phenotype (Ma et al., 2021) and I show successful inhibition of calcium release from the endoplasmic reticulum by 2-APB rescues H_2O_2 levels in the mutant, but in both cases the keratinocyte aggregates remain largely unchanged, indicating the epidermal and inflammatory phenotypes are distinct and occur in parallel with one another.

Cancer cells are well known to have an abnormal metabolic profile, opting to increase glycolysis activity and reduce reliance on the mitochondria and OXPHOS (DeBerardinis & Chandel, 2016). Given the similarities between the *hai1a* mutant and cancer, I found similar metabolic disturbances in the mutant. Specifically, I saw an increase in lactate levels and an apparent reduction in reliance on the mitochondria, as treatment with a mitochondrial inhibitor made no significant difference to mutant lactate levels while driving wild type siblings to increase glycolysis and fermentation to compensate. (However, it is worth noting that I have no way of ascertaining whether the lack of increase in Laconic ratio in the mutants following mitochondrial inhibition is due to saturation of the sensor.) Lactate levels were elevated only in the more severe aggregates in the trunk at 24hpf, but throughout the skin by 48hpf when the epidermal integrity is acutely impeded in all areas and proliferation is significantly increased (Carney et al., 2007) – the coincidence with enhanced proliferation potentially indicates the Warburg effect to accommodate cell growth. Alternatively, the lactate production, and by extension glycolysis activity, may be related to the partial EMT of the keratinocytes which gives them the motility characteristic of a mesenchymal cell, leading to aggregate formation. The brief rise in NADH to NAD+ ratio at 24hpf in the mutant, perhaps indicative of rapid glycolysis and a slower rate of fermentation, is likely regulated and rebalanced by 48hpf, which may explain the lack of difference seen at the later time-point, despite the greater severity of the phenotype.

Together, multiple lines of evidence support my proposal considering the *hai1a* mutant as an unhealing, chronic wound. The mutant, along with with cancer, shares key molecular aspects with the wound response, namely elevated ROS levels, inflammation, later proliferation and MAPK/pERK signalling. Additionally, there appears to be a metabolic reprogramming towards aerobic glycolysis, as is seen in both regenerating and cancer cells, and further study on how altering metabolism affects the inflammatory and epidermal phenotypes of the *hai1a* mutant could provide insight into generating similar results in tumours or driving a regenerative response in classically non-regenerative organisms.

References

Akram, M. (2013). Mini-review on glycolysis and cancer. Journal of Cancer Education: the Official Journal of the American Association for Cancer Education, 28(3), 454–457. https://doi.org/10.1007/s13187-013-0486-9

Amsterdam, A., Burgess, S., Golling, G., Chen, W., Sun, Z., Townsend, K., Farrington, S., Haldi, M., & Hopkins, N. (1999). A large-scale insertional mutagenesis screen in zebrafish. *Genes & Development*, *13*(20), 2713–2724. https://doi.org/10.1101/gad.13.20.2713

Bedard, K., & Krause, K.-H. (2007). The NOX Family of ROS-Generating NADPH Oxidases: Physiology and Pathophysiology. *Physiological Reviews*, *87*(1), 245–313. https://doi.org/10.1152/physrev.00044.2005

Cantó, C., Menzies, K. J., & Auwerx, J. (2015). NAD(+) Metabolism and the Control of Energy Homeostasis: A Balancing Act between Mitochondria and the Nucleus. *Cell Metabolism*, *22*(1), 31–53. https://doi.org/10.1016/j.cmet.2015.05.023

Carney, T. J., Hardt, von der, S., Sonntag, C., Amsterdam, A., Topczewski, J., Hopkins, N., & Hammerschmidt, M. (2007). Inactivation of serine protease Matriptase1a by its inhibitor Hai1 is required for epithelial integrity of the zebrafish epidermis. *Development (Cambridge, England)*, *134*(19), 3461–3471. https://doi.org/10.1242/dev.004556

Coussens, L. M., & Werb, Z. (2002). Inflammation and cancer. *Nature*, *420*(6917), 860–867. https://doi.org/10.1038/nature01322

de Oliveira, S., López-Muñoz, A., Candel, S., Pelegrín, P., Calado, Â., & Mulero, V. (2014). ATP modulates acute inflammation in vivo through dual oxidase 1-derived H2O2 production and NF-κB activation. *Journal of Immunology (Baltimore, Md. : 1950)*, *192*(12), 5710–5719. https://doi.org/10.4049/jimmunol.1302902

DeBerardinis, R. J., & Chandel, N. S. (2016). Fundamentals of cancer metabolism. *Science Advances*, *2*(5), e1600200. https://doi.org/10.1126/sciadv.1600200

Dvorak, H. F. (1986). Tumors: wounds that do not heal. Similarities between tumor stroma generation and wound healing. *The New England Journal of Medicine*, *315*(26), 1650–1659. https://doi.org/10.1056/NEJM198612253152606

Endara, M., Masden, D., Goldstein, J., Gondek, S., Steinberg, J., & Attinger, C. (2013). The role of chronic and perioperative glucose management in high-risk surgical closures: a case for tighter glycemic control. *Plastic and Reconstructive Surgery*, *132*(4), 996–1004. https://doi.org/10.1097/PRS.0b013e31829fe119

Guo, Y.-J., Pan, W.-W., Liu, S.-B., Shen, Z.-F., Xu, Y., & Hu, L.-L. (2020). ERK/MAPK signalling pathway and tumorigenesis. *Experimental and Therapeutic Medicine*, *19*(3), 1997–2007. https://doi.org/10.3892/etm.2020.8454

Hameed, I., Masoodi, S. R., Mir, S. A., Nabi, M., Ghazanfar, K., & Ganai, B. A. (2015). Type 2 diabetes mellitus: From a metabolic disorder to an inflammatory condition. *World Journal of Diabetes*, *6*(4), 598–612. https://doi.org/10.4239/wjd.v6.i4.598

Haughian, J. M., Reno, E. M., Thorne, A. M., & Bradford, A. P. (2009). Protein kinase C alpha-dependent signaling mediates endometrial cancer cell growth and tumorigenesis. *International Journal of Cancer*, *125*(11), 2556–2564. https://doi.org/10.1002/ijc.24633

Heuberger, D. M., & Schuepbach, R. A. (2019). Protease-activated receptors (PARs): mechanisms of action and potential therapeutic modulators in PAR-driven inflammatory diseases. *Thrombosis Journal*, *17*(1), 4–24. https://doi.org/10.1186/s12959-019-0194-8

Jiang, Y., Lim, J., Wu, K.-C., Xu, W., Suen, J. Y., & Fairlie, D. P. (2021). PAR2 induces ovarian cancer cell motility by merging three signalling pathways to transactivate EGFR. *British Journal of Pharmacology*, *178*(4), 913–932. https://doi.org/10.1111/bph.15332

Kidman, K. (2008). Tissue repair and regeneration: The effects of diabetes on wound healing. *The Diabetic Foot Journal*, *Vol 11*(2), 73–80.

Kominsky, D. J., Campbell, E. L., & Colgan, S. P. (2010). Metabolic shifts in immunity and inflammation. *Journal of Immunology (Baltimore, Md. : 1950)*, *184*(8), 4062–4068. https://doi.org/10.4049/jimmunol.0903002

Kumari, S., Badana, A. K., G, M. M., G, S., & Malla, R. (2018). Reactive Oxygen Species: A Key Constituent in Cancer Survival. *Biomarker Insights*, *13*, 1177271918755391. https://doi.org/10.1177/1177271918755391

Lavoie, J. N., L'Allemain, G., Brunet, A., Müller, R., & Pouysségur, J. (1996). Cyclin D1 expression is regulated positively by the p42/p44MAPK and negatively by the p38/HOGMAPK pathway. *The Journal of Biological Chemistry*, *271*(34), 20608–20616.

Lee, R. T. H., Asharani, P. V., & Carney, T. J. (2014). Basal keratinocytes contribute to all strata of the adult zebrafish epidermis. *PLoS ONE*, *9*(1), e84858. https://doi.org/10.1371/journal.pone.0084858

List, K., Szabo, R., Molinolo, A., Sriuranpong, V., Redeye, V., Murdock, T., Burke, B., Nielsen, B. S., Gutkind, J. S., & Bugge, T. H. (2005). Deregulated matriptase causes ras-independent multistage carcinogenesis and promotes ras-mediated malignant transformation. *Genes & Development*, *19*(16), 1934–1950. https://doi.org/10.1101/gad.1300705

Little, A. C., Sulovari, A., Danyal, K., Heppner, D. E., Seward, D. J., & van der Vliet, A. (2017). Paradoxical roles of dual oxidases in cancer biology. *Free Radical Biology and Medicine*, *110*, 117–132. https://doi.org/10.1016/j.freeradbiomed.2017.05.024

Lunt, S. Y., & Vander Heiden, M. G. (2011). Aerobic glycolysis: meeting the metabolic requirements of cell proliferation. *Annual Review of Cell and Developmental Biology*, *27*(1), 441–464. https://doi.org/10.1146/annurev-cellbio-092910-154237

Ma, J., Scott, C. A., Ho, Y. N., Mahabaleshwar, H., Marsay, K. S., Zhang, C., Teow, C. K., Ng, S. S., Zhang, W., Tergaonkar, V., Partridge, L. J., Roy, S., Amaya, E., & Carney, T. J. (2021). Matriptase activation of Gq drives epithelial disruption and inflammation via RSK and DUOX. *eLife*, 10. https://doi.org/10.7554/eLife.66596

Maeda, H., Fukuyasu, Y., Yoshida, S., Fukuda, M., Saeki, K., Matsuno, H., Yamauchi, Y., Yoshida, K., Hirata, K., & Miyamoto, K. (2004). Fluorescent probes for hydrogen peroxide based on a non-oxidative mechanism. *Angewandte Chemie (International Ed. in English)*, *43*(18), 2389–2391. https://doi.org/10.1002/anie.200452381

MacCarthy-Morrogh, L., & Martin, P. (2020). The hallmarks of cancer are also the hallmarks of wound healing. *Science Signaling*, *13*(648). https://doi.org/10.1126/scisignal.aay8690

Martin, C. E., & List, K. (2019). Cell surface-anchored serine proteases in cancer progression and metastasis. *Cancer Metastasis Reviews*, *38*(3), 357–387. https://doi.org/10.1007/s10555-019-09811-7

Martínez-Navarro, F. J., Martínez-Morcillo, F. J., de Oliveira, S., Candel, S., Cabas, I., García-Ayala, A., Martínez-Menchón, T., Corbalán-Vélez, R., Mesa-Del-Castillo, P., Cayuela, M. L., Pérez-Oliva, A. B., García-Moreno, D., & Mulero, V. (2020). Hydrogen peroxide in neutrophil inflammation: Lesson from the zebrafish. *Developmental and Comparative Immunology*, *105*, 103583. https://doi.org/10.1016/j.dci.2019.103583

Maruyama, T., Kanaji, T., Nakade, S., Kanno, T., & Mikoshiba, K. (1997). 2APB, 2-aminoethoxydiphenyl borate, a membrane-penetrable modulator of Ins(1,4,5)P3-induced Ca2+ release. *Journal of Biochemistry*, *122*(3), 498–505. https://doi.org/10.1093/oxfordjournals.jbchem.a021780

Mathias, J. R., Dodd, M. E., Walters, K. B., Rhodes, J., Kanki, J. P., Look, A. T., & Huttenlocher, A. (2007). Live imaging of chronic inflammation caused by mutation of zebrafish Hai1. *Journal of Cell Science*, *120*(Pt 19), 3372–3383. https://doi.org/10.1242/jcs.009159

Matsubayashi, Y., Ebisuya, M., Honjoh, S., & Nishida, E. (2004). ERK activation propagates in epithelial cell sheets and regulates their migration during wound healing. *Current Biology : CB*, *14*(8), 731–735. https://doi.org/10.1016/j.cub.2004.03.060

Morandi, A., Taddei, M. L., Chiarugi, P., & Giannoni, E. (2017). Targeting the Metabolic Reprogramming That Controls Epithelial-to-Mesenchymal Transition in Aggressive Tumors. *Frontiers in Oncology*, *7*(6), 40. https://doi.org/10.3389/fonc.2017.00040

Morris, D. R., Ding, Y., Ricks, T. K., Gullapalli, A., Wolfe, B. L., & Trejo, J. (2006). Protease-activated receptor-2 is essential for factor VIIa and Xa-induced signaling, migration, and invasion of breast cancer cells. *Cancer Research*, *66*(1), 307–314. https://doi.org/10.1158/0008-5472.CAN-05-1735

Moura, J., Rodrigues, J., Gonçalves, M., Amaral, C., Lima, M., & Carvalho, E. (2017). Impaired T-cell differentiation in diabetic foot ulceration. *Cellular & Molecular Immunology*, *14*(9), 758–769. https://doi.org/10.1038/cmi.2015.116

Murphy, M. P. (2009). How mitochondria produce reactive oxygen species. *The Biochemical Journal*, *417*(1), 1–13.

Newton, A. C. (2018). Protein kinase C: perfectly balanced. *Critical Reviews in Biochemistry and Molecular Biology*, *53*(2), 208–230. https://doi.org/10.1080/10409238.2018.1442408

Niethammer, P., Grabher, C., Look, A. T., & Mitchison, T. J. (2009). A tissue-scale gradient of hydrogen peroxide mediates rapid wound detection in zebrafish. *Nature*, *459*(7249), 996–999. https://doi.org/10.1038/nature08119

Oberst, M. D., Singh, B., Ozdemirli, M., Dickson, R. B., Johnson, M. D., & Lin, C.-Y. (2003). Characterization of matriptase expression in normal human tissues. *The Journal of Histochemistry and Cytochemistry : Official Journal of the Histochemistry Society*, *51*(8), 1017–1025. https://doi.org/10.1177/002215540305100805

Palsson-McDermott, E. M., & O'Neill, L. A. J. (2013). The Warburg effect then and now: From cancer to inflammatory diseases. *BioEssays*, *35*(11), 965–973. https://doi.org/10.1002/bies.201300084

Patel, S., Srivastava, S., Singh, M. R., & Singh, D. (2019). Mechanistic insight into diabetic wounds: Pathogenesis, molecular targets and treatment strategies to pace wound healing. *Biomedicine & Pharmacotherapy = Biomedecine & Pharmacotherapie*, *112*, 108615. https://doi.org/10.1016/j.biopha.2019.108615

Putney, J. W., & Tomita, T. (2012). Phospholipase C signaling and calcium influx. *Advances in Biological Regulation*, *52*(1), 152–164. https://doi.org/10.1016/j.advenzreg.2011.09.005

Razzell, W., Evans, I. R., Martin, P., & Wood, W. (2013). Calcium flashes orchestrate the wound inflammatory response through DUOX activation and hydrogen peroxide release. *Current Biology : CB*, *23*(5), 424–429. https://doi.org/10.1016/j.cub.2013.01.058

Renshaw, S. A., Loynes, C. A., Trushell, D. M. I., Elworthy, S., Ingham, P. W., & Whyte, M. K. B. (2006). A transgenic zebrafish model of neutrophilic inflammation. *Blood*, *108*(13), 3976–3978. https://doi.org/10.1182/blood-2006-05-024075

Rigutto, S., Hoste, C., Grasberger, H., Milenkovic, M., Communi, D., Dumont, J. E., Corvilain, B., Miot, F., & De Deken, X. (2009). Activation of dual oxidases Duox1 and Duox2: differential regulation mediated by camp-dependent protein kinase and protein kinase C-dependent phosphorylation. *The Journal of Biological Chemistry*, *284*(11), 6725–6734. https://doi.org/10.1074/jbc.M806893200

Robinson, M. J., & Cobb, M. H. (1997). Mitogen-activated protein kinase pathways. *Current Opinion in Cell Biology*, *9*(2), 180–186.

Sales, K. U., Friis, S., Konkel, J. E., Godiksen, S., Hatakeyama, M., Hansen, K. K., Rogatto, S. R., Szabo, R., Vogel, L. K., Chen, W., Gutkind, J. S., & Bugge, T. H. (2015). Non-hematopoietic PAR-2 is essential for matriptase-driven pre-malignant progression and potentiation of ras-mediated squamous cell carcinogenesis. *Oncogene*, *34*(3), 346–356. https://doi.org/10.1038/onc.2013.563

San Martín, A., Ceballo, S., Ruminot, I., Lerchundi, R., Frommer, W. B., & Barros, L. F. (2013). A genetically encoded FRET lactate sensor and its use to detect the Warburg effect in single cancer cells. *PLoS ONE*, *8*(2), e57712. https://doi.org/10.1371/journal.pone.0057712

Schechter, N. M., Brass, L. F., Lavker, R. M., & Jensen, P. J. (1998). Reaction of mast cell proteases tryptase and chymase with protease activated receptors (PARs) on keratinocytes and fibroblasts. *Journal of Cellular Physiology*, *176*(2), 365–373. https://doi.org/10.1002/(SICI)1097-4652(199808)176:2<365::AID-JCP15>3.0.CO;2-2

Schepis, A., Barker, A., Srinivasan, Y., Balouch, E., Zheng, Y., Lam, I., Clay, H., Hsiao, C.-D., & Coughlin, S. R. (2018). Protease signaling regulates apical cell extrusion, cell contacts, and proliferation in epithelia. *The Journal of Cell Biology*, *217*(3), 1097–1112. https://doi.org/10.1083/jcb.201709118

Schlam, D., Bohdanowicz, M., Chatgilialoglu, A., Chatilialoglu, A., Steinberg, B. E., Ueyama, T., Du, G., Grinstein, S., & Fairn, G. D. (2013). Diacylglycerol kinases terminate diacylglycerol signaling during the respiratory burst leading to heterogeneous phagosomal NADPH oxidase activation. *The Journal of Biological Chemistry*, *288*(32), 23090–23104. https://doi.org/10.1074/jbc.M113.457606

Sena, L. A., Li, S., Jairaman, A., Prakriya, M., Ezponda, T., Hildeman, D. A., Wang, C.-R., Schumacker, P. T., Licht, J. D., Perlman, H., Bryce, P. J., & Chandel, N. S. (2013). Mitochondria are required for antigen-specific T cell activation through reactive oxygen species signaling. *Immunity*, *38*(2), 225–236. https://doi.org/10.1016/j.immuni.2012.10.020

Slater, E. C. (1973). The mechanism of action of the respiratory inhibitor, antimycin. *Biochimica Et Biophysica Acta (BBA) - Reviews on Bioenergetics*, *301*(2), 129–154.

Streb, H., Irvine, R. F., Berridge, M. J., & Schulz, I. (1983). Release of Ca2+ from a nonmitochondrial intracellular store in pancreatic acinar cells by inositol-1,4,5-trisphosphate. *Nature*, *306*(5938), 67–69. https://doi.org/10.1038/306067a0

Wang, Q., Shui, B., Kotlikoff, M. I., & Sondermann, H. (2008). Structural basis for calcium sensing by GCaMP2. *Structure (London, England : 1993)*, *16*(12), 1817–1827. https://doi.org/10.1016/j.str.2008.10.008

Warburg, O. (1925). The Metabolism of Carcinoma Cells. *The Journal of Cancer Research*, *9*(1), 148–163. https://doi.org/10.1158/jcr.1925.148

Wellen, K. E., & Hotamisligil, G. S. (2005). Inflammation, stress, and diabetes. *Journal of Clinical Investigation*, *115*(5), 1111–1119. https://doi.org/10.1172/JCI25102

Williamson, D. H., Lund, P., & Krebs, H. A. (1967). The redox state of free nicotinamide-adenine dinucleotide in the cytoplasm and mitochondria of rat liver. *The Biochemical Journal*, *103*(2), 514–527. https://doi.org/10.1042/bj1030514

Yoo, S. K., Freisinger, C. M., LeBert, D. C., & Huttenlocher, A. (2012). Early redox, Src family kinase, and calcium signaling integrate wound responses and tissue regeneration in zebrafish. *The Journal of Cell Biology*, *199*(2), 225–234. https://doi.org/10.1083/jcb.201203154

Zhao, Y., Yang, Y., Zhao, Y., Hu, Q., Loscalzo, J., Correspondence, Y. Y., Su, N., Cheng, F., Zou, Y., Wang, A., Hu, H., Chen, X., Zhou, H.-M., Yang, K., Huang, X., Yi, J., Zhu, Q., Zhu, L., Wang, X., et al. (2015). SoNar, a Highly Responsive NAD+/NADH Sensor, Allows High-Throughput Metabolic Screening of Anti-tumor Agents. *Cell Metabolism*, *21*(5), 777–789. https://doi.org/10.1016/j.cmet.2015.04.009

6: General Discussion

The overarching aims I set out to achieve in this project, as stipulated in the General Introduction, were to determine the usability of two genetically encoded biosensors for lactate and NADH/NAD+ ratio in the zebrafish. Then, using these sensors, elucidate whether changes in metabolism were occurring during developmental or wound healing and regenerative systems, and if so, their importance.

With molecular cloning, mRNA injections, and various positive and negative controls, I successfully confirmed the suitability of certain biosensors *in vivo*, in the zebrafish embryo. HyPerYFP is already established and used in the zebrafish, however the existing line at my disposal is insufficiently bright for imaging the early embryo. To this end, I generated a transgenic line expressing HyPer2 under the beta-actin (actb2) promoter for imaging hydrogen peroxide (H_2O_2) during embryogenesis, with expression from the one cell stage robust enough for imaging at a magnification as low as 5X. My work with the Laconic and SoNar sensors, for lactate and NADH/NAD+ ratio, respectively, was more novel, in which I established both that the sensors react as expected to their target molecules *in vivo* and created transgenic lines under the control of the ubiquitin (ubb) promoter for Laconic and SoNar, and under the actb2 promoter for Laconic only. This work provides a valuable addition to the toolbox of available biosensors, expanding the scope of metabolic research to more confidently include the use of genetically encoded biosensors *in vivo*. Other *in vivo* studies have also been conducted using alternative biosensors, for elements of metabolism besides reactive oxygen species (ROS) and glycolysis. One instance is the iNap sensors, based on a mutated version of SoNar, for monitoring NADPH level (Tao et al., 2017); iNap1 was originally formulated and tested in cell culture and as mRNA injections in zebrafish embryos, thus additionally supporting the successful use of sensors in model organisms. The creators of iNap revealed that NADPH levels decrease following larval fin amputation, co-localising with H_2O_2, likely as a result of dual oxidase (DUOX) activity consuming NADPH (Tao et al., 2017). Activity of the pentose phosphate pathway (PPP), specifically the enzyme glucose-6-phosphate dehydrogenase, is the main contributor to NADPH production (Spaans et al., 2015), and thus iNap sensors could in future studies be utilised as an indicator of the Warburg effect, which characteristically involves increased glycolysis and PPP activity to supply intermediates for macromolecule biosynthesis.

Once I had established the necessary tools in 2: Generating Tools for Imaging Metabolism in Zebrafish, I went on to utilise the transgenic lines to fulfil the aims I set out in the General Introduction. Firstly, are there detectable changes in metabolism during the first 24 hours of embryogenesis? As I was not able to produce a transgenic line for SoNar under the actb2 promoter, I investigated only lactate and H_2O_2. I found that lactate levels in the embryo began high, and declined over the cleavage stage, before beginning to rise at approximately the tenth division, coinciding with the midblastula transition (MBT). The initial elevated level of lactate may be a result of the final stages of oogenesis, which in mammals requires glycolysis and PPP activity for cytoplasmic maturation (Tsutsumi et al., 1992; Cetica et al., 2002; Xie et al., 2016; Lewis et al., 2020), though this has not been studied in fish. Embryos

undergoing cleavage divisions employ a modified cell cycle that does not include the G1 or G2 growth phases (Gilbert, 2000), and therefore have less of a requirement for substrates for biosynthesis, despite undergoing proliferation. I hypothesise that the later rise in lactate is due to the incorporation of growth into the cell cycle following the end of the synchronous cleavage period, thereby altering the cells' needs to those more akin to highly proliferative cells, such as cancer cells, and the Warburg effect is activated to supplement these needs. In support of this, mouse pre-implantation embryos have been reported to alternate between oxidative and glycolytic metabolism as necessary, which then switches almost entirely to a solely glycolysis based metabolism following implantation (Zhou et al., 2012), which corresponds approximately to the MBT. Cleaving *Xenopus* embryos also display oscillations in metabolic activity, evidenced by the dynamic changes in mitochondrial H_2O_2 in coordination with the cell cycle (Y. Han et al., 2018; Thomson, 2019). I found similar oscillations of H_2O_2 from mitochondrial activity in phase with the cell cycle in early zebrafish embryos. Furthermore, heat oscillations linked with the phosphorylation events of the cell cycle oscillator, the Cdk1-cyclin B1 complex, are present in cleavage stage zebrafish (Rodenfels et al., 2019), demonstrating a varying energetic requirement of the embryo. This may be a potential explanation for the fluctuating metabolic nature, as indicated by the levels of mitochondrial ROS. Inhibition of the mitochondria and thus the production and oscillations of H_2O_2 resulted in a developmental arrest, which is also the case in *Xenopus* (Y. Han et al., 2018), suggesting mitochondrial activity or the generation of H_2O_2 is required for progression of the cell cycle at this stage and is conserved between zebrafish and *Xenopus*. An interesting question for future studies may be to determine whether it is the mitochondrial activity or the presence of H_2O_2, perhaps acting as a second messenger, that is important within the system, for instance by introducing exogenous H_2O_2 and noting if this is sufficient to rescue the developmental arrest caused by mitochondrial inhibition.

The evidence in mouse and *Xenopus* embryos suggest that early cleavage stages possess oscillations of not just H_2O_2, but lactate as well, as metabolism dynamically alternates between an oxidative and Warburg-like metabolism (Zhou et al., 2012; Thomson, 2019). In this project I was unable to detect oscillations in lactate with the Laconic sensor; however it may be that my imaging or the sensor itself was insufficiently sensitive. Work in the future could aim to examine this period in more detail to elucidate whether lactate oscillations also occur in the zebrafish.

My second system of interest was a wound healing and regeneration model, in the larval zebrafish fin. Given the increased level of proliferation involved in the regrowth of lost tissue following amputation, I suspected there could be potential for the Warburg effect. However, I did not detect significantly higher levels of lactate in amputated tails during the outgrowth phase or over the course of regeneration, except in the "notochord bead" blastema-like structure of tail amputated larva. Other work has shown elevated levels of glycolysis gene expression and decreased mitochondrial activity in the blastema-like region during zebrafish heart regeneration (Honkoop et al., 2019), which concurs with the elevated lactate production I witnessed in the analogous structure in larval tail amputation. In fact, elevated glycolysis has been found by others in zebrafish following tail

amputation, and inhibition of glycolysis results in abnormal blastema formation (Sinclair et al., 2020). I did consistently find, however, that a very rapid, very transient increase in lactate occurs immediately following amputation, and have presented reasonable evidence for this increase to be a result of rapid energy production to fuel the contraction of the actomyosin cable responsible for closure and contraction of the wound. Inhibition of lactate dehydrogenase (LDH), the enzyme that converts pyruvate into lactate to regenerate NAD+ and allow continuation of glycolysis independently of mitochondrial activity, results in failure of the wound to contract and a lack of actin re-organisation and concentration at the wound border. Inhibiting mitochondrial activity does not cause an attenuation of wound contraction, suggesting this process is dependent on glycolysis. A role of glycolysis, similar to my hypothesis here, has been shown in the brains of mice, whereby upon brain excitation neurons increase their glucose consumption and glycolysis temporarily exceeds the rate of oxidative metabolism to provide for the rapid increase in energy demand (Díaz-García et al., 2017). It was previously proposed that glycolysis activity occurred predominantly in astrocytes as a means to provide lactate as a fuel for neurons (Mächler et al., 2016), however it was later shown that neuronal metabolism is not affected by uptake of lactate from astrocytes (Díaz-García et al., 2017). Furthermore, enucleation requires contraction of an actomyosin ring; this process in erythrocytes is prevented, and ATP production diminished, when aerobic glycolysis is blocked by inhibition of the glycolytic enzymes glyceraldehyde-3-phosphate dehydrogenase (GAPDH) or LDH (Goto et al., 2019). Thus, the function of glycolysis as a means of rapid ATP production has previously been been demonstrated in other systems, supporting my comparable hypothesis in zebrafish fin amputation wound closure.

Inhibiting LDH or glycolysis itself over the entirety of regeneration resulted in shorter regenerated fin lengths, significantly in tail amputations, suggesting aerobic glycolysis is required for successful regeneration and potentially involved in the formation of the notochord bead, considering the result was not significant following fin fold amputations in which only epidermal tissue is excised. My work therefore suggests glycolysis is important during wound healing and regeneration for two distinct purposes: for the closure of the wound via actomyosin cable, which is a novel finding in this model, and for the formation of the notochord bead blastema, which has been alluded to in other works in the past (Sinclair et al., 2020). Though the blastema is typically highly proliferative, there is an absence of raised lactate levels during the proliferative phase of fin fold regeneration. An importance of lactate or glycolysis in the formation of the blastema may suggest a role aside from the Warburg effect, such that the role of lactate I observed may be to act as a second messenger. For example, lactate has recently been shown to mediate magnesium uptake into the mitochondria (Chubanov & Gudermann, 2020), which in turn has been reported to have a stimulatory effect on oxidative metabolism and may affect calcium flux into and out of the mitochondria (reviewed in Pilchova et al., 2017). The downstream targets and signalling stimulated by lactate in this instance remain unknown, their elucidation a possible direction for future studies to take.

As ROS is known to interact with glycolysis, I sought the effects on lactate production of adding H_2O_2 following fin amputation. H_2O_2 has been shown to drive up-regulation of glycolysis and increased uptake of glucose (Shi et al., 2009; reviewed in Liemburg-Apers et al., 2015), while also having an inhibitory effect on glycolysis enzymes

such as GAPDH, putatively to cause a shunt towards the PPP (Kuehne et al., 2015) and generation of reduced glutathione (GSH) to detoxify H_2O_2. Previous literature shows overall regeneration is impaired by inhibition of H_2O_2 generation (Yoo et al., 2012) and a lack of H_2O_2 has a negative effect on blastema formation (Romero et al., 2018). Non-mitochondrial ROS are required and sufficient for axonal outgrowth following sciatic nerve crush injury in mice, with H_2O_2 pre-treatment increasing recovery rate (Hervera et al., 2018), and adding exogenous H_2O_2 similarly promotes regeneration axons in zebrafish larval fin amputations, while inhibition in *duox* morphants prevents axon regrowth (Rieger & Sagasti, 2011). However, I found upon H_2O_2 treatment lactate levels failed to rise immediately following amputation and wound contraction was significantly lessened, indicating a negative effect from increased levels of H_2O_2. A study in *C. elegans* showed mitochondrial ROS is in fact required for the actin-based wound closure (Xu & Chisholm, 2014); thus perhaps the level of added H_2O_2 in my experiment was over a threshold whereby it transferred from beneficial to detrimental. The dichotomy between previous positive documentation of H_2O_2 on regeneration and my results may also be due to lactate or glycolysis having different roles in each context: for example, in the blastema, lactate maybe be acting as a second messenger to activate downstream signalling cascades, or its elevated levels may be a consequence of the Warburg effect to support the blastema's proliferative requirements. In the newly amputated fin, lactate is likely a result of rapid glycolysis to provide a swift peak of energy. Consequently, H_2O_2 may influence these two instances differently. In the former, there is an additional emphasis on the PPP, thus inhibition of glycolytic enzymes may be beneficial to aid shunting of intermediates to the PPP, whereas an inhibition of glycolysis enzymes during actomyosin contraction would simply hinder the primary source of energy production. In the context of the blastema, H_2O_2 may also act as a second messenger, such as its role in activating Hedgehog signalling in and formation of the notochord bead (Romero et al., 2018).

I attempted only an addition of H_2O_2, and the effect of inhibiting H_2O_2 production on wound closure and contraction in zebrafish fin amputation is not currently known. In future, investigating the more immediate effects of blocking ROS production—for instance with chemical inhibitors such as diphenyleneiodonium (DPI), or with morpholinos against DUOX—could indicate whether the roles of ROS are conserved between species, with a requirement for H_2O_2 in wound contraction in the same manner as *C. elegans*, and a window of ideal ROS levels above or below which regeneration is compromised.

Finally, I investigated the metabolic state in the zebrafish epidermal *hai1a* mutant. I found that the levels of lactate increased in areas corresponding with the severity of the phenotype, and were markedly elevated at 48hpf, when proliferation is also significantly increased (Carney et al., 2007). This suggests increased activity of glycolysis is associated with the epidermal motility and aggregate formation, potentially as an indication of the Warburg effect supplying glycolytic and PPP intermediates for biosynthesis as proliferation increases. Glycolysis has also been shown to be stimulated alongside epithelial to mesenchyme transitions (EMTs) downstream of transforming growth factor beta (TGF-β) signalling in cancer cells (Lee et al., 2015), and a partial EMT occurs in the *hai1a* mutant as epidermal cells gain motility and form aggregates, thus the elevated glycolysis activity in the mutant

may be a result of one or both these elements: proliferation and EMT. EMT, again regulated by TGF-β signalling, is also a key component during wound healing, permitting re-epithelialisation (reviewed in Barriere et al., 2015) and required for formation of the blastema in tail regeneration in the gecko (Gilbert et al., 2013), drawing resemblances between the mutant, cancer, and wound healing.

Though the pattern of lactate production is dissimilar between the *hai1a* mutant and the regenerative response, I found the state of H_2O_2 and calcium levels to be remarkably similar. Both H_2O_2 and calcium are required for the inflammatory immune response activated in the first phase of wound healing and overall regeneration (Niethammer et al., 2009; Yoo et al., 2012), and similarly an inhibition of H_2O_2 production or—to an extent—calcium signalling attenuates the inflammatory response in the mutant (Ma et al., 2021). The similarities the mutant phenotype shares with cancer are also reasons that cancer has been likened to a constantly healing wound, including the involvement of EMT, inflammation, and increased levels of proliferation (reviewed in MacCarthy-Morrogh & Martin, 2020). As such, I proposed the *hai1a* zebrafish mutant as a genetic model of constitutive wound healing. This could be a useful tool in future research, as the impressive healing ability of the zebrafish renders its use for study of chronic wounds more challenging, and this model may provide a method of doing so. For example, the reduced ability to heal in diabetic patients has been linked to high glucose levels (Endara et al., 2013) and oxidative stress is implicated in many of the complications of diabetes (reviewed in Blakytny & Jude, 2006), while addition of GSH to detoxify H_2O_2 aids healing in mice (Mudge et al., 2002). Both glycolysis and H_2O_2 are elevated in the zebrafish *hai1a* mutant, and manipulation of these with the aim to rescue the phenotype may provide insight into potential treatment targets for chronic wounds such as diabetic foot ulcers.

As a whole my work contributes, firstly, several transgenic lines for use in the zebrafish community, and overall I provide further evidence of the importance of aerobic glycolysis, both in a proliferative context and in a non-Warburg-related role for rapid energy generation. I also show a conserved potential role for H_2O_2 or mitochondrial activity in cleavage stage embryos, though future study is required to resolve whether H_2O_2 is required as a second messenger or is an indication of mitochondrial respiration.

Following on from this work, one question that has yet to be answered is whether glycolysis is important following the MBT, the point at which I observed a rise in lactate levels beginning to occur. My attempts at pharmacological intervention were not successful, in that I could not confirm the effects of the drug were as intended, despite yielding promising results with embryos exhibiting arrested development during gastrulation when treated with a drug that supposedly inhibits LDH. With more time, a more suitable solution could be found to address whether aerobic glycolysis is necessary for epiboly and development from the MBT onwards.

Pulses of actomyosin contraction contribute to driving convergence extension processes in embryogenesis (reviewed in Sutherland & Lesko, 2020), including during gastrulation of *Drosophila* (Bertet et al., 2004), *Xenopus* (Kim & Davidson, 2011), and mouse (Williams et al., 2014). Though this has not yet been shown in zebrafish, convergence extension processes similarly occur during epiboly (Warga & Kimmel, 1990). Combining my

hypothesis for glycolysis providing energy for wound contraction, and the increasing lactate levels I witnessed from the onset of gastrulation, potentially a comparable mechanism is occurring in the zebrafish, with punctuated contractions of actomyosin being involved in convergence extension cell movements and requiring rapid energy generated by glycolysis, explaining the rise in lactate at this stage. It would be fascinating to investigate whether these contraction pulses are conserved in zebrafish gastrulation, and if so, whether they are dependent on glycolysis and if inhibition of rapid glycolysis disrupts embryo elongation.

Of additional noteworthy interest is the relationship between ROS and glycolysis. There is evidence linking the two in regulating one another in cancer (Shi et al., 2009), and the next pertinent step may be to determine whether a similar relationship of ROS and glycolysis is also apparent in wounding and regeneration models in the zebrafish. ROS produced at the wound margin of zebrafish larval fin fold amputations is required for expression of the EMT marker *vimentin*, which is required for collagen organisation in the epithelial projections that guide regrowth during regeneration (LeBert et al., 2018), and in gecko tail regeneration TGF-β-induced EMT is involved in blastema formation (Gilbert et al., 2013). TGF-β is one of the pathways ROS is known to interact with, and ROS has in fact been shown to mediate EMT via TGF-β (reviewed in Liu & Desai, 2015). As mentioned previously, glycolysis is stimulated by TGF-β alongside EMT in cancer (Lee et al., 2015). One might ask whether inhibition of H_2O_2—known to attenuate proliferation and the regenerative response—in zebrafish larval tail amputation (Yoo et al., 2012) or zebrafish heart injury (P. Han et al., 2014) also impacts the presence of lactate or glycolysis gene expression in the regenerating tissue or blastema.

Expanding on this link, the interconnections between other various metabolites, or between metabolites and their effects on metabolism, is also an area that still has much potential to be explored. For instance, it is known that calcium is able to regulate oxidative phosphorylation (OXPHOS) by entering the mitochondria (reviewed in Llorente-Folch et al., 2015), but it is not currently known how this fits in with the role calcium may play on activating DUOX and production of H_2O_2, which, as discussed, is implicated in stimulating glycolysis and the Warburg effect, a key component of which is down-regulated mitochondrial activity. The use of genetically encoded sensors, such as GECIs, HyPer, and Laconic, and pharmacological treatments to inhibit each element, may be one approach to comprehend the potential associations between calcium, H_2O_2, and glycolysis. Does calcium stimulate H_2O_2 production, both non- and mitochondrial via DUOX and/or increased OXPHOS? Does this H_2O_2 go on to inhibit mitochondrial respiration enzymes and up-regulate glycolysis via hypoxia-inducible factor-1-alpha (HIF1α) signalling[1]? Does glycolysis then increase lactate production, for activity of lactate as a second messenger? It is clear that a complex web of interactions remain to be deciphered. Revealing the complete interrelationships between the vast array of metabolites is a lofty goal to aspire to, but as an initial step, knowledge in particular of the extent ROS relates to glycolysis would assist in illuminating the molecular pathways involved in successful regeneration, bringing regenerative medical treatment one step closer to realisation.

[1] HIF1α signalling has been previously linked to stimulating glycolysis (reviewed in Nagao et al., 2019; Mathieu et al., 2014; Prigione et al., 2014), as well as shown to be necessary for *Xenopus* tail regeneration (Ferreira et al., 2018), and also activated by H_2O_2 (Bonello et al., 2007).

References

Barriere, G., Fici, P., Gallerani, G., Fabbri, F., & Rigaud, M. (2015). Epithelial Mesenchymal Transition: a double-edged sword. *Clinical and Translational Medicine*, *4*(1), 14. https://doi.org/10.1186/s40169-015-0055-4

Bertet, C., Sulak, L., & Lecuit, T. (2004). Myosin-dependent junction remodelling controls planar cell intercalation and axis elongation. *Nature*, *429*(6992), 667–671. https://doi.org/10.1038/nature02590

Blakytny, R., & Jude, E. (2006). The molecular biology of chronic wounds and delayed healing in diabetes. *Diabetic Medicine : a Journal of the British Diabetic Association*, *23*(6), 594–608. https://doi.org/10.1111/j.1464-5491.2006.01773.x

Bonello, S., Zähringer, C., BelAiba, R. S., Djordjevic, T., Hess, J., Michiels, C., Kietzmann, T., & Görlach, A. (2007). Reactive oxygen species activate the HIF-1alpha promoter via a functional NFkappaB site. *Arteriosclerosis, Thrombosis, and Vascular Biology*, *27*(4), 755–761. https://doi.org/10.1161/01.ATV.0000258979.92828.bc

Carney, T. J., Hardt, von der, S., Sonntag, C., Amsterdam, A., Topczewski, J., Hopkins, N., & Hammerschmidt, M. (2007). Inactivation of serine protease Matriptase1a by its inhibitor Hai1 is required for epithelial integrity of the zebrafish epidermis. *Development (Cambridge, England)*, *134*(19), 3461–3471. https://doi.org/10.1242/dev.004556

Cetica, P., Pintos, L., Dalvit, G., & Beconi, M. (2002). Activity of key enzymes involved in glucose and triglyceride catabolism during bovine oocyte maturation in vitro. *Reproduction (Cambridge, England)*, *124*(5), 675–681.

Chubanov, V., & Gudermann, T. (2020). Lactate as a new second messenger shaping intracellular Mg2+ dynamics and bioenergetics. *Cell Calcium*, *93*, 102329. https://doi.org/10.1016/j.ceca.2020.102329

Díaz-García, C. M., Mongeon, R., Lahmann, C., Koveal, D., Zucker, H., & Yellen, G. (2017). Neuronal Stimulation Triggers Neuronal Glycolysis and Not Lactate Uptake. *Cell Metabolism*, *26*(2), 361–374.e364. https://doi.org/10.1016/j.cmet.2017.06.021

Endara, M., Masden, D., Goldstein, J., Gondek, S., Steinberg, J., & Attinger, C. (2013). The role of chronic and perioperative glucose management in high-risk surgical closures: a case for tighter glycemic control. *Plastic and Reconstructive Surgery*, *132*(4), 996–1004. https://doi.org/10.1097/PRS.0b013e31829fe119

Ferreira, F., Raghunathan, V., Luxardi, G., Zhu, K., & Zhao, M. (2018). Early redox activities modulate Xenopus tail regeneration. *Nature Communications*, *9*(1), 4296–15. https://doi.org/10.1038/s41467-018-06614-2

Gilbert, S. F. (2000). An Introduction to Early Developmental Processes. In *Developmental Biology. 6th edition*. Sinauer Associates.

Gilbert, R. W. D., Vickaryous, M. K., & Viloria-Petit, A. M. (2013). Characterization of TGFβ signaling during tail regeneration in the leopard Gecko (Eublepharis macularius). *Developmental Dynamics : an Official Publication of the American Association of Anatomists*, *242*(7), 886–896. https://doi.org/10.1002/dvdy.23977

Goto, T., Ubukawa, K., Kobayashi, I., Sugawara, K., Asanuma, K., Sasaki, Y., Guo, Y.-M., Takahashi, N., Sawada, K., Wakui, H., & Nunomura, W. (2019). ATP produced by anaerobic glycolysis is essential for enucleation of human erythroblasts. *Experimental Hematology*, *72*, 14–26.e1. https://doi.org/10.1016/j.exphem.2019.02.004

Han, P., Zhou, X.-H., Chang, N., Xiao, C.-L., Yan, S., Ren, H., Yang, X.-Z., Zhang, M.-L., Wu, Q., Tang, B., Diao, J.-P., Zhu, X., Zhang, C., Li, C.-Y., Cheng, H., & Xiong, J.-W. (2014). Hydrogen peroxide primes heart regeneration with a derepression mechanism. *Cell Research*, *24*(9), 1091–1107. https://doi.org/10.1038/cr.2014.108

Han, Y., Ishibashi, S., Iglesias-Gonzalez, J., Chen, Y., Love, N. R., & Amaya, E. (2018). Ca2+-Induced Mitochondrial ROS Regulate the Early Embryonic Cell Cycle. *Cell Reports*, *22*(1), 218–231. https://doi.org/10.1016/j.celrep.2017.12.042

Hervera, A., De Virgiliis, F., Palmisano, I., Zhou, L., Tantardini, E., Kong, G., Hutson, T., Danzi, M. C., Perry, R. B.-T., Santos, C. X. C., Kapustin, A. N., Fleck, R. A., Del Río, J. A., Carroll, T., Lemmon, V., Bixby, J. L., Shah, A. M., Fainzilber, M., & Di Giovanni, S. (2018). Reactive oxygen species regulate axonal regeneration through the release of exosomal NADPH oxidase 2 complexes into injured axons. *Nature Cell Biology*, *20*(3), 307–319. https://doi.org/10.1038/s41556-018-0039-x

Honkoop, H., de Bakker, D. E., Aharonov, A., Kruse, F., Shakked, A., Nguyen, P. D., de Heus, C., Garric, L., Muraro, M. J., Shoffner, A., Tessadori, F., Peterson, J. C., Noort, W., Bertozzi, A., Weidinger, G., Posthuma, G., Grün, D., van der Laarse, W. J., Klumperman, J., et al. (2019). Single-cell analysis uncovers that metabolic reprogramming by ErbB2 signaling is essential for cardiomyocyte proliferation in the regenerating heart. *eLife*, *8*, 98. https://doi.org/10.7554/eLife.50163

Kim, H. Y., & Davidson, L. A. (2011). Punctuated actin contractions during convergent extension and their permissive regulation by the non-canonical Wnt-signaling pathway. *Journal of Cell Science*, *124*(Pt 4), 635–646. https://doi.org/10.1242/jcs.067579

Kuehne, A., Emmert, H., Soehle, J., Winnefeld, M., Fischer, F., Wenck, H., Gallinat, S., Terstegen, L., Lucius, R., Hildebrand, J., & Zamboni, N. (2015). Acute Activation of Oxidative Pentose Phosphate Pathway as First-Line Response to Oxidative Stress in Human Skin Cells. *Molecular Cell*, *59*(3), 359–371. https://doi.org/10.1016/j.molcel.2015.06.017

LeBert, D., Squirrell, J. M., Freisinger, C., Rindy, J., Golenberg, N., Frecentese, G., Gibson, A., Eliceiri, K. W., & Huttenlocher, A. (2018). Damage-induced reactive oxygen species regulate vimentin and dynamic collagen-based projections to mediate wound repair. *eLife*, *7*, 28. https://doi.org/10.7554/eLife.30703

Lee, S. Y., Jeon, H. M., Ju, M. K., Jeong, E. K., Kim, C. H., Yoo, M.-A., Park, H. G., Han, S. I., & Kang, H. S. (2015). Dlx-2 is implicated in TGF-β- and Wnt-induced epithelial-mesenchymal, glycolytic switch, and mitochondrial repression by Snail activation. *International Journal of Oncology*, *46*(4), 1768–1780. https://doi.org/10.3892/ijo.2015.2874

Lewis, N., Hinrichs, K., Leese, H. J., McG Argo, C., Brison, D. R., & Sturmey, R. (2020). Energy metabolism of the equine cumulus oocyte complex during in vitro maturation. *Scientific Reports*, *10*(1), 3493–10. https://doi.org/10.1038/s41598-020-60624-z

Liemburg-Apers, D. C., Willems, P. H. G. M., Koopman, W. J. H., & Grefte, S. (2015). Interactions between mitochondrial reactive oxygen species and cellular glucose metabolism. *Archives of Toxicology*, *89*(8), 1209–1226. https://doi.org/10.1007/s00204-015-1520-y

Liu, R.-M., & Desai, L. P. (2015). Reciprocal regulation of TGF-β and reactive oxygen species: A perverse cycle for fibrosis. *Redox Biology*, *6*, 565–577. https://doi.org/10.1016/j.redox.2015.09.009

Llorente-Folch, I., Rueda, C. B., Pardo, B., Szabadkai, G., Duchen, M. R., & Satrustegui, J. (2015). The regulation of neuronal mitochondrial metabolism by calcium. *The Journal of Physiology*, *593*(16), 3447–3462. https://doi.org/10.1113/JP270254

Ma, J., Scott, C. A., Ho, Y. N., Mahabaleshwar, H., Marsay, K. S., Zhang, C., Teow, C. K., Ng, S. S., Zhang, W., Tergaonkar, V., Partridge, L. J., Roy, S., Amaya, E., & Carney, T. J. (2021). Matriptase activation of Gq drives epithelial disruption and inflammation via RSK and DUOX. *eLife*, 10. https://doi.org/10.7554/eLife.66596

MacCarthy-Morrogh, L., & Martin, P. (2020). The hallmarks of cancer are also the hallmarks of wound healing. *Science Signaling*, *13*(648). http://doi.org/10.1126/scisignal.aay8690

Mächler, P., Wyss, M. T., Elsayed, M., Stobart, J., Gutierrez, R., Faber-Castell, von, A., Kaelin, V., Zuend, M., Martín, A. S., Romero-Gómez, I., Baeza-Lehnert, F., Lengacher, S., Schneider, B. L., Aebischer, P., Magistretti, P. J., Barros, L. F., & Weber, B. (2016). In Vivo Evidence for a Lactate Gradient from Astrocytes to Neurons. *Cell Metabolism*, *23*(1), 94–102. https://doi.org/10.1016/j.cmet.2015.10.010

Mathieu, J., Zhou, W., Xing, Y., Sperber, H., Ferreccio, A., Agoston, Z., Kuppusamy, K. T., Moon, R. T., & Ruohola-Baker, H. (2014). Hypoxia-inducible factors have distinct and stage-specific roles during reprogramming of human cells to pluripotency. *Cell Stem Cell*, *14*(5), 592–605. https://doi.org/10.1016/j.stem.2014.02.012

Mudge, B. P., Harris, C., Gilmont, R. R., Adamson, B. S., & Rees, R. S. (2002). Role of glutathione redox dysfunction in diabetic wounds. *Wound Repair and Regeneration : Official Publication of the Wound Healing Society [and] the European Tissue Repair Society*, *10*(1), 52–58. https://doi.org/10.1046/j.1524-475x.2002.10803.x

Nagao, A., Kobayashi, M., Koyasu, S., Chow, C. C. T., & Harada, H. (2019). HIF-1-Dependent Reprogramming of Glucose Metabolic Pathway of Cancer Cells and Its Therapeutic Significance. *International Journal of Molecular Sciences*, *20*(2), 238. https://doi.org/10.3390/ijms20020238

Niethammer, P., Grabher, C., Look, A. T., & Mitchison, T. J. (2009). A tissue-scale gradient of hydrogen peroxide mediates rapid wound detection in zebrafish. *Nature*, *459*(7249), 996–999. https://doi.org/10.1038/nature08119

Pilchova, I., Klacanova, K., Tatarkova, Z., Kaplan, P., & Racay, P. (2017). The Involvement of Mg2+ in Regulation of Cellular and Mitochondrial Functions. *Oxidative Medicine and Cellular Longevity*, *2017*(3), 6797460–6797468. https://doi.org/10.1155/2017/6797460

Prigione, A., Rohwer, N., Hoffmann, S., Mlody, B., Drews, K., Bukowiecki, R., Blümlein, K., Wanker, E. E., Ralser, M., Cramer, T., & Adjaye, J. (2014). HIF1α modulates cell fate reprogramming through early glycolytic shift and upregulation of PDK1-3 and PKM2. *Stem Cells (Dayton, Ohio)*, *32*(2), 364–376. https://doi.org/10.1002/stem.1552

Rieger, S., & Sagasti, A. (2011). Hydrogen peroxide promotes injury-induced peripheral sensory axon regeneration in the zebrafish skin. *PLoS Biology*, 9(5), e1000621. https://doi.org/10.1371/journal.pbio.1000621

Rodenfels, J., Neugebauer, K. M., & Howard, J. (2019). Heat Oscillations Driven by the Embryonic Cell Cycle Reveal the Energetic Costs of Signaling. *Developmental Cell*, *48*(5), 646–658.e646. https://doi.org/10.1016/j.devcel.2018.12.024

Romero, M. M. G., McCathie, G., Jankun, P., & Roehl, H. H. (2018). Damage-induced reactive oxygen species enable zebrafish tail regeneration by repositioning of Hedgehog expressing cells. *Nature Communications*, *9*(1), 4010–4011. https://doi.org/10.1038/s41467-018-06460-2

Shi, D.-Y., Xie, F.-Z., Zhai, C., Stern, J. S., Liu, Y., & Liu, S.-L. (2009). The role of cellular oxidative stress in regulating glycolysis energy metabolism in hepatoma cells. *Molecular Cancer*, *8*(1), 32–15. https://doi.org/10.1186/1476-4598-8-32

Sinclair, J. W., Hoying, D. R., Bresciani, E., Nogare, D. D., Needle, C. D., Wu, W., Bishop, K., Elkahloun, A. G., Chitnis, A., Liu, P., & Burgess, S. M. (2020). A metabolic shift to glycolysis promotes zebrafish tail regeneration through TGF–β dependent dedifferentiation of notochord cells to form the blastema. *bioRxiv*, *21*(1), 2020.03.03.975318. https://doi.org/10.1101/2020.03.03.975318

Spaans, S. K., Weusthuis, R. A., van der Oost, J., & Kengen, S. W. M. (2015). NADPH-generating systems in bacteria and archaea. *Frontiers in Microbiology*, *6*, 742. http://doi.org/10.3389/fmicb.2015.00742

Sutherland, A., & Lesko, A. (2020). Pulsed actomyosin contractions in morphogenesis. *F1000Research*, *9*(142), 142. https://doi.org/10.12688/f1000research.20874.1

Tao, R., Zhao, Y., Chu, H., Wang, A., Zhu, J., Chen, X., Zou, Y., Shi, M., Liu, R., Su, N., Du, J., Zhou, H.-M., Zhu, L., Qian, X., Liu, H., Loscalzo, J., & Yang, Y. (2017). Genetically encoded fluorescent sensors reveal dynamic regulation of NADPH metabolism. *Nature Methods*, *14*(7), 720–728. https://doi.org/10.1038/nmeth.4306

Thomson, C. (2019). *Metabolic Patterning and Regulation During Early Embryo Development and Appendage Regeneration* (E. Amaya, Ed.).

Tsutsumi, O., Satoh, K., Taketani, Y., & Kato, T. (1992). Determination of enzyme activities of energy metabolism in the maturing rat oocyte. *Molecular Reproduction and Development*, *33*(3), 333–337. https://doi.org/10.1002/mrd.1080330315

Warga, R. M., & Kimmel, C. B. (1990). Cell movements during epiboly and gastrulation in zebrafish. *Development (Cambridge, England)*, *108*(4), 569–580. http://eutils.ncbi.nlm.nih.gov/entrez/eutils/elink.fcgi?dbfrom=pubmed&id=2387236&retmode=ref&cmd=prlinks

Williams, M., Yen, W., Lu, X., & Sutherland, A. (2014). Distinct apical and basolateral mechanisms drive planar cell polarity-dependent convergent extension of the mouse neural plate. *Developmental Cell*, *29*(1), 34–46. https://doi.org/10.1016/j.devcel.2014.02.007

Xie, H.-L., Wang, Y.-B., Jiao, G.-Z., Kong, D.-L., Li, Q., Li, H., Zheng, L.-L., & Tan, J.-H. (2016). Effects of glucose metabolism during in vitro maturation on cytoplasmic maturation of mouse oocytes. *Scientific Reports*, *6*(1), 20764–11. https://doi.org/10.1038/srep20764

Xu, S., & Chisholm, A. D. (2014). C. elegans epidermal wounding induces a mitochondrial ROS burst that promotes wound repair. *Developmental Cell*, *31*(1), 48–60. https://doi.org/10.1016/j.devcel.2014.08.002

Yoo, S. K., Freisinger, C. M., LeBert, D. C., & Huttenlocher, A. (2012). Early redox, Src family kinase, and calcium signaling integrate wound responses and tissue regeneration in zebrafish. *The Journal of Cell Biology*, *199*(2), 225–234. https://doi.org/10.1083/jcb.201203154

Zhou, W., Choi, M., Margineantu, D., Margaretha, L., Hesson, J., Cavanaugh, C., Blau, C. A., Horwitz, M. S., Hockenbery, D., Ware, C., & Ruohola-Baker, H. (2012). HIF1α induced switch from bivalent to exclusively glycolytic metabolism during ESC-to-EpiSC/hESC transition. *The EMBO Journal*, *31*(9), 2103–2116. https://doi.org/10.1038/emboj.2012.71

Appendix

YouTube links to view Supplementary Movies associated with indicated Figures:

Supplementary Movie 1 (FIG 3.1A) – Laconic in development (lateral)

https://youtu.be/tIoEufDrX8k

Tg[actb2:laconic] embryo imaged at 5X every 10 minutes for the first 4 hours, then every 15 minutes until 24 hours.

Supplementary Movie 2 (FIG 3.3A) – HyPerYFP in development (lateral, Singapore)

https://youtu.be/sTCQpFe9maE

Tg[actb2:hyper] embryo imaged at 5X every 15 minutes for 24 hours.

Supplementary Movie 3 (FIG 3.3D) – HyPerYFP oscillations (animal, Singapore)

https://youtu.be/dmnxg32anIw

Tg[actb2:hyper] embryo imaged at 5X every 5 minutes for 8 hours.

Supplementary Movie 4 (FIG 3.3G) – HyPerYFP in development (lateral, Manchester)

https://youtu.be/6MAIQPtwydo

Tg[actb2:hyper] embryo imaged at 5X every 5 minutes for 4.5 hours.

Supplementary Movie 5 (FIG 3.3 I) – HyPerYFP oscillations (lateral, Manchester)

https://youtu.be/gyAUn7kZt3I

Tg[actb2:hyper] embryo imaged at 5X every 5 minutes for 8 hours.

Supplementary Movie 6 (FIG 3.4A) – HyPerYFP in development +NaN_3

https://youtu.be/X4ikKzGonaU

Tg[actb2:hyper] embryo imaged at 5X every 5 minutes for 5 hours.

Supplementary Movie 7 (FIG 5.3A and B) – Calcium in *hai1a*^{fr26} mutants and siblings at 24hpf

https://youtu.be/RZDj3Tngf1M

Confocal imaging maximal Z-projections of the trunk and tail regions of 24hpf *hai1a*^{fr26} homozygous mutants and siblings injected at the one cell stage with GCaMP-6s, imaged every 2 minutes for 10 minutes. YouTube video is looped six times.

Supplementary Movie 8 (FIG 5.4C) – Calcium in *hai1a*^{fr26} mutants with 2-APB treatment at 24hpf

https://youtu.be/EvgFj6Mgq18

Confocal imaging maximal Z-projections of the trunk and tail regions of 24hpf *hai1a*^{fr26} homozygous mutants and siblings injected at the one cell stage with GCaMP-6s and treated with 3μM 2-APB to inhibit calcium signalling, imaged every 2 minutes for 10 minutes. YouTube video is looped six times.

Supplementary Movie 9 (FIG 5.5C) – Lightsheet movies of neutrophils and keratinocytes with PMA treatment at 72hpf

https://youtu.be/QK_LZS844r8

Lightsheet imaging maximal Z-projections of 72hpf *Tg[mpx:EGFP;krtt1c19e:lyn-tdTomato]* embryos treated at 2dpf with 37.5ng/mL PMA.

Supplementary Movie 10 (FIG 5.5D) – Calcium in 24hpf embryos treated with PMA

https://youtu.be/3E-2ESfEWNE

Confocal imaging maximal Z-projections of the trunk and tail regions of 24hpf wild type embryos injected at the one cell stage with GCaMP-6s and either untreated control or treated at 19hpf with 100ng/mL PMA to activate PKC or with DMSO control, imaged every 2 minutes for 10 minutes. YouTube video is looped six times.